KAUNAS UNIVERSITY OF TECHNOLOGY

TOMAS VAITKŪNAS

INTEGRATED EXPERIMENTAL-COMPUTATIONAL APPROACH FOR FAILURE PREDICTION IN COMPOSITE MATERIALS UNDER FATIGUE LOADING

Doctoral dissertation
Technological Sciences, Mechanical Engineering (T 009)

2024, Kaunas

KAUNO TECHNOLOGIJOS UNIVERSITETAS

TOMAS VAITKŪNAS

CIKLIŠKAI APKRAUTŲ KOMPOZITINIŲ KONSTRUKCIJŲ IRIMO PROGNOZAVIMAS NAUDOJANT EKSPERIMENTINIUS-SKAITINIUS METODUS

Daktaro disertacija
Technologijos mokslai, mechanikos inžinerija (T 009)

2024, Kaunas

CONTENTS

LIST OF TABLES

LIST OF FIGURES

8

LIST OF ABBREVIATIONS
AOI – area of interest
BBPD – bond-based peridynamics
CCM – classical continuum mechanics
CFRP – carbon fiber-reinforced composite
CZM – cohesive zone modelling
DIC – digital image correlation
FE – finite elements
FEM – finite element modelling
FOV – field of view
GFRP – glass fiber-reinforced composite
KTF – kinetic theory of fracture
MEI – metrological efficiency indicator
NDT – non-destructive testing
NDE – non-destructive evaluation
NSSD – normalized sum-square difference
PD – peridynamics
PDDO – peridynamic differential operator
SBPD – state-based peridynamics
UTM – universal tensile machine
VCCT – virtual crack closure technique
VSG – virtual strain gauge
XFEM – extended finite elements

INTRODUCTION

Fatigue damage identification and fatigue damage growth prognosis including the final failure of a material are actual engineering tasks in many industries, such as transport, energy, and civil engineering. The question is important not only for metallic, but especially for *Carbon* and *Glass Fiber Reinforced Polymer Composites* (*CFRP* and *GFRP*). Lightweight high strength properties increase the structure performance and make the CFRP/GFRP attractive for use in special industries, such as aviation, wind energy, and sports. Also, polymer composites as materials can be selected due to better corrosion resistance than metallic analogues, as well as because of ecological aspects (since thermoplastic composites can be derived from recycled polymers [1]).

Numerical fatigue modelling of composites faces several challenges. One of them is the discontinuous nature of the fatigue process (fatigue crack initiation and growth). The currently existing *Finite Element* (FE) formulations are based on spatial derivatives of the displacement field and are not valid for the case of crack-resulted discontinuity. Advanced FE, such as the *Extended Finite Element Method* (XFEM) [2], *Cohesive Zone Models* (CZM) [3], and the *Virtual Crack Closure* Technique (VCCT) [4] have already been developed, but they cause additional difficulties, for example, multiple crack parameters are necessary for CZM, the crack path should be previously defined, and complex crack growth problems are difficult to obtain [5]. Another challenge is related with the empirical fatigue models. Numerical cyclic loading process analysis is still somewhat limited, and it is based on empirical coefficients which have to be defined from experiments for the current cyclic loading type (e.g., symmetric, asymmetric). There is still no single model which can predict the fatigue life dependent on the stress ratio, the loading frequency, and the material temperature. Experimental data is not always available, or companies do not have opportunities to perform such testing. Thus, the design of composite structures relies on adding extra material layers in order to ensure safety. This leads to a reduced structure performance (an increased mass) and, on top of that, a higher final cost of the structure. Moreover, lack of the effective fatigue damage identification and monitoring methods results in the structure getting replaced after the estimated working hours without even considering the accumulated fatigue damage and the possibility to extend the exploitation period.

The *Non-Local Peridynamics* (PD) theory, developed by Silling in 2000 [6], offers an integral continuum mechanics approach, thus both continuous and discontinuous field problems can be simulated. PD does not require special discontinuity treatment strategies and does not encounter the difficulties which the previously mentioned FE methods are facing. The average value of various PD models' correlation with experiments is about 90% [7], thus PD is assumed to be an attractive approach, which is already being implemented in the modelling fatigue process [8–10]. As an alternative to the classical fatigue models, the *Kinetic Theory of Fracture* (KTF) was developed in the middle of the 20th century. It is based on the atomistic approach [11]. KTF evaluates fatigue damage with an equation including the process temperature, the loading frequency, the stress level, and the stress ratio variables. Once the KTF equation has been calibrated from the material's S-N curve,

it can be applied to any different loading conditions as opposed to the classical approach where empirical coefficients should be established from an experiment.

As an experimental technique, the *Digital Image Correlation* (DIC), recently developed by Sutton at University of South Carolina, USA [12], is becoming more and more popular in terms of contactless full field displacement and a strain measuring system for structures of various sizes [13,14]. The DIC working principles are based on tracking surface points before and after the deformation. DIC measurements can be employed to identify the (fatigue) damage as a change in the structure surface displacement or the strain field.

The **research object** of the thesis is the damage in continuous fiber-reinforced polymer composites.

The aim of the thesis is to develop a methodology predicting fatigue damage and prognosing its growth in fiber-reinforced polymer composites based on experimental Digital Image Correlation measurements and the non-local peridynamics theory combined with the kinetic theory of fracture.

Five **objectives are identified** to achieve the aim of this work:
1. To establish an experimental Digital Image Correlation system with the peridynamics-based strain computation algorithm in order to improve the Digital Image Correlation strain quality.
2. To create a peridynamics model and calibrate the material model parameters according to experimental full field Digital Image Correlation measurements.
3. To establish the kinetic theory of fracture – peridynamics model suitable for any type of cyclic loading without the necessity of additional experimental data at those loading conditions.
4. To identify damage (or defect) in a composite material from surface Digital Image Correlation measurements and to define the damage position, to quantify the damage (defect) by using a numerical model.
5. To perform the kinetic theory of fracture – peridynamics-based composite fatigue numerical modelling.

Statements to be defended
1. The Peridynamics Theory improves quality of the Digital Image Correlation strain measurements by reducing the noise in strains at high measurement resolution.
2. Digital Image Correlation experimental measurements, applied to the tensile test only, enables to calibrate the peridynamics material model parameters.
3. The fatigue damage of any type cyclic loading can be predicted by using the kinetic theory of fracture and only having the experimental data of symmetric cyclic loading at room temperature.
4. The entire process of fatigue is simulated by using the same peridynamics model without predefined crack paths and initial cracks.

Scientific novelty
1. A 3D Digital Image Correlation system with a noise-effective strain computation

algorithm based on peridynamics has been developed.
2. Bond-based with bond rotation peridynamics model for layered fiber reinforced polymer composite not requiring special software has been designed.
3. An experimentless numerical model capable to simulate the entire fatigue process and predict the fatigue damage for any type cyclic loading for metallic and composite materials has been created.

Practical significance
1. A methodology has been created which can be used in composite manufacturing companies (modelling-based fatigue life prediction at the design stage of the structure instead of adding extra layers for safety). Also, this methodology is applicable to monitor and analyze operating composite structures in the industry (in terms of damage and early failure detection by ensuring the safety of the structure or possible prolonged exploitation).
2. Fatigue life prediction including damage initiation and growth modelling (which are difficult to realize in the conventional numerical models) with minimized experimental testing makes the methodology effective in terms of the incurred costs and attractive to use. The increased use of such a methodology further leads to an increased composite structure performance, as well as a reduced cost of the structure, and prevents waste of expensive materials.

Approbation
        The scientific results, obtained during the current research, have been published in two international journals referred to in *ISI Web of Science* publications. The results of the research have been presented at five international conferences: of these, two conferences were held in Kaunas, Lithuania (these were oral presentations), one in the USA, and two in Italy.

Structure of the thesis
        The dissertation contains an introduction, 4 chapters, conclusions, a list of references, and a list of scientific publications. The dissertation is composed of 180 pages in total, and features 87 figures and 11 tables.
        The introduction presents the problem of the dissertation thesis, and the aim and objectives of the work. Additionally, statements to be defended, along with the scientific novelty and practical significance of the research of the thesis are outlined.
        The first chapter presents the literature review. Firstly, a brief description of defects in fiber-reinforced polymer composites is given. Further, fatigue damage identification methods, used for fiber reinforced composites, are analyzed. Finally, the currently existing numerical models for materials with discontinuity (e.g., a fatigue crack) are described.
        The second chapter describes the research plan and discusses the theoretical, experimental and numerical methodologies applied in this thesis. The PD theory and developed PD models are presented in this section. The *Peridynamic Differential Operator* (PDDO) is also derived and implemented. The PD fatigue model is analyzed. KTF is introduced, and its modifications to ensure correlation to the

experimental results for asymmetric cyclic loading are explained. The PD fatigue model together with KTF applications is analyzed. Finally, PD parameters of bond-based PD (BBPD), state-based PD (SBPD) and BBPD with rotation theories for a layered composite are given. What concerns the research experimental technique, it is mainly focused on DIC. It is also presented in Chapter 2.

The experimental testing results are given in Chapter 3. The conventional DIC strain computation algorithm is replaced with a PDDO-based algorithm in order to increase the DIC strain accuracy. DIC measurements are used to compare strains computed by the conventional DIC and DIC-PDDO; it is also applied for the calibration of PD material parameters. Fatigue tests at symmetric and asymmetric cyclic loadings are performed by selecting an isotropic material, specifically, 316L steel. Statics tests of the CFRP composite are used to identify structure defects with DIC as well as the effective properties of the composite, necessary for the PD modelling.

The fourth chapter presents the results of the numerical simulation. The experimental procedure of PD model calibration from DIC measurements is described. The KTF-PD model of an isotropic material is created, and its correlation to the experimental results at various loading conditions (stress ratios, stress amplitudes) is analyzed. Analysis of a composite with artificial defects is performed. A defect is characterized by an FE updating (FEMU) algorithm from DIC measurements. The BBPD model with bond rotation is created, calibrated from experiments, and the previously validated on isotropic material KTF is used to simulate the fatigue damage (defect growth) in the CFRP composite.

Conclusions of the doctoral thesis together with references and the author's scientific conferences and publications are provided in the final chapter.

1. LITERATURE REVIEW

1.1. Damage Mechanisms in Fiber-Reinforced Polymer Composites

A high strength and low-density ratio make GFRP and CFRP attractive to use in many industries, e.g., in the fields of sport, aviation, or wind energy. In addition to this, fiber-reinforced polymer composites are denoted by better corrosion resistance than metallic structures and excellent fatigue properties [15]. The typical configuration of a fiber reinforced polymer composite is shown in Fig. 1.1.

a

b
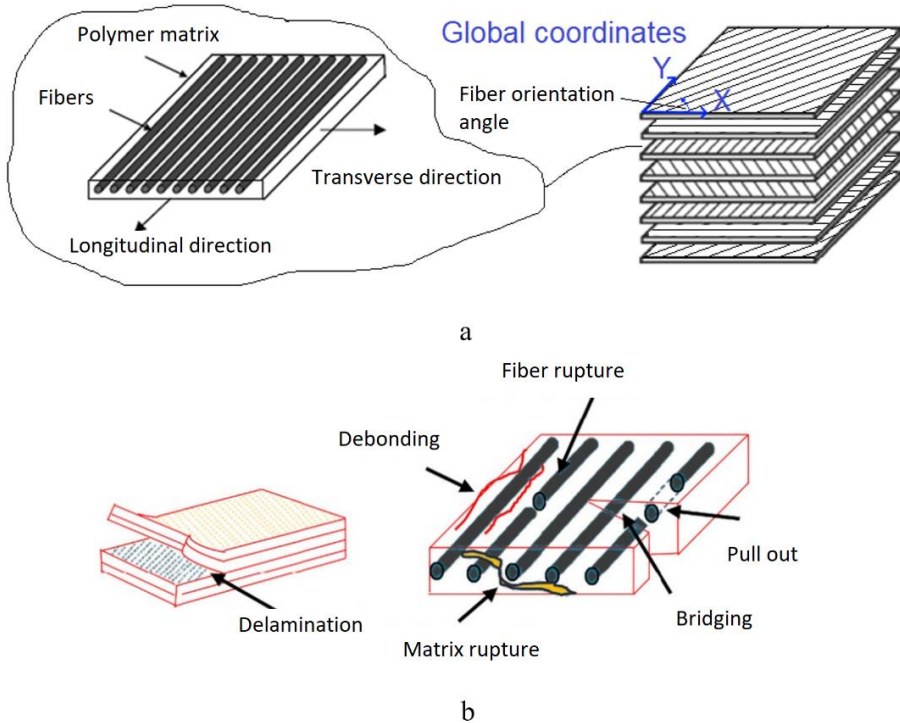
Fig. 1.1 Typical GFRP or CFRP composite: a – configuration; b – most common failure types (scheme adopted from [16])

Each composite layer consists of high strength fiber, orientated at a specific angle to the global coordinates, and a polymer matrix used to bond the fiber. One layer composite is anisotropic and has a high strength in the fiber direction and an about 100 times lower strength to the transverse-to-fiber direction. To make the material properties similar at different directions, composite layers are combined at different fiber orientation angles (Fig. 1.1 a). A composite structure, having symmetric layers of fiber orientation angles $[0/90/\pm45]^o_s$, is close to an in-plane isotropic material (quasi-isotropic).

The fatigue process in a fiber-reinforced composite consists (similarly as in other materials, e.g., metals) of the fatigue crack initiation, growth, and final failure phases. Different cyclic failure modes can be captured in the composite structures, namely, matrix cracking, fiber cracking, delamination between layers, or mixed

modes. In literature [16], besides the previously mentioned failure types, three other failure modes are identified: bridging, fiber pull out, and debonding (Fig. 1.1 b). Fatigue resistance and the failure type of a CFRP/GRFP composite highly depend on the material properties of the fiber and the matrix (resin), the fiber volume fracture in the composite, fiber orientation, layup, loading and composite defects [15]. Fatigue life comparison of composites of different strength/stiffness is presented in Fig. 1.2.
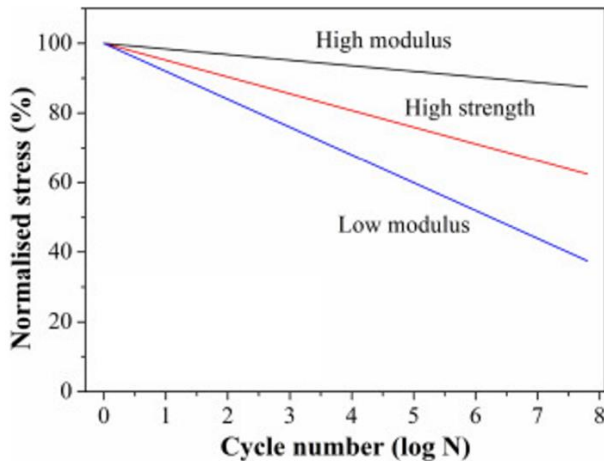
Fig. 1.2 Comparison of different strength/stiffness CFRP composites fatigue life [17]

From Fig. 1.2 [17], it is visible that high stiffness (high modulus) CFRP has the longest fatigue life, resulting in low strains in the stiff structure, which leads to a reduced matrix cracking. The low modulus composite fatigue life is about 40% of the stiff structure life. On the other hand, the failure of a rigid composite is sudden and catastrophic, while a high strength and especially low modulus structure failure is progressive. This can be explained by the energy stored in the composite structure: in rigid structures, a sudden high amount of energy release results in a sudden explosive failure, while, in low modulus structures, smaller amounts of energy cause a gradual and progressive failure. It is worth noting that the monitoring of fatigue damage in high modulus composite structures is a challenging and highly important task due to their sudden explosive cyclic failure type.

Similarly as shown in Fig. 1.2, it is possible to plot the fatigue life according to the composite volume fracture, the matrix, the fiber materials, or the fiber orientation. Investigations [18,19] of composites with different fiber types and the same epoxy matrix showed that the fiber type only exerts a minor effect on the fatigue performance of the structure. The fiber volume fraction directly affects the composite strength and stiffness in the fiber direction; thus, its value is very important in the composite fatigue life, as it has been shown for unidirectional CFRP [20]. The fiber orientation has a effect on the fatigue properties for a single-layered composite only, but, for a symmetric composite consisting of multiple layers (quasi-isotropic), the effect is practically not visible [21]. It can be easily concluded that a higher fiber volume fraction results in a longer fatigue life of the composite. A composite with a low fiber

volume fraction fails by matrix cracks, while fiber breaking dominates in high fiber volume fraction composites. Increasing the matrix fracture toughness should make the composite more resistive to crack growth, but experimental results [22] showed that this does not improve the fatigue life of the composite structure. Instead of this, fatigue properties could be improved by using a ductile matrix together with high modulus fiber, as documented in [23]. Fatigue life improvements can be made by using additives to the composite matrix [15]. Review [24] concludes that there is an optimal fiber volume fraction value at which the composite fatigue life is the highest.

Environment conditions play a role in the composite fatigue life as well. The temperature changes the matrix properties by making the matrix more elastic [25], and experimental results [26] showed that, at a higher temperature, the composite fatigue life is shorter. On the other hand, structure stiffness degradation is greater at lower temperatures. The effect of other environment conditions, such as humidity, corrosion, interactions with chemical materials, is also noticeable; it has been analyzed in [15].

The loading conditions are also important. The stress level not only affects the number of cycles until a failure is reached, but it also determines the failure mode. At a high stress, fiber breaking is dominant, whereas lower stress results in mixed fiber/matrix cracking and debonding. An increasing stress ratio leads to a reduced fatigue life. The loading frequency has an effect only if it affects the matrix temperature which changes the matrix material properties [27].

Another highly important aspect to be considered is composite defects. A preexisting material defect significantly reduces the structure strength and durability, which leads to the growth of a cyclic defect and an earlier final failure of the structure [28].

1.2. Analysis of Defects in Fiber-Reinforced Polymer Composites

Defects in composite materials can occur as a result of the manufacturing process, accidental damage during exploitation (such as impact damage), or fatigue damage. Fiber-reinforced polymer composite manufacturing includes series of operations, and, during each operation, there is a possibility to introduce defects, such as poor material handling, impurities in the surroundings, fiber waviness during the layup, improper resin curing conditions, etc. Another important issue is the impact damage, namely, barely visible impact damage, which is difficult to identify, and, furthermore, the damage can grow, which is bound to result in a catastrophic failure of the material [29]. The typical composite structure defects are classified as matrix, fiber, and interface defects [30,31], as shown in Fig. 1.3 and Fig. 1.4.
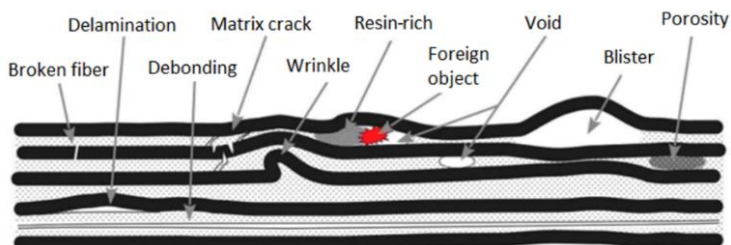
Fig. 1.3 Typical composite defects [30]
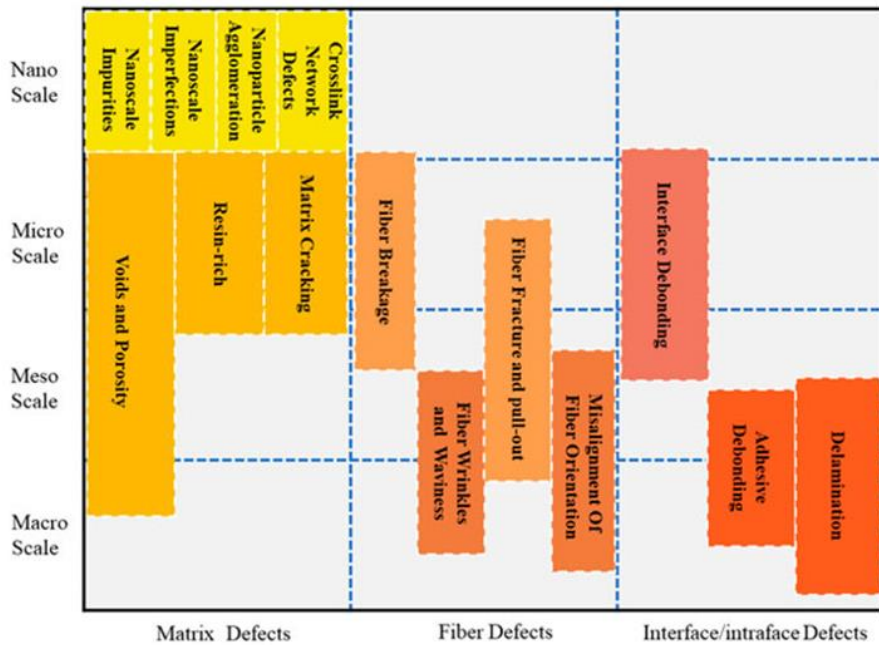
Fig. 1.4 Classification of composite defects (diagram from [31])

Matrix defects (see Fig. 1.3 and Fig. 1.4) are quite common and extensively analyzed in literature. Voids and porosity, as well as foreign objects in a composite matrix significantly affect the mechanical properties of the structure, such as the interlaminar shear strength, compressive strength, fatigue resistance, and flexural properties [31]. Already existing micro voids during fatigue loading can grow to macro voids, which result in a failure of the material. According to the requirements [32], porosity of up to 2% can be acceptable in a composite structure. Matrix defects can be implemented even at the nanoscale (Fig. 1.4).

Fiber waviness and wrinkles are the most common manufacturing defects in composite structures. This specially applies for thick composite structures [33]. Other fiber defects include fiber breakage, fracture, and pull-out, which can be created during the exploitation stage as well (e.g., which are a result of impact damage). Fiber defects strongly affect the material properties as they reduce the composite strength and fatigue life. An example of how fiber waviness can result in matrix damage is explained in review [34] and shown in Fig. 1.5.
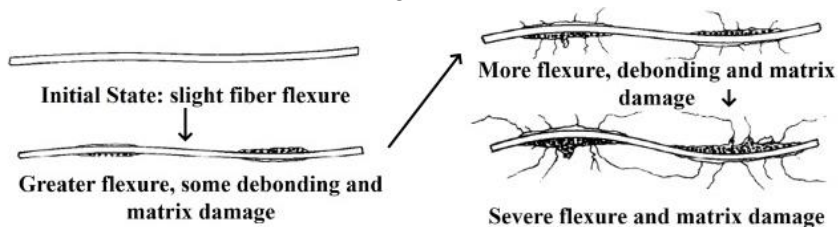
Fig. 1.5 Fiber waviness effect on matrix damage and material failure [34]

21

The initial fiber flexure results in an increased bending strain, and debonding or delamination occurs. Initiated matrix damage is a strain concentrator; thus, a higher strain results in more debonding and delamination. The growth of matrix damage finally leads to an earlier fatigue failure of the structure.

A low transverse and interlaminar shear strength of composite structures are the cause of interface/intraface defects. Delamination propagates parallel to the direction of the fiber placement between the laminates or within a laminate, while deboning is a separation of laminates in an adhesively bonded joint [34]. Delamination is one of the structure strength- and fatigue life-limiting factors [31,34], which can be induced during the manufacturing process by selecting improper plies bonding conditions (e.g., incompatible materials), further structure processing (e.g., drilling), or during exploitation. Static or cyclic tensile loading and impact damage are the main causes of the exploitation period-induced delamination, which especially grows due to direct or bending-caused compressive stress. Even ambient conditions, such as moisture or contaminations, can accelerate further delamination growth [35].

Delamination of a composite mainly depends on the matrix fracture toughness Gc [36]. Several failure criteria are used based on the delamination mode types (Fig. 1.6 a).

Mode I (Opening)

Global

Mode II (Sliding shear)

Local

Mode III (Tearing shear)

Mixed

a   b
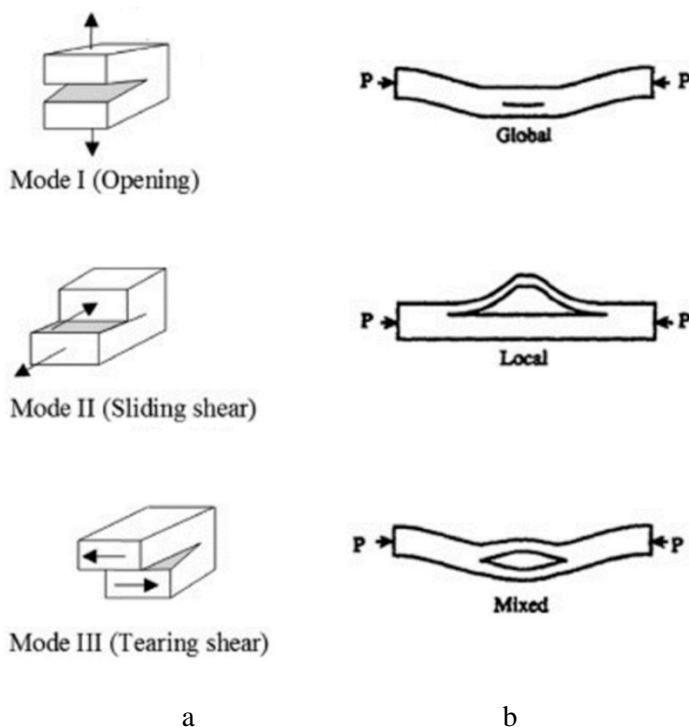
Fig. 1.6 Delamination process: a – modes; b – buckling caused by delamination [37]

The most common criteria are the pure mode [38]:

$$G_i \geq G_{iC} \tag{1.1}$$

and the mixed mode power law [39]:

$$\left(\frac{G_I}{G_{IC}}\right)^{\alpha} + \left(\frac{G_{II}}{G_{IIC}}\right)^{\beta} \geq 1 \qquad (1.2)$$

where α and β are the resin coefficients.

During the exploitation period of a composite structure, it is important not only to determine the critical loading for delamination, but also to prognose the further remaining strength and fatigue properties of a structure which already contains delamination. It should also be considered that delamination detection is a difficult task in most cases [40] because such a structure can behave differently depending on the geometry, material properties, loading, delamination size, and location. For example, delamination existing near the surface creates local buckling (Fig. 1.6 b) of the composite surface, while deep delamination generates mixed or global buckling [37]. According to Fu et al. [41], delamination damage is located parallel to the fiber direction and can be captured as unevenness in the composite structure surface displacement field.

When reviewing the common composite defects, it becomes obvious that defect identification, quantitative and qualitive description, together with monitoring, are crucial for the evaluation of the already existing (fatigue) damage and the prognostic value of the remaining structure fatigue life. These presently mentioned tasks are not simple, and they require special testing methods. *Structure Health Monitoring* (SHM) based on *NonDestructive Testing* methods (NDT) is only possible method to apply on structure during its exploitation.

1.3. NDT for Defects Identification in Composite Structures

There are a variety of different methods established to inspect composite structures [31]. Their advantages and disadvantages are summarized in Table 1.1.

Table 1.1. Most common NDT method for composite testing

Method	Advantages	Disadvantages
Visual inspection	Simple quick inspection without specialized equipment; Helps to determine the regions to be tested with other NDT methods.	Not accurate; Depends on the human factor; Not all defects can be captured.
Acoustic emission	High testing speed; Applicable to composite structures SHM [42]**.**	Contact method [43]; Only an occurring defect can be detected; The structure should allow stress waves propagation; Requires skills and experience to analyze the output signal [31].
Ultrasound testing	High accuracy;	Contact method, air-coupled

	Provides information about the defect location, depth and size [44]; Widely used for testing composite materials [44]; Portable equipment [44].	ultrasound testing is less accurate [45]; Difficult to detect defects near the probe [31].
X-ray computed tomography	Due to its high sensitivity and resolution, the method is used for GFRP and CFRP composites [46,47]; Detailed information of the defect location, depth, size and visualization; Works for most materials.	Low speed; Harmful radiation, requires special testing conditions (e.g., a lab) [31]; The object size is limited [31].
Infrared thermography	High speed; Visual presentation of defects; Can detect delamination [48,49].	Requires thermal heating [50]; Low sensitivity for deep defects; Requires experience to analyze the results and identify the defect type.
Digital Image Correlation	High speed and accuracy; Non-contact technique; Can be applied on an operating structure; Structures from micro [51] to large scale [13] can be tested; Damage progression [52], delamination [53,54] can be detected in composite materials.	Require setup preparation, calibration and speckle pattern on structure surface [55]; Accuracy depends on the lighting, speckle pattern quality [55]; Defect detection depends on the loading and analysis type (static versus dynamic).

When reviewing the NDT methods for composites, their selection mainly focuses on accuracy and availability. DIC, by virtue of being a non-contact full field method, can be applied on operating structures across distance. Also, the DIC measurement accuracy is high (±0.02 px according to [56]), thus DIC has a potential to be developed as part of a non-destructive SHM system applied to composite structures. Moreover, by combining DIC-measured displacement and strain fields with the numerical model, it is possible to predict the remaining strength and lifetime of the structure.

The practical application of DIC based on defect detection from static structure surface displacement fields (Fig. 1.7) [57] shows that measurement resolution of several micrometers is required; thus, surface strain fields are more defect-informative.
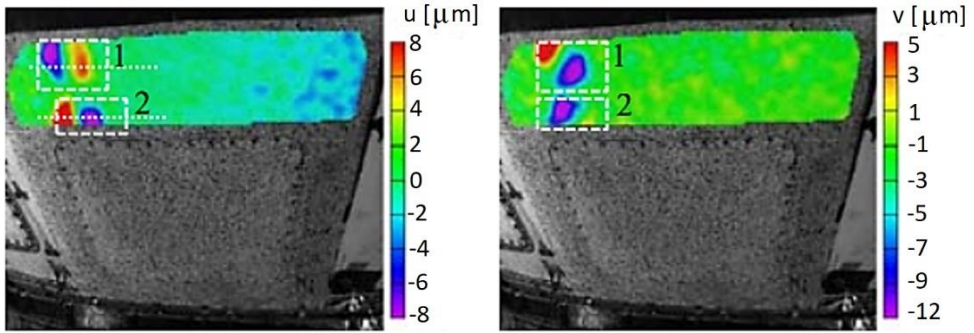
Fig. 1.7 Composite structure defect detection from DIC displacement field measurements on the structure surface [58]

The problem of DIC strain fields is the noise, which limits the DIC strain accuracy and thus the defect detection accuracy. Also, defect detection from surface strains, measured by DIC, strongly depends on the static loading type and the defect depth in the structure. For example, fiber cracks are easier to detect on tensile loading [59,60]. In Fig. 1.8, strain fields, measured during tensile and compressive loadings on the same composite structure surface, are compared. For the case of compression, local buckling generates surface light reflection, which results in an increased DIC measurement noise in strains (Fig. 1.8 b). Noise hides the material defect – fiber cracks which are clearly visible in the tensile strain field (Fig. 1.8 a).
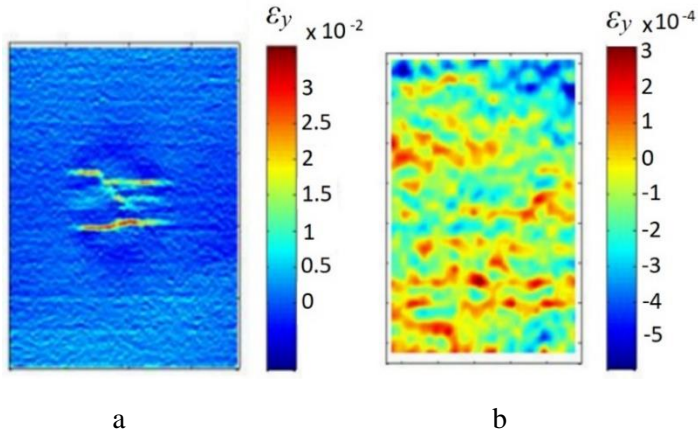
Fig. 1.8 Detection of fiber cracks from a composite structure surface strain field [60]: a – tensile loading; b – compression

Other types of composite defects, such as delamination or deboning, can be identified from surface displacement or strain fields [61] captured during bending loading. Nevertheless, instances of damage, located far away from the structure surface, can even be unseen on the DIC surface displacement or the strain field.

Based on the idea that internal defects influence the dynamic response, methods relying on displacement, deformations changes over time, and acceleration measurements of the structure have been developed [61,62] and have already been

applied with DIC [58]. Contrary to static loading, local defect resonance enables detecting deep damages [63,64], but the defect resonance frequency usually reaches several kilohertz. Thus, special high frequency oscillators and sensors (high frame rate DIC cameras) are necessary to capture the response. Dynamic testing is useful for large and complex structures where natural frequencies are monitored, but the environmental conditions can strongly affect the measurements. Small defects in a composite do not affect the dynamic properties of the structure, and, in this case, they cannot be captured. In addition to this, a dynamic numerical model is necessary to define the defect position and characterize the defect size, shape, and severity; thus, the dynamic characteristics measurement method depends on the model accuracy as well.

1.4. Composite Structures Numerical Modelling Aspects

1.4.1. Material with discontinuity and damage growth

Numerical modelling is a powerful strategy predicting the further behavior of a structure, but the main problem is the model reliability. Although material parameters in a numerical model can be calibrated from experimental tests (especially by using DIC measurements [65] to fit the computed and experimental strain fields), the modelling of a material defect causing discontinuity and a further growth of the defect is an issue. This is because the currently devised FE equations are based on spatial derivatives of the displacement, and thus the derivatives are not valid when discontinuity is manifested. Several special techniques, described further below, are used to cope with this numerical modelling problem.

Virtual crack closure technique (VCCT). To simulate crack growth, the initial crack and the crack path should be defined previously. VCCT takes an assumption that a certain amount of energy is necessary to increase the crack by certain length Δa, as it is shown in Fig. 1.9 [40]. The same amount of energy is required to close the crack.
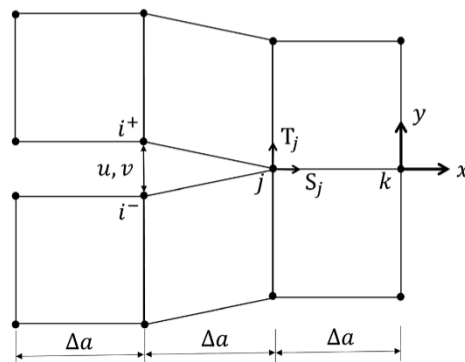
Fig. 1.9 VCCT schematics [40]

Critical energy release rates G_I and G_{II} are used to relate the displacements and forces of the FE points at the crack tip. Since VCCT alone cannot predict the crack paths, the method suits better for delamination modelling. The selection of VCCT [66] is based on the method simplicity and applicability to fatigue crack growth.

26

Cohesive zone model (CZM). Originally, CZM was proposed by Barenblatt [67] to eliminate the stress singularity at the crack tip. The cohesive zone, which is significantly smaller than the crack, is introduced in the model (Fig. 1.10 [68]).
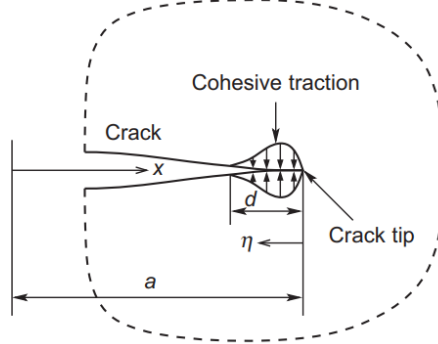
Fig. 1.10 CZM model [68]

It is also assumed that the size of the cohesive zone, the cohesive traction distribution and the magnitude are independent of the crack geometry or external loading. Also, stresses are finite, even at the crack tip. When taking the crack opening mode I (Fig. 1.6) model in an elastic solid [68], stresses can be calculated at the crack tip and in the whole cohesive zone. The method requires only the initial crack to be defined (in comparison to VCCT, where the crack path should also be defined). CZM exists in FE commercials and is also used for modelling composite fracture problems including fatigue [69], fatigue delamination [70], debonding and damage growth in notched composite structures [3]. Nevertheless, CZM requires multiple material parameters to be defined for the model.

Extended Finite Element (XFEM). The method includes extending solutions of differential equations with discontinuous functions. The original XFEM application was fracture modelling [2]. When using special FE enriched with discontinuous functions around the crack (Fig. 1.11), a crack in the material can be simulated by splitting finite elements.
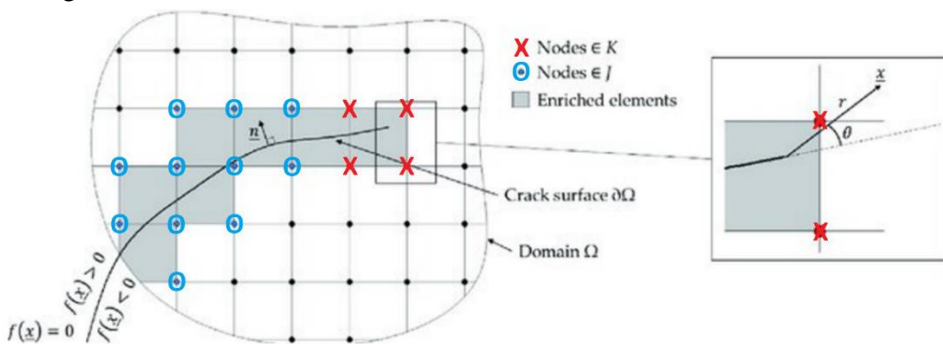
Fig. 1.11 Crack modelling by using XFEM [71]

$f(x)$ in Fig. 1.11 is a function mapping the position of the closest points to the discontinuity. Thanks to this approach, no real discontinuity is modelled, and no

27

meshing/remeshing the discontinuity is necessary. XFEM is well applicable when the crack paths are unknown, or when they have complex trajectories. This method is implemented in some FE commercials, such as *ABAQUS*, *LS-Dyna*, or *ANSYS*. XFEM is already popular in modelling composite structures [72–74]. The results from studies [72–74] confirm that the crack initiation and propagation can be simulated without the knowledge of the initial crack position. Nevertheless, XFEM is sensitive to FE type selection, and modelling a crack in complex materials can be difficult.

  Non-local Peridynamics (PD). PD was originally created by Silling in 2000 [6]. The PD theory reformulates classical continuum mechanics (CCM) by replacing spatial derivatives in the equation of motion by spatial integrals. PD is non-local, and no additional treatment around the discontinuities is necessary. Each material point (depicted with a red dot) in the PD model (Fig. 1.12 [75]) interacts with other points in the interaction range H_x (δ is the interaction range size).
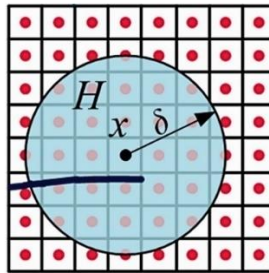
Fig. 1.12 PD model of material [88]

  The PD body equation of motion is constructed from volumetric integrals of the PD material points in their interaction ranges. Any type of discontinuity can be implemented in the model as missing interaction between the PD points. Since PD is a relatively new approach, PD formulations do not exist in many FE software; nevertheless, PD is widely used for composite modelling [76], and composite fatigue analysis [10,77]. The advantage of PD over the previously mentioned FE techniques is its ability to simulate complex cracks, such as crack branching [78], or dynamic cracks [79] without the need for many material parameters, or predefinitions of cracks. A single model for fatigue including three phases (crack initiation, growth and the final failure) implemented in PD was first proposed by Silling and Askari [8]. Practical PD applications for fatigue analysis were further developed and applied for fatigue damage evaluation in metallic structures of various geometries [9,80,81] and fiber-reinforced composites [82–86]. On the other hand, the PD model computation cost is high, thus FE-PD coupling is used to increase the PD computational efficiency [87] applying the PD only in the region of the crack.

  Coupling between the experimental DIC and PD has recently become an actual field of research. Madenci et al. [88], Turner [89] and Li et. al. [90] took displacements from DIC and used in PD simulations to determine the crack paths and the damage in the investigated material. Also, Madenci et al. [91] used the strain compatibility condition computed by applying integral PD equations to the DIC displacement field with the objective to identify possible discontinuities. The aforementioned work of

28

DIC-PD simulation coupling [88–90] is mostly focused on applications to discontinuous fields, and it depends on the accuracy of PD simulation.

In order to perform obvious comparison of the majority of the numerical techniques described above, generalized information is given Table 1.2.

Table 1.2. Numerical modelling techniques used to treat discontinuities

Method	Advantages	Disadvantages
VCCT	Relatively simple; Well applicable when it is necessary to evaluate process energy.	Cannot simulate crack growth alone, the initial crack and the crack path must be defined.
CZM	The crack path is not required; Well applicable for fatigue modelling.	High computational cost; Many parameters of the material are necessary.
XFEM	The crack path is not required; The initial crack is not required; Effective; the computational cost is not high.	Not effective for complex crack problems; Accuracy depends on FE selection.
Non-local PD	The crack path is not required; The initial crack is not required; Any complex cracks can be simulated.	Reformulates CCM by using different parameters instead of CCM strains and stresses; High computational cost.

After looking through the techniques discussed in Table 1.2, it is visible that PD is capable of simulating any type of a crack. The XFEM performance is also good (XFEM can simulate crack growth without the initial crack and the crack path, similarly to PD), but XFEM is not effective for complex crack problems. PD looks promising when considering complex damage mechanisms in composite materials (see Chapter 1.1). The accuracy of XFEM depends on the FE type, which is not the case for PD. Despite the drawbacks of PD regarding different continuum mechanics formulation and the computational time costs, it is worth using PD when predicting the composite structure lifetime from the damage initiation to the damage growth and the final failure of the structure.

1.4.2. Fatigue damage and failure

The S-N curve and Paris' law approaches are used to numerically evaluate the fatigue performance. The S-N curve is different for each material, and it relates the cyclic stress amplitude to the number of cycles until failure. In the case of crack growth, Paris' law [92], relating the crack growth rate da/dN to the stress intensity

factor, is applied. The analytical S-N curve and Paris' law expressions, adopted for a composite material, are shown in Fig. 1.13 [93]:

$$N_f = \left(\frac{\sigma_{max}}{\sigma_c}\right)^{-\beta}, \text{for S} - \text{N curve} \tag{1.3}$$

$$\frac{da}{dN} = CG_{max}{}^{\alpha}, \text{for Paris' law} \tag{1.4}$$

where a is the crack length; N_f is the number of cycles to failure; C, α, β are the material coefficients found from experiments or given in databases.
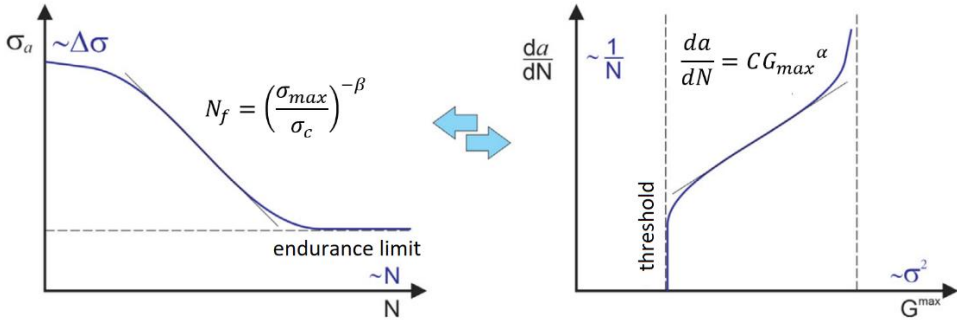
Fig. 1.13 S-N curve and Paris' law for composite material [93]

The typical S-N curve or Paris' law data are given for symmetric cyclic loading (stress ratio $R = -1$) at room temperature and are not valid for other testing conditions, such as a different stress ratio ($R \neq -1$), a different temperature ($T \neq 20°C$), or high cyclic loading frequency.

Lack of physical explanation of the selected Paris' law coefficients (there are no physical process-based equations calculating Paris' law coefficients according to changed process conditions, e.g., an increased temperature) makes authors look for alternative approaches [11]. The *Kinetic Theory of Fracture* (KTF) [11], an atomistic approach which treats fatigue as a thermally activated process, dependent on the temperature, the stress ratio, the stress amplitude and the loading frequency, was created in the mid-20th century by Coleman and Zhurkov separately [94,95]. KTF is accurate in predicting the fatigue life for different conditions over a wide range for materials spanning from metals to polymer composites [96]. Madenci et al. were the first who combined PD and KTF models for metallic materials [96,97] and composites [98].

1.5. Literature-Based Ideas and Trends for the Current Study

When summarizing all the above-mentioned factors, it can be seen that fatigue damage in composite structures is highly complex, and it depends on multiple variables. The existing defects in composite structures are a leading factor to fatigue damage and failure of the structure. Thus, the defect detection and damage monitoring together with the numerical model of the structure are very important for the structure

SHM and fatigue life prediction. Different NDT methods have been suggested; although DIC is attractive due to being a full field non-contact method. The existing numerical models in FE frameworks face with problems when modelling discontinuities, thus the PD theory seems to be the most versatile approach for any type of discontinuities. Moreover, there is no existing and universally used single material fatigue model which could evaluate the fatigue life by taking all the material (e.g., elastic modulus) and process (stress ratio, temperature, frequency, etc.) parameters into its equation. KTF can be treated as a physics-based fatigue model, but is has not been widely developed and used yet.

Thus, this study is based on the motivation to investigate and suggest a composite structure SHM system together with the fatigue life prediction based on DIC experimental measurements for damage detection and damage growth tracking, and the KTF-PD model for predicting the fatigue life and the failure of the structure.

2. RESEARCH METHODOLOGY AND THEORETICAL BACKGROUND

2.1. Work Plan

The study is based on theoretical, experimental and numerical analysis. The work plan is presented in Fig. 2.1. In total, 22 tasks are identified to achieve the previously identified 5 objectives of the study. Each task in Fig. 2.1 is classified as either theoretical (T1–T5), experimental (E1–E8), or numerical modelling (M1–M9). There are tasks which can be performed in parallel, while other tasks can be done only after finishing the previous tasks. For example, research is initiated with the PD theory analysis in parallel with the introduction of the experimental DIC system (Fig. 2.1). Only after analyzing the PD theory and its numerical aspects, the numerical implementation of the PD model in computational software is possible. A combination of the PD numerical model and experimental DIC strain measurements leads to the first objective – a PDDO-based DIC strain computation algorithm (Fig. 2.1). Since the composite material is complex, even cyclic loading is a complex phenomenon, the research according to the plan, given in Fig. 2.1, starts from the static PD model of the isotropic material. According to implemented PD model, an isotropic material static PD model is created, and the second objective – static PD model calibration from experimental DIC measurements – is achieved. As an isotropic brittle material, similarly to the first original BBPD material suggested by Silling [6], *Biresin CH83-2* epoxy resin is selected for the PD model calibrations. Moreover, when modelling CFRP or GFRP composites with epoxy resin, the properties of the resin are necessary to determine the interlaminar normal and shear PD bond stiffness, or even the failure parameters. The theoretical background of the KTF-PD modelling, experimental fatigue tests and the created numerical PD models lead to the third objective. Due to being a new method, the KTF-PD modelling in Objective 3 is also performed on isotropic materials (simpler modelling task) rather than straightly on anisotropic composites (complex modelling task). *316L* stainless steel is selected as this typer of material due to its applicability with CFRP/GFRP composite constructions, e.g., 316L steel together with CFRP/GFRP composites is often used in aviation [99]. Also, high wear and corrosion resistance *CFRP-316L* stainless steel wires composites [100] were recently created. The fourth Objective of CFRP composite defect identification and characterization consists of both experimental and numerical tasks. While the fourth Objective is more experimental (Fig. 2.1), the fifth Objective – KTF-PD composite fatigue modelling – is the most complex and requires a combination of all (theoretical, experimental and numerical) the methods as well as experience accrued while performing all the previous tasks.
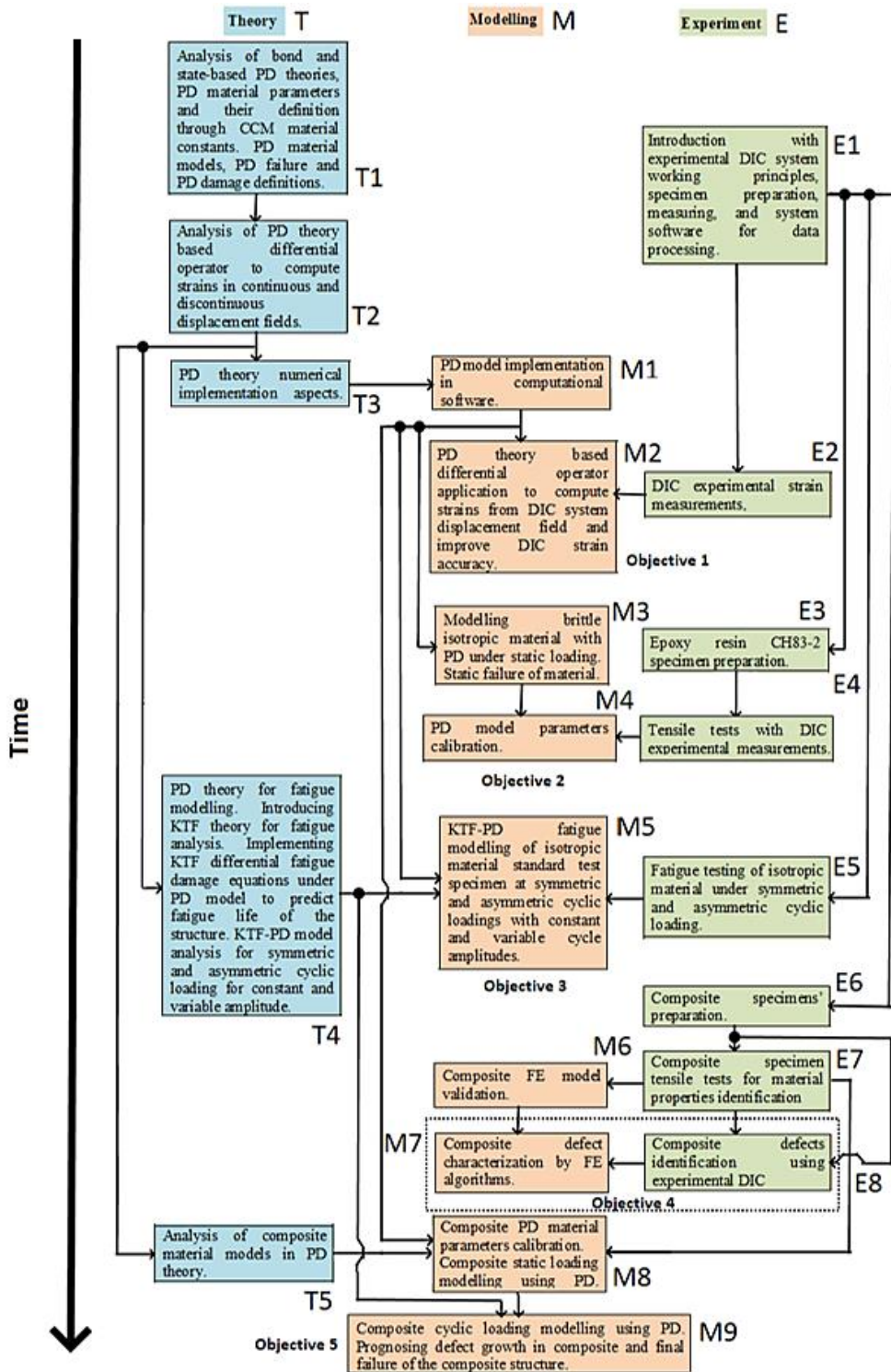
Fig. 2.1 Research methodology and work plan

Summarized information of the planned experimental tasks, shown in Fig. 2.1, is also given in Table 2.1 for enhanced clarity.

Table 2.1. Planned experiments

Task in Fig. 2.1	Equipment	Actions	Materials
E1	3D DIC.	Analysis.	-
E2	▪Universal tensile testing machine *INSTRON E10000*; ▪3D DIC with cameras *Basler acA4112*.	Tensile test.	Specimen of any elastic material, flat, not referred to any standard.
E3	▪Mold; ▪Vacuum pump.	▪Preparing epoxy resin; ▪Molding specimen according to ASTM *D638 – 10* [101], curing at room temperature.	▪Epoxy resin *CH83-2*; ▪Hardener.
E4	▪Universal tensile testing machine *INSTRON E10000*; ▪3D DIC with cameras *Basler acA4112*.	Tensile test.	ASTM D638 – 10 [101] epoxy resin specimen.
E5	Universal tensile testing machine *INSTRON E10000*.	Cyclic tests according to *ASTM E1012* [102].	*ASTM E606/E606M* [103] *316L* stainless steel specimen.
E6	▪Vacuum pump; ▪Circular table saw; ▪CNC milling machine with mounted 1 mm diameter groove mill.	▪Bonding carbon fabrics to 500 mm×500 mm CFRP composite plate with layup [(±45)°/(0/90)°]$_3$s with 4 delaminations of size of 20×60 mm; ▪Cutting specimens from 350 mm×150 mm plate at angles 0° and 45° to *ASTM D3039* [104] specimens; ▪Milling 1 mm width 10 mm length grooves in previously cut *ASTM D3039* [104] CFRP specimens.	▪Carbon fabric, epoxy resin, hardener; ▪CFRP composite plate 350 mm×150 mm, thickness 2 mm, layup [(0/90)°/90°/0°]s.

E7	10 kN tensile machine; External extensiometer.	Tensile test of 0º and 45º angles cut CFRP specimens.	*ASTM D3039* [104] CFRP composite specimen without artificial defects.
E8	▪3D DIC with cameras *Basler acA4112*; ▪Universal tensile testing machine *INSTRON E10000*.	▪Static bending tests using weight load; ▪Static loading at constant tensile force.	▪500 mm×500 CFRP plate with 4 delaminations; ▪*ASTM D3039* [104] CFRP composite specimen with milled grooves.

The following subchapters represent PD, KTF theoretical aspects and experimental DIC working principles.

2.2. Peridynamics Theory

The interaction range between PD points x and x' is a sphere for 3D model (a cylinder for 2D model), called PD horizon H_x and defined by radius δ the way it was formulated in the original Silling PD theory [6]. The interaction between x and x' is defined as a PD bond. This formulation leads to the bond-based PD (BBPD) theory (Fig. 2.2, Fig. 2.3 a) whose equation of motion can be expressed as [105]:

$$\rho\ddot{\boldsymbol{u}}(\boldsymbol{x},t) = \int_{H_x} \boldsymbol{f}(\boldsymbol{u}'(\boldsymbol{x},t) - \boldsymbol{u}(\boldsymbol{x},t), \boldsymbol{x}' - \boldsymbol{x}, \boldsymbol{x})\, dV_x + \boldsymbol{b}(\boldsymbol{x},t) \tag{2.1}$$

where $\boldsymbol{u}$ and $\boldsymbol{u'}$ are displacements, $\boldsymbol{x}$ and $\boldsymbol{x'}$ are the position vectors of material points x and x', respectively (Fig. 2.2); ρ is the material density; V_x is the volume of point x.
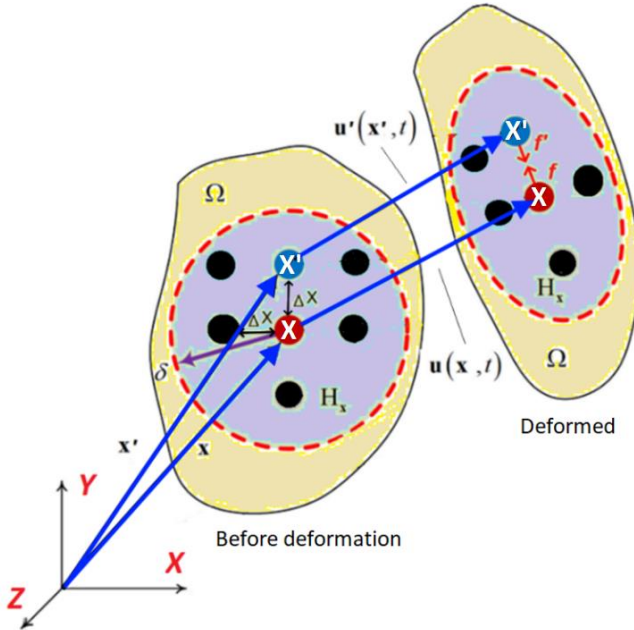
Fig. 2.2 The principles of the original PD theory (BBPD)

Vector f (Eq. (2.2) and Fig. (2.1)) is the force density in the bonds, whereas $b(x, t)$ (Eq. (2.1)) is the vector of the body forces. PD equation (2.1) does not include spatial derivatives; thus, it is valid for both continuous and discontinuous displacement fields. Nevertheless, the original PD theory (BBPD) [105] has several limitations. From the assumption of limited interactions of the PD points (the PD points x and x', bond forces vectors f and f' are equal in magnitudes and parallel in directions so that $f = -f'$), it is derived that a linear isotropic material's Poisson's ratio can be equal to only 0.25 in a 3D body or in the case of plane strain and 0.33 in the plane stress case (a detailed derivation is given in [106]). The Poisson's ratio for such a material can be accepted when modelling most isotropic materials, such as metals or resins, although this would not provide an accurate PD model of a fiber-reinforced polymer composite. Moreover, the BBPD accuracy is limited when modelling plastic deformations in metals because plasticity results in permanent deformation of the material undergoing a volumetric strain (without shear).

To circumvent these limitations, a newer PD theory, namely, the state-based PD (SBPD) was suggested in 2007 [107]. The SBPD theory is based on introduced new mathematical objects – states – which are as an array which stores information about the PD bonds associated with a particular material point x. Then, the SBPD equation of motion is formulated as [107]:

$$\rho \ddot{u}(x, t) = \int_{H_x} \{\underline{T}[x, t]\langle x' - x \rangle - \underline{T}[x', t]\langle x - x' \rangle\} dV_{x'} + b(x, t) \qquad (2.2)$$

Here, $\underline{T}[x, t]\langle x' - x \rangle$ is the force state valued function of position x and time t operating on vector $\langle x' - x \rangle$. The comparison of BBPD and SBPD formulations is given in Fig. 2.3.
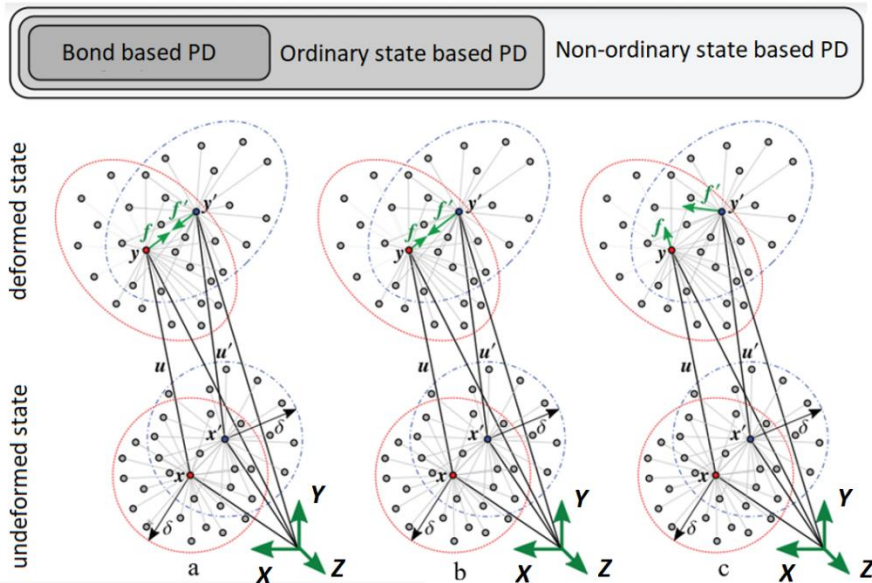
Fig. 2.3 PD theory formulations [108]: a – BBPD; b – ordinary SBPD; c -non-ordinary SBPD

For the case of SBPD (Fig. 2.3 b), the PD bond force vectors f and f' of the interacting points x and x' are not always equal. This is because the PD bond force in SBPD depends not only on the current bond $x' - x$ deformation, but also on the deformations of other PD bonds connected to points x and x'. Finally, this leads to a conclusion that the Poisson's ratio of a material becomes not fixed.

There are two types of SBPD: *ordinary* (OSBPD) and *non-ordinary* (NSBPD). In the OSBPD model, the vectors of PD bond forces are collinear, but not equal in magnitudes (Fig. 2.3 b), while the vectors of NSBPD bond forces are neither collinear nor equal in magnitudes (Fig. 2.3 c). The NSBPD formulation allows modelling the shear deformations of a body [109].

The key variable in both BBPD and SBPD theories is the deformation of the PD bond, called the *stretch*, and it can be determined with the following Equation:

$$s_{xx'} = \frac{(|\boldsymbol{\xi}_{xx'} + \boldsymbol{\eta}_{xx'}| - |\boldsymbol{\xi}_{xx'}|)}{\boldsymbol{\xi}_{xx'}} \tag{2.3}$$

where

$$\boldsymbol{\xi}_{xx'} = \boldsymbol{x}' - \boldsymbol{x} \tag{2.4}$$

is the relative position vector and

$$\boldsymbol{\eta}_{xx'} = \boldsymbol{u}_{x'} - \boldsymbol{u}_x \tag{2.5}$$

is the relative displacement vector. It is worth noting that the PD stretch is not equal to the CCM strain, since the stretch depends on the scale of the interaction that is the radius δ of the PD horizon (Fig. 2.2).

In numerical PD models, the number of the PD points is finite and the distance between two neighborhood points is $\varDelta x$, which leads to the discretization of the body domain $\varOmega$ by equally spaced PD grid (Fig. 2.2). Parameter $\varDelta x$ is called the PD grid spacing, and then the PD horizon size is usually expressed by the ratio of grid spacings, e.g., $\delta = m\varDelta x$. Based on the PD model convergence study [110], the PD horizon size $\delta \approx 3\varDelta x$ is determined, which results in achieving both the accuracy and the stability of the PD model. Horizons other than $\delta \approx 3\varDelta x$ sizes are less commonly used in the PD models, and they are associated with highly specific problems [111–116].

When considering the simplest PD theory, BBPD, the PD bond force vectors can be calculated as their magnitudes proportional to the PD bond stretch:

$$\boldsymbol{f}_{xx'} = -\boldsymbol{f}_{x'x} = cs_{xx'} \frac{\boldsymbol{\xi}_{xx'} + \boldsymbol{\eta}_{xx'}}{|\boldsymbol{\xi}_{xx'} + \boldsymbol{\eta}_{xx'}|} \tag{2.6}$$

where c is the BBPD bond stiffness which can be found by equating the CCM and PD strain energy densities for elastic deformation:

$$W_{CCM} = \frac{1}{2} \sum_{i=1}^{3} \sum_{j=1}^{3} \sigma_{ij} \varepsilon_{ij} \tag{2.7}$$

and

$$W_{BBPD} = \frac{1}{4} \int_{H_x} cs^2 |x' - x| d\xi_{xx'} \tag{2.8}$$

resulting in

$$c = \begin{cases} \dfrac{12E}{\pi\delta^4} & \text{3D case} \\[2mm] \dfrac{9E}{\pi\delta^3} & \text{2D plane stress case} \\[2mm] \dfrac{8E}{\pi\delta^3} & \text{2D plane strain case} \end{cases} \tag{2.9}$$

where E is the elastic modulus of a material. The SBPD formulation is more complex, and thus the PD bond force vector (the notification of t is specially related with the SBPD force density) is expressed as follows [105]:

$$t_{xx'} = 2\delta \left\{ d \frac{\Lambda_{xx'}}{\xi_{xx'}} a\theta_{x'} + 2bs_{xx'} \right\} \frac{\xi_{xx'} + \eta_{xx'}}{|\xi_{xx'} + \eta_{xx'}|} \tag{2.10}$$

where:

$$\Lambda_{xx'} = \frac{\xi_{xx'} + \eta_{xx'}}{|\xi_{xx'} + \eta_{xx'}|} \cdot \frac{\xi_{xx'}}{|\xi_{xx'}|} \tag{2.11}$$

and $\theta_{x'}$ is the SBPD volumetric dilatation term [105]:

$$\theta_{x'} = d \sum_{x=1}^{N} \omega_{xx'} s_{xx'} \Lambda_{xx'} V_x \tag{2.12}$$

where V_x is the volume of point x, N is the number of points in point x horizon H_x, $\omega_{xx'} = \frac{\delta}{|\xi_{xx'}|}$. The remaining SBPD material parameters a–d can be found from CCM material bulk κ and shear modulus μ by the following equations:

$$a = \begin{cases} \dfrac{1}{2}\left(\kappa - \dfrac{5}{3}\mu\right) & \text{3D case} \\[2mm] \dfrac{1}{2}(\kappa - 2\mu) & \text{2D case} \end{cases} \tag{2.13}$$

$$b = \begin{cases} \dfrac{15\mu}{2\pi\delta^5} & \text{3D case} \\[2mm] \dfrac{6\mu}{\pi\delta^4} & \text{2D case} \end{cases} \tag{2.14}$$

$$d = \begin{cases} \dfrac{9}{4\pi\delta^4} & \text{3D case} \\[2mm] \dfrac{2}{\pi\delta^3} & \text{2D case} \end{cases} \tag{2.15}$$

while

38

$$\mu = \frac{E}{2(1+\upsilon)} \tag{2.16}$$

$$\kappa = \begin{cases} \dfrac{E}{3(1-2\upsilon)} \text{ 3D case} \\[2mm] \dfrac{E}{2(1-\upsilon)} \text{ 2D plain stress case} \\[2mm] \dfrac{E}{2(1-\upsilon-2\upsilon^2)} \text{ 2D plain strain case} \end{cases} \tag{2.17}$$

Eq. (2.10) is valid for both SBPD and BBPD. Since $a = 0$ for the BBPD parameter, the first term in Eq. (2.10) vanishes and then Eq. (2.10) becomes equal to Eq. (2.6). Thus, the BBPD can be treated as separate case of SBPD, and BBPD bond stiffness c is equal to

$$c = 4b\delta \tag{2.18}$$

To simulate a failure of a material, the critical PD bond stretch value is considered. Associating the PD strain energy, it is necessary to introduce the crack by removing all PD bonds in the crack surface within the horizons of points x and x', with the classical fracture mechanics energy release rate G_c; Silling and Askari [117] defined the BBPD critical stretch for the 3D model as:

$$s_c = \sqrt{\frac{10G_C}{\pi\delta^5 c}} \tag{2.19}$$

After changing the stiffness c of the BBPD bond, expressed in elastic material constants, s_c definition becomes:

$$s_c = \begin{cases} \sqrt{\dfrac{5G_C}{6E\delta}} \text{ 3D case} \\[3mm] \sqrt{\dfrac{4\pi G_C}{12E\delta}} \text{ 2D plane stress case} \\[3mm] \sqrt{\dfrac{5\pi G_C}{9E\delta}} \text{ 2D plane strain case} \end{cases} \tag{2.20}$$

Madenci and Oterkus [105] extended the s_c concept suitable for the SBPD model as:

$$s_c = \begin{cases} \sqrt{\dfrac{G_C}{\left(3\mu + \left(\frac{3}{4}\right)^4 \left(\kappa - \frac{5}{3}\mu\right)\right)\delta}} & \text{3D case} \\[20pt] \sqrt{\dfrac{G_C}{\left(\frac{6}{\pi}\mu + \frac{16}{9\pi^2}(\kappa - 2\mu)\right)\delta}} & \text{2D case} \end{cases} \tag{2.21}$$

It is important to note that, from Eq. (2.20), Eq. (2.21) yields that s_c is dependent on the PD horizon size δ.

The static failure of the PD bond $x' - x$ can be represented by the history-dependent scalar-valued function φ proposed by Silling and Bobaru [118] and given as Eq. (2.22) (also see Fig. 2.4). The original symbol refers to μ, but, when notifying shear modulus of material μ, notification φ is selected in this study to prevent two variables from being notified by the same symbol.

$$\varphi(x' - x, t) = \begin{cases} 1 \text{ if } s_{xx'}(x' - x, t') < s_c \text{ for all } 0 < t' \\ 0 \text{ otherwise} \end{cases} \tag{2.22}$$

where s_c is the critical stretch of the material.
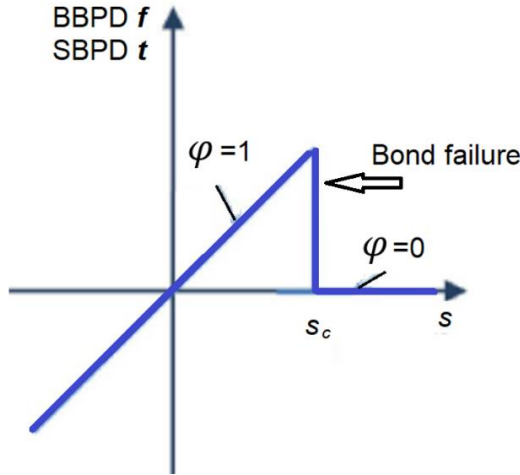
Fig. 2.4 Graphical representation of function φ [119]

Time in Eq. (2.23) is included due to the irreversible PD bond failure, e.g., once the PD bond $x' - x$ is broken after experiencing s_c value stretch, the bond does not exist further, even the relative deformation between the points x and x' is smaller than s_c. Then, the PD damage Φ_x can be evaluated as a ratio of broken PD bonds to the total PD bonds in the point x horizon:

$$\Phi_x = \frac{\sum N_{\varphi(x'-x)=0}}{N} \tag{2.23}$$

40

It is worth noting that the original PD material model [6] is an elastic brittle material model, which is well suitable for materials, such as ceramics, resins, carbon, or glass fibers. Nevertheless, other PD materials, such as viscoelastic or elasto-plastic materials, can be modelled [120]. Furthermore, the critical stretch-based PD model works well for BBPD, while, for a more complex material model or PD formulation (even SBPD), there is no simple approach to determine the PD failure parameters [108,121,122]. For example, Karpeno et al. [121] analyzed seven possible failure assumptions in SBPD, which leads to different values of the failure parameters. To cope with this problem, energy-based approaches were introduced in SBPD by Willberg [123] and Foster [124]. Madenci [105] suggested determining the critical stretch s_c, value for a complex material model, such as viscoelastic, from experimental observations.

2.3. Peridynamic Differential Operator (PDDO)

CCM strains and stresses are not originally included in the PD theory, although they can be calculated from the displacement field by applying PD integral differentiation. In the PD theory, it is known as the peridynamic differential operator (PDDO), which was originally applied by Silling [107] to calculate the strain and stress tensors of PD point x. Wide applications of PDDO have been demonstrated by Madenci et al. [125]: PDDO can be used in signal, images processing for data recovery, or mathematical operations, as shown in Fig. 2.5.
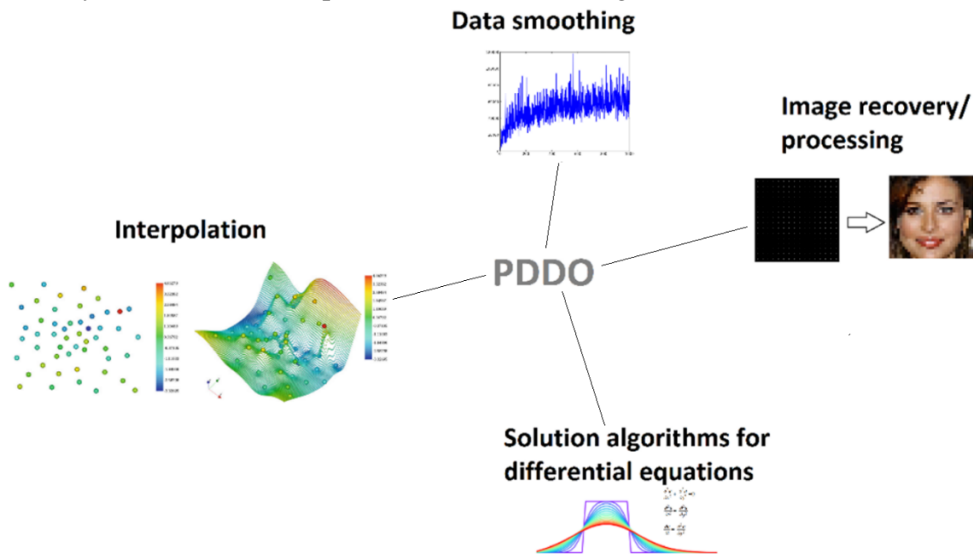
Fig. 2.5. Possible applications of PDDO according to [125]

PDDO provides the computational solution of complex field equations and the evaluation of derivatives of smooth or scattered data in the presence of discontinuities. Also, it serves as a natural filter to smoothen noisy data and to recover missing data.

In the general case, when having M-dimensional space, the Taylor series expansion of a scalar field $f(x') = f(x + \xi)$ with many variables can be expressed as [38]:

$$f(\boldsymbol{x} + \boldsymbol{\xi})$$
$$= \sum_{n_1=0}^{N} \sum_{n_2=0}^{N-n_1} \cdots \sum_{n_N=0}^{N-n_1-\cdots-n_{N-1}} \frac{1}{n_1! \, n_2! \ldots n_N!} \xi_1^{n_1} \xi_2^{n_2} \cdots \xi_M^{n_N} \frac{\partial^{n_1+n_2+\cdots+n_N} f(\boldsymbol{x})}{\partial x_1^{n_1} \partial x_2^{n_2} \cdots \partial x_M^{n_N}} \quad (2.24)$$
$$+ R(N, \boldsymbol{x})$$

where $R(N, \boldsymbol{x})$ represents the remainder. When assuming that the remainder is negligibly small and introducing the property of the orthogonal function $g_N^{p_1, p_2 \ldots p_N}(\boldsymbol{\xi})$, it yields the PD nonlocal expression for the partial derivatives of any order as:

$$\frac{\partial^{n_1+n_2+\cdots+n_N} f(\boldsymbol{x})}{\partial x_1^{n_1} \partial x_2^{n_2} \cdots \partial x_M^{n_N}} = \int_{H_x} f(\boldsymbol{x} + \boldsymbol{\xi}) \, g_N^{p_1, p_2 \ldots p_N}(\boldsymbol{\xi}) dx_1 dx_2 \ldots dx_M \quad (2.25)$$

where p_i is the order of differentiation with respect to variable x_i with $i = 1,\ldots,M$. PD functions $g_N^{p_1, p_2 \ldots p_N}(\boldsymbol{\xi}_{xx\prime})$ is related by the following orthogonality equation:

$$\frac{1}{n_1! \, n_2! \ldots n_N!} \int_{H_x} \xi_1^{n_1} \xi_2^{n_2} \cdots \xi_M^{n_N} \, g_N^{p_1, p_2 \ldots p_N}(\boldsymbol{\xi}) dx_1 dx_2 \ldots dx_M$$
$$= \delta_{n_1 p_1} \delta_{n_2 p_2} \ldots \delta_{n_N p_N} \quad (2.26)$$

and can be constructed for $n_i = 0,\ldots,N$:

$$g_N^{p_1, p_2 \ldots p_N}(\boldsymbol{\xi})$$
$$= \sum_{q_1=0}^{N} \sum_{q_2=0}^{N-q_1} \cdots \sum_{q_N=0}^{N-q_1 \ldots -q_{N-1}} a_{q_1 q_2 \ldots q_N}^{p_1 p_2 \ldots p_N} w_{q_1 q_2 \ldots q_N}(|\boldsymbol{\xi}|) \, \xi_1^{q_1} \xi_2^{q_2} \cdots \xi_M^{q_N} \quad (2.27)$$

where $w_{q_1 q_2 \ldots q_N}(|\boldsymbol{\xi}_{xx\prime}|)$ is the weight function. Errors related with PDDO depend on the horizon size δ, the grid spacing Δx, and the number of variables. The convergence of the nonlocal PDDO to exact local differentiation can be achieved as the horizon decreases and the number of integration points increases with the grid space Δx decreasing [125].

For the first order derivative in 3D space, the PDDO expression becomes:

$$\frac{\delta f}{\delta x_i} = A^{-1} \int_{H_x} \omega(|\boldsymbol{\xi}|) f(\boldsymbol{x} + \boldsymbol{\xi}) \xi_i dV \, , i = 1, 2, 3 \quad (2.28)$$

where

$$A = \int_{H_x} \omega(|\boldsymbol{\xi}|) \begin{bmatrix} \xi_1^2 & \xi_1 \xi_2 & \xi_1 \xi_3 \\ \xi_1 \xi_2 & \xi_2^2 & \xi_2 \xi_3 \\ \xi_1 \xi_3 & \xi_2 \xi_3 & \xi_3^2 \end{bmatrix} dV \quad (2.29)$$

Implementing Eq. (2.28) to SBPD and notifying $\underline{\boldsymbol{Y}}(\boldsymbol{x}' - \boldsymbol{x}) = \boldsymbol{\xi}_{xx\prime} + \boldsymbol{\eta}_{xx\prime}$ as the deformation state, the non-local deformation gradient of point x is given as follows [126]:

$$F = \left[\int_{H_x} \omega\langle|\xi_{xx'}|\rangle(\underline{Y}(\xi_{xx'})\otimes\xi_{xx'})dV_\xi\right] \cdot \left(\int_{H_x} \omega\langle|\xi_{xx'}|\rangle(\xi_{xx'}\otimes\xi_{xx'})dV_\xi\right)^{-1} \quad (2.30)$$

when strain tensors can be calculated by applying CCM formulations [126]. The influence function $\omega\langle|\xi_{xx'}|\rangle$, which depends only on the choice of the bond length, is an important aspect. According to the study by Seleson and Littlewood [127], a linear function is sufficient for 3D problems. In case of a 2D model, a cubic polynomial influence function, such as $\left(1 - \frac{|\xi_{xx'}|}{\delta}\right)^3$, should be used.

2.4. Numerical Implementation of the PD Theory

The key to the numerical implementation of PD is spatial and time numerical integrations. As the number of PD points is finite in the body domain and in the PD horizon, the integrals in the PD equations of motion Eqs. (2.1) – (2.2) are replaced by sums. This also leads to the fact that the PD point volume is not infinitely small, and some PD points are truncated within the limits of PD horizons (Fig. 2.6 a). Another issue is related to truncated PD horizons at body boundaries (Fig. 2.6 b). When performing numerical integration, those effects should be evaluated in order to prevent errors.

a	b
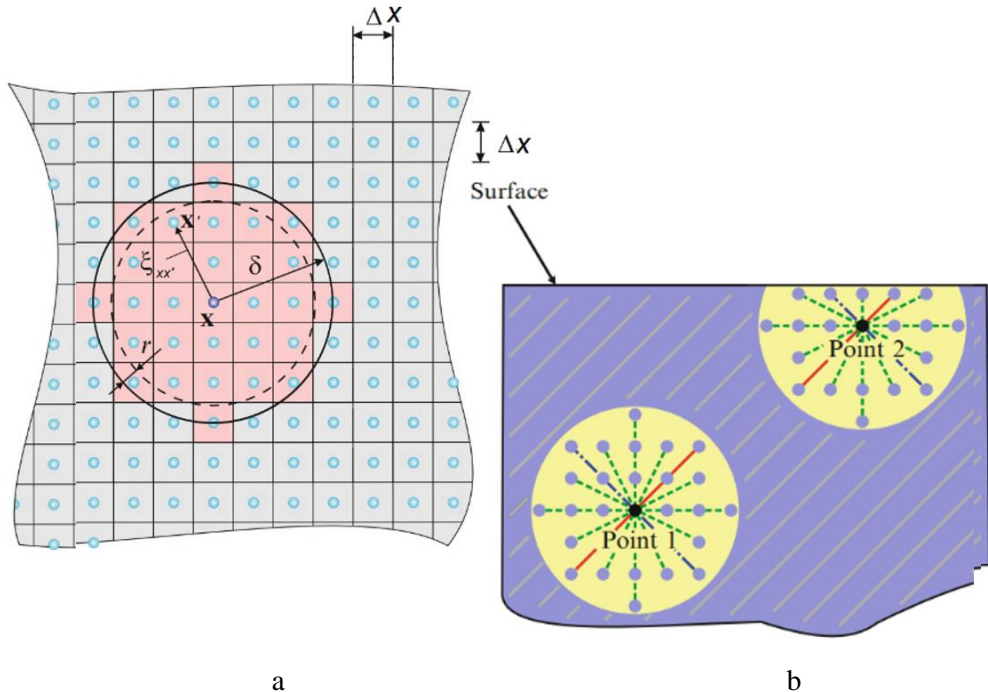
Fig. 2.6 PD numerical implementation issues [105]: a – truncated PD points in the PD horizons; b – not full PD horizons at the boundaries

To solve the problem of PD points truncated volumes (Fig. 2.5 a), special correction factors, called volume corrections, are calculated and applied. The correction of the

43

point x volume V_x is performed by multiplying V_x to the correction factor v_{cx}, as defined in [105]:

$$v_{cx} = \begin{cases} (\delta + r - |\boldsymbol{\xi}_{xx\prime}|)/2 \text{ if } \delta - r < |\boldsymbol{\xi}_{xx\prime}| < \delta \\ 1 \text{ otherwise} \end{cases} \tag{2.31}$$

The issue of not full PD horizons at the boundaries (Fig. 2.6 b) results in effective material properties which are different near the surface and inside the body. This is called the PD surface effect. There is no single solution which would allow to completely eliminate the PD surface effect for complex material deformations, although it can be significantly reduced or completely eliminated for simple load cases. A simple and effective method is bond stiffening when BBPD bond stiffness corrections are calculated according to the volumes of the PD horizons [128]:

$$c_{corrected} = \frac{2V_0}{V(x) + V(x')} c \tag{2.32}$$

where V_0 is the volume of the full PD horizon, and $V(x)$, $V(x')$ are the volumes of the PD horizons of points x and x'.

Other surface correction methods [128] are also based on corrections factors which can be determined by comparing the force densities and the strain energy densities. Alternatively, correction factors can be determined by comparing the restoring forces required to return PD points in the bulk and near the surface to their initial positions after deformation [129]. Moreover, fictitious nodes can be included to prevent the surface effect in the PD model. It is worth noting that the surface effect takes only one horizon size δ for BBPD and two horizons 2δ for SBPD [130]. The surface correction in SBPD is more complex, although, when comparing the displacement fields at the same loading in uncorrected BBPD and SBPD models, Le and Bobaru [128] found that surface distortions are larger in uncorrected BBPD models.

Although PD equations of motion can be solved even without the constraints of the body, but, in many cases, constraints are still necessary to reflect the simulated body boundary conditions. Differently than FE, in the PD model, constraints can be applied only over a specified volume. Based on the study by Macek and Silling [129], displacement and velocity constraints should be applied over a region of a fictious boundary layer equal to the PD horizon size δ so that to correctly reflect the effect of the constraints. The external load $\boldsymbol{P}(t)$ in the PD model can be applied as the body force $\boldsymbol{b}(x,t)$ and calculated according to the boundary region with the layer $\varDelta$ volume [105]:

$$\boldsymbol{b}(\boldsymbol{x}, t) = \frac{\boldsymbol{P}(t)}{A\Delta} \tag{2.33}$$

where A is the boundary surface area where the external load $\boldsymbol{P}(t)$ is applied.

The numerical time integration of the PD equation of motion can be performed by using both explicit [105] and implicit [131] solutions. The explicit solution is simpler, but it leads to stability issues if an insufficient time step size is chosen. A stable time step Δt condition for the SBPD point x is based on standard von Neumann stability analysis, as given by Madenci and Oterkus [105]:

44

$$\Delta t = k \cdot min \left(\sqrt{\frac{2\rho_\mathrm{x}}{\sum \left(2ad\delta \frac{\left(d\delta \sum \left(\frac{1}{|\xi_{x''x}|} + \frac{1}{|\xi_{x''x}'|} \right) \right)}{|\xi_{x'x}|} + \frac{4b\delta}{|\xi_{x'x}|} \right) v_{cx'} V_{x'}}} \right) \quad (2.34)$$

where x, x' and x'' are the PD material points; $V_{x'}$ is the volume of the PD point x'; $v_{cx'}$ is the volume correction factor; $k \leq 1$ is the safety factor. The stable time step strongly depends on the PD horizon size δ because all the PD material parameters a-d are also related with δ. Despite the PD equations of motion (Eq. (2.1) and Eq. (2.2)) being dynamic equations, they can be adopted to solve static problems by introducing artificial damping [132]. Nevertheless, the damping value selection is difficult, especially for the non-linear material model. The *Adaptive Dynamic Relaxation* (ADR) scheme method [133] was proposed by Underwood and was used to calculate the required damping value at each time step so that the dynamic solution settles as quickly as possible.

The final PD theory implementation step is the software selection. EMU was the first PD code written by Silling [117]. Conventional FE packages do not support PD elements, or else the PD element selection is very limited. For example, *LS-Dyna* offers the BBPD material model MAT_ELASTIC_PERI or MAT_ELASTIC_PERI_LAMINATE for composites [134], but there are no more available PD material models in *LS-Dyna*. Alternatively, BBPD elements in the FE software, e.g., *LS-Dyna*, *ANSYS*, or *Abaqus* can be generated by using a truss element for each PD bond [96,129,135]. SBPD still has no equivalents in FE packages, thus it can only be implemented in specific software. In terms of of such software, *Peridigm* [136], molecular dynamics software *LAMMPS* [137] or *Sierra/SolidMechanics* can be used. Finally, internal PD codes can be created by using programming languages or computational software.

2.5. PD Model in MATLAB

The BBPD and OSBPD models are created and implemented in *MATLAB* in this study. The general modelling principles are taken from open sources *MATLAB* codes available in [131,138]. Each created *MATLAB* PD code segment, as shown in Fig. 2.7, is written as a separate function, and can be run in the main PD code file.

The PD model geometry, material properties, PD parameters, namely, the PD horizon size δ and the PD grid spacing Δx, are defined firstly. The horizon size was set to $\delta = 3.1\Delta x$ according to the general recommendations [110] so that to ensure the model stability. Larger values of Δx result in fewer PD points and faster computation, but model discretization becomes coarse. At least 12 PD points per model width are considered in this study to prevent large distortions caused by the PD surface effect. Since explicit time integration is used, after identifying the PD parameters, a stable time step can be calculated (Fig. 2.7). The safety factor $k = 0.5$ per time step is applied (see Eq. (2.34)). PD points coordinates are stored in a matrix whose format is [number

of PD points, number of coordinates]. The same format is used for PD the points displacement, velocity, and acceleration matrices.
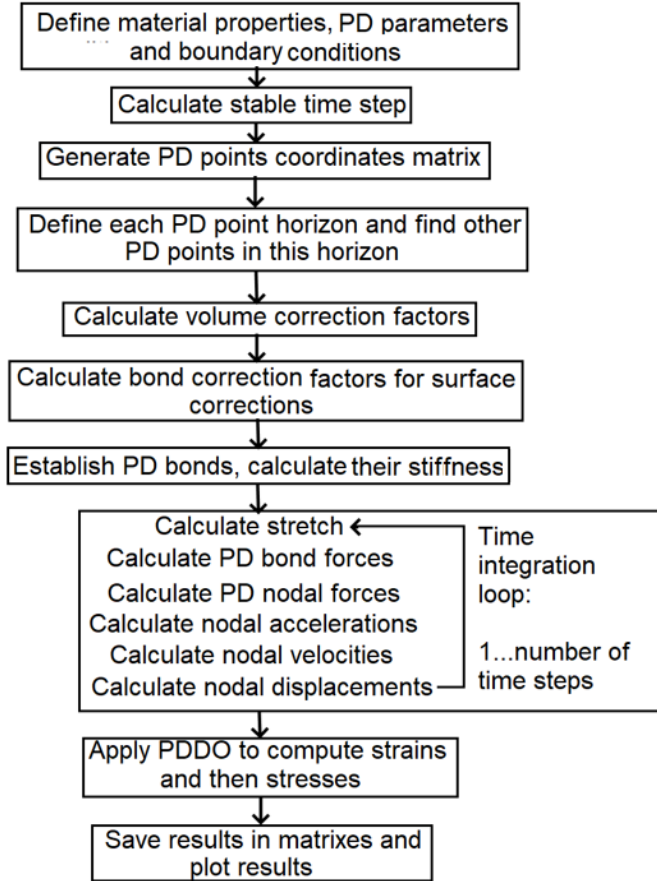
Fig. 2.7 Created PD model MATLAB code schematics

To find the neighbor PD points within the point x horizon, the *MATLAB* function *rangesearch* (COORDINATES, COORDINATES, DELTA) is used. Here, DELTA is the PD horizon size δ. For the BBPD volume method, (Eq. (2.32)) is used to reduce the surface effects, whereas, for OSBPD correction, factors for PD force density and volume dilatation are calculated, thus comparing the CCM and PD strain energy densities for simple loading conditions [131]. When considering the uniaxial strain ε, the CCM dilatation term is $\theta_{CCM} = \varepsilon$, thus the dilatation correction for point x is calculated as follows:

$$S_{\theta x} = \frac{\theta_{CCMx}}{\theta_{PDx}} = \frac{\varepsilon}{d \sum_{x=1}^{N} \omega_{xx'} S_{xx'} \Lambda_{xx'} V_x} \tag{2.35}$$

and, for the case of the shear strain τ: $\theta_{CCM} = 0$, $W_{CCM} = \frac{1}{2}\mu\tau^2$, which leads to the force density correction for point x:

46

$$S_{tx} = \frac{W_{CCMx}}{W_{PDx}} = \frac{\frac{1}{2}\mu\tau^2}{b\delta \sum_{x=1}^{N} \frac{1}{|\boldsymbol{\xi}_{xx'}|} (|\boldsymbol{\xi}_{xx'} + \boldsymbol{\eta}_{xx'}| - |\boldsymbol{\xi}_{xx'}|)^2 V_x} \tag{2.36}$$

Based on the approach that Eq. (2.35) and Eq. (2.36) are valid for such loading conditions in any direction along the coordinate axes *X*, *Y* and *Z* and assuming that the correction factor for each PD bond **x'** – **x** is equal to the average correction factor of points *x* and *x'* as $S_{xx'} = \frac{S_x + S_{x'}}{2}$, the correction factor for the PD bond **x'** – **x** can be defined:

$$S_{xx'} = \frac{1}{\sqrt{\left(\frac{\xi_{xx'\_X}}{S_{xx'\_X}}\right)^2 + \left(\frac{\xi_{xx'\_Y}}{S_{xx'\_Y}}\right)^2 + \left(\frac{\xi_{xx'\_Z}}{S_{xx'\_Z}}\right)^2}} \tag{2.37}$$

_X, _Y, _Z in Eq. (2.37) refer to the vector projections to the coordinate axes *X*, *Y*, *Z* respectively.

Artificial damping of $C = 0 \div 1 \cdot 10^{10}$ kg/s (the values are based on the model dimensions and the material properties because the critical damping of the system equals to $C_c = 2\sqrt{Km}$, where *m* is the mass, and *K* is the stiffness of the system) was introduced to get the quasi-static solution of the PD equation of motion. Then, the PD equations of motion (Eq. 2.1 and Eq. 2.2) in their numerical form become:

$$\rho\ddot{\boldsymbol{u}}(\boldsymbol{x}, t) = \sum_{x=1}^{N} \{\underline{\boldsymbol{T}}[\boldsymbol{x}, t]\langle \boldsymbol{x'} - \boldsymbol{x}\rangle - \underline{\boldsymbol{T}}[\boldsymbol{x'}, t]\langle \boldsymbol{x} - \boldsymbol{x'}\rangle\}v_{cx'}V_{x'} + C\dot{\boldsymbol{u}}(\boldsymbol{x}, t)$$
$$+ \boldsymbol{b}(\boldsymbol{x}, t) \tag{2.38}$$

In order to prevent large accelerations and dynamics forces resulting in failure of the investigated material, the force or prescribed displacement ($\boldsymbol{u}(\boldsymbol{x}, t) \neq 0$ for $t > 0$) boundary conditions of the model are performed by increments for each time step Δt, such as:

$$\boldsymbol{b}(\boldsymbol{x})_i = \frac{i}{N_T}\boldsymbol{b}(\boldsymbol{x}, N_T\Delta t) \tag{2.39}$$

$$\boldsymbol{u}(\boldsymbol{x})_i = \frac{i}{N_T}\boldsymbol{u}(\boldsymbol{x}, N_T\Delta t) \tag{2.40}$$

where $i = 1 \ldots N_T$, N_T is the number of timesteps. The increment size should satisfy the following Equation [139]:

$$\frac{1}{2\rho}[\boldsymbol{b}(\boldsymbol{x}, (i+1)\Delta t) - \boldsymbol{b}(\boldsymbol{x}, i\Delta t)]\Delta t^2 < s_c\Delta x \tag{2.41}$$

Huang et al. [139] also suggested parameter *β* to evaluate the PD model dynamic effects. *β* is used to determine the equilibrium state of the model; if the PD model is in the equilibrium state, it can withstand the existing external loads, and, at the end of the simulation, *β(t)* becomes constant.

$$\frac{\sum(\rho \ddot{u}(x,t) - C\dot{u}(x,t) - b(x,t))^2}{\sum(b(x,t))^2} \leq \beta \tag{2.42}$$

Lower β values are associated with better model accuracy, although the computation time increases.

Nevertheless, the final verification of the quasi-static PD model is done by considering simple loading, e.g., uniaxial tension, and by comparing the computed PD displacement and strain fields with FE or/and analytic solutions. An example of such a PD model implemented in *MATLAB* is presented in Fig. 2.8. A steel plate ($E = 210$ GPa, $\upsilon = 0.3$) of dimensions: length 100 mm, width 50 mm and thickness 12 mm is analyzed. The plate is loaded by 13800 N external tension load in the length direction (Fig. 2.8 a). The load applied for a layer of thickness Δx and the bottom points of the plate in a layer of thickness $3\Delta x$ (Fig. 2.8 a) are fixed by setting their displacement to 0 in all the global coordinate axes X, Y, Z directions. The PD grid spacing is set as $\Delta x = 2$ mm, and the PD horizon size is $\delta = 3.1 \, \Delta x$. The number of time steps $N_T = 1000$ is selected.

a   b
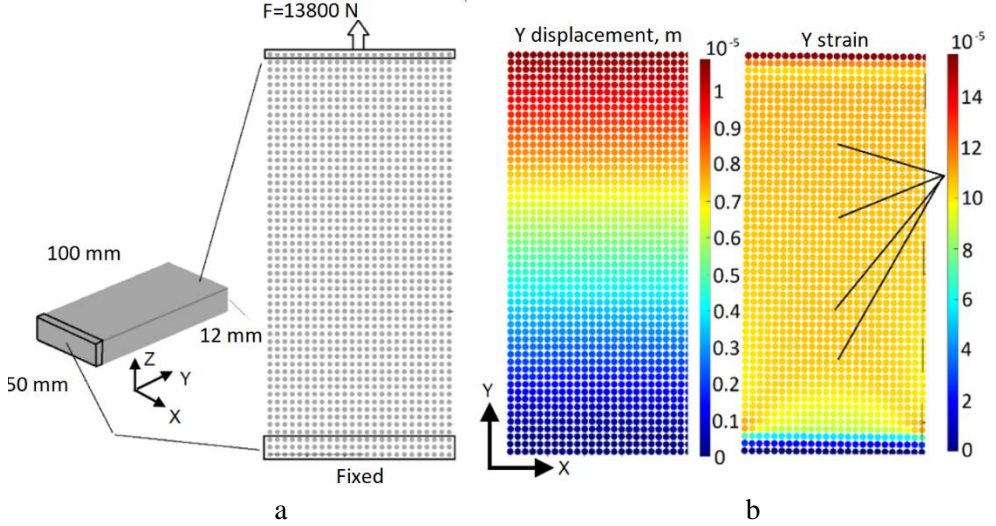
Fig. 2.8. Quasi-static PD model implemented in MATLAB: a – modelling schematics; b – simulated displacement and strain fields in *Y* direction (results identical for both BBPD and SBPD)

A tensile load of 13800 N in the PD model results in a maximum displacement in the *Y* direction of $1.09 \cdot 10^{-2}$ mm, and an almost uniform strain field of value $\varepsilon = 1.09 \cdot 10^{-4}$ in the same direction. Both BBPD and SBPD simulation results comply with the analytic displacement field calculation $u(y) = \frac{F}{EBH}y$ yielding a maximum displacement value of $1.095 \cdot 10^{-2}$ mm and uniform strain in the *Y* direction, equal to $\varepsilon = \frac{F}{EBH} = 1.095 \cdot 10^{-4}$. Parameter β dependence on the artificial damping C value is shown in Fig. 2.9.
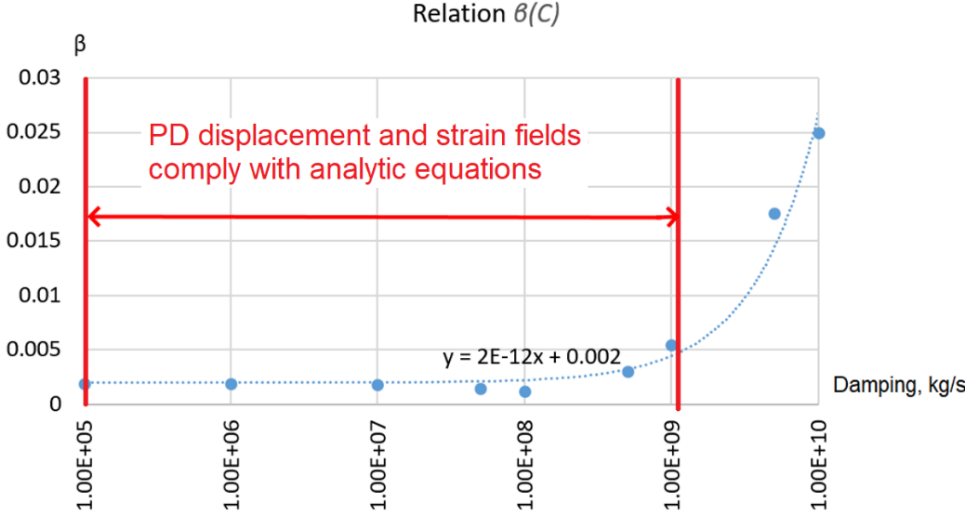
Fig. 2.9 Parameter β relation to various artificial damping values in BBPD model, $\beta(C)$

From the plot results presented in Fig. 2.9, it can be seen that the minimum value of parameter β of $1.2 \cdot 10^{-3}$ is reached at damping of $C = 10^8$ kg/s. Simulated displacement and strain fields correspond to analytic equations in the damping range of $C = 0 \div 1 \cdot 10^9$ kg/s. Higher than 10^9 kg/s damping results suddenly increased the β values and the simulated displacement, whereas the strain fields are not compatible with analytic equations. It is worth noting that different damping values are necessary for BBPD and SBPD models to achieve the β minimum despite the same geometry. Moreover, the computational time is about 15 times longer for the SBPD model comparing to a BBPD model of the same geometry.

2.6. Conventional Fatigue Model under PD

The PD bond remaining life parameter notification q is used in this study (original notification λ [8]) to prevent confusion with the further-used KTF shape factor λ. At the initial state for the bond $\boldsymbol{\xi}_{xx\prime} = \boldsymbol{x}' - \boldsymbol{x}$ $q_{xx}(0) = 1$. With an increasing number of cycles N, the parameter reduces till a cyclic failure of the bond $\boldsymbol{x}' - \boldsymbol{x}$ occurs after N_f cycles resulting in $q_{xx}(N_f) = 0$. Then, the PD failure function can be extended as

$$\varphi(\boldsymbol{\xi}_{xx\prime\prime}, t) = \begin{cases} 1 \text{ if } (s_{xx\prime}(\boldsymbol{x}' - \boldsymbol{x}, t') < s_c \text{ or } q_{xx\prime}(\boldsymbol{x}' - \boldsymbol{x}, t') \leq 0) \text{ for all } 0 < t' \\ 0 \text{ otherwise} \end{cases} \quad (2.43)$$

including both static and cyclic failures.

Similarly as in FE, PD fatigue analysis also consists of static simulation at the maximum cycle loading. The conventional approach, adopted for the PD model [8], is based on the cycle stretch

$$\varepsilon_{xx\prime} = \left| s_{xx\prime}^+ - s_{xx\prime}^- \right| = \left| \frac{\left(\left| \boldsymbol{\xi}_{xx\prime} + \boldsymbol{\eta}_{xx\prime}^+ \right| - \left| \boldsymbol{\xi}_{xx\prime} \right| \right)}{\left| \boldsymbol{\xi}_{xx\prime} \right|} \right| (1 - R) \quad (2.44)$$

49

when R is the stress ratio. Then, the evolution of $q_{xx'}$ according to the number of cycles is expressed as:

$$\frac{dq_{xx'}}{dN} = -A_i \varepsilon_{xx'}{}^{m_i} \qquad (2.45)$$

where A_i and m_i are the empiric coefficients; $i = 1, 2$, and 1 refers to the crack initiation phase and 2 denotes the crack growth phase. For the fatigue crack initiation phase, it is possible to assume that the cyclic stretch does not depend on the numbers of cycles; thus, Eq. (2.45) can be simplified to

$$q_{xx'}(N) = 1 - \frac{1}{A_1 \varepsilon_{xx'}{}^{m_1}} \qquad (2.46)$$

and coefficients A_1, m_1 can be established from the material S-N curve.

PD damage Φ is used as a criterion for the transition from the initiation to the crack growth phases. Coefficients A_1 and m_1 are usually switched to A_2 and m_2 when the PD damage at point x reaches 0.5 ($\Phi_x \geq 0.5$) [8], although there are more conservative studies [9] using a transition criterion $\Phi_x \geq 0.39$. Once the fatigue crack growth phase has started, the values of coefficients A_2 and m_2 should be established. While m_2 can be taken directly from Paris' power law (see Eq. (1.4)), A_2 can only be found after running trial simulation with an arbitrary value A_2'. This leads to the crack growth rate $\widehat{da/dN}$ and then, due to knowing the real crack growth rate da/dN from experiments, it is possible to set the coefficient A_2:

$$A_2 = \frac{da/dN}{\widehat{da/dN}} A_2' \qquad (2.47)$$

Moreover, the coefficient A_2 is dependent on the PD horizon size. If the $A_2{}^0$ value is set for the PD horizon δ^0, for another PD horizon size δ, it should be corrected according to the following Equation [8]:

$$A_2 = A_2{}^0 \delta^{\frac{m_2-2}{2}} \qquad (2.48)$$

Coefficients A_1, m_1, m_2 are independent from δ. The main limitation of such a method is the empirical coefficients A_i, m_i which are different for different loading conditions, such as the stress ratio R, the temperature, and the loading frequency. KTF, presented in the next chapter, is a physical approach which is free from such empirical coefficients.

2.7. Kinetic Theory of Fracture

Fatigue damage n evolution during time t in KTF is treated as a thermally activated process described with a differential equation [140]:

$$\frac{dn}{dt} = (n_0 - n)^\lambda K_b \qquad (2.49)$$

where n_0 is the initial constant, λ is the shape factor, and K_b is the fatigue crack formation and growth rate parameter, derived from the durability Equation [94,95]:

$$\tau = \tau_0 e^{-\frac{U-\gamma\sigma}{kT}} \qquad (2.50)$$

where k – Boltzmann constant; T – process temperature; U and γ – process activation energy and activation volume; σ – applied stress; τ – failure time; $\tau_0 = 10^{-13}$ s – characteristic oscillation period of atoms in a solid body [140]. Although the PD model is not an atom-scale model and the PD body discretization into points is at a macro-scale level, Eq. (2.49) and Eq. (2.50) can be adopted. Then, the fatigue crack formation and growth parameter K_b becomes the PD bond breakage rate parameter, and it can be calculated for each PD bond $\boldsymbol{x'} - \boldsymbol{x}$ from Planck's law:

$$K_{bxx'} = \frac{kT}{h} e^{-\frac{U - \gamma \sigma_{xx'}}{kT}} \tag{2.51}$$

where h is the Planck constant. The term $\sigma_{xx'}$ represents the PD bond $\boldsymbol{x'} - \boldsymbol{x}$ stress. PD bond stress is calculated not from the PD bond stiffness and stretch, but as the average of stresses at the PD points x and x' as $\sigma_{xx'} = \frac{\sigma_x + \sigma_{x'}}{2}$ [97]. The PD bond 'remaining life' parameter $q_{xx'}$ is related to fatigue damage as

$$q_{xx'} = 1 - n_{xx'} \tag{2.52}$$

When determining the cyclic loading history, it is possible to integrate Eq. (2.49). For the case of the constant amplitude triangular cyclic loading history with the cyclic loading frequency f (Fig. 2.10), it can be assumed that the maximum PD bond stress occurs at the time t, whereas the minimum is observed at the time t_1. After the invoking stress ratio R: $\sigma_{\min} = R\sigma_{\max}$, together with loading frequency f: $\Delta t = \frac{N}{f}$, it is possible to perform an integration and derive the PD-KTF fatigue damage equation for each PD bond $\boldsymbol{x'} - \boldsymbol{x}$ [96]:

$$
\begin{aligned}
n_{xx'}&(N, \sigma_{max}, R, T, f) \\
&= n_{0xx'} \\
&\quad - \Bigg\{ (n_{0xx'} - n_{Ixx'})^{1-\lambda} \\
&\quad - (1 - \lambda) \frac{(kT)^2}{h} \frac{N}{\gamma f \sigma_{max_{xx'}}(1 - R)} e^{-\frac{U}{kT}} \left[e^{\frac{\gamma \sigma_{max_{xx'}}}{kT}} \right. \\
&\quad \left. - e^{\frac{\gamma R \sigma_{max_{xx'}}}{kT}} \right] \Bigg\}^{\frac{1}{1-\lambda}} ; \; if \; \lambda \neq 1
\end{aligned}
\tag{2.53}
$$

$$
\begin{aligned}
n_{xx'}&(N, \sigma_{max}, R, T, f) \\
&= n_{0xx'} \\
&\quad - (n_{0xx'} \\
&\quad - n_{Ixx'}) \exp \Bigg\{ -\frac{(kT)^2}{h} \frac{N}{\gamma f \sigma_{max_{xx'}}(1 - R)} e^{-\frac{U}{kT}} \left[e^{\frac{\gamma \sigma_{max_{xx'}}}{kT}} \right. \\
&\quad \left. - e^{\frac{\gamma R \sigma_{max_{xx'}}}{kT}} \right] \Bigg\} ; \; if \; \lambda = 1
\end{aligned}
\tag{2.54}
$$
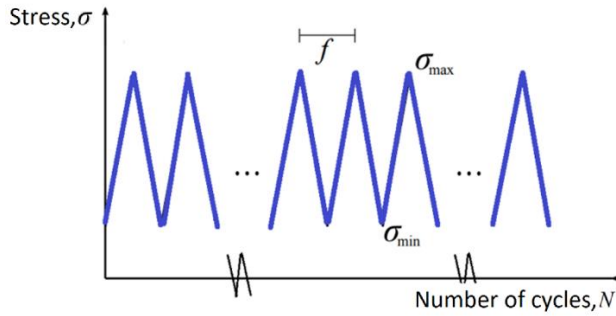
Fig. 2.10. Constant amplitude and frequency triangular shape cyclic loading history

where $n_{Ixx'}$ is the initial fatigue damage of the PD bond $x'- x$ (at the start of the PD simulation $n_{Ixx'} = 0$). The initial constant n_0 can be calculated from the process initial and end conditions [94] resulting in Equation:

$$\int_0^1 \frac{dn}{(n_0 - n)^\lambda} = 1 \qquad (2.55)$$

The effect of the shape factor λ was demonstrated by Bhuyan and Fertig [141] and shown in Fig. 2.11. λ determines the ratio of damage accumulation during the early versus later stages of the fatigue process.
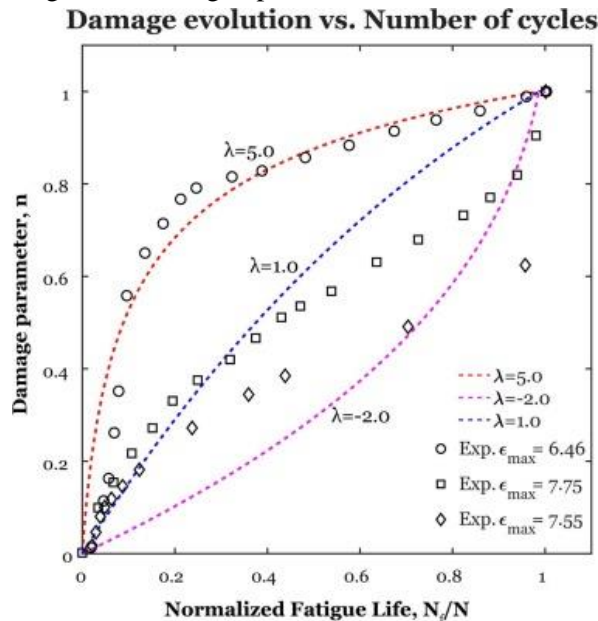
Fig. 2.11 Effect of different shape factors λ to fatigue damage growth in KTF [141]

When comparing the results from Fig. 2.11, it can be seen that λ does not affect the number of cycles to failure, but, as λ values increase, the fatigue damage accumulates faster at the beginning of cyclic loading (curve $\lambda = 5$). Madenci et al. in their studies combining PD and KTF [96,97] used the shape factor $\lambda = 9$, which delivered the result

52

$n_0 = 1.771$.

The same as the conventional PD fatigue model, the KTF-PD model should include the fatigue crack initiation and growth phases. The process activation energy U and the activation volume γ are calibrated for the fatigue crack growth initiation phase from the material S-N curve. Nevertheless, it is usually not possible to find U and γ values corresponding to Eq. (2.53) and Eq. (2.54) to the entire S-N curve of the material, and then U and γ can be calibrated only for a specific stress range as it is shown in Fig. 2.12 a. Zhang and Madenci [96] derived analytic equations to calculate U_i and γ_i values for each stress range by using tangent lines to an S-N curve plotted at S-$\log(N)$ axes. Each tangent line i of the S-N curve crosses the $\log(N)$ axis at value a_i and S axis at value b_i. Then,

$$U_i = -kT \left(\frac{b_i}{a_i} + \ln\left(f\tau_0\right) \right) \tag{2.56}$$

$$\gamma_i = -\frac{kT}{a_i} \tag{2.57}$$

Alternatively, U_i and γ_i values can be found not only by using Eq. (2.56) and Eq. (2.57), but also by minimizing differences between the S-N curve of the material and Eq. (2.53), Eq. (2.54), as it is used further in this study.

The fatigue crack growth is a faster process (in cycles) than the crack initiation; thus, the process activation energy and volume should be updated as $U_i = k_U \cdot U_i$ and $\gamma_i = k_\gamma \cdot \gamma_i$ when $i = 1 \ldots M$ (Fig. 2.12 b). The PD point damage of $\Phi_x = 0.5$ is sufficient to determine the end of the fatigue crack initiation phase and the start of the fatigue crack growth phase.

a   b
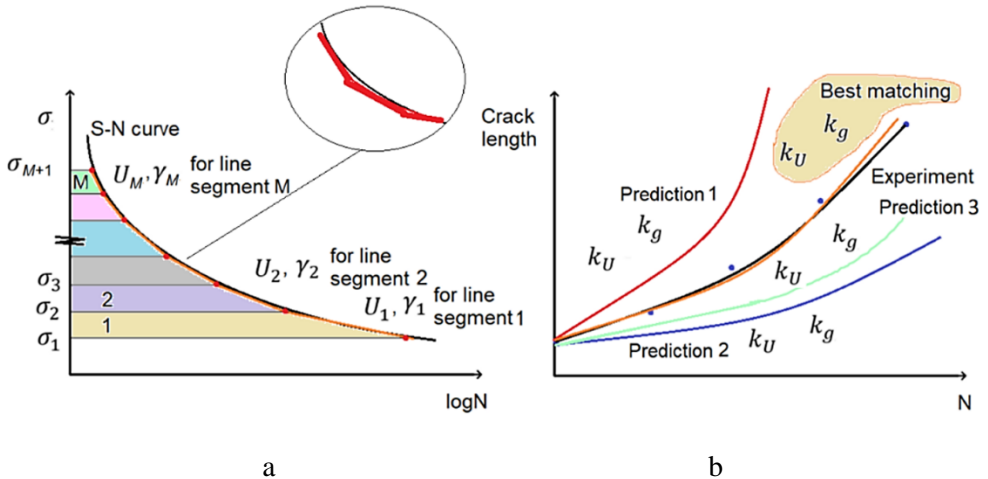
Fig. 2.12. Calibrating process activation energy U and activation volume γ: a – for crack initiation phase from S-N curve; b – for the crack growth phase from the crack length vs. the number of cycles experimental plot

Similarly as for the conventional PD fatigue model, there is no equation to determine

k_U and k_y values; instead, they can be found from trials comparing experimental and KTF-PD simulated fatigue crack lengths versus the number of cycle plots (Fig. 2.12 b).

When comparing the conventional approach from Paris' law $q_{xx'}(N, \sigma_{max}, A, m)$ versus the KTF approach $q_{xx'}(N, \sigma_{max}, R, T, f)$, it is visible that both methods depend on multiple process parameters, but, for the case of KTF, they are related to the process conditions. Once calibrated for symmetric cyclic loading ($R = -1$), the KTF fatigue damage equations (Eq. (2.53) and Eq. (2.54)) should be valid for different testing conditions included into equation, namely, the stress ratio R, the temperature T, and the loading frequency f, while the conventional Paris' law approach, based on the empirical coefficients A, m, can only be applied to specific testing conditions. Nevertheless, the KTF fatigue damage equations Eq. (2.53) and Eq. (2.54), calibrated for symmetric cyclic loading ($R = -1$) at room temperature, yield an incorrect fatigue life when $R \to 1$, as it is shown in Fig. 2.13.
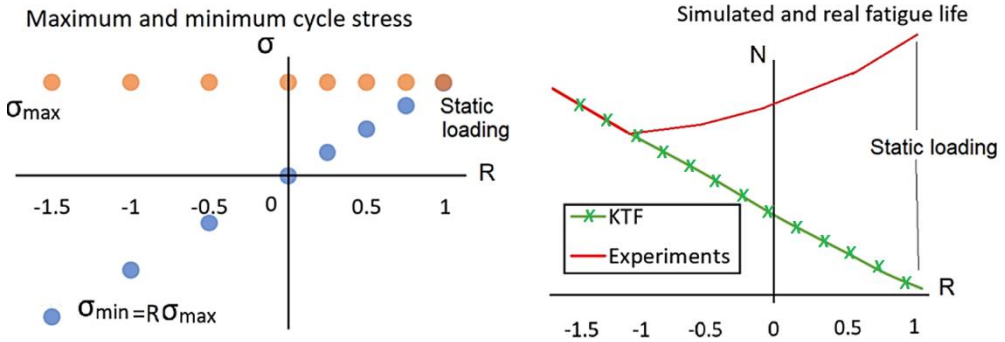
Fig. 2.13. Differences between KTF predicted fatigue life and experiment results

When $R = 1$, $\sigma_{min} = \sigma_{max}$, and this refers to static loading resulting in an infinite fatigue life, but the fatigue life, predicted according to KTF Eq. (2.53) and Eq. (2.54), is close to 0. Fatigue experiments on unidirectional composites [142] also show an increased fatigue life with higher σ_{min} and the same σ_{max} cycle stress, which is opposed to the predicted fatigue life according to KTF Eq. (2.53) and Eq. (2.54). Fertig et al. [143–145] in their studies, based on experimental observations that a higher cycle stress amplitude or a higher loading frequency cause significant heating of the composite structure, included a KTF temperature correction term proportional to the cycle stress amplitude. Then, the temperature term in Eq. (2.53) and Eq. (2.54) is expressed as:

$$T = T^* + \sum_{i=1}^{N} \psi \frac{{\sigma_a}^2}{\Delta t} \tag{2.58}$$

where T^* is the initial temperature, ψ is the proportional constant, $\sigma_a = 0.5(\sigma_{max} - \sigma_{min})$ is the stress amplitude, Δt is the cycle time, and N is the number of cycles. Then, Eq. (2.53) and (2.54) can be rewritten as:

54

$$n_{xx'}(N, \sigma_{max}, R, T, f)$$
$$= n_{0xx'}$$

$$- \left\{ (n_{0xx'} - n_{Ixx'})^{1-\lambda} \right.$$

$$- (1-\lambda) \frac{\left(k\left(T^* + \sum_{i=1}^{N} \psi \frac{\sigma_a^{\,2}}{\Delta t} \right) \right)^2}{h} \frac{N}{\gamma f \sigma_{max_{xx'}}(1-R)} e^{-\frac{U}{k\left(T^* + \sum_{i=1}^{N} \psi \frac{\sigma_a^{\,2}}{\Delta t} \right)}} \quad (2.59)$$

$$\left. \cdot \left[e^{\frac{\gamma \sigma_{max_{xx'}}}{k\left(T^* + \sum_{i=1}^{N} \psi \frac{\sigma_a^{\,2}}{\Delta t} \right)}} - e^{\frac{\gamma R \sigma_{max_{xx'}}}{k\left(T^* + \sum_{i=1}^{N} \psi \frac{\sigma_a^{\,2}}{\Delta t} \right)}} \right] \right\}^{\frac{1}{1-\lambda}} \quad ; if\ \lambda \neq 1$$

$$n_{xx'}(N, \sigma_{max}, R, T, f)$$
$$= n_{0xx'}$$

$$- (n_{0xx'} - n_{Ixx'})\exp\left\{ -\frac{\left(k\left(T^* + \sum_{i=1}^{N} \psi \frac{\sigma_a^{\,2}}{\Delta t} \right) \right)^2}{h} \right.$$

$$\cdot \frac{N}{\gamma f \sigma_{max_{xx'}}(1-R)} \cdot e^{-\frac{U}{k\left(T^* + \sum_{i=1}^{N} \psi \frac{\sigma_a^{\,2}}{\Delta t} \right)}} \left[e^{\frac{\gamma \sigma_{max_{xx'}}}{k\left(T^* + \sum_{i=1}^{N} \psi \frac{\sigma_a^{\,2}}{\Delta t} \right)}} \right. \quad (2.60)$$

$$\left. \left. - e^{\frac{\gamma R \sigma_{max_{xx'}}}{k\left(T^* + \sum_{i=1}^{N} \psi \frac{\sigma_a^{\,2}}{\Delta t} \right)}} \right] \right\} ; if\ \lambda = 1$$

The modified KTF version is valid in predicting the fatigue life of composite structures at any stress ratio once calibrated for symmetric cyclic loading, and as the constant ψ is established. Constant ψ definition requires additional fatigue life data at a different than $R = -1$ stress ratio, but this approach is still better than the empiric Paris' law coefficients having no relation among different testing conditions. Furthermore, it is a motivation to further develop a more detailed physics-based material model for cyclic loading by using KTF equations. Analysis of the fatigue behavior at different stress ratios similar to that conducted by Fertig et al. [143–145] suggested that the correction approach can be applied not only to polymer composite materials, but also to other materials (e.g., metals).

Finally, the general KTF-PD fatigue modelling flowchart can be described by

the following steps, suggested by Madenci et al. [86,96]:

1. Static PD simulation to achieve the maximum cycle stress;
2. Strain tensor of PD point x calculation;
3. Stress tensor of PD point x calculation;
4. Maximum/equivalent or other type, according to material, stress of PD point x calculation;
5. PD bond stress calculation: $\sigma_{xx\prime} = \frac{\sigma_x + \sigma_{x\prime}}{2}$;
6. PD damage calculation. If $\Phi_x < 0.5$, then fatigue crack initiation; otherwise, it is the fatigue crack growth phase. For the fatigue crack growth, phase U and γ have to be updated as $k_U \cdot U$ and $k_\gamma \cdot \gamma$;
7. The number of cycles N to maximum loaded PD bond failure calculation.
8. The fatigue damage parameter n calculation for each PD bond by using the N value computed at Step 7.
9. The number of cycles is incremented by N, and all PD bonds with $n \geq 1$ are removed.
10. The process is repeated from Step 1 to Step 9 till the final failure of the structure is achieved. The final failure criteria can be considered as a structure stiffness reduction by a known value, a specific crack length, the number of damaged PD points, etc.

2.8. Composite PD

2.8.1. General PD theory of layered composite

Fiber reinforced composites consist of layers of unidirectional laminas bonded together. Each lamina has its fiber orientation angle α to the global coordinates axes X, Y (Fig. 2.14). If axis X_1 is aligned to the fiber direction and axis X_2 is transverse to the fiber, then the laminate can be defined with four independent material constants: elastic modulus in X_1 direction E_{11}, elastic modulus in X_2 direction E_{22}, in the plane shear modulus G_{12}, and in the plane Poisson's ratio υ_{12}.
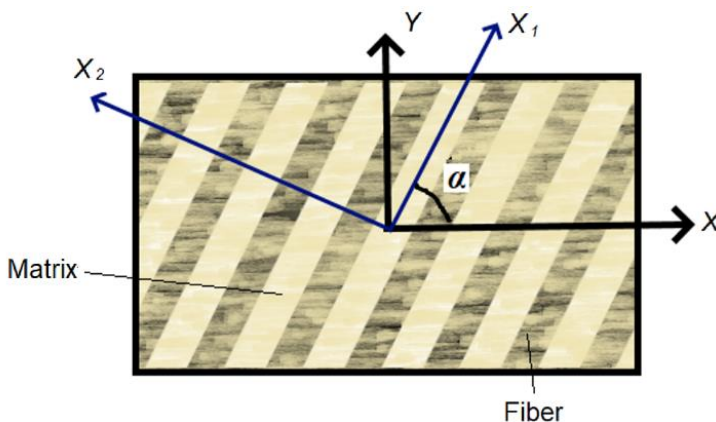
Fig. 2.14. Fiber reinforced lamina

Then stiffness matrix Q, relating stresses to strains of unidirectional composite lamina in material coordinates (X_1, X_2), can be written as:

$$\begin{Bmatrix} \sigma_{11} \\ \sigma_{22} \\ \tau_{12} \end{Bmatrix} = \begin{bmatrix} Q_{11} & Q_{12} & 0 \\ Q_{21} & Q_{22} & 0 \\ 0 & 0 & Q_{66} \end{bmatrix} \begin{Bmatrix} \varepsilon_{11} \\ \varepsilon_{22} \\ \gamma_{12} \end{Bmatrix} \tag{2.61}$$

where

$$Q_{11} = \frac{E_{11}}{1 - \nu_{12}\nu_{21}} \tag{2.62}$$

$$Q_{12} = \frac{\nu_{12}E_{22}}{1 - \nu_{12}\nu_{21}} \tag{2.63}$$

$$Q_{22} = \frac{E_{22}}{1 - \nu_{12}\nu_{21}} \tag{2.64}$$

$$Q_{66} = Q_{12} \tag{2.65}$$

and $\frac{\nu_{12}}{E_{11}} = \frac{\nu_{21}}{E_{22}}$. $\varepsilon_{11}, \sigma_{11}$ and $\varepsilon_{22}, \sigma_{22}$ refer to strains and stresses along the coordinates axes X_1 and X_2, respectively.

Due to the directional dependence of the composite material properties, the PD bond stiffness in the case of a composite also becomes dependent on the bond vector $x - x'$ direction. Different bond types are included in the multilayered fiber reinforced composite PD model, as it is shown in Fig. 2.15.
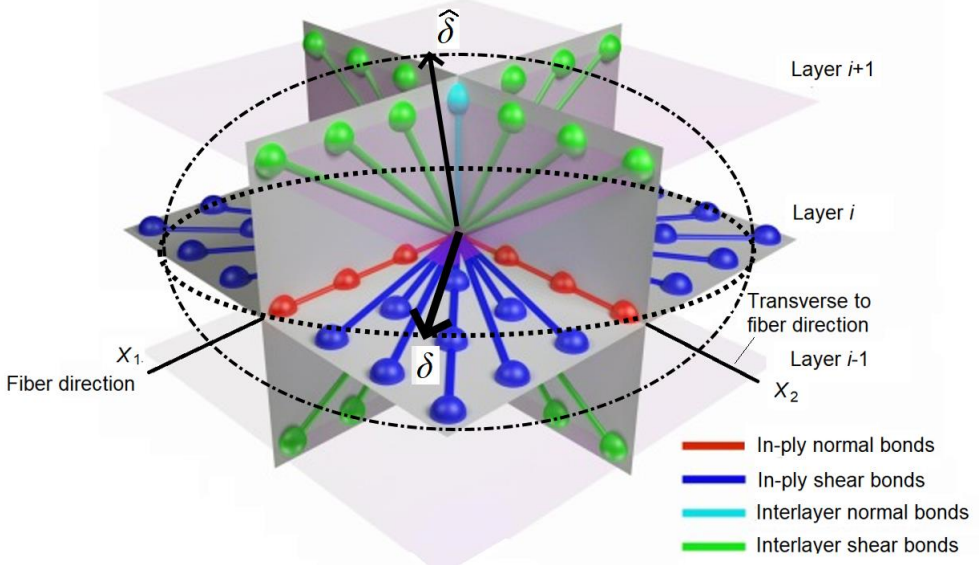
Fig. 2.15. PD model of multilayered fiber reinforced composite

The composite material PD parameters $a - d$ are derived by comparing the CCM and PD strain energy densities. The CCM strain energy density of a unidirectional lamina is computed as:

$$W_{CCM} = \frac{1}{2}(Q_{11}\varepsilon_{11}{}^2 + 2Q_{12}\varepsilon_{12}{}^2 + Q_{66}\gamma_{12}{}^2 + Q_{22}\varepsilon_{22}{}^2) \qquad (2.66)$$

The notifying PD parameter b as b_F – for fiber bonds along axis X_1, b_T – transverse to fiber bonds along axis X_2, b_{FT} – shear bonds, the PD strain energy density of point x in a unidirectional lamina can be written as:

$$
\begin{aligned}
W_{PDx} = a\theta_x{}^2 + b_F \sum_{x'=1}^{F_N} \frac{\delta}{|\xi_{xx'}|}(|\eta_{xx'}| - |\xi_{xx'}|)^2 V_{x'} \\
+ b_{FT} \sum_{x'=1}^{\infty} \frac{\delta}{|\xi_{xx'}|}(|\eta_{xx'}| - |\xi_{xx'}|)^2 V_{x'} \\
+ b_T \sum_{x'=1}^{F_N} \frac{\delta}{|\xi_{xx'}|}(|\eta_{xx'}| - |\xi_{xx'}|)^2 V_{x'}
\end{aligned}
\qquad (2.67)
$$

where F_N – the number of PD bonds either in the fiber or the transverse direction in the PD horizon. The PD dilatation θ_x for a unidirectional lamina is expressed as:

$$\theta_x = d \sum_{x'=1}^{\infty} \frac{\delta}{|\xi_{xx'}|}(|\eta_{xx'}| - |\xi_{xx'}|)\Lambda_{xx'}V_{x'} \qquad (2.68)$$

The PD strain energy densities of an isotropic elastic material (resin) for n-th composite layer normal and shear deformations can be written as [105]:

$$\widehat{W}_{Nx}^n = b_N \sum_{m=n+1,n-1} \frac{\hat{\delta}}{|x_x^m - x_x^n|}(|y_x^m - y_x^n| - |x_x^m - x_x^n|)^2 V_x^m \qquad (2.69)$$

$$
\begin{aligned}
\widehat{W}_{Sx}^n = b_S \sum_{m=n+1,n-1} \sum_{x'=1}^{\infty} \frac{\tilde{\delta}}{|x_x^m - x_x^n|}[(|y_{x'}^m - y_x^n| - |x_x^m - x_x^n|) \\
- (|y_x^m - y_{x'}^n| - |x_x^m - x_{x'}^n|)]^2 V_{x'}^m
\end{aligned}
\qquad (2.70)
$$

where $y = x + u$, and $\hat{\delta}$ is the horizon size in the thickness direction, $\tilde{\delta} = \sqrt{\delta^2 + \hat{\delta}^2}$ (Fig. 2.15).

In order to specify the lamina in the plane PD material parameters $a - d$, equilibrium between Eq. (2.66) and Eq. (2.67) is analyzed at different loading conditions, namely, simple shear $\gamma_{12} = \zeta$, uniaxial deformations at X_1 and X_2 directions and biaxial deformations, and X_1 and X_2 directions [105].

In the case of the simple shear, dilatation term $\theta_x = 0$, and only the in-ply shear bonds experience a stretch resulting in equilibrium between Eq. (2.66) and (2.67), such as:

$$b_{FT} \sum_{x'=1}^{\infty} \frac{\delta}{|\xi_{xx'}|}(|\eta_{xx'}| - |\xi_{xx'}|)^2 V_{x'} = \frac{1}{2}Q_{66}\zeta^2 \qquad (2.71)$$

following the parameter b_{FT} as:

58

$$b_{FT} = \frac{6Q_{66}}{\pi h \delta^4} \tag{2.72}$$

where h is the thickness of the lamina.

Considering the same value ζ uniaxial stretch in directions X_1 and X_2 and biaxial stretch respectively ($\varepsilon_{11} = \varepsilon_{22} = \zeta$), the following equilibriums are yielded [105]:

$$a\theta_x{}^2 + b_F \sum_{x'=1}^{F_N} \frac{\delta}{|\boldsymbol{\xi}_{xx'}|}(|\boldsymbol{\eta}_{xx'}| - |\boldsymbol{\xi}_{xx'}|)^2 V_{x'}$$
$$+ b_{FT} \sum_{x'=1}^{\infty} \frac{\delta}{|\boldsymbol{\xi}_{xx'}|}(|\boldsymbol{\eta}_{xx'}| - |\boldsymbol{\xi}_{xx'}|)^2 V_{x'} = \frac{1}{2}Q_{11}\zeta \tag{2.73}$$

$$a\theta_x{}^2 + b_{FT} \sum_{x'=1}^{\infty} \frac{\delta}{|\boldsymbol{\xi}_{xx'}|}(|\boldsymbol{\eta}_{xx'}| - |\boldsymbol{\xi}_{xx'}|)^2 V_{x'}$$
$$+ b_T \sum_{x'=1}^{F_N} \frac{\delta}{|\boldsymbol{\xi}_{xx'}|}(|\boldsymbol{\eta}_{xx'}| - |\boldsymbol{\xi}_{xx'}|)^2 V_{x'} = \frac{1}{2}Q_{22}\zeta^2 \tag{2.74}$$

$$a\theta_x{}^2 + b_F \sum_{x'=1}^{F_N} \frac{\delta}{|\boldsymbol{\xi}_{xx'}|}(|\boldsymbol{\eta}_{xx'}| - |\boldsymbol{\xi}_{xx'}|)^2 V_{x'}$$
$$+ b_{FT} \sum_{x'=1}^{\infty} \frac{\delta}{|\boldsymbol{\xi}_{xx'}|}(|\boldsymbol{\eta}_{xx'}| - |\boldsymbol{\xi}_{xx'}|)^2 V_{x'}$$
$$+ b_T \sum_{x'=1}^{F_N} \frac{\delta}{|\boldsymbol{\xi}_{xx'}|}(|\boldsymbol{\eta}_{xx'}| - |\boldsymbol{\xi}_{xx'}|)^2 V_{x'} = \zeta^2(Q_{11} \tag{2.75}$$

The CCM dilatation for a uniaxial stretch is equal to ζ, and, when equalized to Eq. (2.68), the PD parameter d can be defined as:

$$d = \frac{2}{\pi h \delta^3} \tag{2.76}$$

The substitution of the parameters b_{FT} and d to Eq. (2.73) – Eq. (2.75) leads to a system of three equations with three unknown variables a, b_F, b_T. Upon solving these equations, the system provides definitions of the PD parameters a, b_F, b_T:

$$a = \frac{1}{2}(Q_{12} - Q_{66}) \tag{2.77}$$

$$b_F = \frac{(Q_{11} - Q_{12} - 2Q_{66})}{2\delta\left(\sum_{x=1}^{F_N}|\boldsymbol{x}^n - \boldsymbol{x}'^n|V_x^n\right)} \tag{2.78}$$

$$b_T = \frac{(Q_{22} - Q_{12} - 2Q_{66})}{2\delta\left(\sum_{x=1}^{F_N} |x^n - x'^n| V_x^n\right)} \tag{2.79}$$

Superscript ^{n} in Eq. (2.78), Eq. (2.79) refers to the n-th composite layer. Due to the fixed Poisson's ratio in BBPD and the non-existing PD dilatation term, the parameters a and b_T vanish in BBPD, resulting in constraints $Q_{12} = Q_{66}$ and $Q_{22} = 3Q_{12}$.

Similarly as for in-plane deformations, PD parameters b_N and b_S are derived considering the transverse stretch $\varepsilon_{33} = \zeta$ and the simple transverse shear $\gamma_{13} = \zeta$. The CCM strain energy densities for the transverse stretch and the simple transverse shear can be computed according to the following equations:

$$\widehat{W}_{CCM} = \frac{1}{2} E_m \zeta^2 \text{ and } \widetilde{W}_{CCM} = \frac{1}{2} G_m \zeta^2 \tag{2.80}$$

where E_m and G_m are the matrix elastic and shear modulus. Equalizing Eq. (2.69) – Eq. (2.70) and Eq. (2.80) derives the PD parameters b_N for interlayer normal bonds and b_S for the interlayer shear bonds as:

$$b_N = \frac{E_m}{\hat{\delta}[(h_{n+1} + h_n)V_x^{n+1} + (h_{n-1} + h_n)V_x^{n-1}]} \tag{2.81}$$

$$b_S = \frac{G_m}{8\pi\tilde{\delta}H_S} \tag{2.82}$$

where the term H_S is calculated:

$$H_S = \left(\frac{h_{n+1} + h_n}{2}\right)^3 \left(\frac{\delta^2 + 2\left(\frac{h_{n+1} + h_n}{2}\right)^2}{\sqrt{\delta^2 + \left(\frac{h_{n+1} + h_n}{2}\right)^2}} - (h_{n+1} + h_n)\right)$$
$$+ \left(\frac{h_{n-1} + h_n}{2}\right)^3 \left(\frac{\delta^2 + 2\left(\frac{h_{n-1} + h_n}{2}\right)^2}{\sqrt{\delta^2 + \left(\frac{h_{n-1} + h_n}{2}\right)^2}} - (h_{n-1} + h_n)\right) \tag{2.83}$$

The composite PD numerical model faces the same issue at free surfaces requiring surface corrections (see Chapter 2.4). The definition of surface correction factors depends on loading and can be derived the same way as in Eq. (2.35) – Eq. (2.37). Because of this, it is difficult to define correction factors for any type of loading. The definition of correction factors for a specific loading type as a uniaxial stretch in fiber, transverse to fiber, and transverse to lamina can be found in the PD literature; see [105].

2.8.2. Composite BBPD including bond rotation

The BBPD composite formulation yielding the constraints of material properties $Q_{12} = Q_{66}$ and $Q_{22} = 3Q_{12}$ leads to a fixed Poisson's ratio value of the composite of $v = 0.33$ and a fixed shear modulus of $G_{12} = \frac{(1-v_{12})E_{22}}{2(1-v_{12}v_{21})}$ [120]. These limitations are not compatible with many composite materials; thus, the BBPD modelling accuracy becomes poor. Otherwise, the SBPD composite model is free of limitations, but the model implementation is limited (except for special software or in-house codes).

Many BBPD model extensions are offered to circumvent the Poisson's ratio limitation [120], and, by summarizing them, Madenci et al. [146] developed a BBPD model including PD bond rotation. The PD model is free of a fixed Poisson's ratio, can be implemented in FE software by using the terms of already existing FE formulations, and can be adopted to a fiber-reinforced composite model. In a BBPD with rotation, the PD bond forces are computed from stretch and rotation vector $\boldsymbol{r}$ (also see Fig. 2.16) by using the PD bond stiffness for elongation c_c and rotation c_d:

$$\boldsymbol{f}_{xx'} = c_c s_{xx'} \boldsymbol{n}_{xx'} + c_d \boldsymbol{r}_{xx'} \tag{2.84}$$

where the vector $\boldsymbol{n}_{xx'} = \frac{\xi_{xx'}}{|\xi_{xx'}|}$.
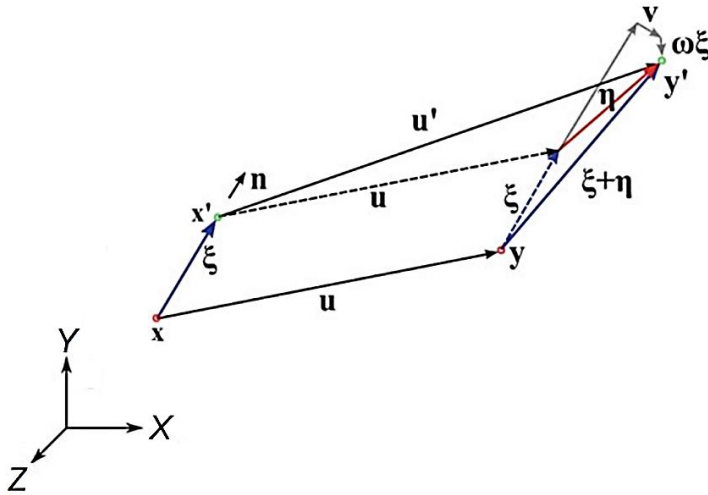
Fig. 2.16. BBPD with rotation bond kinematics [146]

The rotation angle of the PD bond $x'-x$ vector $\boldsymbol{r}_{xx'}$ from Fig. 2.16 can be defined as:

$$\boldsymbol{r}_{xx'} = \frac{\left((\boldsymbol{u}(x') - \boldsymbol{u}(x)) - (\boldsymbol{u}(x') - \boldsymbol{u}(x)) \cdot \boldsymbol{n}_{xx'}\right) \cdot \boldsymbol{n}_{xx'} - \boldsymbol{\omega}(x)\xi_{xx'}}{|\xi_{xx'}|} \tag{2.85}$$

where $\boldsymbol{\omega}(x) = \frac{1}{2}(\nabla\boldsymbol{u} - \boldsymbol{u}\nabla)$ – the infinite small rotation tensor. As $(\boldsymbol{n}_{xx'} \otimes \boldsymbol{n}_{xx'})\boldsymbol{\omega}(x)\boldsymbol{n}_{xx'} = \boldsymbol{0}$, the bond rotation angle vector can be defined in terms

of the strain tensor of the point x $\boldsymbol{\varepsilon}(\boldsymbol{x})$:

$$\boldsymbol{r}_{xx\prime} = \frac{(\boldsymbol{I} - \boldsymbol{n}_{xx\prime} \otimes \boldsymbol{n}_{xx\prime})}{|\boldsymbol{\xi}_{xx\prime}|} \varepsilon(x) \boldsymbol{\xi}_{xx\prime} \tag{2.86}$$

where $\boldsymbol{I}$ is the identity matrix and the strain tensor $\boldsymbol{\varepsilon}(\boldsymbol{x})$ of the point x computed by applying PDDO from Eq. (2.30).

PD bond elongation and rotation stiffness for the case of a composite can be derived by taking the same approach of the strain energy density equilibrium for the conventional PD. Then, BBPD with the rotation strain energy density of a fiber-reinforced composite is expressed as:

$$\begin{aligned} W_{PDx} = \frac{1}{2} \Bigg(&\int_{H_x} \frac{1}{2} (c_{cF} s_{xx\prime}{}^2 + c_{dF} r_{xx\prime}{}^2) |\boldsymbol{\xi}_{xx\prime}| dV_{x\prime} \\ &+ \int_{H_x} \frac{1}{2} (c_{cFT} s_{xx\prime}{}^2 + c_{dFT} r_{xx\prime}{}^2) |\boldsymbol{\xi}_{xx\prime}| dV_{x\prime} \Bigg) \end{aligned} \tag{2.87}$$

where c_{cF}, c_{dF} refer to the fiber bonds elongation and rotation stiffness, and c_{cFT}, c_{dFT} denote the matrix bonds elongation and rotation stiffness. BBPD with the rotation PD bond force is determined as:

$$\begin{aligned} \boldsymbol{f}_{xx\prime} = &(c_{cF} + c_{cFT})(\boldsymbol{n}_{xx\prime} \otimes \boldsymbol{n}_{xx\prime}) \frac{\boldsymbol{u}(x\prime) - \boldsymbol{u}(x)}{|\boldsymbol{\xi}_{xx\prime}|} \\ &+ (c_{dF} + c_{dFT})(\boldsymbol{I} - \boldsymbol{n}_{xx\prime} \otimes \boldsymbol{n}_{xx\prime}) \frac{\boldsymbol{u}(x\prime) - \boldsymbol{u}(x) - \boldsymbol{\omega}(x) \boldsymbol{\xi}_{xx\prime}}{|\boldsymbol{\xi}_{xx\prime}|} \end{aligned} \tag{2.88}$$

Eq. (2.88) [120] satisfies the linear momentum balance, but it does not satisfy the angular momentum balance unless the PD fiber bonds rotational stiffness $c_{dF} = \frac{2N}{\pi h \delta^3 (m+1)} (Q_{12} - Q_{22} + 2Q_{66})$ is removed. Then, BBPD with the rotation composite model consists of three PD parameters, namely, the fiber bonds elongation stiffness c_{cF} and matrix elongation c_{cFT} and the rotation stiffness c_{dFT} (for the sake of simplicity, let us further notify the matrix bond stiffness as $c_{cM} = c_{cFT}$; $c_{dM} = c_{dFT}$):

$$c_{cM} = \frac{6}{\pi h \delta^3} (Q_{22} + Q_{12}) \tag{2.89}$$

$$c_{dM} = \frac{6}{\pi h \delta^3} (Q_{22} - 3Q_{12}) \tag{2.90}$$

$$c_{cF} = \frac{2N}{\pi h \delta^3 (m + 1)} (Q_{11} - Q_{22}) \tag{2.91}$$

where N is the number of PD bonds in the PD horizon, and m is the number of fiber bonds in the PD horizon. BBPD with the rotation composite model only has the constraint ($Q_{12} - Q_{22} + 2Q_{66} = 0$), leading to the fixed material shear modulus being equal to:

$$G_{12} = \frac{E_{22}(1 - v_{12})}{2(1 - v_{21}v_{12})} \qquad (2.92)$$

Due to the capabilities of matrix bonds to elongate and rotate, their forces are computed by using PDDO for the rotational part. PDDO does not require the full PD horizon, and thus surface corrections are not necessary for the matrix bonds. Nevertheless, the fiber bond stiffness c_{cF} must be corrected near the boundaries, as otherwise the simulation would be incorrect because of missing fiber bonds. Another aspect to be considered is the failure criteria of the BBPD with the rotation model. Critical stretch s_c and critical bond skew angles γ_c are used. As described by Madenci et al. [120], bond skew angles are defined as a ratio of the relative PD bond displacement projection in the fiber direction to the relative PD bond position projection transverse to the fiber (Fig. 2.17):

$$\gamma_{xx\prime} = \frac{(\boldsymbol{u}\prime - \boldsymbol{u}) \cdot \boldsymbol{n}_f}{\xi_{xx\prime} \boldsymbol{n}_t} \qquad (2.93)$$
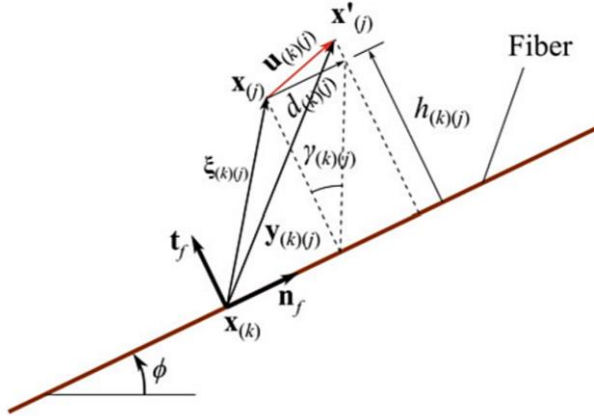
Fig. 2.17 Definition of rotation angle of PD matrix bond [120]

While the s_c and γ_c values for an isotropic material can be derived from the material fracture toughness G_I and G_{II}, for BBPD with the rotation composite model, there is no simple approach to determine the critical PD bond stretch s_c and the skew angle γ_c. One of the most accurate approaches is the s_c and γ_c calibration from experiments. Additionally, several failure assumptions must be considered for BBPD with the rotation composite model [120]:

1. Fiber bonds do not fail. Only matrix bonds fail due to tension and shear. For the case of compression, a matrix bond can only fail due to rotation (shear);

2. $s_{xx\prime} < s_c$; $\gamma_{xx\prime} < \gamma_c$ – PD bond active;

3. $s_{xx\prime} > s_c$; $\gamma_{xx\prime} < \gamma_c$ – PD bond fails due to tension, resulting in $f_{xx\prime} = 0$, and the bond interaction is removed;

4. $s_{xx\prime} < s_c$; $\gamma_{xx\prime} > \gamma_c$ – PD bond fails due to shear, resulting in $f_{xx\prime} = 0$, but the bond interaction is maintained;

5. $s_{xx'} > s_c; \gamma_{xx'} > \gamma_c$ – PD bond fails due to both tension and shear, resulting in $f_{xx'} = 0$, and the bond interaction is removed;

6. The maximum possible PD damage Φ_x at point x cannot be greater than 0.6 to ensure the model stability.

2.9. Experimental Digital Image Correlation (DIC)

DIC uses optical cameras to track points on the measured object's surface (also see Chapter 1.3). A view of the current 3D DIC system is shown in Fig. 2.18 a, while, in Fig. 2.18 b and c, the basic working principles of the system are presented in detail. The use of the system consists of specimen and system preparation, taking images, and results postprocessing in the computer software.
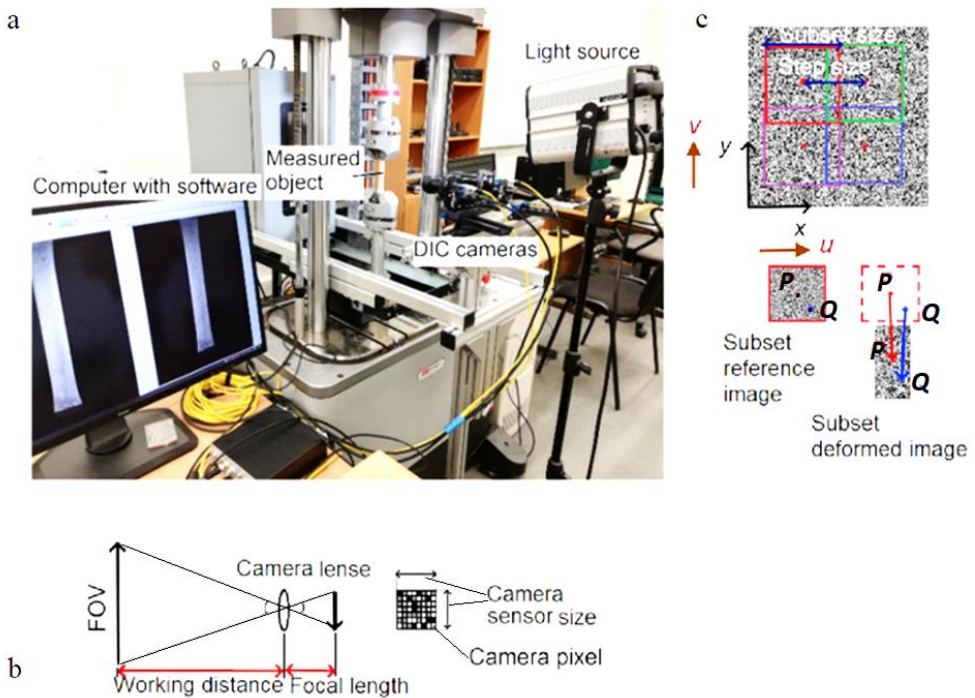
Fig. 2.18 Current 3D DIC: a – general experimental setup; b – parameters of cameras and lenses; c – DIC point tracking principles [147]

In order to track the measured object's surface points with cameras, the surface must contain some pattern. Rarely, a natural material's surface structure is sufficient to form a natural pattern, but, in most cases, an artificial speckle pattern is necessary. Different methods can be applied to create a pattern, such as painting, inks and dyes, powder particles, laser engraving, etc. [148]. A painted speckle pattern is quite popular due to the method simplicity and high quality. A high-quality pattern is denoted by a high contrast, is randomly positioned, and is uniform in size. The pattern size is selected according to the field of view (FOV) and should satisfy the condition of being in the range of $3 \times 3 \div 7 \times 7$ camera's pixels. Before the experiment, the camera's resolution in pixels, the camera's sensor size, focal length (FL) and object size (OS)

64

are known (Fig. 2.18 b); thus, the required speckle pattern size (PaS) can be calculated as:

$$PaS = (3 \div 7)\frac{FL}{WD} \cdot OS \qquad (2.94)$$

Where the working distance (WD) should be not less than the minimum working distance of the camera (WD $\geq$ WD$_{min}$). The optimal pattern density is 50%. Strong pattern adhesion to the object surface is also important. Additional requirements for the speckle pattern depend on the testing conditions, such as the pattern temperature stability for high temperature testing.

The picture of an undeformed speckle pattern (the object surface) and a series of pictures of a deformed pattern (the object surface) are used to compute object surface displacements and strains. The choice of a camera is related to the length scale of the object so that to achieve proper magnification. The object size, the camera's sensor size and the focal length (Fig. 2.18 b), related to the camera optics, are necessary to determine the current applicability of the camera in use for the selected test object. Capturing localized effects in a quasi-static process requires a high-resolution camera with a smaller pixel size. For dynamic problems, e.g., high speed cyclic loading, a camera with a high frame rate is required. A general rule between the camera resolution and the frame rate is the inverse relation, which means that a high-resolution camera cannot have a high frame rate as well. As camera pixels should be related to the actual object dimensions, DIC calibration before taking images is required. While for 2D DIC, only a single value is necessary to identify the dimensions, for 3D DIC, about 20÷30 calibration images captured at different orientation angles are required. Special calibration plates with a known grid size are used to calibrate the system. The quality of calibration images (e.g., a good focus, or a high number of recognized in the software calibration points of the calibration plate) is important to prevent measuring errors. Perfect focus and lightening conditions are crucial to perform reliable DIC measurements. The light source and the cameras have to be adjusted to ensure enough exposure of the object, but not too much, so that the maximum lightning value at sensor pixels should not be reached. Lighting fluctuations, electronics and the camera itself introduce some noise nevertheless, which can be minimized by properly adjusted lighting conditions [149].

The final step of DIC is the post-processing of images. A portion of the speckle, called the subset, instead of separate pattern points (Fig. 2.18 c), is tracked to compute the displacements and strains of each subset's center point P. The distance between each subset is called the *step size* (Fig. 2.18 c), and subsets can overlap each other. The first image (the image of an undeformed object) is used as a reference to compute the displacements of the subsets' center point P in other pictures captured on a deformed object's surface. The subset shape depends on the DIC software, and, for the current DIC system software *VIC-3D*, square subsets are used [150]. The subset and step sizes are user-defined parameters in the software VIC-3D, nevertheless, the DIC software VIC-3D suggests subset values according to the speckle size and estimates possible errors in pixels related to the selected subset size. A general recommendation for the subset size is that it should contain at least three speckles

[148] because too small subsets cannot be extracted from each other, and tracking speckle points is then almost impossible. However, excessively large subsets can undergo a complex deformation resulting in a reduced accuracy of the measurement. Moreover, a large subset increases the computational time. By reducing DIC step size, the spatial resolution increases, because more data points are taken, but the computation time and the noise increase, too [151]. The optimum value of the step size is about 1/4 of the subset size.

After the measured object's surface deformation, the subset from a deformed image is matched against the subset from the reference image to find each subset's center point P (Fig. 2.18 c). To evaluate the similarity between the subset in the reference image and the subset in the deformed image, a correlation criterion is used [152]. The default algorithm in the DIC software VIC-3D [150] is the *Normalized Sum-Squared Difference* (NSSD) criterion defined as:

$$\chi^2_{NSSD} = \sum \left(\frac{\sum F_i G_i}{\sum G_i^2} G_i - F_i \right)^2 \tag{2.95}$$

where F and G are the pixel values taken from the reference and the deformed images, respectively.

When a subset is deformed, its shape is changed. To find the position and displacements of the internal subset point Q (Fig. 2.18 c) after the subset deformation, mapping based on the deformation continuity principle is done. As the center point in the subset of the reference image remains the center point in the deformed subset, the coordinates of all the subsets' internal points can be expressed by the shape functions relating each subset point Q coordinates (x_Q, y_Q) to the subset center point P coordinates (x_P, y_P) as:

$$x_Q = x_P + \zeta(x_Q, y_Q)$$
$$y_Q = y_P + \eta(x_Q, y_Q) \tag{2.96}$$

where ζ, η are DIC shape functions. The most used DIC shape functions [152] are the first order:

$$\zeta_1(x_Q, y_Q) = u_P + \frac{\partial u}{\partial x} \Delta x + \frac{\partial u}{\partial y} \Delta y$$
$$\eta_1(x_Q, y_Q) = v_P + \frac{\partial v}{\partial x} \Delta x + \frac{\partial v}{\partial y} \Delta y \tag{2.97}$$

or, for more complex problems, such as high strain gradients, the second order:

$$\zeta_2(x_Q, y_Q) = u_P + \frac{\partial u}{\partial x} \Delta x + \frac{\partial u}{\partial y} \Delta y + \frac{1}{2} \frac{\partial^2 u}{\partial x^2} \Delta x^2 + \frac{1}{2} \frac{\partial^2 u}{\partial y^2} \Delta y^2 + \frac{\partial^2 u}{\partial x \partial y} \Delta x \Delta y$$
$$\eta_2(x_Q, y_Q) = v_P + \frac{\partial v}{\partial x} \Delta x + \frac{\partial v}{\partial y} \Delta y + \frac{1}{2} \frac{\partial^2 v}{\partial x^2} \Delta x^2 + \frac{1}{2} \frac{\partial^2 v}{\partial y^2} \Delta y^2 + \frac{\partial^2 u}{\partial x \partial y} \Delta x \Delta y \tag{2.98}$$

where $\Delta x = x_Q - x_P, \Delta y = y_Q - y_P$. In some versions of the DIC software, the shape function selection is determined by the user, but for the case of the current setup with VIC-3D software, the DIC shape function cannot be selected. As the internal subset

point Q in the deformed subset can be located between pixels, sub-pixel interpolation is also necessary to define these point displacements. The interpolation algorithm depends on the software, and 4th, 6th or even 8th order polynomials are available in the VIC-3D software [150].

Once displacements of the object surface points are calculated, strains can be found by applying numerical differentiation. As it is mentioned in the VIC-3D manual [153], strains are computed without differentiating the DIC displacement shape functions (Eqs. 2.96–2.97), but rather by constructing artificial triangle finite elements. Vertexes of each triangle are the subsets' center points P with the previously computed displacements (Fig. 2.18 c, Fig. 2.19 a). By applying strain shape functions defined over each triangular element, strains at any internal point of the triangle (Fig. 2.19 a) can be computed. Since these triangular elements are several pixels in size, the computed strain at such a small 'strain gauge' are very noisy; thus, strain filtering (smoothing over a selected area) is used (Fig. 2.19 b).
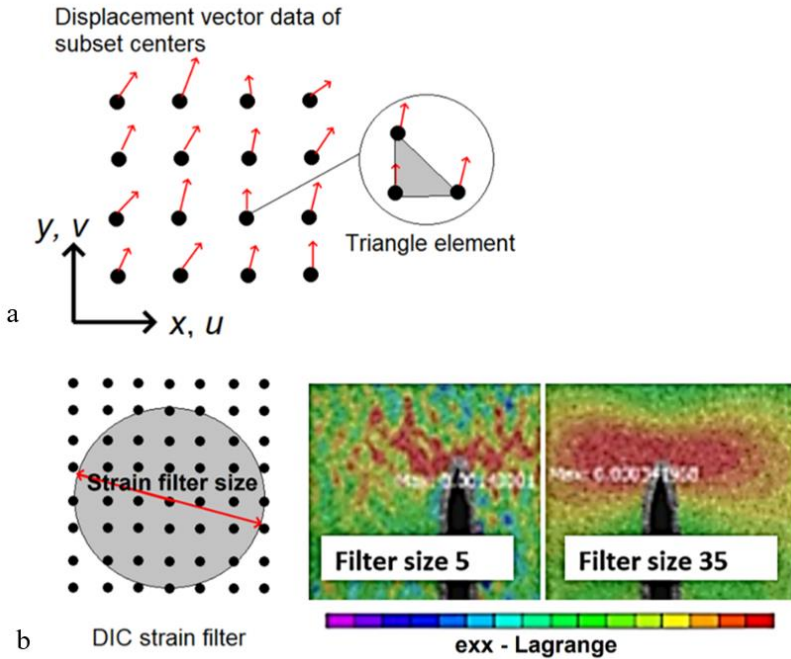
Fig. 2.19 Strain computation algorithm in software VIC-3D [147]: a – artificial triangle finite elements; b – strain filtering.

The strain filter size (Fig. 2.19 b) in the software VIC-3D is a user-defined parameter which is expressed as the number of step sizes: filter 5 – 5 step sizes, filter 35 – 35 step sizes. Small strain filters produce localized, more accurate, but noisy strain fields, compared to large strain filters resulting in smooth, but highly averaged strain fields. There are no general recommendations for the optimum filter size value selection.

The accuracy of DIC measurements depends on multiple parameters, namely, the subset size (SS), the step size (ST), or the strain filter size (FS), and their different

combinations can lead to the same displacement or strain results. Therefore, the *International DIC Society* [154] combines those parameters into single parameter, called the *Virtual Strain Gauge* (VSG) which is expressed as:

$$VSG = (FS - 1)ST + SS \qquad (2.99)$$

To summarize all of the above-mentioned factors, affecting the DIC measurements accuracy, the relevant information is outlined in Table 2.2.

Table 2.2. Factors determining the accuracy of DIC measurements

Stage	Factor	Evaluation criteria
Preparation	Speckle pattern	Speckle size according to requirements of 3÷7 camera pixels (Eq. (2.94)). Visual inspection of speckle randomness, contrast.
	Camera selection	Camera magnification, minimum working distance, resolution, frame rate satisfies the requirements for the current test.
Experiment	Calibration	20÷30 calibration images at different orientation angles. Calibration score not higher than 0.1 (refers to VIC-3D software).
	Lighting	Evaluation in software as a measuring error in pixels.
	Camera focus	Evaluation in software as a measuring error in pixels.
	System noise	Difficult to evaluate, its effect visible in results.
Post-processing	Subset size	According to requirement of at least 3 speckles size. Software VIC-3D suggests the optimum subset size and computes the measuring error in pixels with the current subset size.
	Step size	About 1/4 subset size. Smaller steps for localized problems.
	Subset shape function	Higher order for localized problems (not refers to software VIC-3D).
	Sub-pixel interpolation	Higher order for localized problems.
	Strain filter size	Smaller filters for localized strains, but the results are noisier. A higher filter for smooth strain fields, but the results are less accurate.

2.10. DIC Strain Computation Issues

The accuracy of DIC measurements has always been a topic of high relevance. Nevertheless, the accuracy of the DIC strain has been less analyzed in the literature, but it is even more important, especially in fatigue analysis. The DIC strain computation issues are related with numerical differentiation. Since strains are found as displacements' spatial derivatives, similarly as in FE, they do not exist in the presence of discontinuity. Difficulties in detecting strains in discontinuous fields limit the application of DIC to fatigue analysis, especially in the case of local fatigue damage, or fatigue crack initiation. Another aspect of relevance is that differentiation approaches amplify the existing displacement noise, which results in significantly more noise in strains. Noise is a limiting factor in the strain accuracy even in continuous displacement fields.

The DIC strain accuracy problem demonstrated on a plate with hole (images are taken from DIC Challenge 1.0 [155]) was analyzed by Turner [156–158] (Fig. 2.20).
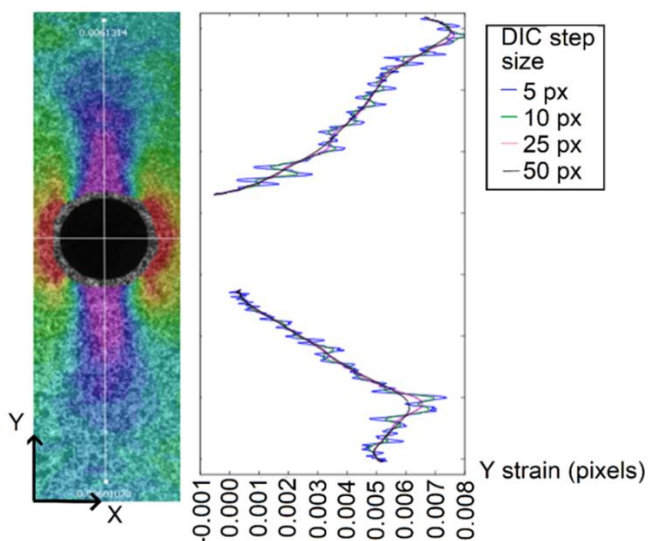
Fig. 2.20 Plots of DIC-computed strains on a plate with hole surface (plate loaded in tension) for various values of the DIC step [156–158]

From Fig. 2.20, it can be seen that, as the DIC step size increases, the strain fields of the vertical symmetry axis of the hole become smoother, but the strain accuracy decreases. On the other hand, smaller steps lead to more accurate strains, although their exact values are hidden by noise. This means that, from Fig. 2.20, exact strain values cannot be found by using DIC; they can only be determined by comparing Fig. 2.20 strain plots with analytic/FE solutions.

2.11. Observations from Theoretical Methodology Analysis

Replacement of the presently existing numerical differentiation-based strain computation algorithms in DIC with PDDO should improve the DIC strain quality. Noise in the strains should be significantly reduced due to the removal of the

conventional differentiation. This would lead to a more accurate strain field for both continuous and discontinuous problems. On the other hand, DIC measurements can be employed for the selection of PD model parameters. This approach is useful for determining the PD failure parameters, such as the critical stretch. BBPD with the rotation model offers the advantage of simplicity, the possibility to be implemented in the currently available FE formulations, and it has the only one constraint imposed by material properties; thus, BBPD with the rotation model is worth further developing so that it could be applied for modelling composite structures. By combining BBPD with the rotation model for a unidirectional lamina with interlayer PD bonds, it is possible to create a PD model of a multilayered fiber-reinforced composite. The composite BBPD with rotation PD bond constants together with the critical stretch and skew angles can also be established from the experiment with DIC measurements.

3. EXPERIMENTAL TESTING

3.1. New Method Based on PDDO to Increase the DIC Strain Accuracy

Several PPDO applications to the DIC displacement field are further analyzed in this study. Firstly, a tensile specimen with a hole (similar to the problem presented in Fig. 2.20) is used to analyze strains computed by the conventional DIC and DIC with applied PDDO. Specimen dimensions of 180 mm × 35 mm and a hole diameter of 10 mm are not referred to any specific standard. The specimen material is DIBOND composite – a sandwich material of total thickness 3 mm, composed of three layers: the polyethylene core of a thickness of 2.4 mm, and aluminum *EN AW 5005* external layers of a thickness of 0.3 mm each. According to material characteristics, the maximum tensile force does not exceed 400 N; thus, a tensile test with experimental DIC measurements can be performed on an electromechanical testing machine *INSTRON E10000* with the maximum force of 10 kN. The selected tensile speed is 3 mm/min. Summarized DIC setup information is given in Table 3.1.

A fragment of the PD MATLAB code (Chapter 2.5) with the part of PDDO was applied to the DIC experimental displacement fields to compute strains. Finally, a comparison between strains, computed by applying the DIC and DIC-PDDO methods, was performed. Schematics of DIC strains analysis is shown in Fig. 3.1.
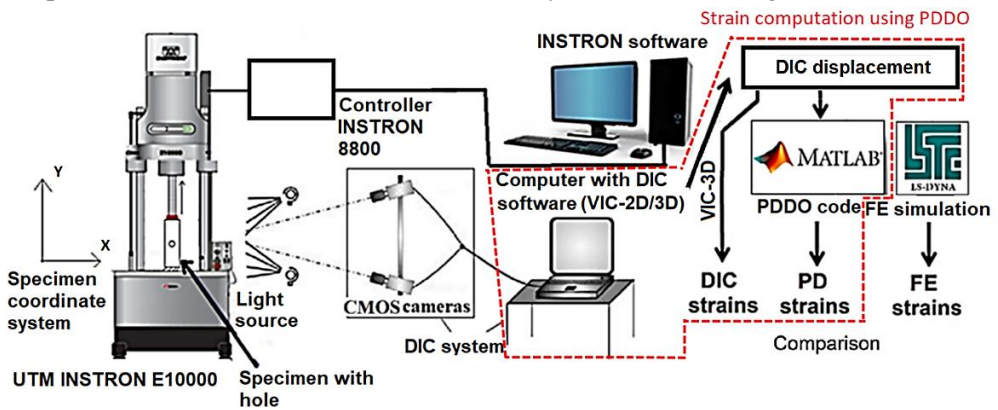
Fig. 3.1 Schematics of DIC and DIC-PDDO methods to compute strains

Table 3.1. DIC setup for experimental measurements of a specimen with a hole

Stage	Parameter	Value
Preparation	Camera resolution	12 Mpx
	Camera sensor size	14.1 mm × 10.3 mm
	Camera focal length	25 mm
	Calibration	25 images of 14 × 10 dots calibration plate
	Pattern	Black dots of 0.18 mm size, painted with roller
Experiment	Lighting	*ProfiluxLED1000* LED

		lamp, max power 185 W
	Number of images	104
Post-processing	Sub-pixel interpolation	6th order polynomial
	Subset size	29 px
	Step size	7 px
	Strain filter size	15

To confirm the correctness of both DIC and DIC-PDDO methods, additional FE simulation in *LS-Dyna* was included (Fig. 3.1).

   PDDO was directly applied to the displacement data points exported from experimental DIC measurements at a uniform square grid. Software VIC-3D export options *Pixel Grid* or *Metric nodes* [150] were used. *Pixel Grid* exports data at a regular square grid to a .csv file by the given grid spacing in pixels without the number of points limitations. *Metric nodes* exports data at a regular square grid with the step expressed in mm, but the grid is limited to 200×200 points per area of interest (AOI). Since the strain computation over the entire specimen area is time consuming and useless for strain analysis near the hole, only the 30 mm×30 mm AOI was selected (Fig. 3.2).
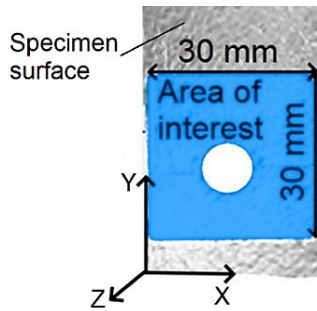
Fig. 3.2 AOI of DIBOND composite specimen for DIC and DIC-PDDO strain comparison

   The experimental data from DIC was exported as a matrix of size [numbers of points; 9] defined as $Data = [X\, Y\, Z\, u\, v\, w\, \varepsilon_{xx}\, \varepsilon_{yy}\, \varepsilon_{xy}]$, where X, Y, Z – points coordinates at the reference (undeformed) image; u, v, w – DIC displacements of the points; $\varepsilon_{xx}, \varepsilon_{yy}, \varepsilon_{xy}$ – DIC strains of the same points. The matrix *Data* was directly imported into the PDDO MATLAB code and used for calculations. No additional transformations of the matrix *Data* in MATLAB, such as the interpolation between points, or coordinates reposition, were applied.

   The PDDO code in MATLAB was adopted for the 2D plane stress case occurring on the DIBOND composite specimen's surface. PDDO (Eq. (2.30)) was discretized in order to apply the DIC displacement data exported at a regular grid. According to [127], cubic PDDO influence function ω was chosen as $\omega(|\xi_{xx\prime}|) = \delta^3/|\xi_{xx\prime}|^3$. This finally leads to the discrete form of the deformation gradient $\boldsymbol{F}(x)$ of the point x, calculated by using PDDO for the 2D plane stress case and expressed as:

$$F(x) = \left[\sum_{x'=1}^{N} \frac{\delta^3}{|\xi_{xx'}|^3} \left((u_{x'} + x_{x'}) - (u_x + x_x) \right) \otimes \xi_{xx'} \right]$$

$$\cdot \left[\sum_{x'=1}^{N} \omega(|\xi_{xx'}|)(\xi_{xx'} \otimes \xi_{xx'}) \right]^{-1} \tag{3.1}$$

where N is the number of material points in the point x horizon H_x. Eq. (3.1) does not include any spatial derivatives and can compute the strain gradient of the point x. Then, the Lagrange strain tensor, the same as computed in the DIC software VIC-3D, can be found from the PDDO computed strain gradient $F(x)$ by the following Equation:

$$\mathbf{E} = \frac{1}{2}(F^T + F + F^T \cdot F) \tag{3.2}$$

All the necessary information to apply PDDO for the DIC displacement field is stored in the matrix *Data*: the points' coordinates at the reference image and the points' displacements. The material properties of the specimen are not required because PDDO is applied directly to DIC displacements. The PD horizon was set to $\delta = 3.1\Delta x$, while the data at a fine grid of $\Delta x = 0.167$ mm was exported from DIC (180×180 points per AOI).

An FE model of the DIBOND composite test specimen was created in LS-PrePost 4.6, and an FE simulation was run in *LS-Dyna R11.0*. To prevent errors, stemming from differences between the real (experimental) conditions and the idealized conditions (the FE model), several additional steps, shown in the model scheme in Fig. 3.3 a, were included.
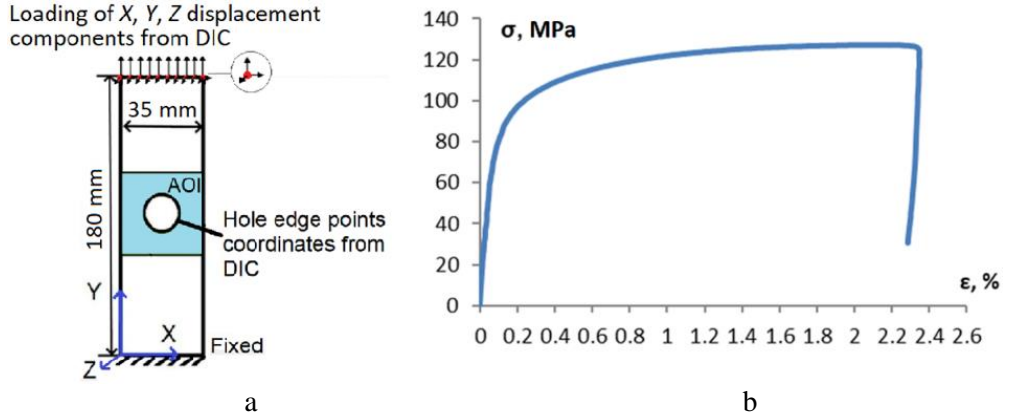
Fig. 3.3 FE modelling of the DIBOND composite specimen: a – model geometry and boundary conditions in *LS-Prepost*; b – DIBOND composite tensile curve

The hole edge coordinates in the FE model were taken from DIC rather than by defining a hole as the ideal circle in *LS-PrePost*. This technique helps evaluating the stress concentration near the hole in the FE model more effectively. The second step

was related with the specimen loading, which is not ideal tension due to the imperfect specimen alignment in the tensile machine. Because of this, a virtual specimen in the FE model was loaded by 10 points of top of the specimen prescribed displacements in the directions *X, Y, Z*, whose values were taken from DIC. A tensile test of the DIBOND composite material was also performed, and the tensile curve shown in Fig. 3.3 b was used to identify the material properties necessary for FE simulation.

As it is impossible to run the FE simulation at the FE mesh which would be equal to DIC artificial FE with the same shape functions, some strain differences between the DIC and FE strains are still expected. The average size of $5 \cdot 10^{-4}$ mm mixed quadratic-triangle fully integrated 1st order SHELL elements in *LS-Prepost* was used. The material model PIECEWISE_LINEAR_PLASTICITY was selected in *LS-Dyna*. The effective properties of the DIBOND composite according to the tensile curve from Fig. 3.3 b was used, namely, the effective elastic modulus $E_f = 43$ GPa, the effective Poisson's ratio $v = 0.3$, and the yield limit $\sigma_y = 100$ MPa. The 'define curve' option was enabled, and the tensile curve, shown in Fig 3.3 b, was uploaded in *LS-Prepost*. Non-linear implicit time integration with the Broyden–Fletcher–Goldfarb–Shanno algorithm [174] was selected.

The results of the strains, computed by using experimental DIC, applying PDDO to the experimental DIC displacement field, and from the FE simulation in *LS-Dyna*, are presented in Fig. 3.4.
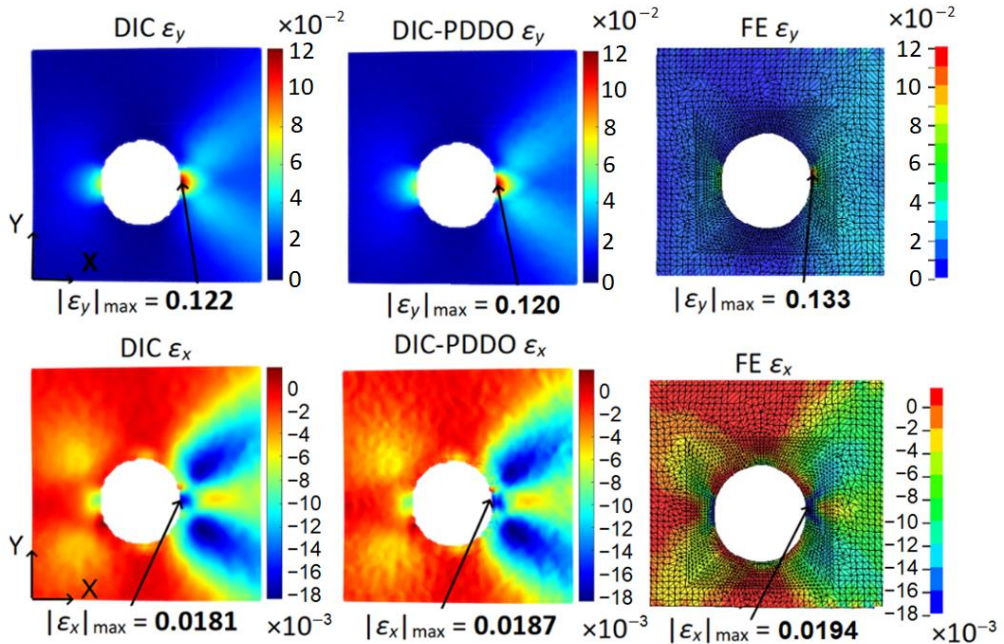
Fig. 3.4 Comparison of strain components $\varepsilon_{xx}, \varepsilon_{yy}$ computed in AOI of the DIBOND composite specimen surface under tension by DIC, DIC-PDDO and FE simulation

From the results presented in Fig. 3.4, good agreement both in terms of the magnitude and locations of the absolute maximum strains as well as the general DIC, DIC-PDDO and FE strain fields was observed. The maximum strain differences between the DIC and DIC-PDDO methods computed maximum strains are up to 3%. Nevertheless, the differences between FE and DIC or DIC-PDDO strains are larger (about 8% on average for both $\varepsilon_{xx}, \varepsilon_{yy}$ strains). The FE mesh size and shape in *LS-Dyna*, the remaining differences in the boundary conditions between the experiment and the simulation, and the differences between the FE formulation in *LS-Dyna* and DIC are the main factors resulting in those differences between the *LS-Dyna* simulation and the experiment. The differences between the DIC and DIC-PDDO strains can be explained by the possible better noise filtering in the DIC-PDDO strains. The DIC strain filter size, the PD data grid spacing Δx, and the PD horizon size δ exert an effect on the DIC and DIC-PDDO strain fields and their maximum strain values. Finally, the differences between the strains computed by using experimental DIC, DIC-PDDO and FE simulation, are small enough to confirm the correctness of the experimental DIC strain field and validate the DIC-PDDO method for strain computation.

The effect of strain filtering with DIC strain filters and the PD horizon can be demonstrated on the same test specimen at the presence of noise in DIC measurements. By using the same DIC parameters as given in Table 3.1, except for the DIC step size equal to 1 px, a slightly noisy *X* direction DIC displacement and a significantly noisy DIC ε_x strains field are obtained with the maximum value of a strain of up to 0.04 (Fig. 3.5 a). The PDDO computed strain field from the noisy *X* direction DIC displacement is also compared to the DIC strains in Fig. 3.5 a. The correct DIC strain field as a reference (the same as in Fig. 3.4), computed with a step value of 7 px, is given in Fig. 3.5 b.
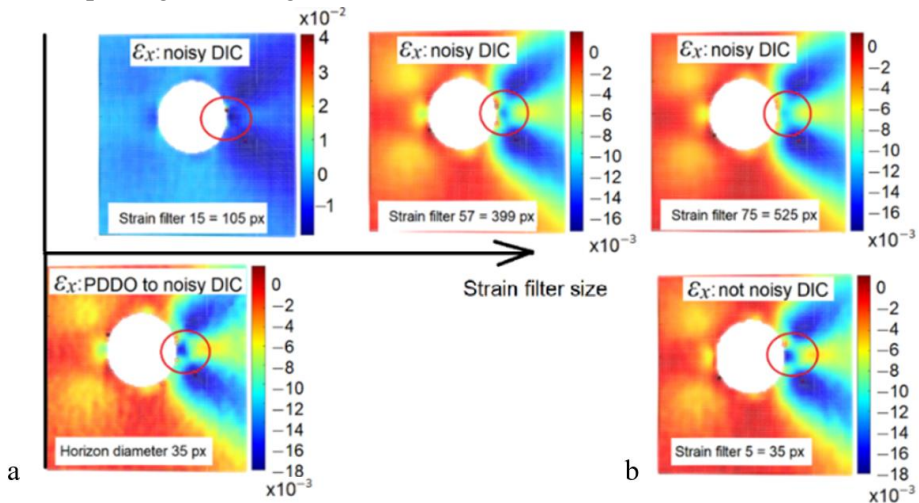
Fig. 3.5 Strain filtering with DIC strain filters and PD horizons in case of noisy DIC data: a – comparison of strain fields; b – correct strain field from Fig. 3.4

The size of the PD horizon in Fig. 3.5 is expressed in terms of the horizon

diameter in pixels for a comparison with the DIC strain filter diameter, also measured in pixels in Fig. 3.5. From Fig. 3.5 a, it can be seen that the minimum size of the DIC strain filter necessary to remove the strain noise and achieve the correct strain values (the same as 'not noisy DIC' strain in Fig. 3.5 b) is 525 px. On the other hand, a strain filter of this value averages the strain field in such a way that strain peaks are filtered out (compare strains in the red circle) between Fig. 3.5 a (filtered) and Fig. 3.5 b (the correct strain field). For the case of PDDO, applied to noisy DIC displacement, only the PD horizon diameter of 35 px is enough to reduce the noise, and it results in an almost correct strain field like 'noisy DIC' with the 399 px filter, but without the lost strain extremums. Thus, the DIC-PDDO method is more than 11 times more efficient (399 px vs. 35 px) in terms of strain filtering, noise removal, and strain data recovery (it does not filter out strain peaks) than the current VIC-3D strain computation algorithm.

In order to test the PDDO strain computation algorithm in DIC and rely not only on in-house examples, some specific metrics are necessary. A recently created DIC metrological efficiency indicator (*MEI*) [159,160] combines both DIC spatial and measurements resolutions. MEI is computed on special *DIC Challenge 2.0* [163] 'Star 6' synthetic images. The set of 'Star 6' synthetic images consists of an undeformed reference image, deformed with a sinusoidal vertical strain amplitude of 5% 'star' pattern image, and an artificial noise image. The MEI score for DIC strains is calculated as:

$$\text{MEI} = n^2 l_{10\%} \tag{3.3}$$

where n is the standard deviation of the noise level in strains computed from a noisy image at the horizontal central axis (Fig. 3.6); and $l_{10\%}$ is the cutoff period to the 10% fractional strain bias (Fig. 3.6). According to the MEI description [159], the cutoff period $l_{10\%}$ can be found from the following Equation:

$$l_{10\%} = 10 + 290/3999 \cdot (X - 1) \tag{3.4}$$

where X is the minimum X coordinate in px of the deformed image when the 90% signal value (in this case, 4.5% strain) is achieved at the image horizontal center line. In general, lower MEI values indicate better algorithm performance.

A comparison of the DIC and DIC-PDDO strain computation algorithms on MEI is shown in Fig. 3.6 – Fig. 3.7. The DIC VSG = 81 px size and the corresponding PD horizon diameter $2\delta = 140$ px was used to achieve the same spatial resolution at a cutoff period of $l_{10\%} = 207$ px (X = 2721 px).
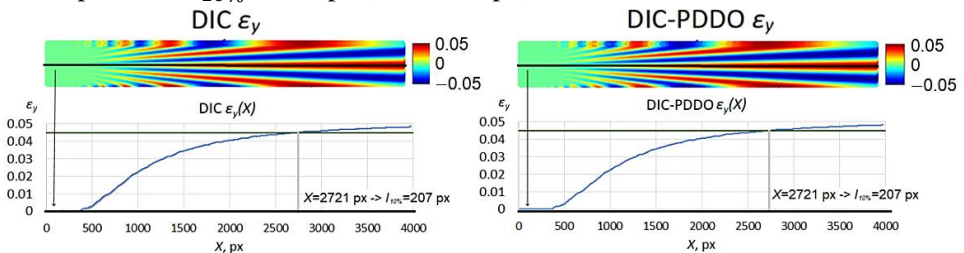
Fig. 3.6 Comparison of DIC and DIC-PDDO strain fields at the same spatial resolutions by using MEI
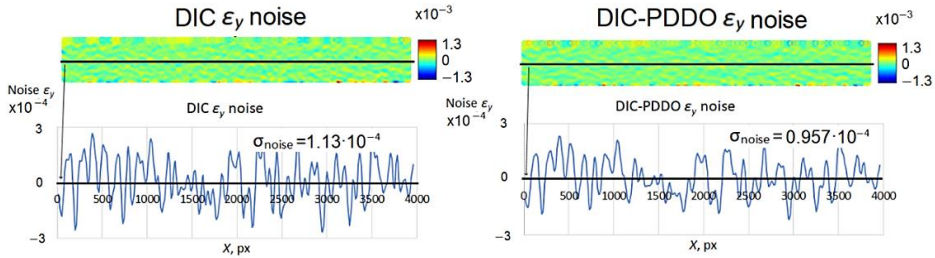
Fig. 3.7 Comparison of DIC and DIC-PDDO strain noise (measurement resolution) at the same spatial resolutions by using MEI

For the same spatial resolution of $l_{10\%} = 207$ px, noise standard deviations are $1.13 \cdot 10^{-4}$ for DIC, and $0.957 \cdot 10^{-4}$ for DIC-PDDO. These values yield $MEI_{DIC} = 2.65\ \mu\varepsilon^2 \cdot px$ and $MEI_{DIC\text{-}PDDO} = 1.98\ \mu\varepsilon^2 \cdot px$ showing that the DIC-PDDO method's performance is 1.34 times better than the current DIC software algorithm. Several DIC and DIC-PDDO MEI comparisons at different spatial resolutions were performed for further testing. The results are plotted in Fig. 3.8; they were compared against the most commonly used DIC strain computation algorithms from [159].
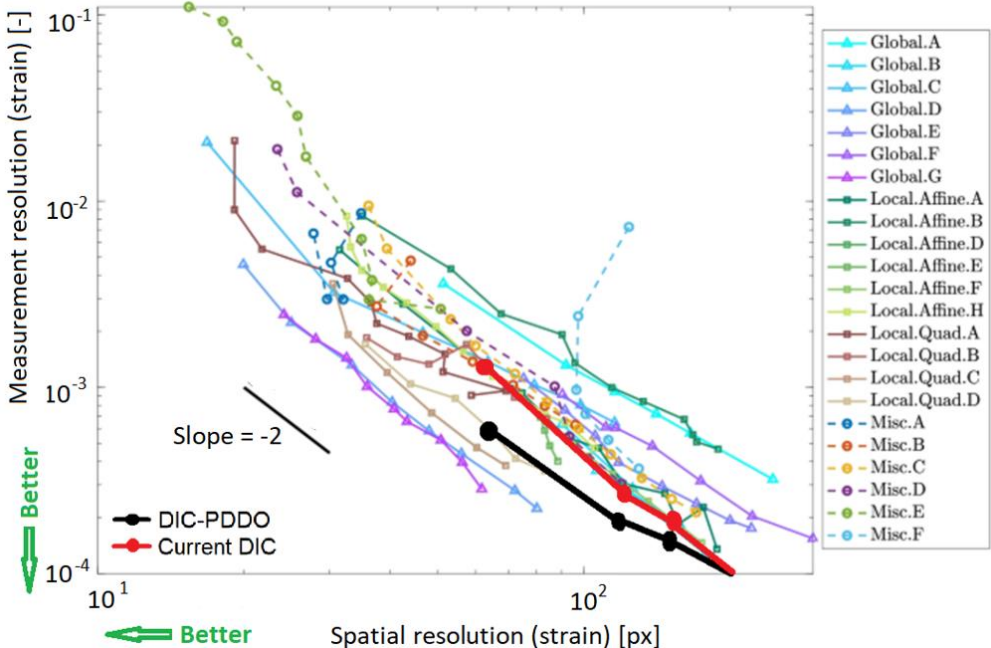
Fig. 3.8 Comparison of DIC strain computation algorithms in terms of spatial and measurement resolution. Data from [159] is extended with tested current DIC and DIC-PDDO algorithms

The proposed DIC-PDDO method offers a better measurement resolution compared to the current DIC algorithm for each testing point (Fig. 3.8) when the DIC and DIC-PDDO spatial resolutions are the same. This leads to square proportionally better performance (lower MEI values) for DIC-PDDO. Moreover, the DIC-PDDO performance is increasing for lower spatial resolution values (see the differences between the 'DIC-PDDO' and the 'Current DIC' curves in Fig. 3.8); thus, the DIC-PDDO method works better for localized strains, such as the fatigue crack initiation, a defect, or damage detection in the material. The use of the DIC-PDDO algorithm instead of the conventional DIC in fatigue analysis is relevant for this study.

3.2. Epoxy Resin Static Tests for PD Model Calibration

The PD material parameters (Chapter 2.2) can be calculated from the CCM parameters, namely, the elastic modulus E and the Poisson's ratio υ, while the PD failure parameters, such as the determination of the critical stretch s_c requires fracture experiments to find the critical energy release rate G_c. Instead of performing such complex experiments, only the tensile test with the DIC full field displacement and strain measurements on the specimen surface is performed. Data from DIC measurements, compared with the PD simulation results in the optimization software, allows the selection of the PD material, especially the failure parameters, which best match to the experiment was observed in the PD model. The optimization approach is essential for complex PD material models, such as SBPD, the composite PD model, the BBPD with bond rotation model, etc.

The idea of DIC-based full field material model calibration is inspired by [65,161,162]. The studies [65,161,162] deal with the selection of the material plasticity parameters for the FE model in *LS-Dyna* and are based on experimental DIC measurements. Experimental force-strain curves at multiple specimen points are compared to *LS-Dyna*-simulated curves in the optimization software *LS-Opt* when selecting the material constants. The constants' values which would best fit the experimental and FE simulated force-strain curves are determined. A similar method using the same optimization software *LS-Opt* is available to calibrate the PD model parameters. The LS-Opt interface with *MATLAB*, where the PD code is written, is also possible [163].

The selected *CH83-2* epoxy resin material properties from the literature [164,165] are elastic modulus E=2.9÷3.4 GPa, Poisson's ratio $\upsilon = 0.3 \div 0.4$, tensile strength $\sigma_u = 5 \div 97$ MPa, and fracture toughness $G_c = 1.0 \div 1.6$ kJ/m². ASTM D638 – 10 [101] specimen of a gauge length of 50 mm, a width of 13 mm, and a thickness of 6.5 (Fig. 3.9 a) was used for testing. The expected maximum tensile failure load of the specimen, calculated according to the maximum tensile strength $\sigma_u = 84$ MPa [164,165], is lower than 10 kN; thus, the same electromechanical tensile testing machine *INSTRON E10000* is sufficient. The tensile tests were run at a crosshead speed of 2 mm/min. Lighting was provided with an adjustable power LED lamp. The speckle pattern on the specimen surface was 0.18 mm-sized black dots created by using a painting roller from *Correlated Solutions*, as it is visible in Fig. 3.9 b. 100 points on the specimen surface DIC strain data (the points' coordinates are shown in Fig. 3.9 b) from DIC measurements were exported and used for the calibration of the PD model parameters in *LS-Opt*.

78
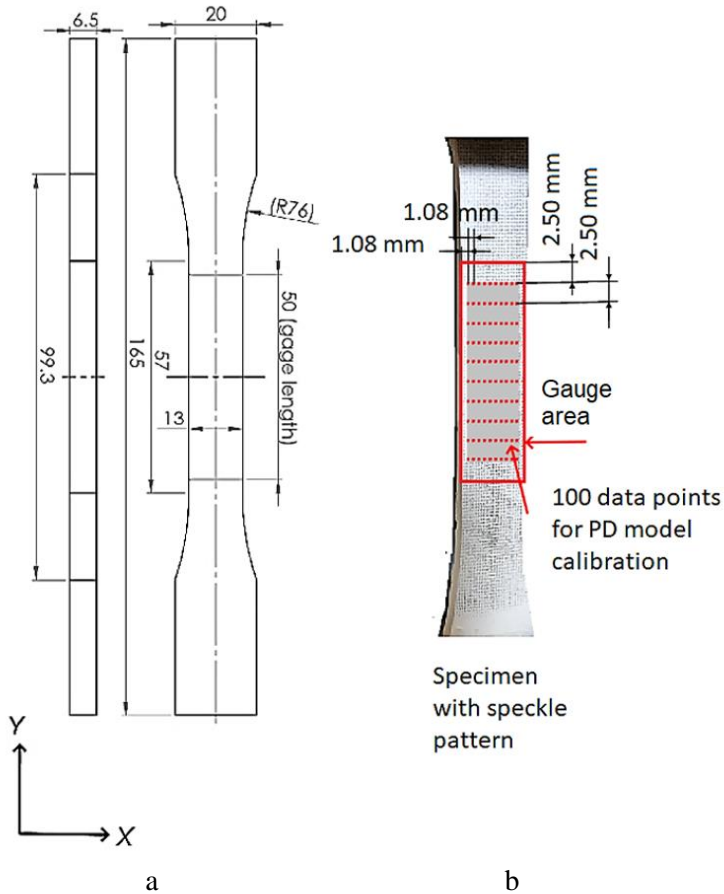
Fig. 3.9 Epoxy CH83-2 resin test specimen: a – drawing; b – pattern and used data points for PD model calibration

The calibration of the DIC system before the experiment was performed on a 14×10 dots calibration plate with 5 mm dot spacing selected according to the specimen dimensions. 30 calibration images were done, and then the calibration score was 0.05. Images of the deformed specimen were recorded with a frequency of 5 Hz and synchronized to the testing machine *INSTRON E10000* through a signal cable. Such a setup enables each image of the deformed specimen (the full field displacement and strain data) with the corresponding tensile load measured from tensile machine. A subset size of 41 px (1.23 mm) and a step size of 8 px (0.24 mm) were used in the DIC software VIC-3D for the post-processing of the images. The values of such a subset and the step sizes yielded the results of the DIC measurements with the confidence interval computed in the VIC-3D software as a sigma value equal to $8.69 \cdot 10^{-3}$ px ($2.64 \cdot 10^{-4}$ mm).

The results of tensile test of the epoxy *CH83-2* specimen with DIC full field displacement and strain measurement are presented in Fig 3.10.
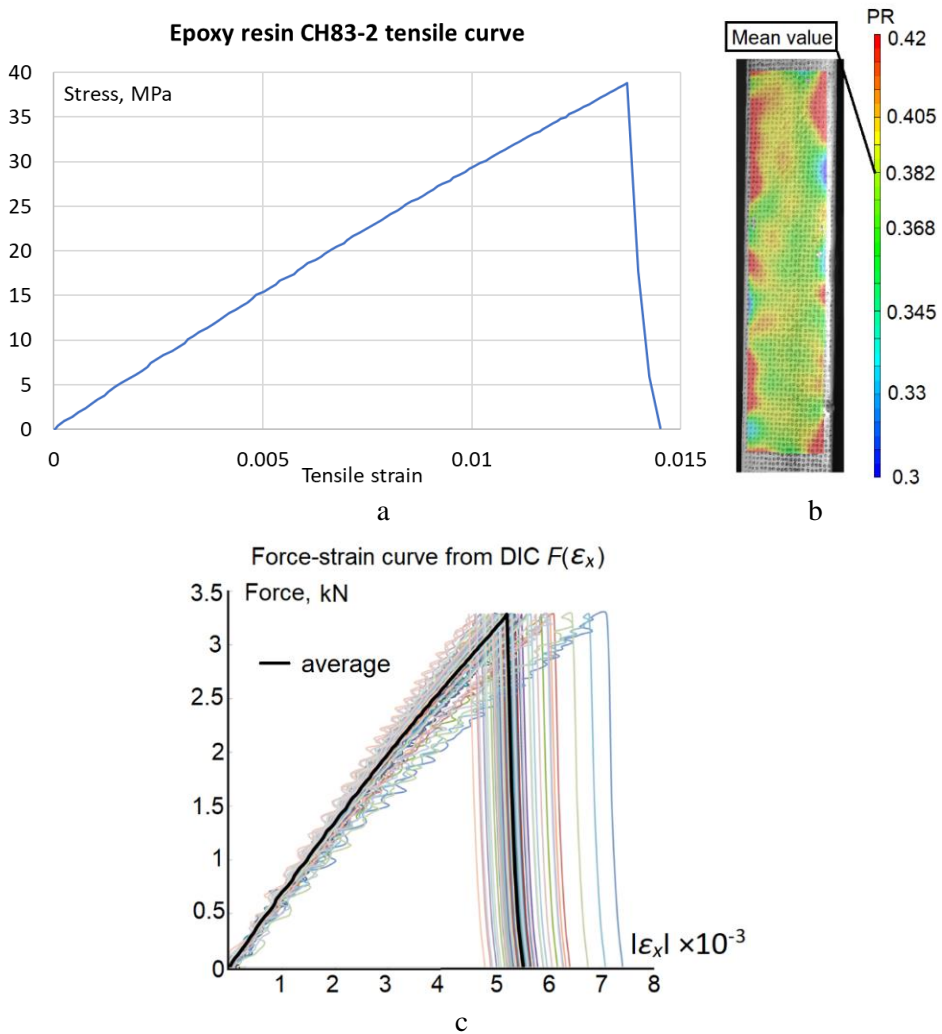
Fig. 3.10 Experimental testing of CH83-2 epoxy resin specimen results: a – tensile curve; b – plot of Poisson's ratio from DIC at loading of 0.6 kN; c – 100 points on the specimen surface force-strain curves for PD model calibration

From the specimen tensile curve, presented in Fig. 3.10 a, it can be seen that the ultimate strength of the epoxy CH83-2 specimen, prepared by using the above-mentioned curing regimes, is 39 MPa. The failure strain of the specimen is 0.0145, although it cannot be considered as a PD critical stretch value due to the PD horizon dependence. The elastic modulus of the specimen, computed from the tensile curve strain range up to 0.005, is 3.1 GPa. The average Poisson's ratio value calculated from full field DIC strain measurements of the transverse ε_x and longitudinal strains ε_y ratio at 0.6 kN loading is 0.382. The plot of the specimen material Poisson's ratio computed in the DIC software VIC-3D is shown in Fig. 3.10 b. Raw 100 points force-strain curves from the the specimen surface (Fig. 3.9 b) are plotted in Fig. 3.10 c. The black

curve in Fig. 3.10 c represents averaged and filtered out force-strain data further used for the PD epoxy resin specimen model calibration. Transverse instead of longitudinal (tensile ε_y) strains from DIC measurements are selected for more effective PD model calibration matching not only regarding the longitudinal elastic and failure behavior of the virtual specimen in the PD model of the experiment, but also by including the specimen transverse deformation behavior, reflected through the Poisson's ratio of the material.

3.3. *316L* Steel Material Cyclic Tests

Standard *316L* stainless steel cylindrical test samples of a diameter of 5 mm, and gauge length 15 mm, as shown in Fig. 3.11, were used. The testing standard requires that the bending strain in the specimen gauge area cannot exceed 5% of the axial strain (percentage bending ratio). As the construction of the original *INSTRON E10000* testing machine does not allow the required percent bending which would result in a more than 10 times shorter fatigue life in cycles (this result is compared to the material's S-N curve [166]) due to excessive bending, a special specimen centering flange was made and mounted onto the testing machine (Fig. 3.11).
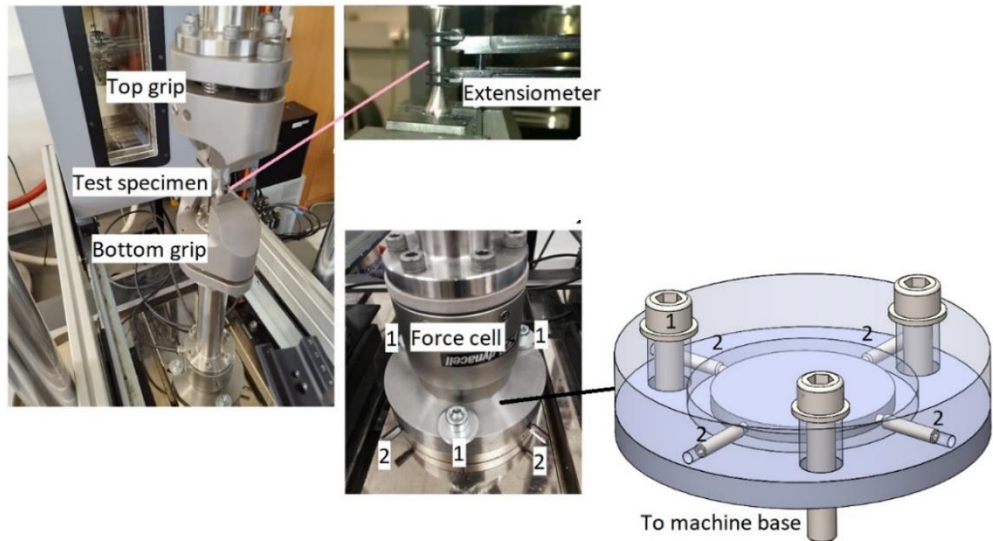
Fig. 3.11 Experimental setup of cyclic tests with an adjustable flange on the testing machine to center the specimen

The flange is mounted onto the machine base with bolts '1' (Fig. 3.11), and it has four centricity adjustment screws '2' (Fig. 3.11) allowing adjustments of up to 1 mm.

The following fatigue tests were performed: 1.) a symmetric ($R = -1$) strain controlled cyclic loading test with a strain amplitude of $\varepsilon_a = 0.0018$; 2.) an asymmetric cyclic loading test consisting of blocks of 1 symmetric $\varepsilon_a = 0.006$ cycle and 200 asymmetric cycles of $\varepsilon_a = 0.0018$ with a mean strain of $\bar{\varepsilon} = -0.0042$ ('POL' loading); 3.) an asymmetric cyclic loading test consisting of blocks of 1 symmetric $\varepsilon_a = 0.006$ cycle and 200 asymmetric cycles $\varepsilon_a = 0.0018$ with a mean strain of $\bar{\varepsilon} = 0.0042$ ('PUL'

loading). A graphical representation of the loading histories is shown in Fig. 3.12. Only 3 cyclic loading tests in total: 1 symmetric, 1 POL loading, and 1 PUL loading, were performed.

a

b

c
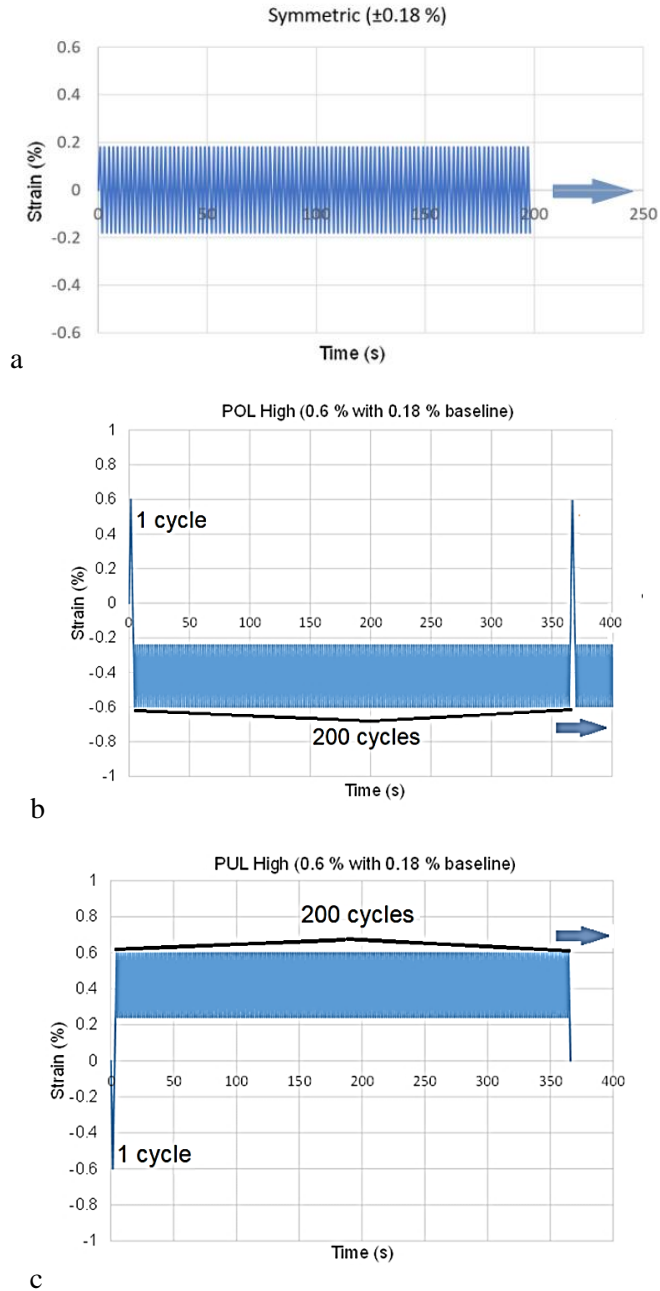
Fig. 3.12 Cyclic loading tests graphs: a – symmetric ±0.0018 strain loading; b – asymmetric variable amplitude POL loading; c – asymmetric variable amplitude PUL loading

Other testing conditions include a temperature of 20 ℃ and a loading frequency of 0.56 Hz. The specimen loading of 0.0018 strain is close (as the resultant stress is several MPa higher) to the material 316L stainless steel yield limit of 206 MPa.

The results of the cyclic tests are presented in Fig. 3.13 – Fig. 3.17. The failure criterion of the specimen is the maximum cycle stress reduction of more than 25% (which is further called N25 failure), which is visible on the maximum cycle stress vs. the linear cycle plot, as it is shown for symmetric cyclic loading in Fig. 3.13. N25 failure compared to the S-N curve of the loading of such a type [166] is demonstrated in Fig. 3.14.
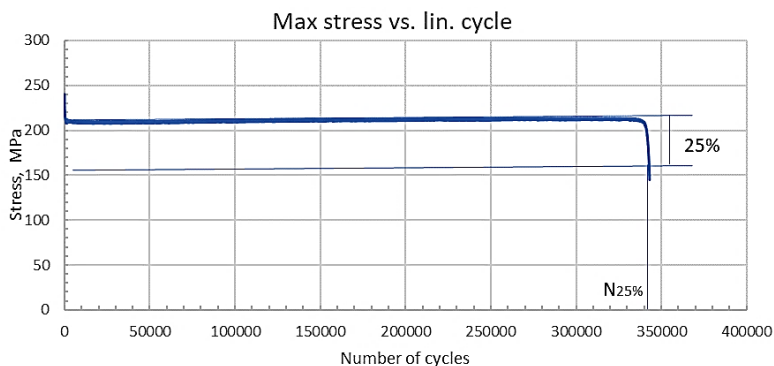
Fig. 3.13 Maximum cycle stress vs. the number of cycles plot for symmetric cyclic loading
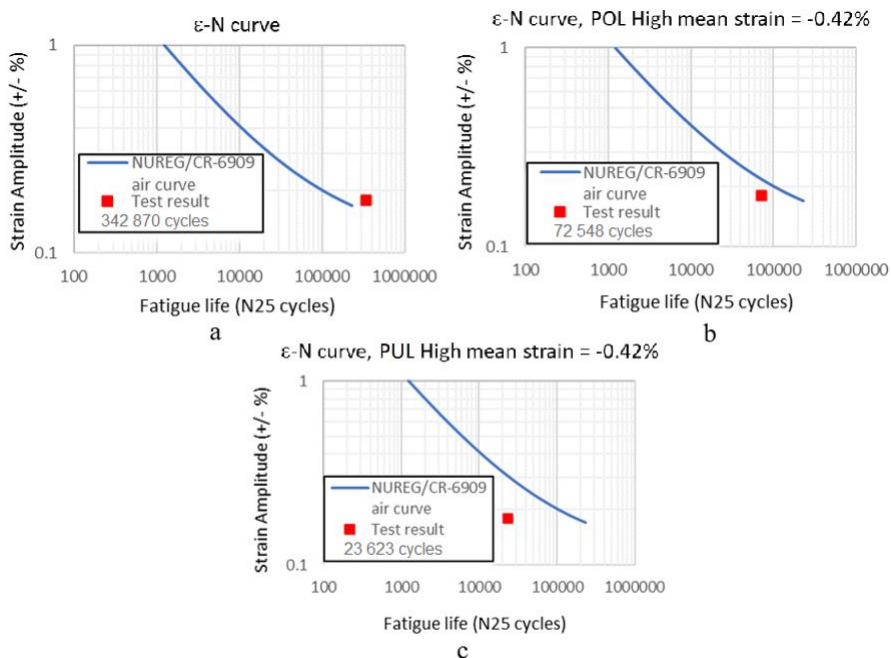
Fig. 3.14 Number of cycles to N25 failure vs. material S-N curve [166]: a – symmetric ±0.18% strain loading; b – POL loading; c – PUL loading

The failure of the test specimens occurred after 342870, 72548, and 23623 N25 cycles for symmetric, POL, and PUL loadings, respectively. A several times larger difference compared to the material's S-N curve for PUL loading is observed, although the results are comparable to such loading tests [166]. Experimental cycle hysteresis loops, which are further necessary for numerical modelling to determine the stress ratio, calculate the process energy losses for KTF fatigue damage Eq. (2.59) – Eq. (2.60) are used; their visualizations are presented in Fig. 3.15 – Fig. 3.17.
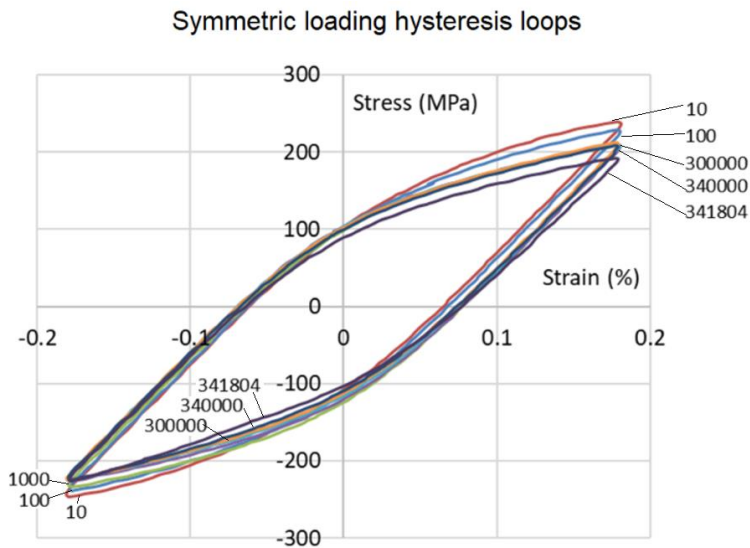
Fig. 3.15. Experimental cycle hysteresis loops for symmetric ±0.18% strain loading
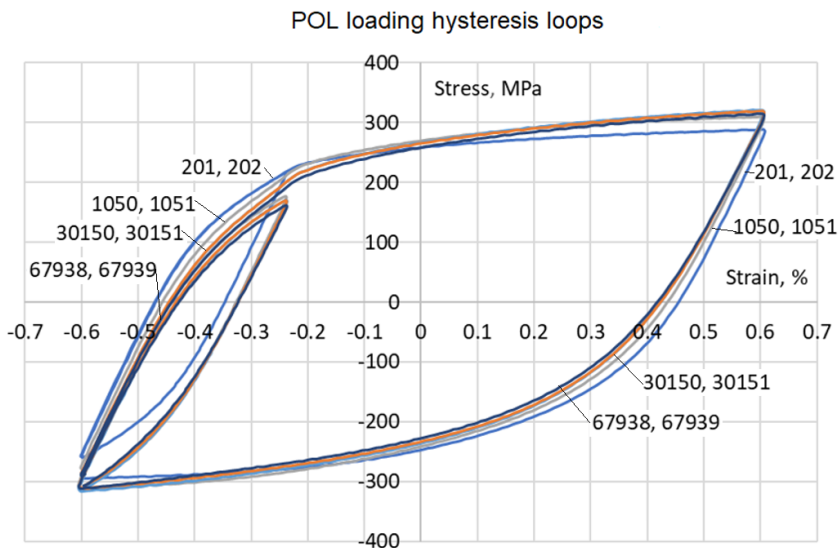
Fig. 3.16 Experimental cycle hysteresis loops for POL loading
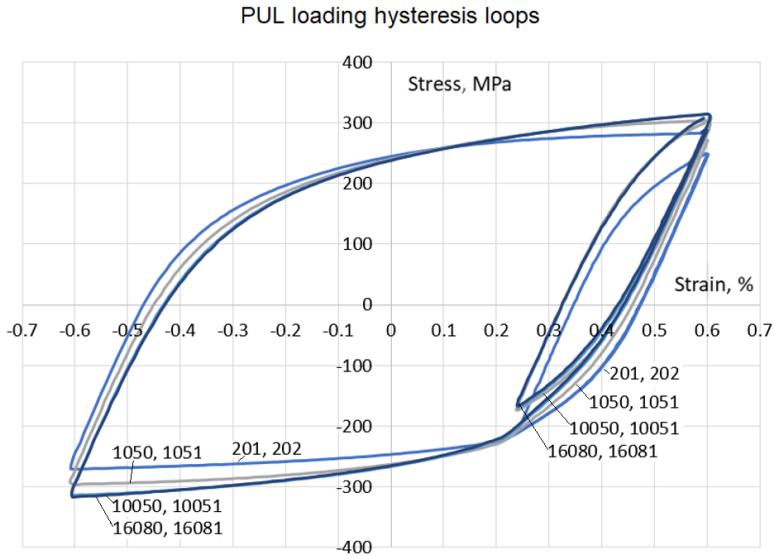
Fig. 3.17 Experimental cycle hysteresis loops for PUL loading

3.4. Composite Material Tests

3.4.1. Static testing of CFRP composite specimens

Due to the high strength of the CFRP specimens, tensile tests were performed on a 100 kN tensile testing machine, as it is shown in Fig. 3.18. While the specimen width of 25 mm was determined according to the Standard ASTM D3039, there are no direct requirements for the specimen length which varies from 124 to 150 mm. Differences of the specimen length have no effect for the current testing. Force and displacement sensors from HBM were used. Strains were measured with an external extensimeter DD1 of the accuracy class 0.1, a base length of 50 mm, and measuring limits of ±2.5 mm. A force cell with an accuracy of 0.05% was used. The output signals from the testing machine were amplified, post-processed, and exported to the *EXCEL* software.
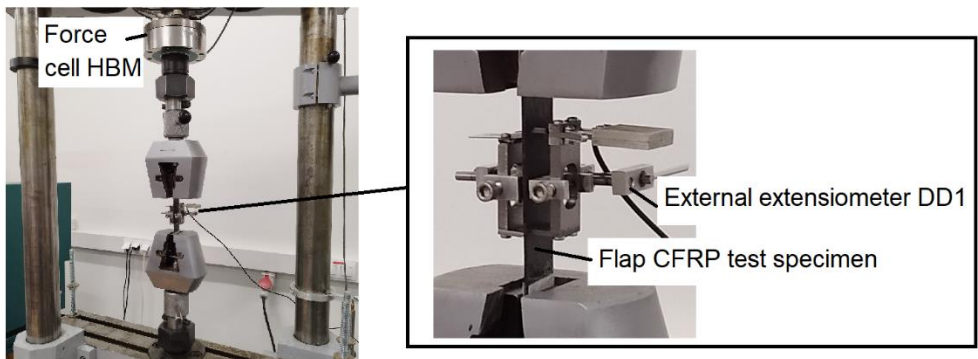
Fig. 3.18 Experimental tensile testing setup for CFRP specimens

The tensile curves of the specimens, cut from a CFRP plate measuring 350 mm×150 mm at 0° and 45° angles, are shown in Fig. 3.19 – Fig. 3.20. Due to the CFRP plate layers configuration of fiber orientation angles [(0′90)°/90 °/0°]s, a specimen cut at an angle of 90° from the CFRP plate is identical to a specimen cut at 0° angle.

CFRP [(0/90)°/90°/0°]s tensile diagram (cut angle 0°)
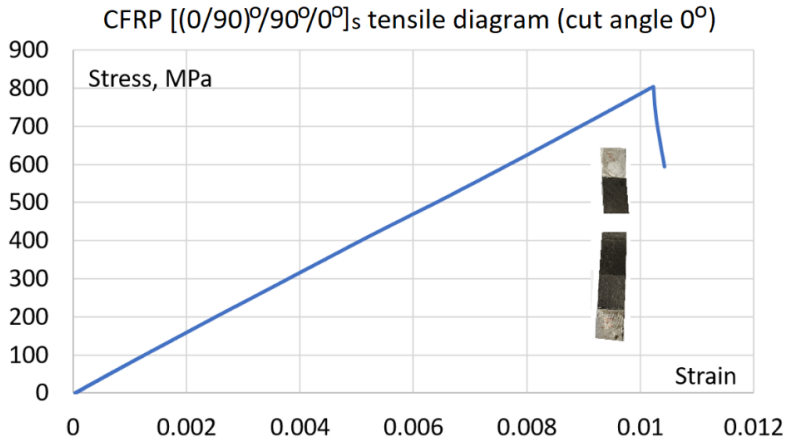
Fig. 3.19 Tensile curve of CFRP composite specimen, cut at angle 0°

CFRP [±45°/-45°/45°]s tensile diagram (cut angle 45°)
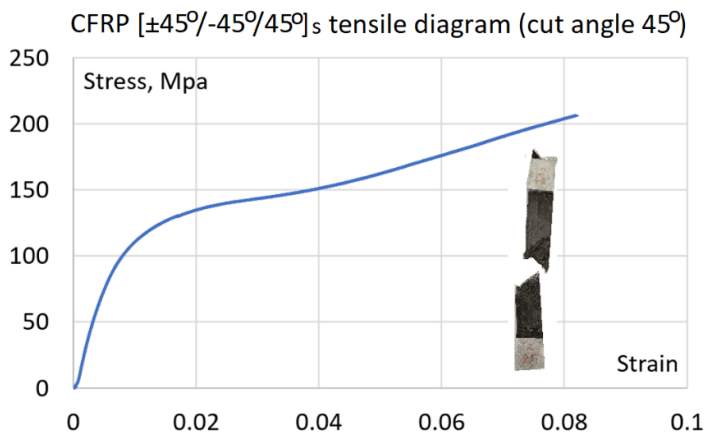
Fig. 3.20 Tensile curve of CFRP composite specimen, cut at angle 45°

The failure of the specimen cut at 0° angle occurs at a strain approximately equal to 0.0102 (Fig. 3.19). The ultimate strength of the specimen is 800 MPa. The specimen experiences ideal linear elastic behavior of an effective elastic modulus E_0 = 78 GPa and pure brittle failure. For the case of the specimen cut at an angle of 45° ((Fig. 3.20), the specimen's stiffness is about 5 times lower compared to the tensile curve from Fig. 3.19, thus resulting in an effective elastic modulus of E_a = 15.2 GPa computed in the strain range 0.0005 ÷ 0.005. Failure of this specimen occurs due to shear and breakage is visible at angle of 45°). The values of effective elastic modulus of the specimens, cut at 0° and 45° orientation angles, are necessary for the calibration

of the FE and PD CFRP composite models so that to select such fiber and matrix properties resulting in an effective stiffness of the specimen in the model which would be equal to the stiffness of the test specimens found from the tensile curves from Fig. 3.19 – Fig. 3.20.

3.4.2. CFRP composite with material defects – defect detection

Based on assumptions that internal defects of composite structures strongly affect the service life of the composite [28] and that no composite structure can be completely perfect, composite fatigue analysis focuses on a composite with defects. Two common defect types – notably, delamination and fiber breakage – are initially considered, and their detection with DIC is analyzed.

The delamination locations in the CFRP plate are shown in Fig. 3.21.
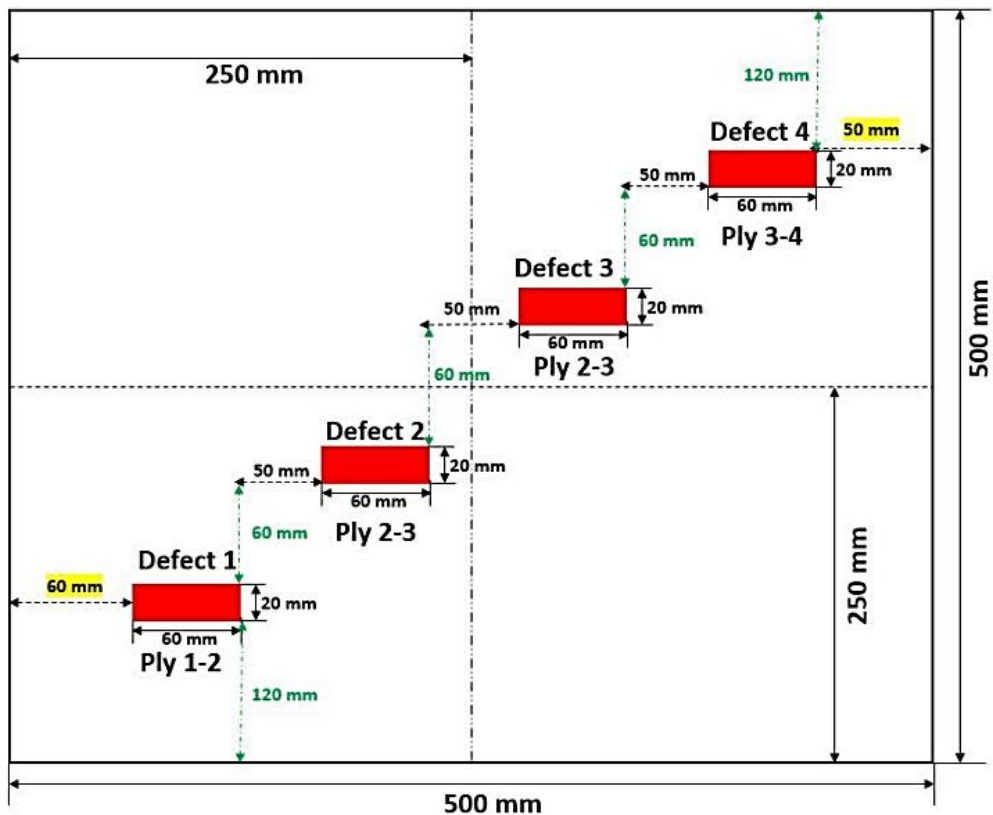
Fig. 3.21 CFRP plate with 4 delaminations [167]

The experimental testing of the CFRP plate with delaminations was performed for the bending loading of 10.45 N force, as it is shown in the experimental setup presented in Fig. 3.22. Bending loading was added by using two weights of 0.5 kg each, mounted to the plate edge with 2 neodymium magnets (magnet weight 23 g per magnet). Two CMOS cameras *Basler acA4112* were used for taking images of the plate. A pattern size of 0.66 mm for DIC measurements on the CFRP plate's surface was applied by

painting the roller. Calibration was performed on 10 × 14 points calibration plate with a point spacing of 28 mm. The processing of images in the DIC software *VIC-3D* was done by using a subset size of 89 px, a step size of 15 px, and a strain filter size of 71. The results of the DIC strain measurements are shown in Fig. 3.23. In order to increase the strain measurement quality by reducing the noise at a high spatial resolution, the strains were computed by using the DIC-PPDO method, as it is shown in Fig. 3.24. The PD horizon size was $\delta = 10.1, 20.1, 40.1$ and $80.1\Delta x$, whereas the PD grid spacing, at which the points were exported from DIC, was $\Delta x = 0.4$ mm.
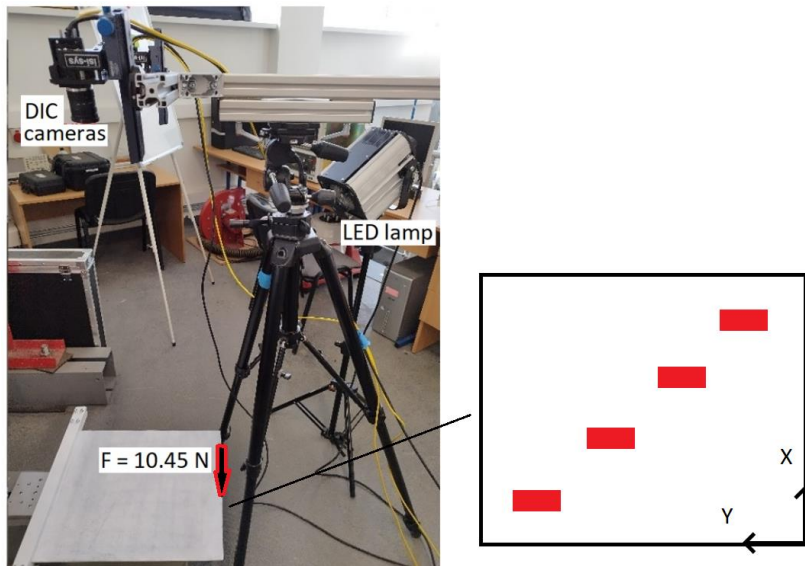
Fig. 3.22 DIC experimental testing setup for CFRP plate with 4 delaminations
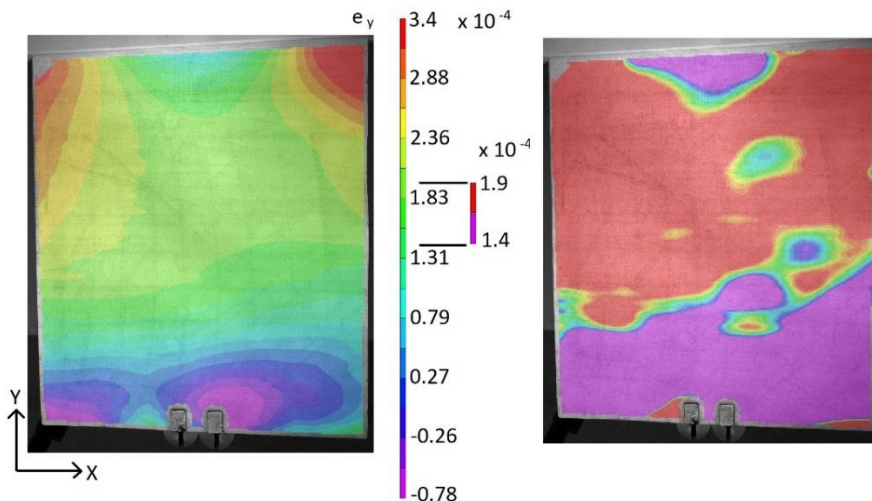
Fig. 3.23 Measured DIC surface strain field of CFRP plate with 4 delaminations
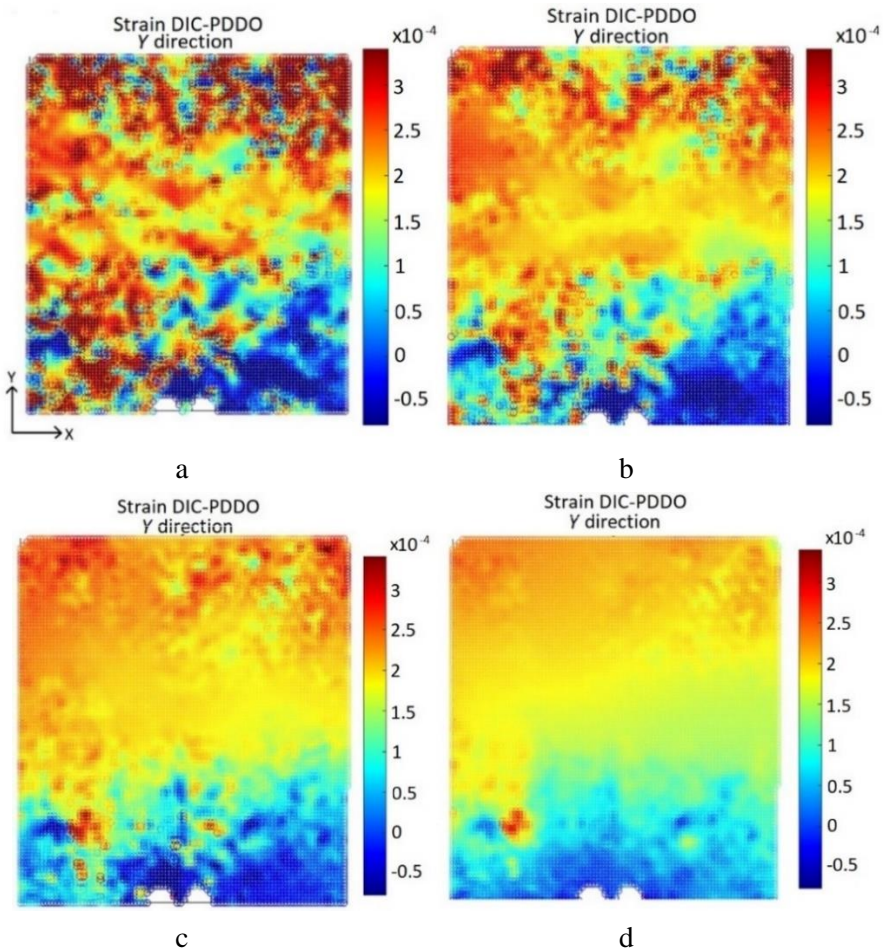
Fig. 3.24 Strains on the CFRP plate with 4 delaminations surface computed using DIC-PDDO ($\Delta x = 0.4$ mm): a – for $\delta = 10.1\Delta x$; b – for $\delta = 20.1\Delta x$; c – for $\delta = 40.1\Delta x$; d – for $\delta = 80.1\Delta x$

From the surface strain field of the CFRP plate with delaminations, shown in Fig. 3.23 and Fig. 3.24, the effect of delamination on the strain field cannot be observed. Even if the colormap limits are adjusted, or if the improved strain computation algorithm (DIC-PDDO) is used, the identification of the delamination positions cannot be determined. When applying the PDDO strain computation algorithm to DIC at very low PD horizon values, the CFRP plate surface unevenness disturbs the strain results, and no delamination can be detected, either. It can be stated that delamination detection is not simple [40], the delamination depth is very important, and, even at 0.25 of the CFRP plate thickness, the existing delamination of 12% of plate width is invisible from the DIC surface strain measurements for this case. After further analysis of this CFRP plate with FE modelling, it was concluded that practical applications of the static DIC surface strain measurements for the current CFRP plate and FE models are inappropriate to identify the existing delaminations.

Nevertheless, the dynamic characteristics, as natural frequency changes, can determine such delaminations in the CFRP plate [167]. As the focus of this study is DIC and as the dynamic material characteristics are beyond the topic of this study, analysis is further performed for the second case of the composite defect – composite cracks only.

Composite specimens with artificial cracks – milled grooves of 1.5 mm and 1 mm, length 10 mm, orientation angle to the tensile direction 45º – were made, as it is shown in Fig. 3.25 a.

a   b
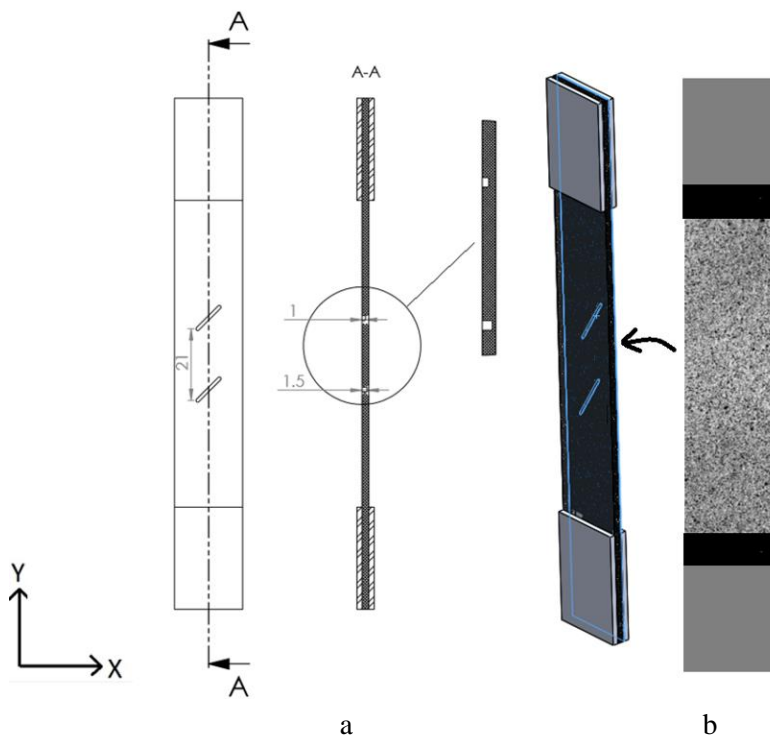
Fig. 3.25 Scheme of the CFRP specimen with 2 fiber cracks (milled slots): a – geometry; b – speckle pattern for DIC measurements

A speckle pattern of a size of 0.05 mm was created on a white coated specimen's surface by using black paint, sprayed with an airbrush. Static tensile loading in the Y direction of the specimen, shown in Fig. 3.25 b, was done with a tensile machine. Images of the undeformed and deformed specimen surface were recorder with DIC cameras. The specimen was loaded with up to 3000 N tensile force and then unloaded to prevent defect growth and failure of the entire specimen. A calibration plate of DIC 9×9 points of a size of 3 mm was used for the DIC system calibration. The subset size was 57 px, whereas the step size was 11 px. The strain fields at the tensile direction Y for static tensile loading of a force of 3000 N, computed by using both conventional DIC and DIC-PDDO algorithms, are shown in Fig. 3.26. 'Defect 1' in Fig. 3.26 refers to a 1 mm-deep groove on the back side of the specimen (its depth from the surface where the strains are measured is 1 mm, too); 'Defect 2'

90

refs to a similar groove with a depth of 1.5 mm (the depth from the surface where the strains are measured is 0.5 mm).
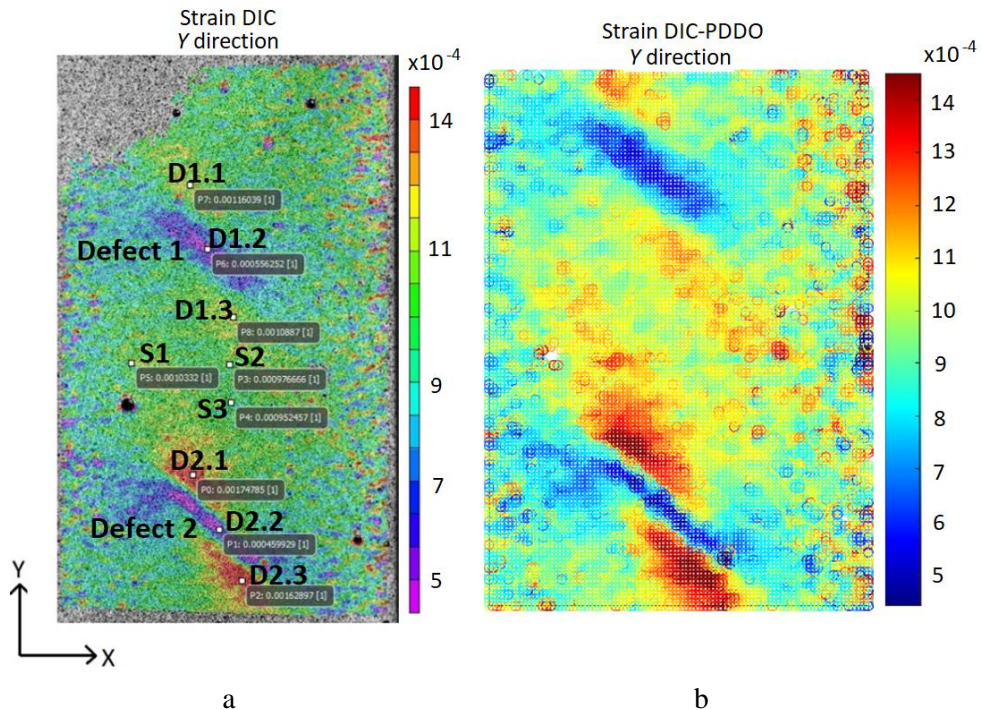
Fig. 3.26 Longitudinal (tensile direction) strain fields on the CFRP specimen with 2 fiber cracks (milled slots) surface: a – conventional DIC; b – DIC-PDDO

Artificial defects in the specimen (defects 1 and 2) are seen in both DIC and DIC-PDDO specimen surface strain fields. Thus, even the conventional DIC is sufficient to detect fiber cracks in a composite material. The strain field computed by the DIC-PDDO method is identical to the original DIC strain field for this current testing of the CFRP composite. Moreover, the defect location and, partially, the shape (especially for 'Defect 2') can be estimated from such strain measurements.

In order not only to detect the existing defects/damages in composite structures during their service life, but also to qualify the damage according to the dimensions, FE model updating (FEMU) can be applied. After determining the deformation control points (Fig. 3.26), around the defect (strains D1.1–D1.3 or D2.1–D2.3) and in the non-defect zone (S = average of S1–S3), it is possible to compute the strain ratios D_{ij}/S. The next step is FE modelling of the analyzed structure with defects. The material properties in the FE model can be calibrated from static tests of the same material, or even from the DIC measurements themselves. The geometry of defects in the FE model, e.g., the length, width, and depth, should be parametrized. By performing optimization in the FE software with the objective to find the defect dimensions (parameters), minimal differences between the stated strain ratios D_{ij}/S in the FE model and experimental measurements are observed, and the dimensions of the unknown defect can be found.

4. NUMERICAL MODELLING

4.1. PD Model of Isotropic Material for Static Loading Calibration

PD models of epoxy resin *CH83-2* standard test specimen are created in *MATLAB* by using 2D plane stress formulations of both BBPD and SBPD theories. The PD grid spacing is $\Delta x = 1.08$ mm, and the PD horizon size is set to the conventional value of $\delta = 3.1\Delta x$. The boundary conditions and the modelling scheme are shown in Fig. 4.1.
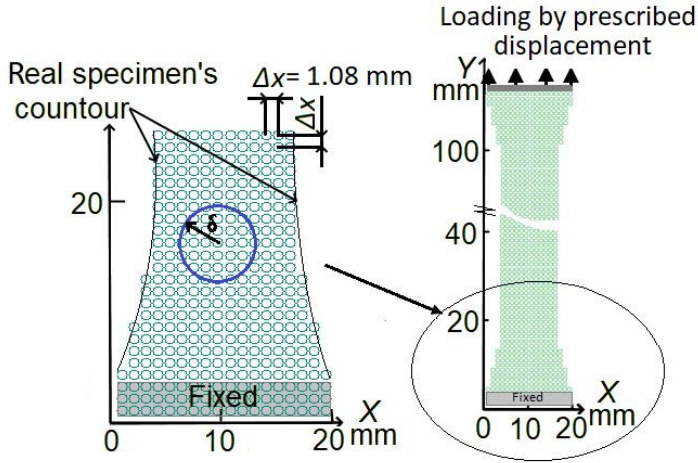
Fig. 4.1 PD model of *CH83-2* epoxy resin specimen

The specimen width in the gauge is selected at least to 4 PD horizons (12 PD points) to prevent distortions due to the PD surface effect. The fillets of the specimen are stepwise discretized according to the selected PD grid size. A finer PD grid could be selected for better discretization of the fillets, but the computational time cost forces us to select coarse PD grids. PD volume correction for BBPD and the force density with dilatation corrections for SBPD are used to reduce the PD surface effect. The PD model boundary conditions include the top of the specimen loading by the prescribed displacement in the *Y* direction, while the bottom of the specimen is fixed at the node layer of the PD horizon δ (Fig. 4.1). Explicit time integration with artificial damping is used to get a quasi-static solution. The amount of artificial damping is selected according to the minimum parameter β value and for the BBPD model, which yields $C = 10^6$ kg/s when, for the SBPD model, damping of $C = 10^9$ kg/s is necessary.

Three material parameters are included in the calibration procedure performed in the optimization software *LS-Opt*: the elastic modulus *E*, the Poisson's ratio *v*, and the PD critical stretch s_c. The elastic modulus and the Poisson's ratio were selected to analyze their effect to the PD model parameters *a*, *b*, *c* and *d* (Eq. (2.9), Eq. (2.13) – Eq. (2.15)) which are expressed as functions of *E* and *v*. Nevertheless, the main focus of the PD model calibration is the PD critical stretch s_c as the material failure parameter. The calibrated material parameters, their ranges and initial values are shown in Table 4.1. For the 2D BBPD formulation, the Poisson's ratio can only

be up to 0.33, and its effect can only be analyzed in the SBPD model.

Table 4.1. Parameters and their ranges for the calibration of BBPD and SBPD models

	BBPD model			SBPD model		
	min	max	initial	min	max	initial
Elastic modulus E, GPa	2.5	3.5	3.1	2.5	3.5	3.1
Poisson's ratio v	Fixed to 0.33			0.3	0.42	0.38
Critical stretch s_c	0.011	0.022	0.016	0.011	0.022	0.016

The starting value for the resin *CH83-2* elastic modulus *E* selection is based on the average elastic modulus of 3.1 GPa found from in-house experimental testing and value of 3 GPa given in the material datasheet [164]. Wider *E* optimization limits of 2.5÷3.5 GPa are defined to analyze the effect of different *E* values on the PD model. While the Poisson's ratio is fixed to 0.33 for the BBPD model, it is calibrated by allowing values from 0.3 to 0.42 established from in-house DIC measurements, as it is visible in Fig. 3.10 b. By using Eq. (2.21) as the analytic expression of the PD critical stretch, the fracture toughness G_c values for the epoxy resin, given in [168], and the in-house measured values of *E* and *v*, the PD critical stretch calibration range is determined as 0.011÷0.022 with the starting value of 0.016 (Table 4.2).

For the current PD material model calibration from in-house DIC experimental measurements, the linear polynomial metamodel with the D-Optimal point selection in the software *LS-Opt 7.0* [163] was used. The resulting *LS-Opt* optimization problem setup in the *LS-Opt* software is shown in Fig. 4.2 [169].
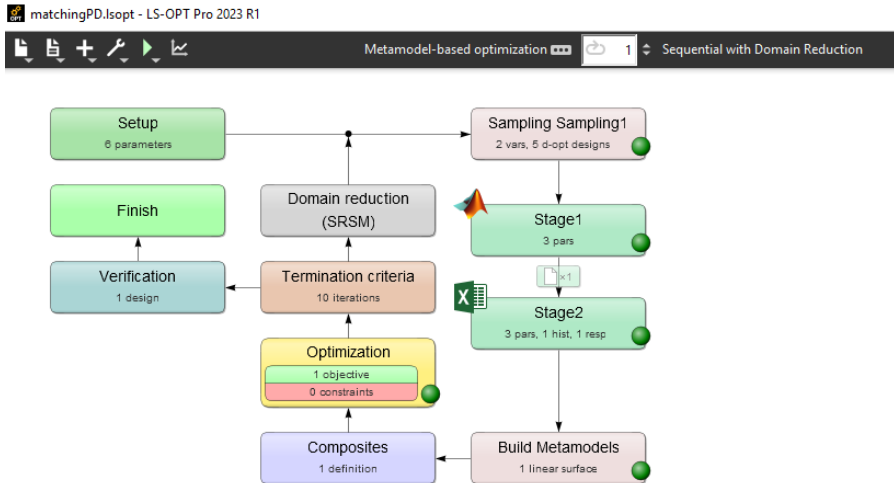
Fig. 4.2 BBPD and SBPD models calibration setup using *LS-Opt* with interface to *MATLAB* and *Excel*

The block, called 'Stage 1' in Fig. 4.2, consists of the *MATLAB* input file with three

input variables (parameters): E, v and s_c, the definition and the code for the force-strain curve data points (history in the *LS-Opt* terms) calculation. In the course of the PD simulation, 100 points of the specimen's reaction force from x component strain $F = f_i(\varepsilon_x)$ ($i = 1 \dots 100$) curves data were calculated and averaged to one curve $F = f(\varepsilon_x)$. Coordinates of those 100 points in the PD simulation are the same as the coordinates of the experimental data points, also shown in Fig. 3.9. Due to the issues of exporting the history directly from the *MATLAB* file for this current code, an Excel stage (the block 'Stage 2' in Fig. 4.2) was added. The curve points exported to an Excel file by using the command `writematrix(A,filename,'Sheet',1, 'Range','D1:E100')` was included. Also, the values of the parameters E, v and s_c were printed to an *Excel* file for the second stage optimization. Finally, an *Excel* file transferred from the stage 1 to stage 2 as it is shown in Fig. 4.2. Because the results needed to be computed several times within *LS-Opt* for the tasks of Stages 1 and 2, the *Excel* input file also needed to be parameterized. For this reason, 3 additional parameters were created, equal to the *MATLAB* parameters E, v, $s_{c,}$. Thus, a total of 6 optimization parameters are visible in the 'Setup' block in Fig. 4.2. A simulated force-strain curve in Stage 2 is identified as the *EXCEL* history in *LS-Opt* by defining the *Excel* file created by the PD *MATLAB* code in Stage 1. The experimental curve (the average of DIC force-strain curves) in Stage 2 in *LS-Opt* is defined as the 'Target history' by using experimental curve points written in a .txt file. The calibration of the material parameters E, v and s_c was performed by comparing the average force-strain tensile curves from the DIC experimental measurements and the PD simulation, and selecting the parameters E, v and s_c to get the best matching between the experimental and computational curves (Fig. 4.3). No additional optimization constraints were applied. An optimization algorithm termination of 10 iterations was selected as optimal in terms of the optimization time and accuracy. Automatic optimization space reduction after each iteration in *LS-Opt* (the 'Domain reduction' block in Fig. 4.2) with the Sequential Response Surface Method according to the *LS-Opt* default [163] was used to reduce the computation time and enable a wider range of the variables E, v and s_c without losing the optimization accuracy.
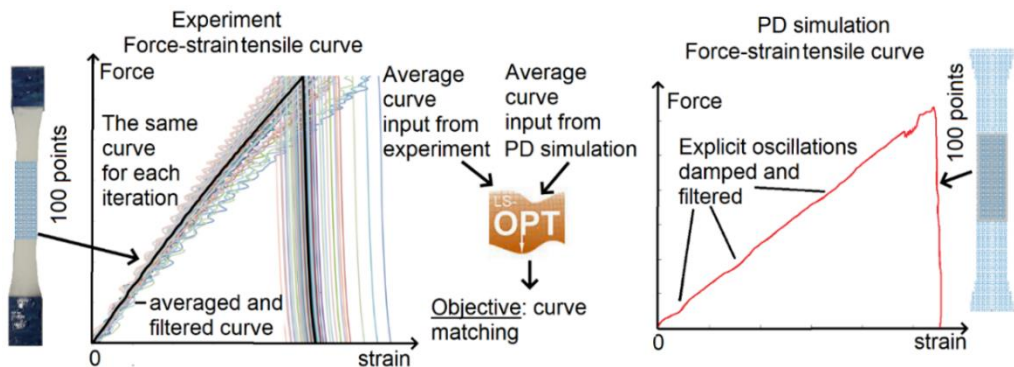
Fig. 4.3 Schematics of the PD model calibration procedure

After the analysis of the different curve matching algorithms, which are available in *LS-Opt* [161,163], the *Partial Curve Mapping* (PCM) algorithm was

selected. PCM is based on mapping the points of one curve onto the second curve and then computing the area between the two curves. To prevent errors when computing the area between those two curves, the experimental and computational curves should consist of a similar number of data points. The matching between the two curves with the PCM algorithm is performed parametrically in *LS-Opt*, according to the optimization objective value which defines the normalized difference between the summation of areas below individual segments of the curves. Also, for the PCM algorithm, the curves should be firstly filtered from noise (a filtered experimental curve is shown in Fig. 4.3). Smaller dynamic oscillations in the PD tensile curve, caused by the inertia vibrations of the model during loading and during the PD bonds breakage when using a quasi-static explicit time integration scheme, can be seen in Fig. 4.3. These small oscillations do not significantly affect the PCM curve matching algorithm accuracy; also, if necessary, they can be removed by using time filters, applied to the PD curve.

The calibrated material parameters for the current BBPD and SBPD models, along with the procedure computational time, are presented in Table 4.2. A comparison of experimental (DIC) and PD simulated force-strain tensile curves, plotted on a single graph, is shown in Fig. 4.4 a for BBPD and in Fig. 4.4 b for SBPD.

Table 4.2. Calibration results of PD models

	BBPD	SBPD
Calibrated material parameters		
E [GPa]	3.13	3.26
v	0.33 (fixed)	0.384
s_c	0.0173	0.0177
Calibration time [s]	1343	4379
PD model computation time [s]	4.2	61.8

a   b
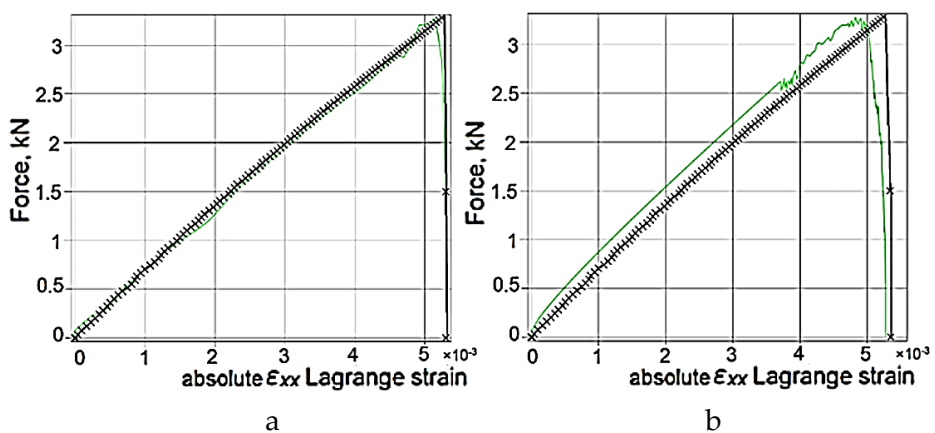
Fig. 4.4 Experimental (x) and PD model (-) force-strain curves matching after 10 iterations in *LS-Opt*: a – BBPD and experimental; b – SBPD and experimental

The *LS-Opt* calibrated value of the elastic modulus of 3.13 GPa for BBPD and 3.26 GPa for SBPD are very close to the experimental value of 3.1 GPa. The calibrated Poisson's ratio for the SBPD model of 0.384 is almost equal to the average of in-house experimental DIC measurements of 0.382. Once such a calibration procedure is valid for the isotropic PD material model elastic constants definition, the main purpose to calibrate E and v is its application for a complex material or a complex behavior of a material, for example, non-linearity. It is also essential to calibrate the effective elastic modulus of the further-used composite PD model, where different PD bonds stiffnesses are dependent on the elastic modulus of the fiber and the matrix. The calibrated critical stretch values for the SBPD and BBPD models are comparable and fall within the range of the theoretical values predicted by Eq. (2.21). Nevertheless, using Eq. (2.21) to calculate the PD critical stretch requires knowing the material critical energy release rate Gc, which requires more complex experimental testing than the tensile test of standard specimens. Therefore, it is possible to consider the suggested calibration procedure as a more straightforward, efficient, and precise approach to figuring out the PD critical stretch.

It can be observed that the SBPD model calibration in *LS-Opt* required 3× more computational time than the BBPD model calibration, which is related to the computational efficiency of the proposed PD model calibration procedure. The Poisson's ratio, an extra calibration parameter in the SBPD calibration procedure, is one of the causes of the longer computation time. Furthermore, the SBPD model formulation causes a 15× increase in the model computing time in the PD *MATLAB* stage (4.2 seconds for the BBPD model vs. 61.8 seconds for the SBPD model). Fig. 4.4 shows that the calibrated PD curves correlate well with the experimental curves. However, the results of the BBPD model calibration indicate that the optimization algorithm-derived objective value is $3 \cdot 10^{-4}$ after 10 calibration iterations while, after the same number of iterations, the computed objective value for the SBPD model is 0.05. This implies that additional calibration iterations and, correspondingly, the longer calculation time are necessary to provide even better curve matching for the calibration of the SBPD model. Furthermore, despite the limitations imposed by the Poisson's ratio, BBPD appears to be more appealing for use in the majority of simple PD modelling applications on an isotropic material due to its significantly lower computational cost, model calibration computational cost, and – still – very good correlation with the experimental results (Fig. 4.4 a).

Fig. 4.5 [169] presents the experimental and simulated displacement and strain plots. It displays both qualitative (distribution) and quantitative (values) agreement between the calibrated PD model results and the experimental measurements in the elastic regime. However, there is still some mismatch because of the non-homogeneities in the material structure that are evident in the DIC experimental strain field measurements (Fig. 4.5 b, c) and because of the boundary effects that are not entirely eliminated in the PD computational fields (namely, the ε_x component of strain (Fig. 4.5 c) due to the current PD model discretization). Rather than comparing material parameters at a single point, full field DIC based calibration offers a better approach which is able to prevent PD model calibration errors (for example, a strain gauge that may be positioned at an unidentified local material defect zone) of the

specimen.
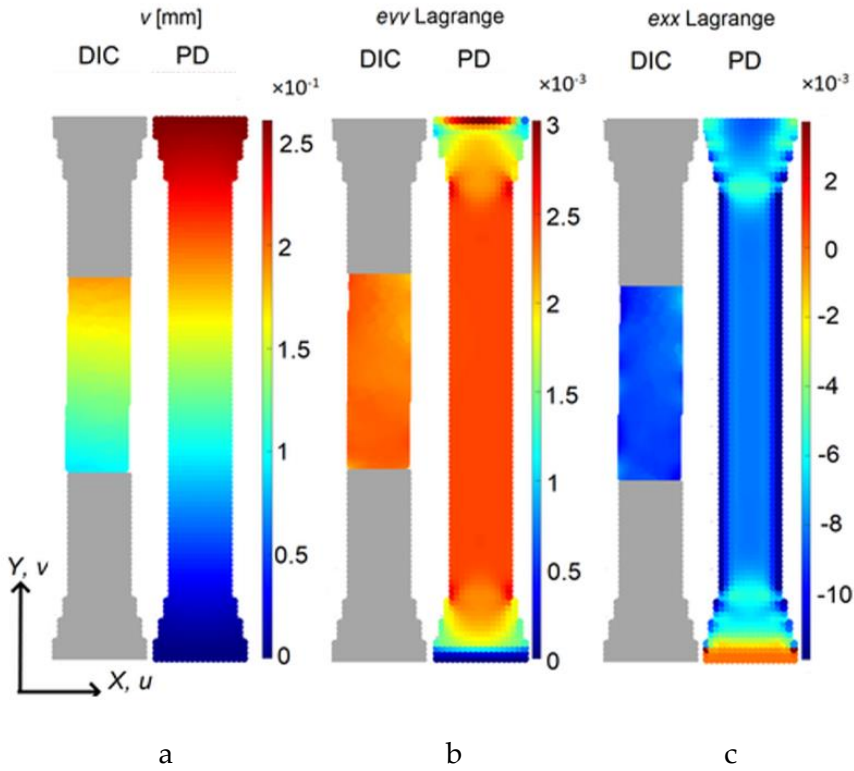
Fig. 4.5 Experimental DIC and computational PD field results: a – displacement v on longitudinal loading direction Y; b –strain ε_{yy} on longitudinal direction; c – strain ε_{xx} on transverse direction (results for BBPD and SBPD models were similar)

A good match of the damage events on the computational and experimental curves in Fig. 4.4 confirms the accuracy of the calibrated PD critical stretch value. While the breakage of the real specimens occurs in the gauge area (Fig. 4.6 a) due to inherent material imperfections in the gauge area if they have a higher effect than the stress concentration at the fillet zone, the specimen in the PD model breaks near the fillets (Fig. 4.6 b) due to stress concentrations at the fillets zone and no material defects over the specimen's gauge area. Several techniques can be applied to address this phenomenon and incorporate the genuine failure behavior in the computational model: material failure parameter distribution [170], the material microdefects probabilistic distribution [171] at the gauge area, or just 'turning off' failure on the particular model zones [9]. By disabling the PD bond damage at the boundaries and at the fillet zones, the effect of the stress concentrator at the fillet zones in the PD model was eliminated, similarly as described in study [9]. This resulted in an agreement between the failure crack type and the position in the gauge area (Fig 4.5 b), which is thought to be the relevant failure area and mechanism for the calibration of the material properties.
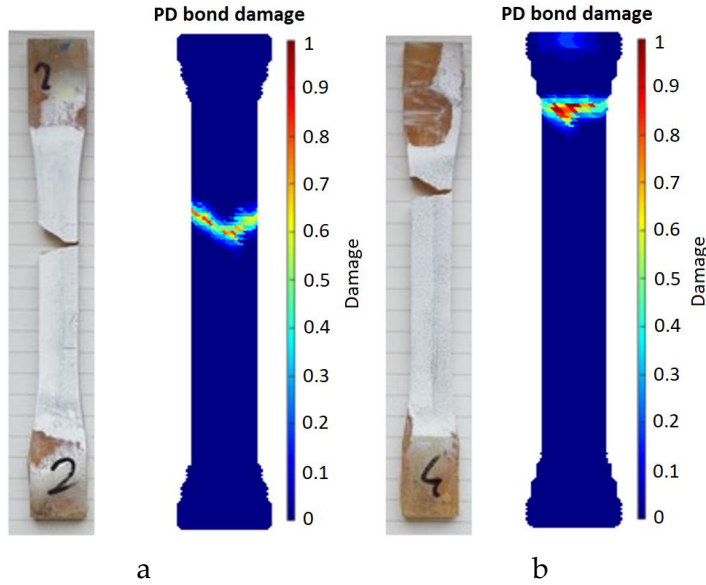
Fig. 4.6 Experimental and simulated (PD bond damage fields) failure of the specimen (results are the same for both the BBPD and SBPD models): a – at the gauge area;
b – at the fillet zone

Nonlinear material behavior, such as the material ductile damage characteristic, is another factor to consider when analyzing the PD model of isotropic materials. Based on the material under consideration, the original PD formulation proposed by Silling [6] and used in this work is the one used for brittle material failure (Chapter 3.3). The value of the plasticity power law constants and the proportional or yield limit stretch s_p could also be included in the calibration process for elasto-plastic materials. Then, the PD force density vector from Eq. (2.10) employing the power law is changed as follows, in a manner akin to the traditional stress-strain curve approximation techniques utilized in FEM [172]:

$$\boldsymbol{t}_{xx\prime} = \begin{cases} \text{Eq. (4), if } s_{xx\prime} \leq s_p \\ \boldsymbol{t}_{pxx\prime}\left(\dfrac{s_{xx\prime}}{s_p}\right)^{m}, \text{if } s_{xx\prime} > s_p \end{cases} \tag{4.1}$$

where $\boldsymbol{t}_{pxx\prime}$ is the PD bond force density vector between points x and x' at the proportional or yield limit deformation, calculated according to Eq. (2.10) by using the stretch value of $s_{xx\prime} = s_p$; where m – the exponent constant.

Another calibration example for elasto-plastic PD model parameters is analyzed in this study by using a test specimen made of sheet steel *CR210IF* ($E = 210$ GPa, $\upsilon = 0.3$) and having the same geometry as that shown in Fig. 4.1. Full field DIC strain measurements of a specimen, made of such a material [161], are used to calibrate the PD model. As illustrated in Fig. 4.7 a and outlined in Table 4.3, the calibration procedure, which was ran in this study, involves three elasto-plastic PD

98

material model parameters: the proportional limit stretch s_p, the material critical stretch s_c, and the exponent constant m. Since the properties of an elastic material (E and v) are assessed directly, they are not included in the calibration. Initial guesswork is used to choose the optimization ranges and the initial values of the calibrated PD model parameters in *LS-Opt* while considering the plastic behavior of the material. From DIC measurements [161], the calibration process uses an average experimental force-strain curve shown in Fig. 4.7b with the '×' markers.

Type		Name	Starting	Minimum	Maximum
Continuous	∨	sp	0.003	0	0.01
Continuous	∨	s	0.6	0.3	0.8
Continuous	∨	m	0.05	0.01	0.2
Dependent	∨	s_plastic	Definition: sp		
Dependent	∨	s_critical	Definition: s		
Dependent	∨	power_law	Definition: m		

a
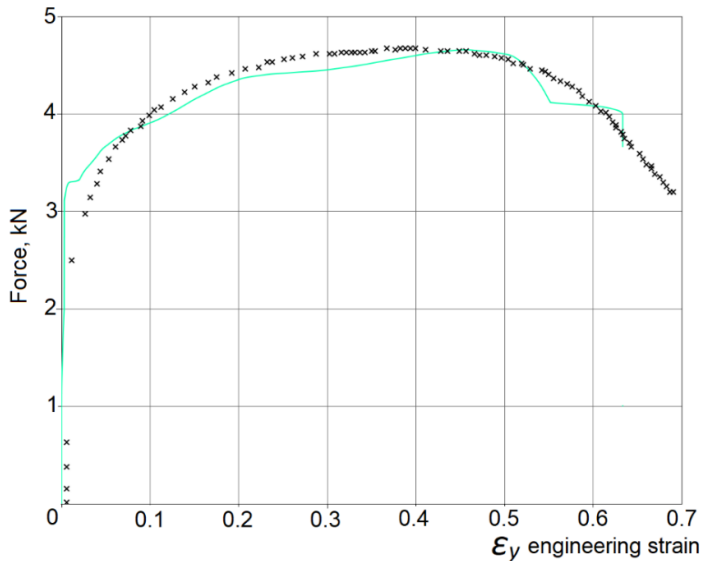
b

Fig. 4. 7. Elastoplastic BBPD model calibration: a – PD plasticity parameters used for calibration, their ranges and initial values; b – curve matching in LS-Opt ('×' represents the DIC experimental curve from [161])

Table 4.3. Parameters of calibrated PD elasto-plastic material models

Calibrated material parameters	
proportional limit stretch s_p	0.0033
critical stretch s_c	0.46
exponent law m	0.115

An optimization objective value of $1.1 \cdot 10^{-3}$ was attained after 6 iterations in *LS-Opt*, which yielded the computational tensile curve of the PD models in agreement with the experimental curve [161] (Fig. 4.7 b). Table 4.3 presents the values of the calibrated PD material model plasticity parameters. It should be noted that the calibrated PD elasto-plastic model parameters of s_p and s_c are straightforwardly evaluated by using the proposed method while not having analogues of the values equal to their classical continuum mechanics (s_p – to the yield limit strain, s_c – to the failure strain). A good agreement between the experimental and computational tensile curves indicates the correctness of the calibrated elasto-plastic PD model (Fig. 4.7 b).

4.2. Modelling Isotropic Material Cyclic Loading with KTF-PD

The 3D BBPD theory is applied to the PD fatigue model of the standard *ASTM E606/606M* test specimen made of *316L* stainless steel. The current PD model discretization yields 726 material points (17 points per specimen diameter), and the PD horizon size is set to $\delta = 3.1\Delta x$ (Fig. 4.8). Only the specimen gauge area is modelled to save the computational time. The PD bond failure is active in the middle of the model only (Fig. 4.8 a) to prevent a false failure at the boundaries similar to that in the epoxy resin *CH83-2 PD* model (Fig. 4.6 b). The required maximum cycle strain value of $1.8 \cdot 10^{-3}$ for symmetric cyclic loading, given in the testing conditions [166], is achieved by loading the model by the prescribed displacement at the top and fixing it at the bottom by the δ layer of nodes (Fig. 4.8 b).

a   b
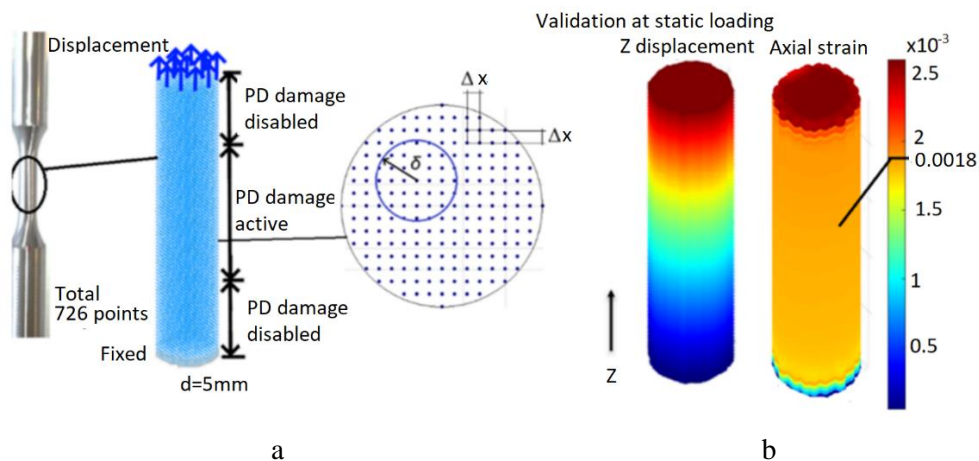
Fig. 4.8 PD model of the 316L stainless steel standard specimen: a – geometry; b – validation at static loading

Initially, the PD model was tested for static loading. Dynamic effects in the PD model were suppressed by artificial damping of $1.6 \cdot 10^4$ kg/s. The fastest static solution, ensuring the correct displacement and strain fields (correctness evaluation is based on a comparison to the analytic solution at a given loading that $u(z) = \varepsilon_z z; \ \varepsilon_z(z) = const.$), is achieved at least of 150 time steps. The in-house cyclic experiments first cycle hysteresis loops from Fig. 3.15 – symmetric cycle loading, Fig. 3.16 – POL loading, segments are used as the 316L steel tensile curves and are displayed in Fig. 4.9.

316L hysteresis loop segment used as tensile curve

$E = 193$ GPa

$\sigma = E\varepsilon$

$\sigma = -0.242 \cdot \varepsilon^{-0.891} + 295$ MPa

$\varepsilon = 0.18$ %

$\varepsilon_p = 0.066$ %

Experimental (±0.18 % cycle)

Experimental (POL specimen)

PD simulated with power approximation

Stress, MPa
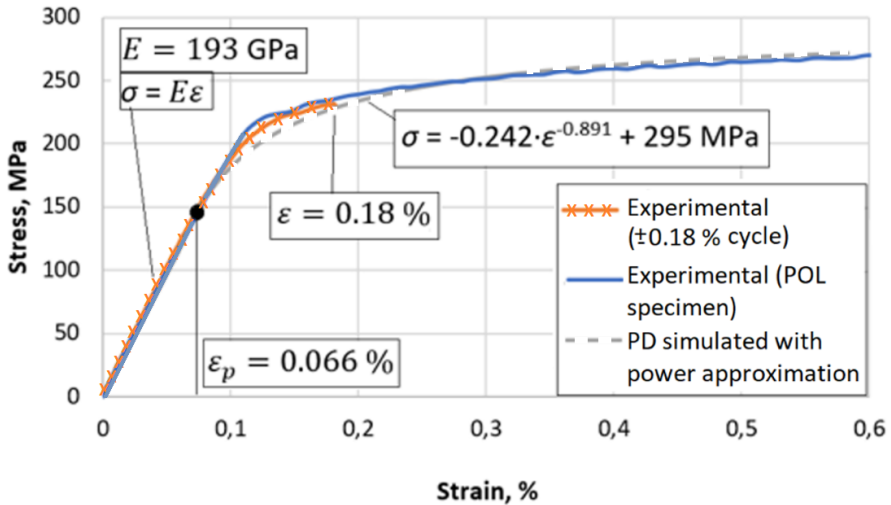
Strain, %

Fig. 4.9 Stainless steel 316L tensile curves

To assess the elasto-plastic behavior of the material, the linear-power law tensile curve approximation is used in the force-stretch and stress-strain relations. Then, the plastic stress region is described as $\sigma = $ -0.242$\cdot\varepsilon^{-0.891} + 295$ MPa, if $\varepsilon > \frac{\sigma_y}{E} = 6.6 \cdot 10^{-4}$. An equivalent material plastic stretch value $s_p = 6.98 \cdot 10^{-4}$ and the *316L* stainless steel critical stretch value $s_c = 8.23 \cdot 10^{-3}$ were found by matching the PD simulated and experimental tensile curves the same way as in the elasto-plastic PD material calibration procedure, as presented in Fig. 4.7.

4.2.1. Symmetric constant amplitude cyclic loading

The PD fatigue model is developed in the static PD model of the standard test specimen by introducing the fatigue crack initiation and crack growth phases. The fatigue failure, predicted from the material S-N curve at a given stress, would occur in the entire model (a virtual specimen) without any initiated cracks since the specimen in the model is perfect, i.e., without any defects. To avoid this problem, a Gaussian distribution of the material's elastic modulus ($E = 193 \pm 3$ GPa, values selected from experimental observations) is used to create a point in the specimen where the strain is maximal (Fig. 4.10 a). At that point, the S-N curve predicts the minimum number of cycles in the entire virtual specimen required for the local material failure (the PD bond failure) to cause a fatigue crack. The material activation energy U and the activation volume γ for the fatigue crack imitation phase are calibrated by using the NUREG/CR-6909 curve [173], as it is shown in Fig. 4.10 b. The σ-N curve, which is essential for calibrating the KTF model, is obtained from the NUREG/CR-6909 ε-N curve. The stresses for the σ-N curve are computed from strains using the material in-house experimental tensile curve, as presented in Fig. 4.9.
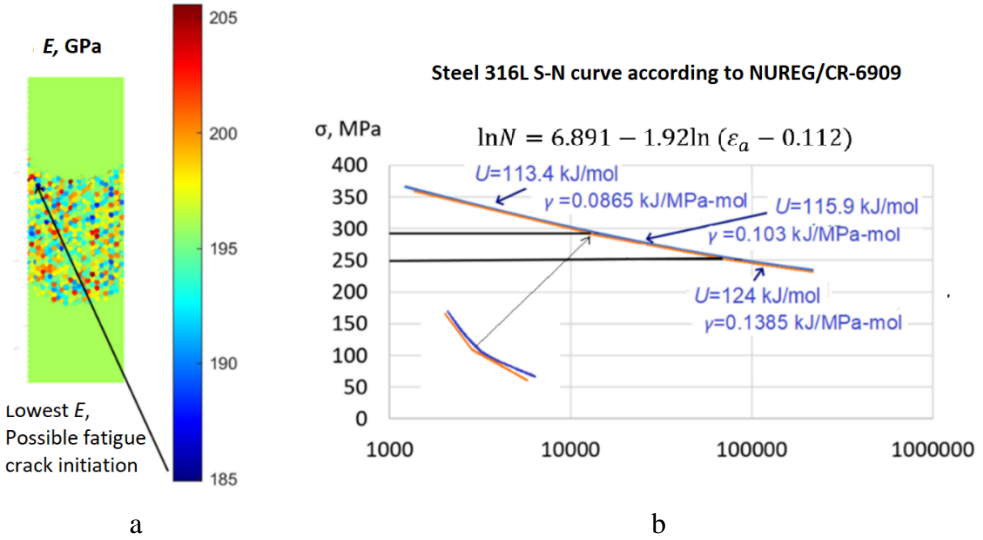
Fig. 4.10 Parameters for the fatigue crack initiation phase: a – probabilistic material elastic modulus distribution to define the crack start position; b – material activation energy U and activation volume γ calibration from S-N curve

For the current PD model and material, the material S-N curve is divided into three-line segments: $\sigma \leq 250$ MPa, 250 MPa $< \sigma \leq 290$ MPa, and $\sigma > 290$ MPa, respectively. This is achieved by choosing such material activation energy U and activation volume γ values which would produce the minimum differences between the fatigue life predicted from the material S-N curve (Fig. 4.10) at the same stress level and the fatigue life calculated by using Eqs. (2.52) and (2.53). The values of U and γ were established by the *Dynamic Time Wrapping* curve matching algorithm [163] applied in the optimization software *LS-Opt*. Although more line segments can be added for better material S-N curve approximation, but the NUREG/CR-6909 curve three-line segment approximation yields $5.02 \cdot 10^{-5}$ remaining area between the curves, expressed in relative units; thus, the approximation accuracy is acceptable. In addition to this, no significant differences between the NUREG/CR-6909 curve and its approximating line segments can be seen in Fig. 4.10.

The fatigue crack growth phase can be started once a fatigue crack is initiated on the virtual specimen's surface. Based on the PD point x damage $\Phi_x \geq 0.5$, this criterion for transitioning from the crack initiation to the crack growth phase is applied. For the fatigue crack growth phase, the activation energy and the activation volume updates as $k_U \cdot U$ and $k_\gamma \cdot \gamma$ can be found from the experimental maximum stress vs. the linear cycle plot, as shown in Fig. 4.11, alternatively to the plot of the crack length vs. the number of cycles. As illustrated in Fig. 4.11, the fatigue crack growth phase, with a duration in cycles of ΔN, begins with an increase of the maximum stress reduction rate. N25 failure [166] is considered as the end of the fatigue crack growth phase criterion in the PD simulation.
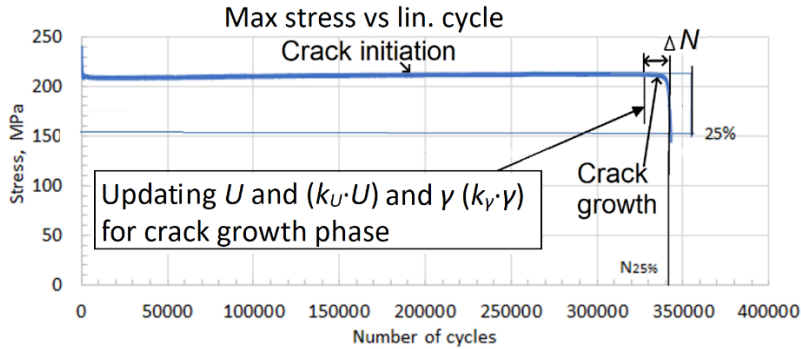
Fig. 4.11 Determination of coefficients k_U and k_γ for the fatigue crack growth phase from the experimental maximum stress vs. linear cycle plot

The values of $k_U = 1.2$ and $k_\gamma = 1$ yield the same number of cycles ΔN in the PD model (Fig. 4.11) as in the experiment when the maximum stress reduction of 25% is achieved. Fig. 4.12 presents the general schematics for symmetric cycle loading when following the PD-KTF modelling sequence.
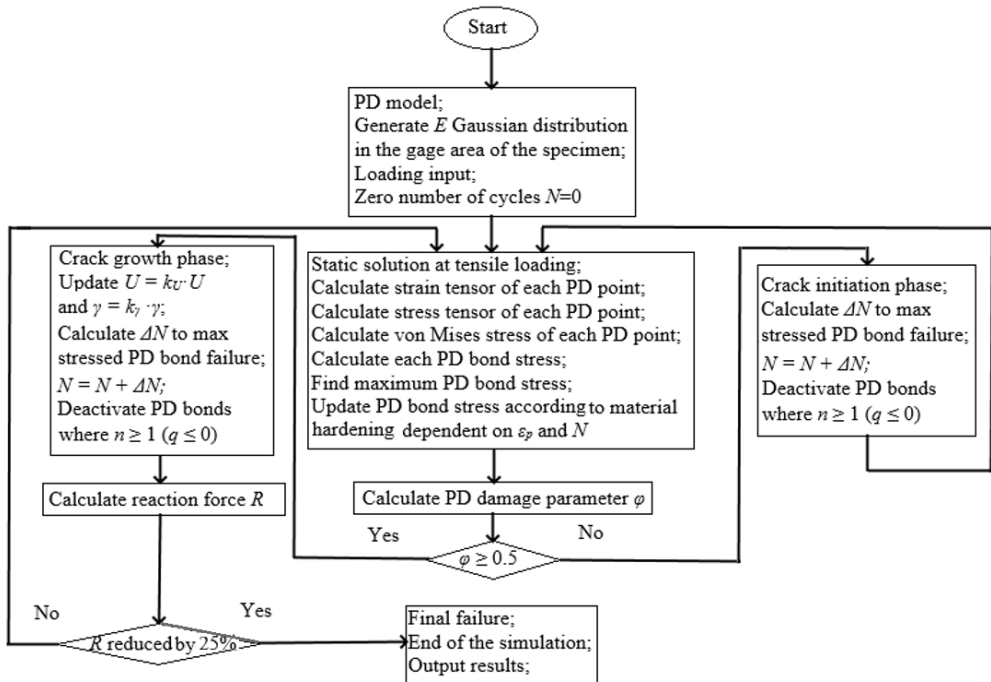
Fig. 4.12. PD-KTF fatigue model schematics for symmetric constant amplitude cyclic loading

4.2.2. Asymmetric variable amplitude cyclic loading

The same PD-KTF modelling methods were applied for asymmetric variable amplitude cyclic loading based on the POL and PUL loading schemes. PD-KTF

103

models were calibrated by using the same symmetric cyclic loading *NUREG/CR-6909* curve. The original KTF (Eq. (2.53) – Eq. (2.54)) resulted in an improper fatigue life prediction for asymmetric cycles with increased R ratios; hence, both standard KTF and improved (Eq. (2.59), Eq. (2.60)) KTF, which account for cycle energy losses, are employed. The cyclic loading process hysteresis loop area refers to the cycle energy losses, and it is logical to apply KTF correction factors proportional to the loading hysteresis loop areas. The proper stress ratios R, the maximum cycle stresses, and the hysteresis loop areas from in-house experimental testing (Fig. 3.15 – Fig. 3.17) of asymmetric cycles were taken into KTF Eq. (2.59), Eq. (2.60) (as it is shown in Fig 4.13) to assess the asymmetric loading effect. The experimental hysteresis loop areas for asymmetric POL and PUL loading cycles differ from symmetric cycles at the same maximum stress loading, as it is illustrated in Fig. 4.13. When considering POL loading, the maximum asymmetric cycle ($R = -1.5$) stress is 230 MPa, and the asymmetric cycle hysteresis loop area is equal to 78% of the symmetric cyclic loading ($R = -1$) hysteresis loop area with the same maximum stress of 230 MPa (Fig. 4.13 a). The same way for asymmetric PUL cycles, the maximum asymmetric cycle ($R = -0.78$) stress is 270 MPa, but such an asymmetric cycle hysteresis loop area is 45% of symmetric cyclic ($R = -1$) with a maximum stress of 270 MPa hysteresis loop area (Fig. 4.13 b).
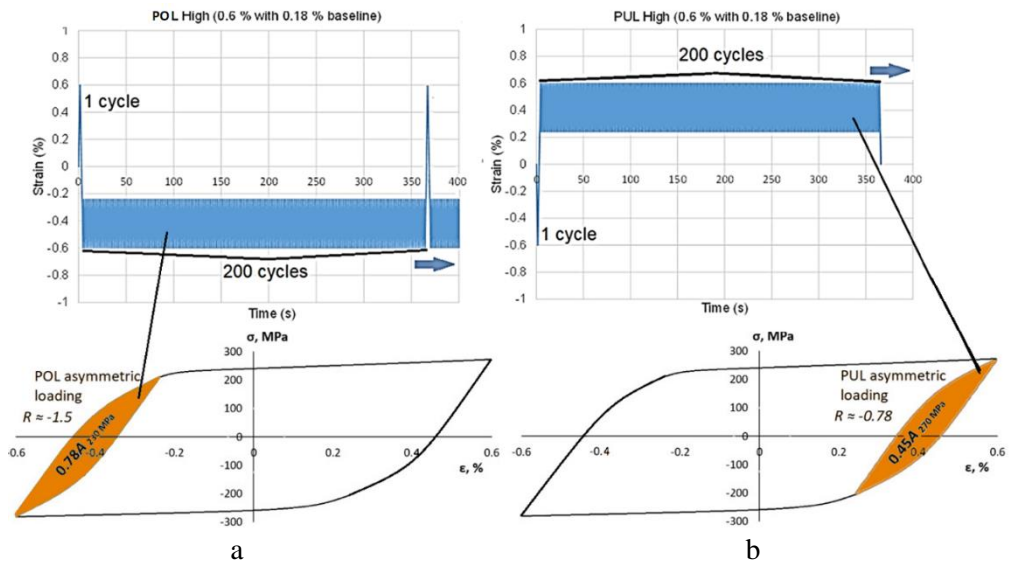
Fig. 4.13 Areas of hysteresis loops measured from the in-house experiment and used for PD-KTF modelling: a – POL loading; b – PUL loading. A_{230MPa}, $A_{270\ MPa}$ refers to hysteresis loops of symmetric cycle and maximum stress of 270 MPa and 230 MPa, respectively

The hysteresis loop area of an average stress of each stress range from Fig. 4.10 is included in the KTF activation energy U and the activation volume γ selection for the modified KTF equation. For example, if $\sigma = 260$ MPa, then the cycle of the average stress $(250+290)/2 = 270$ MPa hysteresis loop area is included, because 260 MPa is

104

positioned in the stress range of 250 ÷ 290 MPa. Based on this approach, three different areas of hysteresis loops as a middle stress of each stress range (210 MPa $<$ $\sigma \leq$ 250 MPa; 250 MPa $< \sigma \leq$ 290 MPa; 290 MPa $< \sigma \leq$ 330 MPa) are used for computations, namely, 230 MPa, 270 MPa and 310 MPa. For the current KTF equation, the term kT in KTF Eq. (2.53), Eq. (2.54) is adjusted to represent the process energy with the hysteresis loop areas as $k(T^* + \psi A)$. Based on Madenci KTF-PD research [86,96], the KTF shape factor $\lambda = 9$ value is selected, yielding KTF Eq. (4.2).

$$
\begin{aligned}
n_{xx'}&(N, \sigma_{max}, R, T, f) \\
&= n_{0xx'} \\
&- \Bigg\{ (n_{0xx'} - n_{Ixx'})^{1-\lambda} \\
&- (1 - \lambda)\frac{\left(k(T^* + \psi A)\right)^2}{h}\frac{N}{\gamma f \sigma_{\max_{xx'}}(1 - R)} e^{-\frac{U}{k(T^* + \psi A)}} \\
&\cdot \left[e^{\frac{\gamma \sigma_{\max_{xx'}}}{k(T^* + \psi A)}} - e^{\frac{\gamma R \sigma_{\max_{xx'}}}{k(T^* + \psi A)}} \right] \Bigg\}^{\frac{1}{1-\lambda}} \quad ; \text{ if } \lambda \neq 1
\end{aligned}
\tag{4.2}
$$

The optimization software *LS-Opt* was employed to calibrate the activation energy U and activation volume γ by using modified KTF Eq. (4.2). The same three stress ranges were used, and U and γ for each stress range are computed by comparing the *NUREG/CR-6909* S-N curve to Eq. (4.2), as it is illustrated in Fig. 4.14.
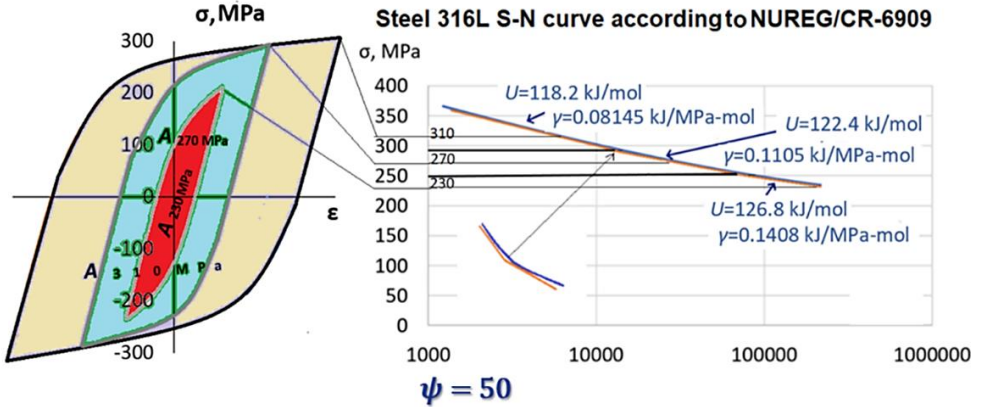
Fig. 4.14 Process activation energy U and activation volume γ calibration for *316L* steel using the updated KTF theory when the cycle hysteresis loop is considered

Through trials and errors, constant $\psi = 50$ was determined by comparing the results of the cyclic experiments with the PD simulation. Multiple calibrations in *LS-Opt* could be performed firstly by establishing the U and γ values for the KTF-PD simulation, and then by running the KTF-PD simulation in *LS-Opt* with the objective to find the constant ψ. Nevertheless, such an approach requires an extremely complex *LS-Opt* setup, is very expensive in terms of the computational time, and is very difficult to implement in practice. Based on this, ψ was selected after manual trials

and errors. Only two experimental results are required to set the constant ψ: one for symmetric cyclic loading, and another for any asymmetric cyclic loading.

Fig. 4.15 demonstrates the modelling schematics for asymmetric variable amplitude cyclic loading, as it is presented for the POL loading. Since the principles of PUL loading are the same, the PUL modelling scheme is not separately provided.
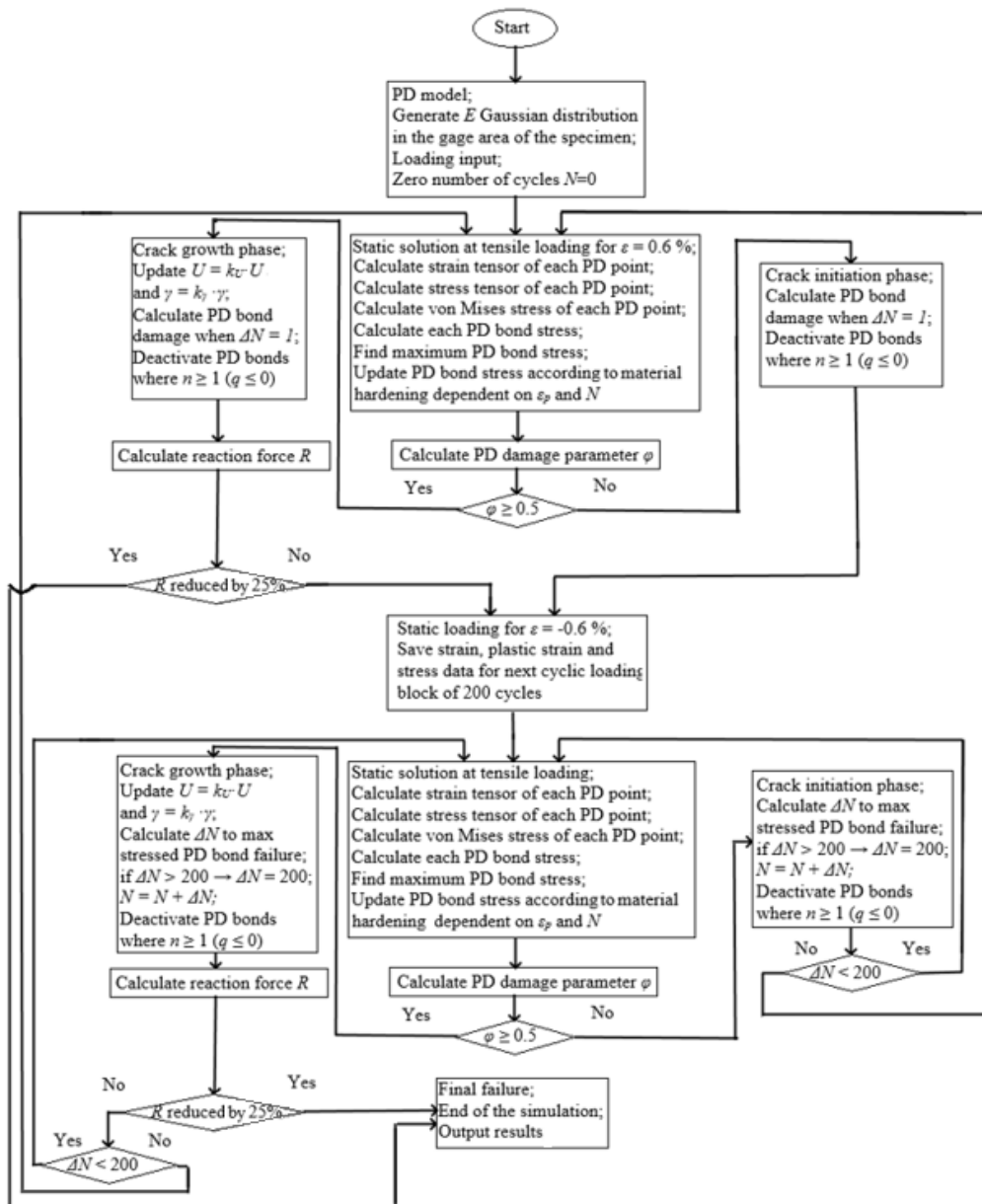
Fig. 4.15 KTF-PD modelling schematics for POL loading (the PUL loading principles are the same)

4.2.3. Comparison of modelling results

Fig. 4.16 is used to compare the experimental and the simulated fatigue lives for symmetric and asymmetric cyclic loading applying both the improved (Eq. (4.2)) and the conventional (Eq. (2.53)) KTF theories. Fig. 4.17 a presents the plots of the simulated PD fatigue crack initiation and growth processes as PD damage plots (ratios of the broken PD bonds to the total PD bonds of each PD point, see Eq. (2.22)). An image of the experimental crack, captured on the test specimen, is shown in Fig. 4.17 b.
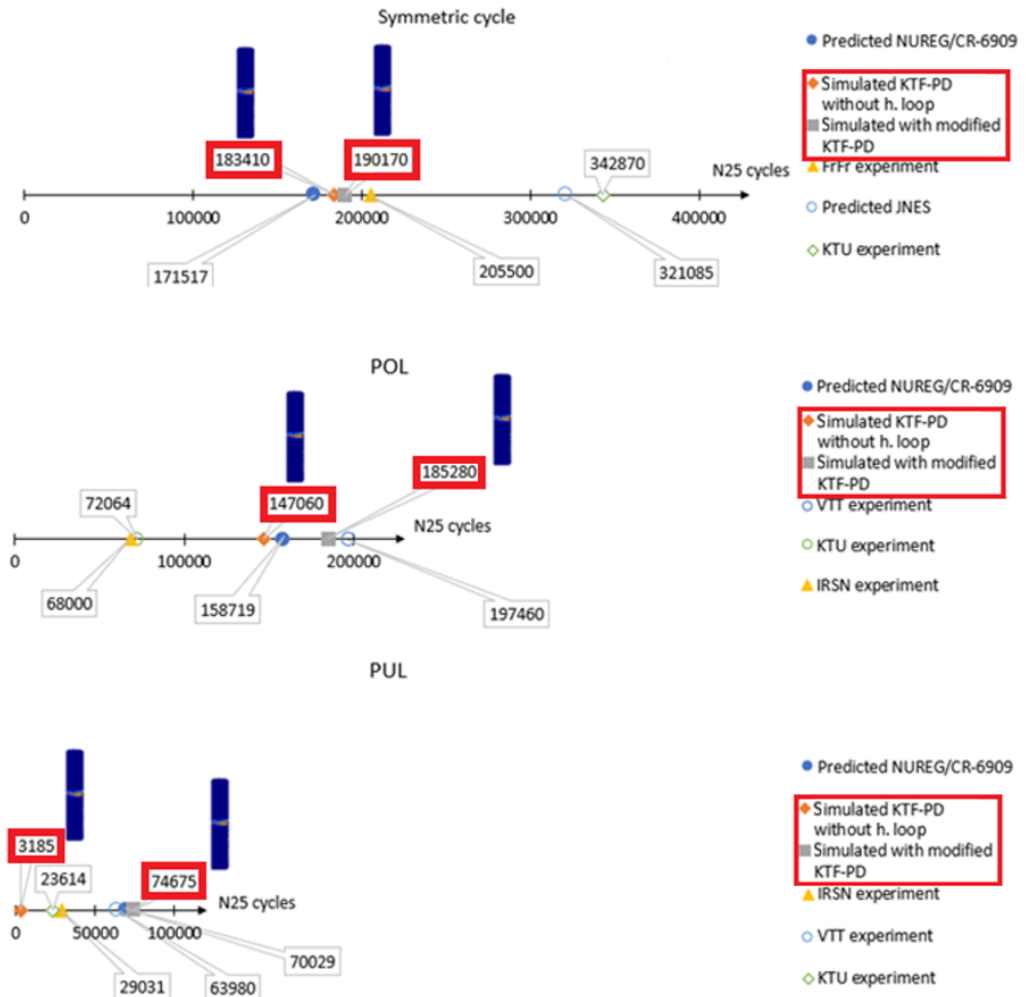
Fig. 4.16 Comparison of experimental (results of tests conducted by other laboratories; sourced from [166]) and KTF-PD simulation results for symmetric ±0.18% strain and asymmetric POL and PUL loadings at room temperature

107
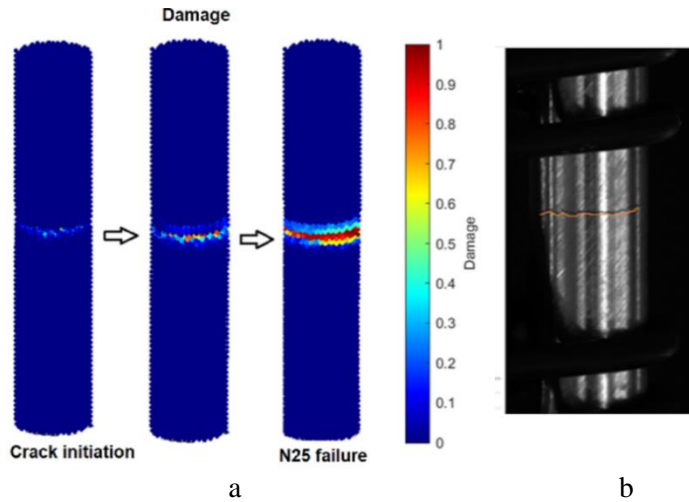
Fig. 4.17 Fatigue damage in *316L* steel specimen comparison: a – simulated fatigue crack; b – fatigue crack captured on the in-house experimental test specimen at N25 failure

The simulated fatigue lives of 183410 cycles (the conventional KTF) and 190170 cycles (the improved KTF) for symmetric ±0.18 % strain cyclic loading (Fig. 4.17) are in accordance with the theoretical prediction of 171517 cycles from the *NUREG/CR-6909* curve and the experimental testing in the *FrFr* laboratory [166] (205500 cycles). Both the conventional and the improved KTF theories (the model is calibrated from the symmetric cycle *NUREG/CR-6909* curve) under the PD framework resulted in a similar number of cycles compared to the asymmetric *NUREG/CR-6909* curve for the POL loading and the VTT laboratory experiment [166] (Fig. 4.17). Nevertheless, better agreement to the POL loading S-N curve predicted result can be achieved by using the conventional KTF (147060 cycles for the conventional KTF, 185280 cycles for the modified KTF, and 158719 cycles for the NUREG curve). In contrast to this, only the modified KTF approach is correct for the PUL loading (Fig. 4.17). While the conventional KTF only forecasts 3185 cycles, the modified KTF predicts 74675 cycles. The simulated result of 74675 cycles is accurate in terms of the NUREG curve for the PUL loading which estimates 70029 cycles, whereas the PUL loading experimental results (Fig. 4.17) vary in the range from 24000 to 70000 cycles.

A review of the experimental and simulation results (Fig. 4.17) shows that the modified KTF, calibrated according to only the symmetric loading S-N curve, predicts the fatigue life for all types of cyclic loads with acceptable for fatigue analysis agreement between the experiment results and the theoretical calculations (represented by the *NUREG CR/6909* curve) leading to average differences of 15%.

4.3. Composite Material Models for Static Loading

Since the fatigue model consists of a set of static simulations under the maximum cycle load, the first step in the cyclic modelling of the composite material is to validate the model under static load.

108

4.3.1. Defect identification in the composite structure using DIC

Based on the detection of defects in the CFRP specimen with the DIC surface strain measurements at tensile loading, as shown in Fig. 3.26, 'Defect 2' characterization with FEMU is analyzed. The FE model of the CFRP specimen only with 'Defect 2' is created in the software *ANSYS Workbench*. The FE model structure and the boundary conditions are shown in Fig. 4.18.

a   b
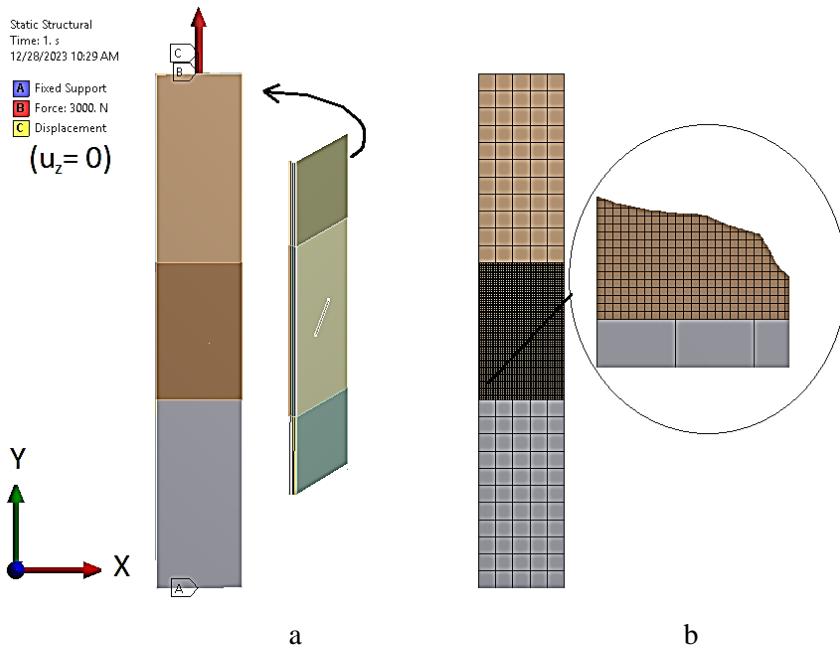
Fig. 4.18 CFRP specimen with 1.5 mm depth groove FE model in ANSYS: a – boundary conditions; b – FE mesh

The CFRP specimen model (Fig. 4.18 a) consists of 6 composite layers per thickness, whereas each layer has a thickness of 0.333 mm. The composite FE model SHELL formulation is not valid for any depth material defect (e.g., a defect depth of 1.5 composite layer thickness). To overcome this issue, the CFRP specimen is modelled with SOLID elements defining each composite layer as a separate body with a separate anisotropic material (Fig. 4.18 a). The loading of the virtual specimen, shown in Fig. 4.18 a, is the same as in the experiment: the bottom of the specimen is fixed, while the top of the specimen is constrained in the Z direction and loaded by 3000 N force in the Y direction. Due to the small material defect (a groove width of 1 mm), an extremely small FE mesh is required in the defect zone, and a fine mesh elsewhere is not suitable in order to reduce the computational time. The virtual specimen is divided into the defect zone with a uniform square FE mesh of 0.5 mm, and a 5 mm-sized FE mesh is used in the other zones of the specimen, as it is shown in Fig. 4.17 b. The contact type 'Bonded' is set between all the bodies in the model.

The definition of the material properties of each CFRP specimen body is based on the tensile experimental tests of the CFRP specimens without defects, cut at 0º and

45° angles from a composite plate. The specimen layup configuration of [(0/90)°/90°/0°]s and an effective elastic modulus of the specimen in the tensile direction of 78 GPa suggest that we should use a similar value for the elastic modulus of the virtual specimen's composite material in the fiber direction. The elastic material's modulus transverse to the fiber direction and the shear modulus are determined from the tensile curve of a specimen featuring a 45° cut angle. After several iterations of the manual selection of the material properties, the established material's elastic constants for the current FE modelling are given in Table 4.4.

Table 4.4. CFRP specimen material properties used in the ANSYS model

Layers 1, 6		Layers 2, 5		Layers 3, 4	
E_x, GPa	75	E_x, GPa	75	E_x, GPa	5
E_y, GPa	75	E_y, GPa	5	E_y, GPa	75
E_z, GPa	5	E_z, GPa	5	E_z, GPa	5
G_{xy}, GPa	4	G_{xy}, GPa	4	G_{xy}, GPa	4
G_{yz}, GPa	1	G_{yz}, GPa	1	G_{yz}, GPa	1
G_{xz}, GPa	1	G_{xz}, GPa	1	G_{xz}, GPa	1
v_{xy}	0.2	v_{yx}	0.012	v_{xy}	0.012
v_{yz}	0.4	v_{yz}	0.4	v_{yz}	0.4
v_{xz}	0.4	v_{xz}	0.4	v_{xz}	0.4

The material stiffness to the interlaminar direction is set the same as transverse to the fiber direction. The values of the in-plane Poisson's ratio are chosen based on the literature [174] and the in-house DIC measurements. Once the specimen surface strain field shown in Fig. 3.26 has been computed in *VIC-3D*, the average of the transverse and longitudinal strains ratio was found to be equal to 0.05. The specimen surface layers with a fiber direction of 0/90° is close to the isotropic material, and thus their Poisson's ratio should also be similar to the isotropic carbon fiber Poisson's ratio of 0.2÷0.3 given in the ANSYS database of materials. The Poisson's ratio of the unidirectional carbon fiber layers is selected in such a way that an average Poisson's ratio of the virtual specimen would be equal to the Poisson's ratio of 0.05 measured by DIC. Based on this assumption, a Poisson's ratio value of 0.2 for the surface layers and $v_{xy} = 0.012$ for the internal 3, 4 layers, $v_{yx} = 0.012$ for the internal 2, 5 layers were established. The current setup of the material properties ensure an effective elastic modulus of the virtual specimen with a layup of [(0/90)°/90°/0°]s 78 GPa and 15 GPa for a layup of [(±45)°/-45°/45°]s equal to the values found from in-house experiments. The effect of different interlaminar stiffness and interlaminar Poisson's ratio values to the virtual specimen deformation was not significant for the current FE model.

Moreover, the determination of the composite material failure parameters was not necessary for this FE model because no damage occurred for the current loading.

The selected strain control points on the surface of the experimental and the virtual specimens for defect description are shown in Fig. 4.19 a. Since the defect location and shape can be initially evaluated directly from the strain field shown in Fig. 4.19 a, the defect depth remains an unknown parameter (P12 in ANSYS, see Fig. 4.19 b). Nevertheless, the defect depth can be found by using the *FEMU* algorithm. The 'Seek target' optimization option was used to ensure that the FE model in the ANSYS strains would be equal to the DIC measured strains at the points P12, P13, P14.

a

b

Fig. 4.19 Defect characterization in the CFRP specimen with DIC-FEMU: a – the selected strain control points on the specimen surface; b – the optimization result where the defect depth has been found

The accuracy of the defect shape definition according to Fig. 4.19 is sufficient for the present application. This conclusion is based on the statement that, in a further modelling task of the CFRP specimen (Fig. 3.25), the sharp contours of cracks cannot be defined by uniform PD grid spacing [9]; rather, they are included as missing PD bonds. Opposingly to FE, where the mesh is refined at the crack regions, no PD grid refinements are used or even required; thus, the defect geometry in the PD models cannot be very precise. The aforementioned procedure is also not possible to be implemented directly into the PD model due to difficulties involving the complex geometry description in the in-house-developed PD code.

Three possible defect depths were found with the ANSYS optimization (Fig. 4.19 b), although 'Candidate Point 1' has the highest strain values agreement at points P12 and P14 and can be treated as the only possible defect depth. The strain

equilibrium was mostly satisfied at the control strain point P12 (Fig. 4.19 b), while, for point P13, the FE strains were two times higher than the experimental ones. Nevertheless, the groove depth in the CFRP specimen of 1.53 mm found by FEMU is very close to the real depth of 1.5 mm (with a relative error of 1.8%); thus, the proposed method can be validated for the detection of defects in composite materials. A comparison of the experimental (DIC) and ANSYS simulated specimen surface strain fields is given in Fig. 4.20.
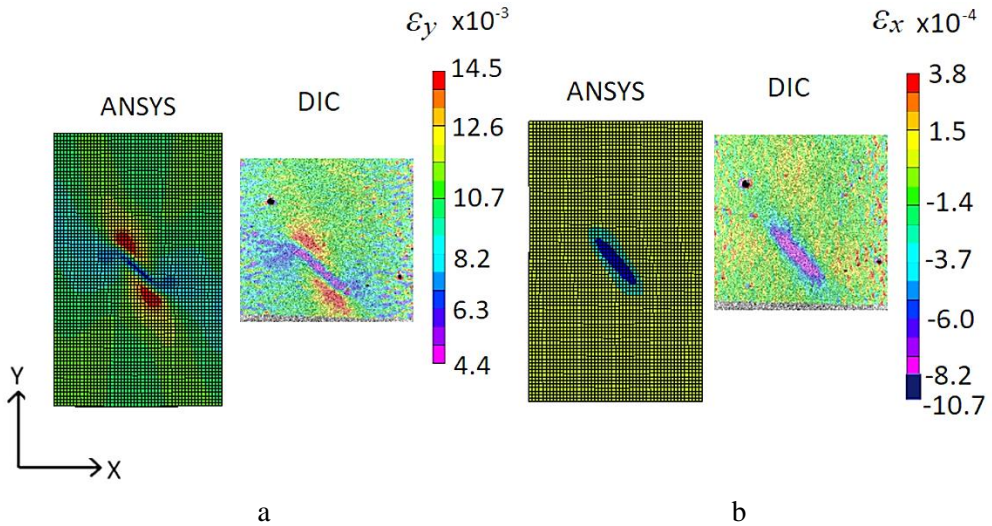
Fig. 4.20 Experimental and ANSYS simulated CFRP specimen with 1.5 mm depth groove surface strain fields: a – tensile direction Y; b – transverse direction X

The coincidence of both the color and the shape can be observed in the ANSYS simulated and experimental DIC strain fields, thereby validating the FE model of the CFRP specimen. Nevertheless, some strain differences at the defect center were found to exist. For the case of the longitudinal strain, the minimum DIC tensile strain was determined to equal $\varepsilon_{y\_min} = 4.4 \cdot 10^{-3}$, while ANSYS simulated a value of $\varepsilon_{y\_min} = 8.2 \cdot 10^{-3}$. Similarly, for transverse strains, $\varepsilon_{x\_min} = -8.2 \cdot 10^{-3}$ for DIC and $\varepsilon_{x\_min} = -10.7 \cdot 10^{-3}$ for ANSYS was obtained. The differences are mostly due to the high strain gradients at the center of the defect, and the FE mesh should be even finer to precisely capture those strain gradients. On the other hand, this example illustrates that the control strain points should be selected not at the high strain gradients zones, but away from the defect (e.g., P12 or P14) in order to characterize the defects by FEMU.

To analyze the accuracy of the proposed DIC-FEMU defect detection method, a control point P12 (Fig. 4.19) Y direction strain vs. the defect bottom depth from the non-defective specimen surface (on which strains are measured with DIC) is plotted in Fig. 4.21. It should be noted that the X axis of the plot in Fig. 4.21 does not show the depth of the defect (a milled slot), and the defect depth from the surface is calculated as the CFRP specimen's thickness minus the crack depth.

From the numerical analysis results presented in Fig. 4.21, it can be seen that the Y direction strain at the control point P12 is inversely proportional to the defect

depth from the specimen's surface with the 4th order relation.
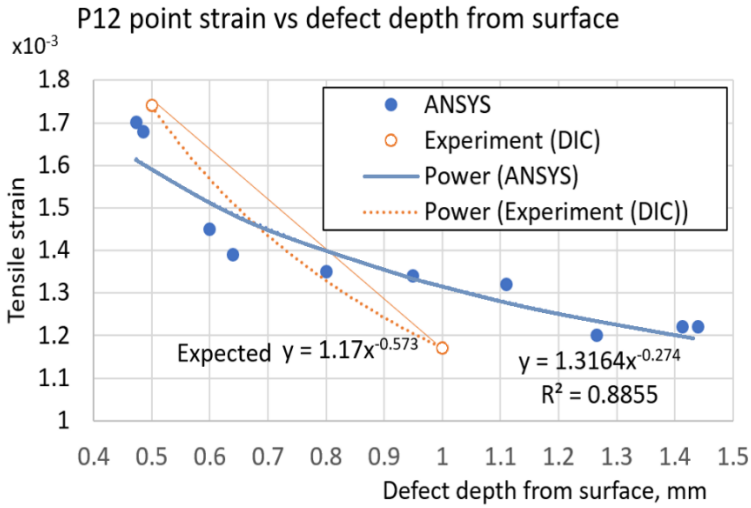
Fig. 4.21 Control point P12 *Y* direction strain dependence on the defect distance from the surface on which strains are measured

The experimental DIC strain measurements of the specimen's defect 1 and defect 2 is expected to have an almost inverse square proportionality ($y = 0.0012x^{-0.537}$), although more data points in Fig 4.21 are necessary to confirm such a relation. Strain differences between ANSYS and DIC increase with the defect depth from the specimen's surface (for a depth of 0.5 mm – the strain difference was 2.2%, for a depth of 1 mm – the difference of up to 14% was determined). From the current data, as presented in Fig. 4.21, it can be concluded that the proposed DIC-FEMU defect detection method is accurate regarding defects up to 0.8 mm from the surface on which the strains are being measured. The defects analysis was performed for a defect with a width of 30% of the specimen's width. Moreover, it is worth noting that the differences in the material properties and geometry, the loading conditions (a possible specimen misalignment in the testing machine for the current case), DIC measurement errors are determining the accuracy of the DIC-FEMU defect detection method.

4.3.2. PD composite models

A CFRP composite specimen with a defect is modelled by using BBPD composite formulation with PD bond rotation for each composite layer. The connection between the composite layers is made by interlaminar PD bonds without the rotation feature. The purpose of such model is its final application for the KTF-PD based fatigue analysis. Nevertheless, the model should be firstly calibrated for the case of static loading.

Only a specimen with a 45 mm long defective fragment is modelled, and the PD model consists of 75 nodes per specimen width (Fig. 4.22). The PD grid spacing $\Delta x = 0.33$ mm and the PD horizon size $\delta = 3.1 \Delta x$ are set. An accurate PD grid is selected to describe the defect geometry as accurately as possible. The defect in the

virtual specimen is evaluated as missing PD points in the defect zone in the specimen. PD bond damage is deactivated at the boundaries of the model so that to prevent a false static and cyclic failure (Fig. 4.22).
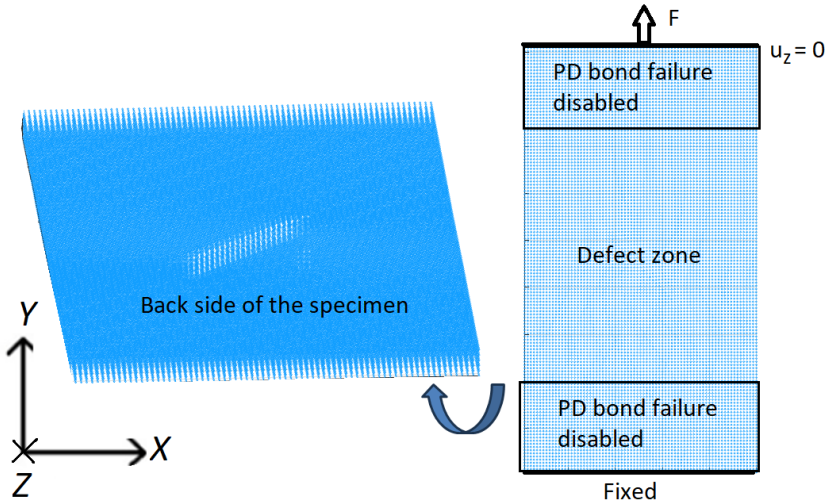
Fig. 4.22 PD model of the CFRP specimen with a defect

The boundary conditions of the PD model are identical to those used for the CFRP specimen FE model in ANSYS. The bottom of the specimen is completely fixed, while the top of the specimen is fixed in the Z direction and loaded by the external force F in the Y direction (Fig. 4.22).

For the composite BBPD with the rotation model, four different types of PD bonds must be defined, namely: fiber, matrix, interlaminar normal, and interlaminar shear bonds. As the PD bond definition depends on the PD bond direction, the vector is $\xi_{xx'} = [X_{x'} - X_x; Y_{x'} - Y_x; Z_{x'} - Z_x]$, and components are employed to identify the PD bond direction. For example, if the fiber in the current composite layers is oriented in the Y direction, then:

1. if $Z_{x'} - Z_x = 0$:

1.1. if $X_{x'} - X_x = 0$; it is the fiber bond;

1.2. otherwise, it is the matrix bond;

2. if $Z_{x'} - Z_x \neq 0$:

2.1. if $(X_{x'} - X_x)(Y_{x'} - Y_x) = 0$; it is the normal interlaminar bond;

2.2. otherwise, it is the shear interlaminar bond.

The procedure in *MATLAB* is implemented by using the 'if' conditions, and it is applied to each of the composite layers. A similar code is necessary to determine the surface correction coefficients for fiber bonds in the BBPD with rotation composite model. The *MATLAB* code for the definitions of the [(0/90)°/90°/0°]s and [(±45)°/-45 °/45°]s layups composites PD bonds is given in Appendix A.

Once the CFRP specimens of the PD model have been created in *MATLAB*, its material properties and failure parameters should be established. The stiffness values

114

of the composite layer in-plane PD bonds can be computed according to Eq. (2.89) – Eq. (2.91), while, for interlaminar PD bonds, Eq. (2.81) – Eq. (2.83) can be applied. This refers to the elastic constants of five different PD bonds, in the *MATLAB* code defined as: C_MAT1 – the fiber bond stiffness; C_MAT2 – the matrix bond stiffness; C_MAT3 – the normal interlaminar bond stiffness; C_MAT4 – the shear interlaminar bond stiffness; D_MAT2 – the matrix rotational bond stiffness. Moreover, PD failure parameters, namely, the critical stretch for the fiber, matrix and interlaminar PD bonds, the critical rotation angle for the matrix PD bonds must be defined. Based on the calibration of the PD model parameters for an isotropic material, the calibration approach is applied for the current PD composite model.

Firstly, the CFRP specimen's PD model is calibrated for the elastic behavior only. The calibration procedure is also performed in the optimization software *LS-Opt*. The five aforementioned PD bond stiffness constants (C_MAT1 – C_MAT4, D_MAT2) are included directly into optimization in *LS-Opt*. PD Equations (Eqs. 2.80–2.82), and (Eqs. 2.88–2.90) are used to determine the starting value of the PD bond constants. As the material model is complex, and as the effect of each parameter on the PD model is not known, wide optimization ranges C_MAT1- C_MAT4, D_MAT2 are used for each parameter. The optimization range limits for each PD parameter are also computed from Equations (Eqs. 2.80–2.82), and (Eqs. 2.88–2.90) while taking the limit values of the fiber elastic modulus (E_MAT1), the transverse to fiber direction elastic modulus (E_MAT2), the Poisson's ratio v_{12} and in the plane shear modulus G_{12}, as given in Table 4.5. The resultant optimization ranges and starting values of the PD parameters in *LS-Opt* are shown in Fig. 4.23.

Table 4.5. Definition of the intervals of material CCM elastic constants for PD parameters

Parameter	Min	Starting	Max
Elastic modulus in fiber direction E_MAT1, GPa	20	80	120
Elastic modulus transverse to fiber direction E_MAT2, GPa	0.1	1	20
Poisson's ratio v_{21}	0.1	0.2	0.48
In-plane shear modulus G_{12}, GPa	0.1	2	10

Problem global setup

| Parameter Setup | Stage Matrix | Sampling Matrix | Resources | Features |

☐ Show advanced options

Type		Name	Starting	Minimum	Maximum
Continuous	∨	C_MAT1	1.306e24	1.562e22	2.061e24
Continuous	∨	C_MAT2	1.13e23	7.386e21	2.8e23
Continuous	∨	C_MAT3	1.29e23	0	4.65e24
Continuous	∨	C_MAT4	1.465e17	7.327e15	1.4e18
Continuous	∨	D_MAT2	4.785e21	2.24e20	5.77e22

Fig. 4.23 PD composite bonds parameters C_MAT1 – C_MAT4, D_MAT2 in *LS-Opt* for the calibration of the composite PD model elastic behaviour

Since the PD model of the CFRP specimen, shown in Fig. 4.22, takes about 20 minutes to compute, it cannot be used for the calibration of the parameters. To overcome this issue, a PD model fragment of 15 points per width, 45 points per length, and 6 points per thickness with the same PD grid spacing and PD horizon size was created and used for calibration. This yielded 15 times fewer PD points compared to the PD model shown in Fig. 4.22, and the computational time is reduced 10 times. This PD model boundary conditions are identical to those described in Fig. 4.22.

Two consistent PD simulations of a specimen with a layup of [(0/90)°/90°/0°]s and [(±45)°/-45°/45°]s are run in the single *MATLAB* code, used for calibration in *LS-Opt* (Fig. 4.24). During the first simulation of [(0/90)°/90°/0°]s CFRP specimen, the specimen is loaded by a tensile force of 8000 N (resulting in 800 MPa tensile stress from the tensile curve, as shown in Fig. 3.19), and the tensile strain ε_{PD_0} is computed. During the second PD simulation, a specimen of a layup of [(±45)°/-45°/45°]s is loaded by 2000 N tensile force, and the tensile strain ε_{PD_45} is computed. Since the calibration is performed only for elastic PD bond constants, the PD failure is disabled to all PD bonds. Then, the optimization objective *STRAIN* for *LS-Opt* tasks is defined as the sum of the absolute differences between the PD computed strains $\varepsilon_{PD\_0}, \varepsilon_{PD\_45}$ and the experimental $\varepsilon_{exp\_0} = 1.03 \cdot 10^{-3}$, $\varepsilon_{exp\_45} = 1.32 \cdot 10^{-3}$ strains computed according to the effective stiffness of the CFRP specimens at the same loading as in PD simulations:

$$STRAIN = \left|\varepsilon_{PD\_0} - \varepsilon_{exp\_0}\right| + \left|\varepsilon_{PD\_45} - \varepsilon_{exp\_45}\right| \tag{4.3}$$

The optimization task is to minimize the parameter *STRAIN* resulting minimum differences between the PD simulation and the experimental effective stiffness for both [(0/90)°/90°/0°]s and [(±45)°/-45°/45°]s layup configuration specimens. The termination criterion of 10 iterations is used. Automatic variables range reduction for each iteration ('Domain reduction' in Fig. 4.24) is included. The general calibration setup in the *LS-Opt* window is shown in Fig. 4.24.
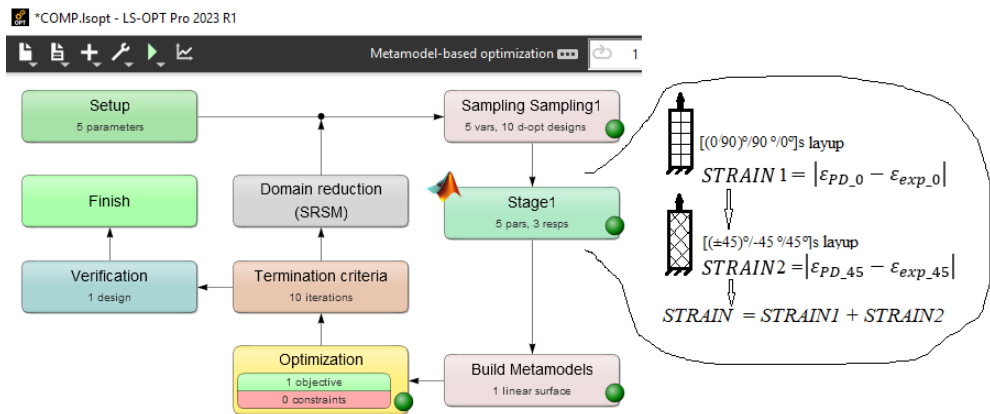
Fig. 4.24 BBPD with rotation composite model calibration setup in *LS-Opt*

After 10 optimization iterations, the optimization objective of 0.0037 was achieved in *LS-Opt*. The elastic characteristics of the calibrated PD composite model

116

are given in Table 4.6. The whole calibration procedure took about 6 hours of computational time.

Table 4.6. Calibrated stiffnesses of composite PD bonds

Parameter	Value
Fiber bond stiffness C_MAT1, GPa/m^4	$1.91 \cdot 10^{23}$
Matrix bond stiffness C_MAT2, GPa/m^4	$8.25 \cdot 10^{22}$
Normal interlaminar bond stiffness, C_MAT3, GPa/m^4	$3.93 \cdot 10^{24}$
Shear interlaminar bond stiffness, C_MAT4, GPa/m^4	$4.89 \cdot 10^{16}$
Matrix bond rotation stiffness D_MAT2, GPa/m^4	$2.39 \cdot 10^{22}$

After calibrating the PD composite model elastic constants, the next step is to select the PD failure parameters. Three different failure parameters are used for the current PD model: the fiber bonds critical stretch s_{fc}, the matrix bonds critical stretch s_{mc}, and the matrix bonds critical rotation angle γ_{mc}. The interlaminar bonds failure in this PD model is determined by a critical stretch equal to the matrix bonds critical stretch s_{mc}. The selection of different PD composite model failure parameters leads not only to differences in the experimental and PD simulated tensile curves, but also to different failure modes of the virtual specimen. A comparison of failure modes between the experimental and the virtual specimens cannot be performed in *LS-Opt*; it can only be done manually. Based on these observations, the PD failure parameters were manually selected, as described further.

The values of the fiber and matrix critical stretch $s_{fc} = s_{mc} = 0.0085$ and the critical matrix bonds rotation angle of $\gamma_{mc} = 0.012$ leads to acceptable agreement between the experimental and the PD simulated tensile curves for [(0/90)º/90 º/0º]s and [(±45)º/-45 º/45º]s layup specimens (the maximum differences between the stress values are 13%) as well as failure modes. Comparisons between the experiment and PD simulation results are shown in Figs. 4.25–4.26.

CFRP specimen tensile diagrams

— 0º experiment ([(0/90)º/90º/0º]s)
---- 0º PD simulation ([(0/90)º/90º/0º]s)
-- 45º experiment ([±45º/-45º/45º]s)
— 45º PD simulation ([±45º/-45º/45º]s)
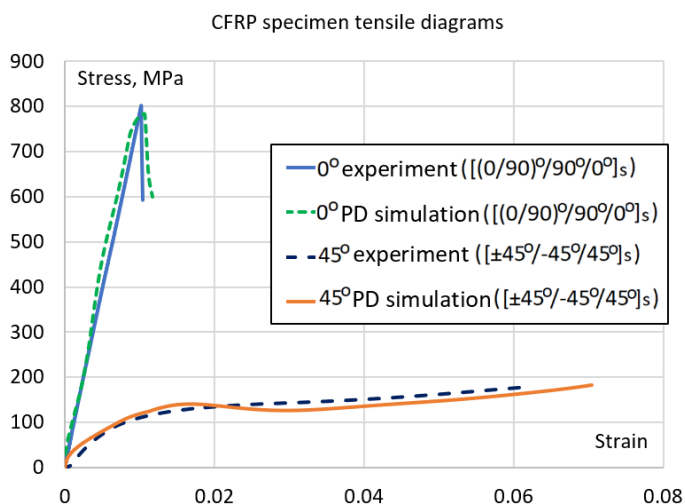
Fig. 4.25 BBPD with rotation CFRP composite specimen model and experimental tensile curves comparison for both [(0/90)º/90º/0º]s and [(±45)º/-45 º/45º]s layups
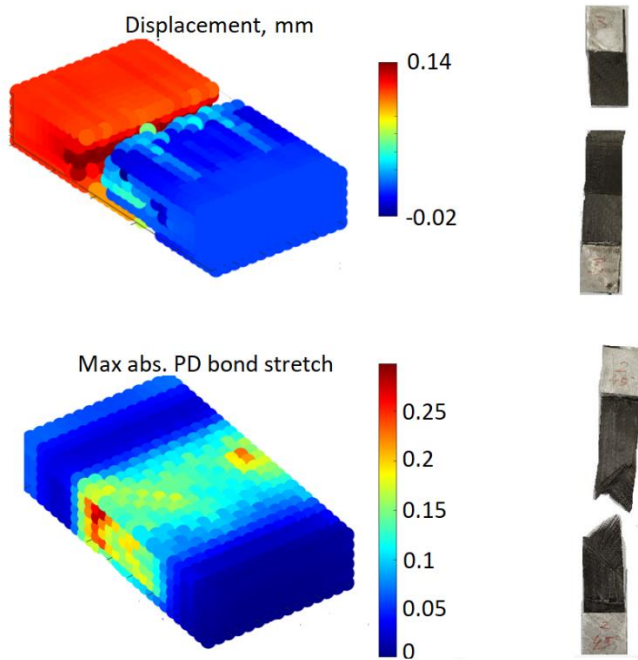
Fig. 4.26 BBPD with rotation CFRP composite specimen model and experimental failure modes comparison: a – specimen [(0/90)°/90°/0°]s layup, where the simulated failure is visible on the displacement plot; b – specimen [(±45)°/-45 °/45°]s layup, where the simulated failure is visible on the PD stretch plot

In case of [(0/90)°/90 °/0°]s layup specimen (Fig. 4.25, Fig. 4.26 a), agreement between the simulation and the experimental tensile curves is observed in Fig. 4.25, although the PD model is slightly less stiff than the real specimen. The same failure type of the experimental and the virtual specimens can be seen in Fig. 4.26 a. Despite the recommendation provided in the literature [120] to suppress the PD fiber bonds failure, the fiber failure is still visible during the experimental failure (Fig. 4.26 a); thus, the failure of fiber bonds is enabled in the current PD model of the [(0/90)°/90°/0°]s layup specimen to replicate the experimental failure behavior. The critical fiber bonds stretch s_{fc} has the highest effect on the simulated specimen failure mode shown in Fig. 4.26 a as well as the agreement between the tensile curves (Fig. 4.25). For the case of [(±45)°/-45 °/45°]s layup specimen, a failure due to a shear occurs, and the fiber bonds breakage in the PD model can be disabled. The selection of the critical matrix bonds rotation angle of $\gamma_{mc} = 0.012$ has a major effect on the agreement between the tensile curves and the failure modes, as shown in Fig. 4.25 and Fig. 4.26 b. The simulated specimen is slightly stiffer than the experimental one, as it is visible in Fig. 4.25. The shear failure mode, replicated in the virtual specimen, is visible the clearest on the absolute PD bonds stretch plots as the increased PD bond stretch values (Fig. 4.26 b). Nevertheless, some differences between the experimental and the simulated tensile curves in Fig. 4.25 are generated by dynamic effects in the

PD model which are difficult to completely dampen for the composite PD model. Moreover, the fixed composite in the plane shear modulus G_{12} value leads to the remaining differences between the experiment and the simulation, especially for the $[(\pm 45)/-45/45]°$ s layup specimen.

4.4. Composite PD Model for Cyclic Loading

After developing the PD composite specimen model and calibrating it for elastic deformations and failure behavior, the final step in PD modelling is the composite cyclic model based on KTF. The same PD model, as the one shown in Fig. 4.22, is used for the fatigue analysis of the CFRP specimen with a defect: 1 mm width and 1.5 mm depth milled slot (Defect 2 in Fig. 3.26). Since no special test program is used, a symmetric cyclic tensile load of 6000 N is applied for fatigue simulation.

According to Madenci [143], the effective stress value, computed from the normal to fiber stresses σ_{22} and shear stresses τ_{12} as $\sigma_{ef} = \sqrt{\sigma_{22}{}^2 + \tau_{12}{}^2}$ should be used for composite fatigue analysis under the KTF-PD approach. It is assumed that the cyclic matrix bonds failure rather than the cyclic fiber failure occurs. This statement is valid for low stress levels (see Chapter 1.1) and can be taken for the current PD model according to the loading of a force of 6000 N. Then resulting effective stresses at maximum 6000 N tensile loading are plotted in Fig. 4.27 and further used for the KTF fatigue damage equation.
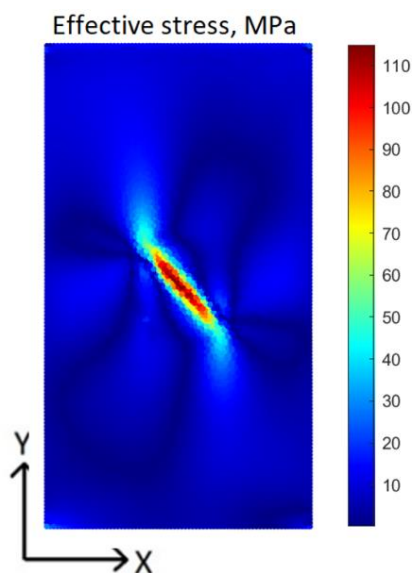
Fig. 4.27 PD simulated effective stress field on the CFRP specimen's surface with a defect under 6000 N tensile loading

The KTF activation energy U and the activation volume γ values could be directly calibrated from the S-N curve of the CFRP composite. Although no such calibration was performed, the PD fatigue model can still be run, and the defect growth can be simulated, as shown in Fig. 4.28.
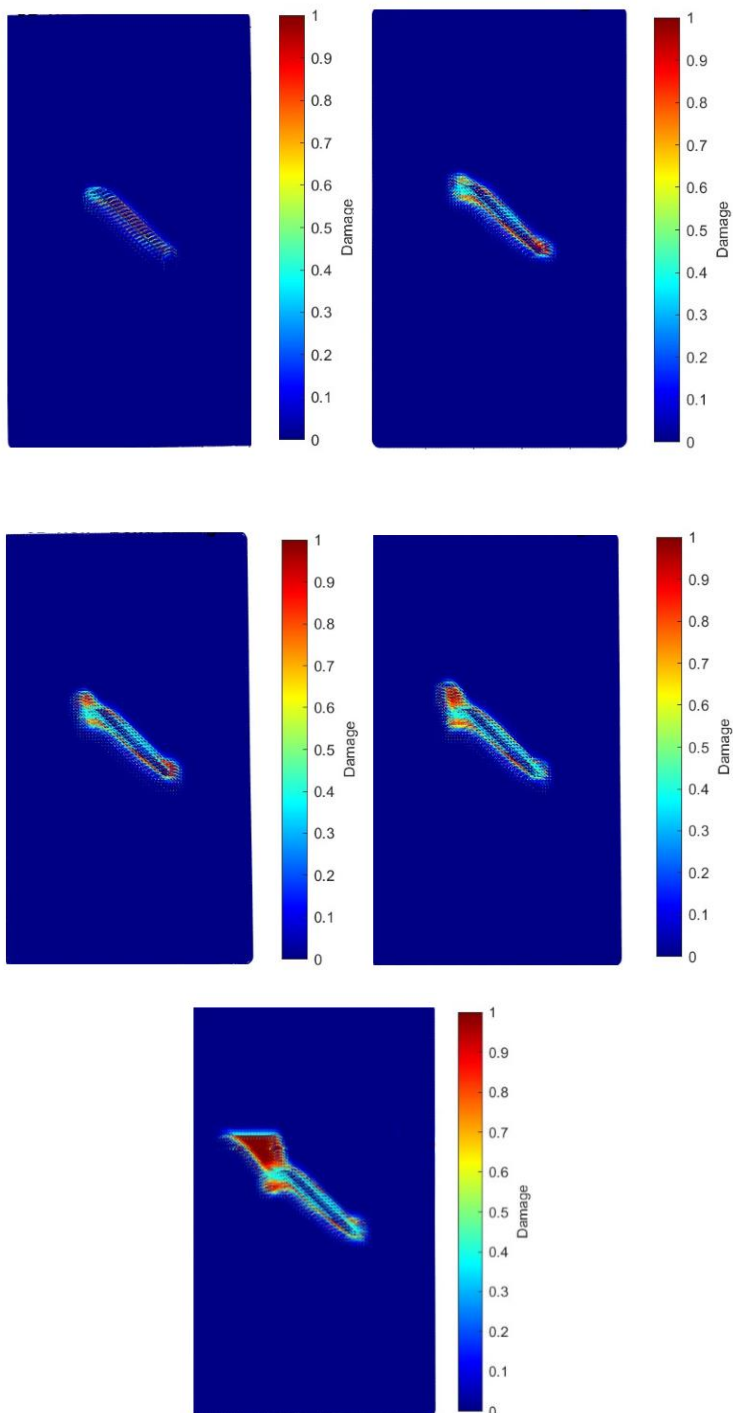
Fig. 4.28 Simulated defect growth in the CFRP specimen shown on PD bond damage plots

The PD damage plots, as shown in Fig. 4.28, were generated after one week computation of the created KTF-PD model. It is visible that the material defect grows with the number of cycles leading to the failure of the specimen. Once the model has been calibrated from the composite material's S-N data, it can be applied for this composite material, and the fatigue life can be predicted.

5. CONCLUSIONS

1. Replacement of the DIC strain computation algorithm by PDDO reduces the noise in strains. The noise filtering effect is demonstrated on a tensile specimen with a circular hole strain field computed by PDDO from a noisy DIC displacement field. The DIC-PDDO method is able to reduce the noise in strains and does not filter out the strain peaks. Such a reduction in the strain field noise is impossible to achieve by using the conventional DIC algorithm. Moreover, the DIC-PDDO method increases both the measurement and the spatial strain resolutions shown on a 1.34-times lower metrological efficiency indicator value compared to the conventional DIC. DIC-PDDO is effective for localized strains, such as a material defect, or crack detection with DIC.

2. The PD critical stretch calibration is performed based on DIC surface strain measurements and done in the optimization software *LS-Opt* achieving an average optimization objective value of 0.025. Such a procedure circumvents complex experimental testing of material fracture toughness and increases the accuracy of the PD model by the accurately selected critical stretch value. Moreover, the proposed calibration procedure simplifies the selection of the parameters of complex PD material models, such as composites, SBPD, non-linear materials, etc.

3. After introducing process energy correction coefficients, based on the cycle hysteresis loop area (the areas were measured from experimental testing), the KTF model, calibrated from the S-N curve for symmetric cyclic loading only, yielded the correct predicted fatigue life for both symmetric and asymmetric cyclic loading. Average errors of 15% between the experiment and the simulation were obtained by comparing symmetric, asymmetric $R = -1.5$ and $R = -0.67$ variable amplitude *316L* steel cyclic tests results. In addition to this, the PD theory enables to simulate the fatigue crack initiation and growth phases without any predefined crack paths.

4. Cracks in composite structures can be identified from the structure surface strain field measured by DIC under static loading, as it was demonstrated on CFRP composite tensile specimens with 1 mm-wide milled slots. The defect depth in the structure was determined by the FEMU algorithm in the ANSYS software with a relative error of 1.8%. Cracks of 30% width of the structure being up to 0.8 mm depth from the structure surface can be detected even by using the conventional DIC strain computation algorithm. For the case of delamination, a comparison of dynamic characteristics between an intact and a damaged structure should be used.

5. Polymer composites can be modelled with acceptable accuracy even by using BBPD composite formulation when including the matrix PD bonds rotation. PD bond constants of the CFRP composite were identified from the optimization approach by ensuring the agreement (maximum difference up to 13%) of the elastic and failure behavior between the PD and experiment for [(0/90)º/90º/0º]s and [(±45)º/-45º/45º]s layup CFRP specimens. The KTF, implemented into the created BBPD with a bond rotation composite model, enables to simulate the defect growth in the CFRP specimen.

6. SANTRAUKA

ĮVADAS

Nuovargio pažeidimų nustatymas ir nuovargio pažeidimų augimo prognozė, įskaitant galutinį medžiagos suirimą, yra daugeliui pramonės šakų aktualūs uždaviniai, pavyzdžiui, transporto pramonėje, energetikoje, statybų inžinerijoje. Tai aktualu ne tik metalinėms, bet ypač anglies ir stiklo pluoštu armuotų polimerinių kompozitų (angl. CFRP ir GFRP) konstrukcijoms, kurios dėl didelio stiprumo ir mažos masės yra patrauklios naudoti siekiant pagerinti konstrukcijų eksploatacines savybes (pvz., aviacijoje, sporto įrangoje). Be to, polimeriniai kompozitai gali būti naudojami dėl geresnio atsparumo korozijai nei metalai, taip pat dėl ekologinių aspektų (termoplastikiniai kompozitai iš perdirbtų polimerų [1]).

Skaitinis nuovargio modeliavimas susiduria su keliomis problemomis. Viena iš jų – nuovargio plyšio atsiradimo ir augimo procesas. Esamos baigtinių elementų (angl. FE) formuluotės, pagrįstos dalinėmis poslinkio lauko išvestinėmis pagal koordinates, nėra tinkamos plyšio atveju. Buvo sukurti modifikuoti FE, pavyzdžiui, papildytas baigtinių elementų metodas (angl. *Extended Finite Element Method*, XFEM) [2], kohezinių zonų modeliai (angl. *Cohesive Zone Models*, CZM) [3], virtualus plyšių uždarymo metodas (angl. *Virtual Crack Closure Technique*, VCCT) [4], tačiau juos taikant kyla papildomų sunkumų, pavyzdžiui, CZM reikalingi papildomi plyšio parametrai, plyšio trajektorija turi būti iš anksto apibrėžta, sunku modeliuoti sudėtingos trajektorijos plyšių augimą [5]. Kita problema yra susijusi su empiriniais nuovargio modeliais. Šie aprašomi empiriniais koeficientais, kurie gali būti nustatomi tik iš eksperimentų esamam ciklinės apkrovos tipui (simetrinis, asimetrinis). Vis dar nėra vieningo modelio, pagal kurį būtų galima be eksperimento prognozuoti atlaikomų ciklų skaičių, priklausomai nuo ciklinės apkrovos, jos asimetrijos, apkrovos dažnio ir temperatūros. Eksperimentiniai duomenys ne visada prieinami arba įmonės neturi galimybių atlikti tokių bandymų, todėl projektuojant kompozitines konstrukcijas remiamasi papildomų medžiagos sluoksnių pridėjimu, siekiant užtikrinti konstrukcijai keliamus saugos reikalavimus. Dėl to pablogėja konstrukcijos eksploatacinės savybės (padidėja masė) ir išauga konstrukcijos kaina. Be to, nesant veiksmingų nuovargio pažeidimų nustatymo ar stebėsenos metodų, konstrukcija keičiama po numatytų darbo valandų, neatsižvelgiant į esančius nuovargio pažeidimus ir galimą ilgesnį eksploatavimo laikotarpį.

Sillingo 2000 m. sukurta nelokalios peridinamikos (PD) teorija [6] siūlo integralinę kontinuumo mechanikos formuluotę, todėl ją taikant galima modeliuoti ir tolydaus, ir netolydaus lauko problemas. PD nereikalauja specialių metodų modeliuojant netolydų lauką ir neturi anksčiau minėtų modifikuotų FE metodų sunkumų, PD modelių atitikimas eksperimentų rezultatams yra labai geras [7], todėl PD atrodo patrauklus metodas, taip pat jau taikomas modeliuojant nuovargio procesus [8–10]. Kaip alternatyva klasikiniams nuovargio modeliams nuovargio pažeidimams įvertinti gali būti naudojama XX a. viduryje sukurta kinetinė irimo teorija (angl. KTF) [11], pagrįsta atomistiniu požiūriu. Jos nuovargio pažeidimų lygtis apima proceso temperatūrą, apkrovos dažnį ir ciklo įtempius, įtempių asimetrijos koeficientą, todėl, sukalibravus lygtį pagal medžiagos S-N kreivę, ją galima taikyti bet kokioms skirtingoms apkrovos sąlygoms, priešingai nei klasikinis metodas, kai empiriniai

koeficientai gali būti nustatomi tik iš eksperimento atitinkamomis ciklinio apkrovimo sąlygomis.

Pažeidimams nustatyti gali būti taikoma neardomoji bekontaktė paviršiaus viso lauko poslinkių ir deformacijų matavimo sistema, t. y. skaitmeninė vaizdų koreliacija (angl. DIC). DIC veikimo principai grindžiami paviršiaus taškų stebėjimu prieš deformaciją ir po jos. DIC, kurią neseniai sukūrė Suttonas Pietų Karolinos universitete (JAV) [12], tampa vis populiaresne poslinkio ir deformacijų matavimo sistema įvairaus dydžio konstrukcijoms [13,14] tirti.

Disertacijos tyrimų objektas – pažeidimai ištisiniais pluoštais armuotuose polimeriniuose kompozituose.

Disertacijos tikslas – išvystyti nuovargio pažeidimų pluoštu armuotame polimeriniame kompozite identifikavimo ir jų augimo prognozavimo metodiką, pagrįstą eksperimentiniais skaitmeninių vaizdų koreliacijos matavimais ir nelokalia peridinamikos teorija kartu su kinetine irimo teorija.

Darbo tikslui pasiekti **iškelti penki uždaviniai**:

1. Modifikuoti eksperimentinę skaitmeninių vaizdų koreliacijos sistemą peridinamika pagrįstu deformacijų skaičiavimo algoritmu, siekiant pagerinti skaitmeninių vaizdų koreliacijos sistemos deformacijų kokybę.
2. Sukurti peridinamikos modelį ir sukalibruoti peridinamikos modelio parametrus pagal eksperimentinius viso lauko skaitmeninių vaizdų koreliacijos matavimus.
3. Sujungti kinetinę irimo ir peridinamikos teorijas sukuriant modelį, tinkamą bet kokio tipo ciklinėms apkrovoms vertinti be papildomų eksperimentinių duomenų tomis apkrovos sąlygomis.
4. Nustatyti pažeidimą (arba defektą) kompozitinėje medžiagoje pagal paviršiaus skaitmeninių vaizdų koreliacijos matavimus ir apibrėžti pažeidimo vietą, kiekybiškai įvertinti pažeidimą (defektą) taikant skaitinį modelį.
5. Atlikti kinetinės irimo teorijos – peridinamikos pagrindu sukurtą kompozito nuovargio skaitinę analizę.

Ginamos tezės

1. Peridinamikos teorija pagerina skaitmeninių vaizdų koreliacijos deformacijų matavimų kokybę sumažinant deformacijų triukšmą esant didelei matavimo skiriamajai gebai.
2. Skaitmeninių vaizdų koreliacijos eksperimentiniai matavimai, taikomi tik tempimo bandymui, leidžia kalibruoti peridinamikos modelio parametrus.
3. Nuovargio pažeidimai esant bet kokio tipo ciklinei apkrovai prognozuojami taikant kinetinę irimo teoriją ir remiantis tik simetrinės ciklinės apkrovos kambario temperatūroje eksperimentiniais duomenimis.
4. Taikant peridinamikos teoriją visas nuovargio procesas modeliuojamas naudojant tą patį modelį be iš anksto nurodytų plyšio trajektorijų ir pradinių plyšių medžiagoje.

Mokslinis naujumas

1. 3D skaitmeninių vaizdų koreliacijos sistema su triukšmus filtruojančiu peridinamika pagrįstu deformacijų skaičiavimo algoritmu.

124

2. Daugiasluoksnio pluoštu armuoto polimerinio kompozito ryšiais grįstas peridinamikos modelis su ryšių pasukimu, realizuojamas be specialios programinės įrangos.
3. Metalinių ir kompozitinių medžiagų bet kokio tipo ciklinio apkrovimo proceso skaitinis modelis, nereikalaujantis eksperimento modelio parametrams parinkti.

Praktinė reikšmė
1. Sukurta metodika, kuri gali būti naudojama kompozitinių medžiagų gamybos įmonėse (modeliavimu pagrįstas nuovargio prognozavimas konstrukcijos projektavimo etape, užuot pridėjus papildomus kompozito sluoksnius saugumui užtikrinti). Be to, metodika taikytina pramonėje eksploatuojamoms kompozitinėms konstrukcijoms stebėti ir analizuoti (defektų ir irimo nustatymas – galimybė užtikrinti konstrukcijos saugumą, priešingu atveju galimas prailgintas eksploatavimo periodas).
2. Nuovargio prognozavimas, įskaitant pažeidimų atsiradimo ir augimo modeliavimą (kurį sunku realizuoti taikant įprastinius skaitinius modelius), atliekant minimalius eksperimentinius bandymus, daro metodiką ekonomiškai efektyvią ir patrauklią naudoti. Platesnis tokios metodikos taikymas dar labiau pagerina kompozitinių konstrukcijų eksploatacines savybes, sumažina konstrukcijos kainą ir leidžia išvengti brangių kompozitinių medžiagų švaistymo.

Tyrimo rezultatų aprobavimas
Šio tyrimo rezultatai paskelbti dviejuose tarptautiniuose žurnaluose, nurodytuose ISI Web of Science leidiniuose. Tyrimo rezultatai buvo pristatyti penkiose tarptautinėse konferencijose: dvi vyko Kaune, Lietuvoje (žodinis pranešimas), viena – JAV ir dvi Italijoje.

Disertacijos struktūra
Disertaciją sudaro įvadas, 4 skyriai, išvados, literatūros sąrašas ir mokslinių publikacijų sąrašas. Iš viso disertaciją sudaro 180 puslapių, 87 paveikslėliai ir 11 lentelių.

Įvade pateikiama disertacijos darbo problema, taip pat darbo tikslas ir uždaviniai. Be to, pateikiami ginamieji teiginiai, taip pat disertacijos tyrimo mokslinis naujumas ir praktinė reikšmė.

Pirmajame skyriuje pateikiama literatūros apžvalga. Pirmiausia trumpai apibūdinami pluoštu armuotų kompozitų defektai. Toliau analizuojami pluoštu armuotiems kompozitams naudojami (nuovargio) pažeidimų identifikavimo metodai. Galiausiai aprašomi esami skaitiniai modeliai, skirti medžiagoms su plyšiais (pvz., nuovargio plyšiu).

Antrajame skyriuje pateikiamas tyrimų planas kartu su teorine, eksperimentine ir skaitinio modeliavimo metodika. Aprašoma PD teorija ir sukurti PD modeliai. Taip pat išvedamas ir pristatomas peridinamikos diferencialinis operatorius (PDDO). Analizuojamas PD nuovargio modelis. Pristatoma ir modifikuojama KTF, siekiant užtikrinti koreliaciją su eksperimentiniais rezultatais asimetrinės ciklinės apkrovos atveju. Paaiškinamas KTF-PD nuovargio modelis ir jo taikymas. Galiausiai

pateikiami ryšiais grįstos PD (angl. BBPD), būsenomis grįstos PD (angl. SBPD) ir BBPD su PD ryšių pasisukimo laisvės laipsniu teorijų parametrai sluoksniuotam kompozitui. Kaip tyrimų eksperimentiniam metodui daugiausia dėmesio skiriama DIC, kuri pristatoma taip pat 2 skyriuje.

Eksperimentinių tyrimų rezultatai pateikiami 3 skyriuje. Įprastinis DIC deformacijų skaičiavimo algoritmas pakeistas PDDO pagrįstu algoritmu, siekiant padidinti DIC metodo tikslumą. DIC matavimai naudojami įprastinio DIC ir DIC-PDDO metodu apskaičiuotoms deformacijoms palyginti, taip pat PD medžiagos parametrams kalibruoti. Atliekami izotropinės medžiagos nuovargio bandymai esant simetriniam ir asimetriniam cikliniam apkrovimui. CFRP kompozito statiniai bandymai naudojami defektams nustatyti taikant DIC, taip pat PD modeliavimui reikalingoms kompozito efektyviosioms savybėms gauti kalibruojant PD modelį.

Ketvirtajame skyriuje pateikiami skaitinio modeliavimo rezultatai. Aprašoma PD modelio kalibravimo procedūra pagal eksperimentinio DIC matavimus. Sukuriamas izotropinės medžiagos KTF-PD modelis ir analizuojama jo koreliacija su eksperimentų rezultatais esant įvairioms apkrovos sąlygoms (įtempių asimetrijoms, įtempių amplitudėms). Atliekama kompozito su imituotais defektais analizė. Defekto gylis randamas FEMU algoritmu iš DIC matavimų. Sukuriamas BBPD modelis su sukimu, kalibruojamas pagal eksperimentus ir naudojamas CFRP kompozito nuovargio pažeidimams (defektų augimui) modeliuoti.

Baigiamajame skyriuje pateikiamos daktaro disertacijos išvados ir literatūros šaltiniai bei autoriaus moksliniai pranešimai ir publikacijos.

6.1. LITERATŪROS APŽVALGA

Dėl didelio stiprumo ir mažo tankio GFRP ir CFRP yra patrauklūs naudoti daugelyje pramonės šakų, pavyzdžiui, sporte, aviacijoje, vėjo energetikoje. Be to, pluoštu armuoti polimeriniai kompozitai pasižymi geresniu atsparumu korozijai nei metalinės konstrukcijos ir puikiomis nuovargio savybėmis [15]. Tipinė pluoštu armuoto polimerinio kompozito struktūra parodyta 6.1 pav.

a

b
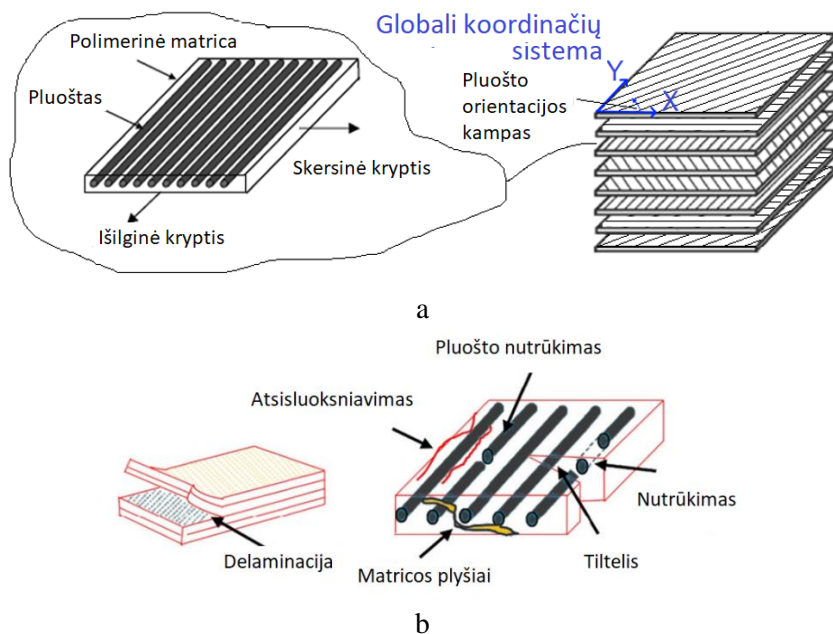
6.1 pav. Tipiškas GFRP arba CFRP kompozitas: a – struktūra, b – dažniausiai pasitaikantys pažeidimų tipai (schema paimta iš [16])

Kiekvieną kompozito sluoksnį sudaro didelio stiprumo pluoštas, orientuotas tam tikru kampu su globaliomis koordinatėmis, ir polimerinė matrica, naudojama pluoštui surišti. Vieno sluoksnio kompozitas yra anizotropinis ir pasižymi dideliu stiprumu pluošto kryptimi ir maždaug 100 kartų mažesniu stiprumu skersai pluošto krypties. Kad medžiagos savybės skirtingomis kryptimis būtų panašios, kompozito sluoksniai sujungiami skirtingais pluošto orientacijos kampais (6.1 pav., a).

Didelio standumo (didelio tamprumo modulio) CFRP turi didžiausią ciklinį patvarumą, standžioje konstrukcijoje yra mažos deformacijos, o tai lemia mažesnį matricos įtrūkimą. Mažo tamprumo modulio kompozito ciklinis patvarumas yra apie 40 % standžios konstrukcijos ciklinio patvarumo. Kita vertus, standaus kompozito suirimas yra staigus, o didelio stiprumo ar mažo tamprumo modulio kompozito irimas yra laipsniškas. Tai galima paaiškinti kompozitinėje konstrukcijoje sukaupta energija: standžiose konstrukcijose staiga išsiskyręs didelis energijos kiekis sukelia staigų sprogstamąjį suirimą, o mažo tamprumo modulio konstrukcijose mažesni energijos kiekiai sukelia laipsnišką progresuojantį irimą. Pažymėtina, kad didelio tamprumo modulio kompozitinių konstrukcijų nuovargio pažeidimų stebėsena yra sudėtingas ir

labai svarbus uždavinys dėl tokio staigaus, sprogstamojo pobūdžio ciklinio suirimo tipo.

Galima išvesti nuovargio grafikus pagal kompozito tūrio, matricos, pluošto medžiagų ar pluošto orientacijos kryptį. Kompozitų su skirtingais pluošto tipais ir ta pačia epoksidine matrica tyrimai [18,19] parodė, kad pluošto tipas turi tik nedidelę įtaką konstrukcijos nuovargio savybėms. Pluošto tūrio dalis tiesiogiai veikia kompozito stiprumą ir standumą pluošto kryptimi, todėl yra labai svarbi kompozito patvarumui, kaip buvo nustatyta vienakrypčiam CFRP [20]. Pagal Alok ir kt. tyrimą [21], pluošto orientacija turi didelę įtaką statinėms ir nuovargio savybėms viensluoksniame kompozite, tačiau simetriniam kompozitui, sudarytam iš kelių sluoksnių (kvazizotropinis kompozitas), įtaka praktiškai nepastebima. Galima daryti išvadą, kad didesnė pluošto tūrio dalis lemia ilgesnį kompozito tarnavimo laiką. Kompozitas su maža pluošto tūrio dalimi suyra dėl matricos įtrūkimų, o kompozituose su didele pluošto tūrio dalimi vyrauja pluošto trūkinėjimas. Padidėjus matricos atsparumui lūžiams, kompozitai turėtų tapti atsparesni įtrūkimų augimui, tačiau tyrimo [24] eksperimentiniai rezultatai parodė, kad tai nepagerina kompozitinės konstrukcijos ciklinio patvarumo. Vietoj to nuovargio savybes galima pagerinti naudojant tąsią matricą kartu su didelio tamprumo modulio pluoštu, kaip aprašyta [23]. Nuovargio trukmę galima pagerinti naudojant kompozitinės matricos priedus [15]. Apžvalgoje [24] daroma išvada, kad yra optimali pluošto tūrio dalies vertė, kuriai esant kompozito ciklinis patvarumas yra didžiausias.

Aplinkos sąlygos taip pat turi įtakos kompozito nuovargio trukmei. Temperatūra keičia matricos savybes, todėl matrica tampa elastingesnė [25], o eksperimentiniai rezultatai [26] rodo, kad esant aukštesnei temperatūrai kompozito ciklinis patvarumas yra trumpesnis. Kita vertus, konstrukcijos standumo degradacija buvo didesnė esant žemesnei temperatūrai. Kitų aplinkos sąlygų, tokių kaip drėgmė, korozija, sąveika su cheminėmis medžiagomis, poveikis taip pat pastebimas ir analizuojamas specialiuose tyrimuose [15].

Svarbios ir apkrovimo sąlygos. Ciklo įtempiai turi įtakos ne tik ciklų skaičiui iki suirimo, bet ir suirimo būdui. Esant dideliems įtempiams vyrauja pluošto trūkimas, o esant mažiems įtempiams atsiranda mišrus pluošto ir matricos įtrūkimas ir atskyrimas. Didėjantis įtempių asimetrijos koeficientas lemia trumpesnį konstrukcijos tarnavimo laiką. Apkrovos dažnis turi įtakos tik tada, jei veikia matricos temperatūrą, nes tada keičiasi matricos medžiagos savybės [27].

Kitas labai svarbus aspektas, į kurį reikia atsižvelgti, yra kompozito defektai. Esantys medžiagos defektai labai sumažina konstrukcijos stiprumą ir ciklinį patvarumą, nes defektai cikliškai auga ir lemia galutinį suirimą [28]. Defektai kompozitinėse medžiagose gali atsirasti dėl gamybos proceso, atsitiktinių pažeidimų eksploatacijos metu (pvz., smūginių pažeidimų) arba nuovargio pažeidimų. Pluoštu armuotų polimerinių kompozitų gamyba apima keletą operacijų, ir kiekvienos operacijos metu yra defektų atsiradimo galimybė, pavyzdžiui, netinkamas medžiagos laikymas, aplinkos priemaišos, pluošto bangavimas klojant, netinkamos dervos kietėjimo sąlygos ir t. t. Kita svarbi problema yra smūginiai pažeidimai, t. y. vos matomas smūginis pažeidimas (angl. *barely visible impact damage*), kurį sunku nustatyti, o pažeidimas gali didėti ir sukelti katastrofišką medžiagos suirimą [29].

Tipiniai kompozito defektai pavaizduoti 6.2 pav.
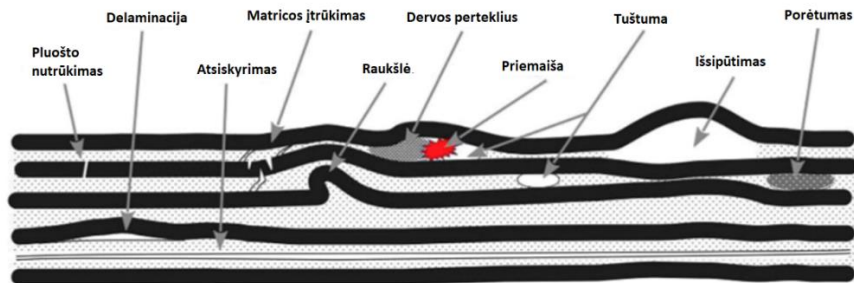
6.2 pav. Tipiniai kompozitų defektai [30]

Matricos defektai (6.2 pav.) yra gana dažni ir gerai išanalizuoti literatūroje. Tuštumos ir porėtumas, svetimkūniai kompozitinėje matricoje daro didelę įtaką mechaninėms konstrukcijos savybėms, tokioms kaip tarpsluoksnio šlyties stiprumas, gniuždymo stiprumas, atsparumas nuovargiui ir lenkimui [31]. Esančios mikrotuštumos nuovargio apkrovos metu gali išaugti į makrotuštumas, dėl kurių medžiaga suyra.

Pluošto banguotumas ir raukšlėtumas yra labiausiai paplitę kompozitinių konstrukcijų gamybos defektai. Tai ypač būdinga storoms kompozitinėms konstrukcijoms [33]. Kiti pluošto defektai – tai pluošto lūžimas, nutrūkimas, kurie gali atsirasti ir eksploatacijos etape (pvz., dėl smūginių pažeidimų). Pluošto defektai daro didelę įtaką medžiagos savybėms, mažindami kompozito stiprumą ir ciklinį patvarumą.

Mažas kompozitinių konstrukcijų skersinis ir tarpsluoksnio šlyties stiprumas yra tarpsluoksnio ir (arba) vidinių defektų priežastis. Delaminacija plinta lygiagrečiai su pluošto išsidėstymo kryptimi tarp laminatų arba laminato viduje, o atsiklijavimas – tai laminatų atsiskyrimas klijais sujungtoje jungtyje [34]. Delaminacija yra vienas iš konstrukcijos stiprumą ir ciklinį patvarumą ribojančių veiksnių [31,34]. Ji gali atsirasti gamybos proceso metu dėl netinkamų sluoksnių sukibimo sąlygų (pvz., nesuderinamų medžiagų, jų paruošimo), gamybos (pvz., gręžiant kompozitinę konstrukciją) arba eksploatacijos metu. Statinė arba ciklinė tempimo apkrova, ypač smūginė apkrova, yra pagrindinės eksploatavimo laikotarpiu sukeltos delaminacijos priežastys, atsisluoksniavimo pažeidimai ypač didėja dėl tiesioginio gniuždymo arba lenkimo sukelto gniuždymo įtempio. Netgi aplinkos sąlygos, tokios kaip drėgmė ar užterštumas, gali paspartinti tolesnį delaminacijos augimą [35].

Kompozitinės konstrukcijos eksploatavimo laikotarpiu svarbu ne tik nustatyti kritinę apkrovą delaminacijai atsirasti, bet ir prognozuoti konstrukcijos, kurioje jau yra delaminacijų, tolesnes išliekamąsias stiprumo ir ciklines savybes. Daugeliu atvejų delaminacijos nustatymas yra sudėtingas uždavinys [40], nes tokia konstrukcija gali elgtis skirtingai, priklausomai nuo geometrijos, medžiagos savybių, apkrovos, delaminacijos dydžio ir vietos. Pavyzdžiui, arti paviršiaus esančios delaminacijos sukelia lokalų kompozito paviršiaus išlinkimą, o gilios delaminacijos – mišrų arba globalų išlinkimą [37]. Remiantis Fu ir kt. tyrimu [41], delaminacijos pažeidimas yra lygiagretus pluošto krypčiai ir gali būti užfiksuotas kaip kompozitinės konstrukcijos

paviršiaus poslinkio lauko netolygumas.

Apžvelgiant dažniausiai pasitaikančius kompozito defektus akivaizdu, kad defektų identifikavimas, kiekybinis ir kokybinis charakterizavimas kartu su defektų stebėsena yra labai svarbūs esamų (nuovargio) pažeidimų įvertinimui ir likusios konstrukcijos ciklinio patvarumo prognozei. Šie uždaviniai nėra paprasti ir reikalauja specialių bandymų metodų. Konstrukcijos būklės stebėsena (angl. SHM), pagrįsta neardomojo bandymo metodais (angl. NDT), yra vienintelis galimas metodas, pritaikomas konstrukcijai jos eksploatavimo laikotarpiu.

(Kompozitinėms) konstrukcijoms tikrinti yra sukurta įvairių metodų [31]: akustinė emisija, ultragarsas, rentgeno tomografija, infraraudonųjų spindulių termografija, skaitmeninių vaizdų koreliacija (DIC). Metodo pasirinkimas priklauso nuo daugelio priežasčių, tokių kaip konstrukcijos medžiagos, dydis, kontakto su konstrukcija galimybės, defekto dydis, vieta. Gali būti taikomas vienas ar keli kombinuoti metodai. Dėl metodų įvairovės sunku juos klasifikuoti, todėl 6.1 lentelėje analizuojami labiausiai paplitę ir aktualūs metodai.

6.1 lentelė. Labiausiai paplitę kompozitų NDT metodai

Metodas	Privalumai	Trūkumai
Vizualus įvertinimas	Paprastas ir greitas įvertinimas be specialios įrangos; Padeda pasirinkti zonas, kurios vėliau tiriamos kitais metodais.	Netikslus; Priklauso nuo stebėtojo; Ne visi defektai gali būti pastebėti.
Akustinė emisija	Didelis bandymo greitis; Pritaikomas kompozitinėms konstrukcijoms tirti [42].	Reikalingas kontaktas [43]; Galima aptikti tik atsiradusį defektą; Struktūra turi leisti sklisti įtempių bangoms; Reikalingi įgūdžiai ir patirtis analizuojant išėjimo signalą [31].
Ultragarsas	Didelis tikslumas; Suteikia informacijos apie defekto vietą, gylį ir dydį [44]; Pritaikomas kompozitinėms konstrukcijoms tirti [44]; Nešiojama įranga [44].	Kontaktinis metodas [45]; Sunku aptikti defektus šalia liestuko [31].
Rentgenas	Didelis jautrumas ir skiriamoji geba, dėl to plačiai naudojamas kompozitams tirti [46,47]; Išsami informacija apie defekto vietą, gylį, dydį ir vizualizacija; Tinka daugumai medžiagų.	Mažas greitis; Kenksminga spinduliuotė, reikalingos specialios bandymo sąlygos (pvz., laboratorijoje) [31]; Objekto dydis ribotas [31].

Infraraudonųjų spindulių termografija	Didelis greitis; Vizualus defektų pateikimas; Galima aptikti delaminacijas [48,49]**.**	Reikalingas medžiagos kaitinimas [50]; Mažas jautrumas giliems defektams; Reikalinga patirtis vertinant rezultatus ir nustatant defekto dydį bei tipą.
Skaitmeninių vaizdų atpažinimo sistema	Didelis greitis ir tikslumas; Nekontaktinis metodas; Galima atlikti matavimus konstrukcijos eksploatacijos metu; Pritaikomumas nuo mikro- [51] iki didelių matmenų [13] konstrukcijoms; Aptinkamas pažeidimų augimas [52], delaminacijos [53,54] kompozitinėse konstrukcijose.	Reikalingas pasiruošimas, t. y. taškinis raštas ant tiriamo objekto paviršiaus [55]; Tikslumas priklauso nuo apšvietimo, taškinio rašto kokybės [55]; Defektų nustatymas priklauso nuo apkrovos, analizės tipo (statinės ar dinaminės).

     Skaitinis modeliavimas yra efektyvus konstrukcijos elgsenos, pavyzdžiui, joje esančio defekto, prognozavimo metodas, tačiau pagrindinė problema yra modelio patikimumas. Nors skaitinio modelio medžiagos parametrus galima kalibruoti pagal eksperimentus (ypač naudojant DIC matavimus [65]) taip, kad sumodeliuotos ir eksperimentinės deformacijos ar poslinkiai sutaptų, tačiau kyla problemų dėl tolesnio defektų augimo modeliavimo. Taip yra dėl to, kad esamų FE formuluotė pagrįsta poslinkio lauko dalinėmis išvestinėmis, o esant netolydžiam poslinkio laukui išvestinių rasti neįmanoma. Šiai skaitinio modeliavimo problemai spręsti naudojami keli specialūs metodai: virtualus plyšių uždarymo metodas (angl. VCCT), kohezinių zonų metodas (angl. CZM), papildytas baigtinių elementų metodas (angl. XFEM), peridinamika (angl. PD), jie aprašyti 6.2 lentelėje.

6.2 lentelė. Netolydaus lauko modeliavimo metodai

Metodas	Privalumai	Trūkumai
VCCT	Palyginti paprastas; Gerai pritaikomas, kai reikia įvertinti proceso energiją.	Negalima modeliuoti plyšio augimo, jei nėra nurodytas pradinis plyšys ir plyšio trajektorija.
CZM	Nereikalinga plyšio trajektorija; Gerai pritaikomas nuovargiui modeliuoti.	Didelės skaičiavimo sąnaudos; Modeliui aprašyti reikia daug medžiagos parametrų.
XFEM	Plyšio trajektorija nebūtina; Pradinis plyšys nebūtinas; Efektyvus, skaičiavimo	Neveiksmingas esant sudėtingiems plyšiams; Tikslumas priklauso nuo FE pasirinkimo.

	sąnaudos nėra didelės.	
Peridinamika	Plyšio trajektorija nereikalinga; Pradinis plyšys nebūtinas; Galima modeliuoti bet kokius sudėtingus plyšius.	Pertvarko klasikinę kūno mechanikos teoriją, vietoj deformacijų ir įtempių naudodama kitus parametrus; Didelės skaičiavimo sąnaudos.

S-N kreivės ir Pario dėsnis naudojami skaitiniam nuovargio proceso modeliavimui. S-N kreivė yra skirtinga kiekvienai medžiagai ir sieja ciklo įtempių amplitudę su ciklų skaičiumi iki suirimo. Nuovargio plyšio augimo atveju taikomas Pario dėsnis [92], siejantis plyšio augimo greitį da/dN su įtempių intensyvumo koeficientu. Analitinės S-N kreivės ir Pario dėsnio išraiškos, pritaikytos kompozitinei medžiagai, pateiktos (1) ir (2) priklausomybėse:

$$N_f = \left(\frac{\sigma_{max}}{\sigma_c}\right)^{-\beta}, \text{S} - \text{N kreivė;} \qquad (6.1)$$

$$\frac{da}{dN} = C G_{max}{}^{\alpha}, \text{Pario dėsnis;} \qquad (6.2)$$

čia a – plyšio ilgis, N_f – ciklų skaičius iki suirimo, C, α, β – medžiagos koeficientai, rasti iš eksperimentų ar pateikiami medžiagos duomenų bazėse. Tipiniai S-N kreivės ir Pario dėsnio duomenys pateikiami simetrinei ciklinei apkrovai (asimetrijos koeficientas R = -1) kambario temperatūroje ir negalioja kitoms bandymo sąlygoms, pavyzdžiui, skirtingam asimetrijos koeficientui ($R \neq$ -1), skirtingai temperatūrai ($T \neq$ 20ºC), aukšto dažnio cikliniam apkrovimui.

Pasirinktų Pario dėsnio koeficientų fizikinio paaiškinimo trūkumas (nėra fizikiniais procesais pagrįstų lygčių, skaičiuojančių Pario dėsnio koeficientus pagal pasikeitusias ciklinio apkrovimo sąlygas, pvz., pakilusią temperatūrą) verčia ieškoti tobulesnių metodų [11]. XX amžiaus viduryje Colemanas ir Žurkovas atskirai [94,95] sukūrė kinetinę irimo teoriją (KTF) [11]. Tai atomistinis požiūris, kuris traktuoja nuovargį kaip termiškai aktyvuotą procesą, priklausantį nuo temperatūros, ciklo asimetrijos koeficiento, įtempių amplitudės ir apkrovos dažnio. KTF gali tiksliai prognozuoti įvairių medžiagų, įskaitant metalus ir polimerinius kompozitus [96], ciklinį patvarumą esant skirtingoms apkrovimo sąlygoms.

Apibendrinant visus išvardintus veiksnius matyti, kad nuovargio pažeidimai kompozitinėse konstrukcijose yra labai sudėtingi, priklausomi nuo daugelio kintamųjų. Esami kompozitinių konstrukcijų defektai yra pagrindinis veiksnys, lemiantis nuovargio pažeidimus ir konstrukcijos irimą, todėl defektų aptikimas, pažeidimų stebėjimas kartu su skaitiniu konstrukcijos modeliu yra labai svarbūs konstrukcijos SHM ir ciklinio patvarumo prognozei. Siūlomi įvairūs NDT metodai, tačiau DIC yra patraukliausias dėl viso lauko nekontaktinių matavimų. Esami skaitiniai modeliai FE kompiuterinėse programose susiduria su problemomis modeliuojant netolydžius poslinkių laukus, todėl PD teorija, leidžianti modeliuoti bet kokius laukus, atrodo perspektyvus metodas. Be to, nėra esamo ir naudojamo vieningo medžiagos nuovargio modelio, kuris galėtų įvertinti ciklinį patvarumą, įtraukdamas į lygtį visus medžiagos (pvz., tamprumo modulio) ir proceso (asimetrijos koeficientas,

temperatūra, dažnis,..) parametrus. KTF gali būti traktuojamas kaip toks fizikos pagrindu sukurtas nuovargio modelis, tačiau jis dar nėra plačiai išnagrinėtas ir naudojamas. Taigi, šis tyrimas yra pagrįstas kompozitinės konstrukcijos stebėsenos kartu su ciklinio patvarumo prognoze sistemos analize ir kūrimu. Sistema remiasi DIC eksperimentiniais matavimais, skirtais pažeidimams aptikti ir sekti, ir KTF-PD modeliu, skirtu cikliniam patvarumui ir konstrukcijos irimui prognozuoti.

6.2. TYRIMŲ METODIKA IR TEORINIAI PAGRINDAI

6.2.1. Darbo planas

Tyrimas pagrįstas teorine, eksperimentine ir skaitine analize. Darbo planas pateiktas 6.3 pav. Iš viso išskirtos 22 užduotys, skirtos anksčiau nustatytiems 5 tyrimo uždaviniams pasiekti. Kiekviena užduotis 6.3 pav. priskiriama teorinei (T1-T5), eksperimentinei (E1-E8) arba skaitinio modeliavimo (M1-M9) kategorijai. Yra užduočių, kurias galima atlikti lygiagrečiai, tačiau kitas užduotis galima atlikti tik užbaigus ankstesnes užduotis. Pavyzdžiui, tyrimai pradedami nuo PD teorijos analizės lygiagrečiai susipažįstant su eksperimentine DIC sistema (6.3 pav.). Tik išanalizavus PD teoriją ir jos skaitinius aspektus, galima realizuoti PD modelį programinėje įrangoje. Skaitinio PD modelio ir eksperimentinių DIC deformacijų matavimų derinys leidžia pasiekti pirmąjį uždavinį – sukurti PDDO pagrįstą DIC deformacijų skaičiavimo algoritmą (6.3 pav.). Kadangi kompozitinė medžiaga yra sudėtinga, net ciklinė apkrova yra sudėtingas reiškinys, pradžioje sukuriamas izotropinės medžiagos statinis PD modelis ir pasiekiamas antrasis uždavinys – statinio modelio kalibravimas pagal eksperimentinius DIC matavimus. Panašiai kaip ir Sillingo [6] pasiūlytas originalus BBPD trapios medžiagos modelis, PD modelio kalibravimui pasirinkta Biresin CH83-2 epoksidinė derva. Be to, modeliuojant CFRP arba GFRP kompozitus su epoksidine derva, dervos savybės yra būtinos norint nustatyti tarpsluoksninio normalinio ir šlyties PD ryšių standumus ar šių ryšių PD irimo parametrus. KTF-PD modeliavimo, eksperimentinių nuovargio bandymų ir sukurtų skaitinių PD modelių teorinis pagrindas lemia atliktą trečiąjį uždavinį. Kadangi tai yra naujas metodas, KTF-PD modeliavimas pagal 3-čią uždavinį atliekamas izotropinei medžiagai, o ne iš karto taikomas anizotropiniam kompozitui. 316L nerūdijantis plienas pasirinktas dėl jo naudojimo su CFRP/GFRP kompozitinėmis konstrukcijomis, pavyzdžiui, aviacijoje [99], dėl naujų didelio atsparumo dilimui ir korozijai CFRP-316L nerūdijančio plieno kompozitų [100], taip pat dėl to, kad metalinėms medžiagoms KTF-PD modeliai nėra plačiai išnagrinėti esant asimetriniam cikliniam apkrovimui. Ketvirtasis uždavinys – kompozitų defektų identifikavimas ir apibūdinimas susideda iš eksperimentinių ir skaitinių užduočių. Ketvirtasis uždavinys daugiausia grindžiamas eksperimentiniais bandymais (6.3 pav.), o penktajam uždaviniui – KTF-PD kompozitinių medžiagų nuovargio modeliavimui – reikia derinti visus (teorinius, eksperimentinius ir skaitinius) metodus, taip pat sukauptą visų ankstesnių uždavinių patirtį.

Teorija T   **Modeliavimas** M   **Eksperimentas** E

Laikas

Ryšiais ir būsenomis grįstų PD teorijų analizė: PD medžiagos parametrai, jų apibrėžimas ir išvedimas pagal klasikinės mechanikos parametrus, PD medžiagų modeliai, irimas ir PD pažeidimai. **T1**

Susipažinimas su eksperimentine įranga: DIC sistema, jos veikimo principais, bandinių paruošimu, matavimais ir programine įranga duomenų apdorojimui. **E1**

PD pagrįsto diferencialinio operatoriaus analizė ir taikymas tolydiems ir netolydiems poslinkių laukams skaičiuojant deformacijas. **T2**

PD teorijos skaitinio realizavimo aspektai. **T3**

PD modelio realizavimas programinėje įrangoje. **M1**

PD teorija pagrįsto diferencialinio operatoriaus taikymas DIC deformacijų skaičiavimui iš DIC poslinkių lauko. DIC deformacijų kokybės pagerinimas. **M2**

DIC eksperimentiniai deformacijų matavimai. **E2**

Objective 1

Trapios izotropinės medžiagos modeliavimas esant statiniam apkrovimui ir irimui taikant PD. **M3**

Bandinių paruošimas iš epoksidinės dervos CH83-2. **E3**

PD modelio parametrų kalibravimas. **M4**

Tempimo bandymai su DIC deformacijų matavimais siekiant kalibruoti PD modelį. **E4**

Objective 2

PD teorijos taikymas nuovargio modeliavimui. KTF taikymo nuovargio modeliavimui analizė. KTF nuovargio lygčių realizavimas PD modelyje vertinant medžiagų ciklinį patvarumą. KTF-PD modelio analizė esant simetriniam ir asimetriniam cikliniam apkrovimui su pastovia ir kintama ciklo amplitude. **T4**

Izotropinės medžiagos standartinio bandinio nuovargio modeliavimas taikant KTF-PD esant simetriniam ir asimetriniam cikliniam apkrovimui bei pastoviai ir kintamai amplitudei. **M5**

Izotropinės medžiagos nuovargio bandymai esant simetriniam ir asimetriniam cikliniam apkrovimui. **E5**

Objective 3

Kompozitinių bandinių paruošimas. **E6**

Kompozito skaitinio modelio validavimas. **M6**

Kompozitinių bandinių tempimo eksperimentai savybių nustatymui. **E7**

Kompozito defekto charakterizavimas taikant skaitinius algoritmus. **M7**

Kompozito defektų aptikimas iš eksperimentinių DIC matavimų. **E8**

Objective 4

PD kompozitinių medžiagų modelių analizė. **T5**

Kompozito PD modelio kalibravimas. Kompozito PD modeliavimas esant statiniam apkrovimui. **M8**

Kompozito ciklinio apkrovimo modeliavimas taikant KTF-PD. Kompozito defekto augimo ir medžiagos suirimo prognozavimas. **M9**

Objective 5

6.3 pav. Tyrimų metodologija ir darbo planas

Apibendrinta informacija apie planuojamas eksperimentines užduotis, pavaizduotas 6.3 pav., pateikiama 6.3 lentelėje.

6.3 lentelė. Planuojami eksperimentai

Užd. 3 pav.	Įranga	Veiksmai	Medžiagos
E1	3D DIC.	Analizė	-
E2	▪Universali tempimo mašina INSTRON E10000; ▪3D DIC su kameromis Basler acA4112.	Tempimo bandymas.	Bet kuri tampri medžiaga, bandinys plokščias, nepriskiriamas jokiam standartui.
E3	▪Liejimo forma; ▪Vakuuminis siurblys.	▪Dervos maišymas; ▪ASTM D638 – 10 [101] bandinių liejimas, dervos džiovinimas kambario temperatūroje.	▪Epoksidinė derva CH83-2; ▪Kietiklis.
E4	▪Universali tempimo mašina INSTRON E10000; ▪3D DIC su kameromis Basler acA4112.	Tempimo bandymas.	Epoksidinės dervos bandiniai pagal ASTM D638 – 10 [101].
E5	Universali tempimo mašina INSTRON E10000.	Cikliniai bandymai pagal ASTM E1012 [102].	316L nerūdijančio plieno bandiniai pagal ASTM E606/E606M [103].
E6	▪Vakuuminis ▪siurblys; Diskinis stalinis pjūklas; ▪CNC frezavimo staklės ir 1 mm skersmens griovelinė freza.	▪Anglies pluošto audinio klijavimas gaminant 500 mm×500 mm CFRP plokštę su sluoksnių išdėstymu $[(\pm45)^o/(0/90)^o]_3$s su 4 20×60 mm dydžio delaminacijomis; ▪Bandinių pagal ASTM D3039 [104] pjovimas iš 350 mm×150 mm plokštės 0° ir 45° kampais; ▪1 mm pločio 10 mm ilgio griovelių frezavimas ASTM D3039 [104] CFRP	▪Anglies pluošto audinys, epoksidinė derva, kietiklis. ▪350 mm×150 mm dydžio 2 mm storio CFRP kompozito plokštė, sluoksniavimas $[(0'90)^o/90'^o/0^o]$s.

		bandiniuose.	
E7	▪10 kN jėgos tempimo mašina; ▪Išorinis ekstensiometras.	0º ir 45º laipsnių kampais išpjautų CFRP bandinių tempimo bandymas.	ASTM D3039 [104] CFRP kompozito bandiniai be defektų.
E8	▪3D DIC su kameromis Basler acA4112; ▪Universali tempimo mašina INSTRON E10000.	▪Statiniai lenkimo bandymai naudojant svorio apkrovą; ▪Statinė apkrova, veikiant pastoviai tempimo jėgai.	▪500 mm×500 CFRP plokštė su 4 delaminacijomis; ▪ASTM D3039 [104] CFRP kompozito bandiniai su išfrezuotais grioveliais.

Tolesniuose poskyriuose pristatomi PD, KTF teoriniai aspektai ir supažindinama su eksperimentinio DIC veikimo principais.

6.2.2. Peridinamikos teorija

Originalioje Sillingo PD teorijos formuluotėje [6] daroma prielaida, kad kiekvienas PD medžiagos taškas x sąveikauja su kitu medžiagos tašku x' sąveikos zonoje H_x, vadinamoje PD horizontu. Sąveikos zona yra sfera 3D modelyje (cilindras 2D modelyje), apibrėžta spinduliu δ. Sąveika tarp x ir x' apibrėžiama kaip PD ryšys. Ši formuluotė veda prie ryšiais pagrįstos PD (angl. BBPD) teorijos (6.4 pav.), kurios judėjimo lygtis gali būti išreiškiama kaip [105]:

$$\rho\ddot{\boldsymbol{u}}(\boldsymbol{x},t) = \int_{H_x} \boldsymbol{f}(\boldsymbol{u}'(\boldsymbol{x},t) - \boldsymbol{u}(\boldsymbol{x},t), \boldsymbol{x}' - \boldsymbol{x}, \boldsymbol{x})dV_{x'} + \boldsymbol{b}(\boldsymbol{x},t); \qquad (6.3)$$

čia $\boldsymbol{u}$ ir $\boldsymbol{u'}$ – atitinkamai medžiagų taškų x ir x' (4 pav., jų padėties vektoriai $\boldsymbol{x}$ ir $\boldsymbol{x'}$) poslinkiai; ρ – medžiagos tankis, V_x – taško x tūris.
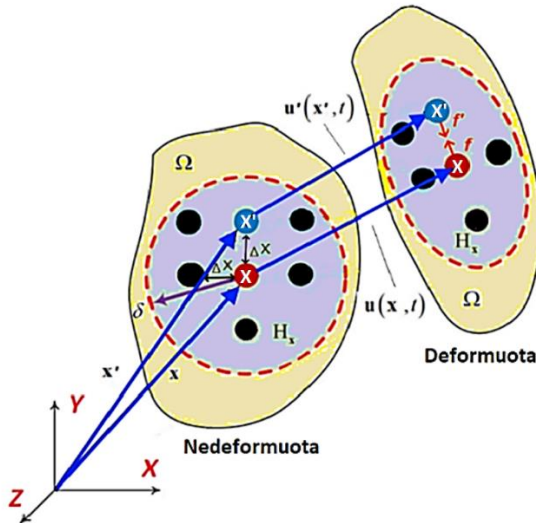
6.4 pav. Ryšiais grįstos peridinamikos teorijos (BBPD) principai

136

Čia vektorius f ((3) lygtis ir 6.4 pav.) yra jėgos tankis PD ryšiuose, $b(x, t)$ yra kūno jėgų vektorius. PD lygtyje (3) nėra dalinių išvestinių, todėl ji galioja tiek tolydžiam, tiek netolydžiam poslinkio laukams. Remiantis (3) lygtimi ir 6.4 pav., išplaukia ryšiais grįstos peridinamikos teorijos esminis apribojimas – fiksuotas medžiagos Puasono koeficientas, kuris gali būti tik 0,25 3D modelyje, ir 0,33 – 2D plokščio įtempių būvio atveju.

Siekiant modeliuoti medžiagas su bet kokiu norimu jos Puasono koeficientu, buvo sukurta būsenomis grįsta peridinamikos teorija (angl. SBPD), kurios lygtis užrašoma:

$$\rho \ddot{u}(x, t) = \int_{H_x} \left\{ \underline{T}[x, t]\langle x' - x \rangle - \underline{T}[x', t]\langle x - x' \rangle \right\} dV_{x'} + b(x, t); \quad (6.4)$$

kai $\underline{T}[x, t]\langle x' - x \rangle$ yra jėgos būsenos funkcija, priklausanti nuo padėties x ir laiko t ir aprašanti vektorių $\langle x' - x \rangle$. Šiuo atveju vektoriai f ir f' (6.4 pav.) yra nebūtinai vienodos skaitinės vertės.

Pagrindiniai peridinamikos (tiek BBPD, tiek SBPD) kintamieji yra ryšio $x' - x$ santykinė deformacija $s_{xx'}$ ir ryšio jėgos vektorius $t_{xx'}$:

$$s_{xx'} = \frac{(|\xi_{xx'} + \eta_{xx'}| - |\xi_{xx'}|)}{\xi_{xx'}}; \quad (6.5)$$

$$t_{xx'} = 2\delta \left\{ d \frac{\Lambda_{xx'}}{\xi_{xx'}} a\theta_{x'} + 2bs_{xx'} \right\} \frac{\xi_{xx'} + \eta_{xx'}}{|\xi_{xx'} + \eta_{xx'}|}; \quad (6.6)$$

kai $\xi_{xx'} = x' - x$ ir $\eta_{xx'} = u_{x'} - u_x$, $\theta_{x'} = d \sum_{x=1}^{N} \omega_{xx'} s_{xx'} \Lambda_{xx'} V_x$ – PD tūrinis išsiplėtimas, a-d – PD medžiagos parametrai, apskaičiuojami pagal medžiagos tamprumo modulį E ir Puasono koeficientą v bei PD formuluotę (3D, 2D plokščias įtempių ar deformacijų būvis).

Irimas PD modeliuose įvertinamas pagal kritinę ryšio deformacijos vertę s_c, kuri gali būti apskaičiuota remiantis Madenci ir Oterkus pateikta priklausomybe [105] nuo medžiagos šlyties modulio μ, tūrinio modulio κ bei atplėšimo energijos G_c:

$$s_c = \begin{cases} \sqrt{\dfrac{G_C}{\left(3\mu + \left(\dfrac{3}{4}\right)^4 \left(\kappa - \dfrac{5}{3}\mu \right) \right)\delta}} & \text{3D atvejis} \\[30pt] \sqrt{\dfrac{G_C}{\left(\dfrac{6}{\pi}\mu + \dfrac{16}{9\pi^2}(\kappa - 2\mu) \right)\delta}} & \text{2D atvejis} \end{cases} . \quad (6.7)$$

Ryšys tarp taškų x ir x' laikomas nutrauktu, jei jo deformacija viršija kritinę vertę s_c. Tai aiškiai matoma PD ryšio jėgos ir deformacijos grafike, kuris, esant idealiai tampriai ir trapiai medžiagai, pavaizduotas 6.5 pav.
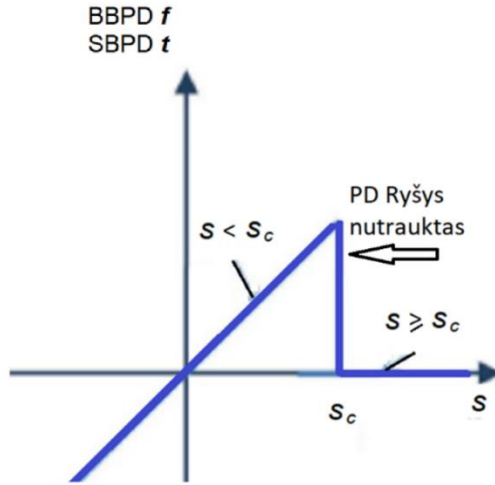
6.5 pav. PD ryšio jėgos ir deformacijų priklausomybė (idealiai tampri ir trapi medžiaga)

Taško x pažeidimai peridinamikoje vertinami kaip santykis tarp nutrauktų ir visų turimų taško ryšių to taško horizonte H_x.

Deformacijos ir įtempiai nėra įtraukti į PD teorijos judesio lygtis, tačiau juos galima apskaičiuoti iš poslinkio lauko taikant peridinamikos diferencialinį operatorių (PDDO). PDDO taip pat pagrįstas vien integraline išraiška siekiant apskaičiuoti poslinkio išvestines pagal koordinates. Platų PDDO taikymą demonstruoja Madenci ir kt. [125]: PDDO gali būti naudojamas signalams, vaizdams apdoroti duomenims atkurti, matematinėms operacijoms. Taikant deformacijų būsenos žymėjimą $\underline{Y}(x' - x) = \xi_{xx\prime} + \eta_{xx\prime}$ deformacijų gradientas F taške x gali būti apskaičiuotas [126]:

$$F = \left[\int_{H_x} \omega\langle|\xi_{xx\prime}|\rangle\big(\underline{Y}(\xi_{xx\prime})\otimes\xi_{xx\prime}\big)dV_\xi\right] \cdot \left(\int_{H_x} \omega\langle|\xi_{xx\prime}|\rangle(\xi_{xx\prime}\otimes\xi_{xx\prime})dV_\xi\right)^{-1} \quad (6.8)$$

Tuomet deformacijų tenzoriai gali būti gauti taikant klasikinės kontinuumo mechanikos (angl. CCM) formules [126]. Svarbus aspektas yra svorio funkcija $\omega\langle|\xi_{xx\prime}|\rangle$, kuri priklauso tik nuo PD ryšio ilgio. Pasak Selesono ir Littlewoodo tyrimo [127], 3D uždaviniams pakanka tiesinės funkcijos, o 2D modelio atveju turėtų būti naudojama kubinė daugianario funkcija, pavyzdžiui: $\left(1 - \frac{|\xi_{xx\prime}|}{\delta}\right)^3$.

PD skaitiniame modelyje reikalinga erdvinė ir laiko skaitinė integracijos. Kadangi PD taškų skaičius kūno srityje PD horizonte yra baigtinis, integralai PD judesio lygtyse (3) – (4) pakeičiami sumomis. Problemos, su kuriomis susiduriama skaitiniuose modeliuose, yra pilnai netelpantys PD taškai PD horizontuose (6.6 pav., a) ir nepilni PD horizontai kūne (6.6 pav., b).

138
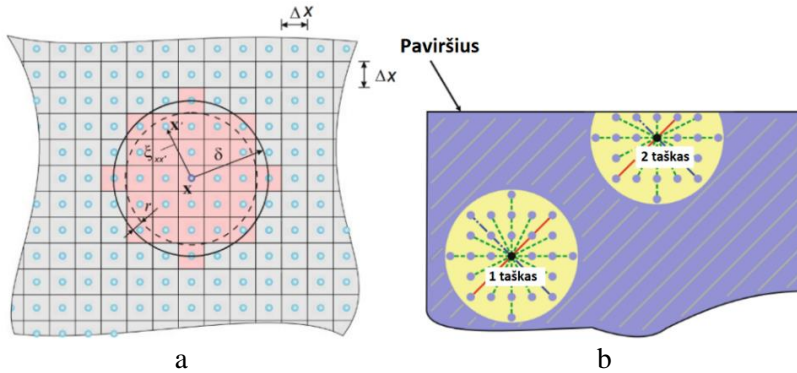
6.6 pav. PD skaitinio modelio problemos [105]: a – nepilni PD taškai PD horizontuose, b – nepilni PD horizontai ties paviršiais

6.6 pav. pavaizduotoms problemoms spręsti naudojami korekcijos koeficientai, kuriais įvertinami pilnai netelpančių PD taškų tūrio dalis PD horizontuose bei PD ryšių standumas koreguojamas esant nepilniems PD horizontams. Laiko atžvilgiu PD judesio lygtims (3) – (4) integruoti taikomas tiek *explicit*, tiek *implicit* integravimo metodas. *Explicit* integravimo metodas paprastesnis, tačiau, siekiant užtikrinti modelio stabilumą, integravimo laiko žingsnis turi tenkinti Madenci ir Oterkus pateiktą sąlygą [105]. Esant statiniam uždaviniui ir siekiant PD judesio lygčių statinio sprendinio, taikomas dirbtinis slopinimas. Slopinimo vertę galima rasti naudojant adaptyvų dinaminės relaksacijos metodą [133].

6.2.3. Kinetinė irimo teorija (KTF)

Nuovargio pažeidimų n raida per laiką t KTF traktuojama kaip termiškai aktyvuotas procesas, aprašytas diferencine lygtimi [140]:

$$\frac{dn}{dt} = (n_0 - n)^\lambda K_b; \tag{6.9}$$

čia n_0 – pradinė konstanta, λ – formos faktorius ir $K_{bxx'}$ – PD ryšių nutrūkimo greičio parametras, skaičiuojamas:

$$K_{bxx'} = \frac{kT}{h} e^{-\frac{U - \gamma \sigma_{xx'}}{kT}}; \tag{6.10}$$

čia k – Boltzmano konstanta; T – proceso temperatūra; U ir γ proceso aktyvacijos energija ir aktyvacijos tūris, τ – irimo laikas, $\tau_0 = 10^{-13}$ s – savasis atomų virpesių periodas kietame kūne [140], h Planko konstanta. Narys $\sigma_{xx'}$ parodo PD ryšio $x' - x$ įtempius, skaičiuojamus kaip įtempių vidurkis PD taškuose x ir x': $\sigma_{xx'} = \frac{\sigma_x + \sigma_{x'}}{2}$ [97]. PD ryšio „likusio gyvavimo laiko" parametras $q_{xx'}$ yra susijęs su nuovargio pažeidimu $n_{xx'}$ kaip $q_{xx'} = 1 - n_{xx'}$. Kuomet PD ryšio „likusio gyvavimo laiko" parametras $q_{xx'}$ po N ciklų tampa lygus 0, laikoma, jog PD ryšys $x' - x$ yra cikliškai suardytas.

Priimant, jog $\lambda \neq 1$ ir ciklinė apkrovos spektras yra pastovios amplitudesės, dažnio f ir trikampės formos, galima daryti prielaidą, kad didžiausias PD ryšio įtempis atsiranda momentu t, o minimalus – momentu t_1. Pažymėjus $\sigma_{\min} = R\sigma_{\max'}$, $\Delta t = \frac{N}{f}$

139

ir integruojant (9) lygtį, gaunama nuovargio proceso lygtis, priklausanti nuo ciklo įtempių $\sigma_{max'}$, ciklų skaičiaus N, asimetrijos R, temperatūros T ir dažnio f:

$$n_{xx'}(N, \sigma_{max}, R, T, f) = n_{0xx'} - \left\{ (n_{0xx'} - n_{Ixx'})^{1-\lambda} - (1 - \right.$$

$$\left. \lambda)\frac{(kT)^2}{h} \frac{N}{\gamma f \sigma_{max_{xx'}}(1-R)} e^{-\frac{U}{kT}} \left[e^{\frac{\gamma \sigma_{max_{xx'}}}{kT}} - e^{\frac{\gamma R \sigma_{max_{xx'}}}{kT}} \right] \right\}^{\frac{1}{1-\lambda}} ; (\lambda \neq 1); \tag{6.11}$$

čia $n_{0xx'}$ – pradiniai PD ryšio $x - x'$ pažeidimai proceso pradžioje, n_0 – pradinė konstanta, nustatoma iš pradinių ir kraštinių proceso sąlygų (priimant $\lambda = 9$, $n_0 =$ 1.771).

KTF lygtis (6.11) prieštarauja eksperimentų duomenims esant asimetriniam ciklui, ypač kai $R \to 1$. Remiantis Fertig ir kt. [143–145] tyrimais, siekiant užtikrinti lygties (6.11) atitikimą eksperimentų rezultatams su kompozitinėmis medžiagomis, proceso temperatūra T lygtyje (11) skaičiuojama:

$$T = T^* + \sum_{i=1}^{N} \psi \frac{\sigma_a^2}{\Delta t} ; \tag{6.12}$$

čia T^* – pradinė temperatūra, ψ – proporcingumo konstanta, $\sigma_a = \frac{1}{2}(\sigma_{max} - \sigma_{min})$ – įtempių amplitudė. Šiuo atveju įvertinami ciklinio apkrovimo metu atsiradę energijos nuostoliai, kurie keičia proceso temperatūrą ir yra proporcingi ciklo įtempių amplitudes kvadratui.

6.2.4. Kompozito peridinamika

Dėl kompozitinės medžiagos savybių priklausomybės nuo krypties (tamprumo moduliai E_{11}, E_{22}, šlyties modulis G_{12}) kompozito atveju PD ryšio standumas taip pat tampa priklausomas nuo ryšio vektoriaus $x - x'$ krypties. Į daugiasluoksnio pluoštu armuoto kompozito PD modelį įtraukti skirtingi PD ryšių tipai, kaip parodyta 6.7 pav.
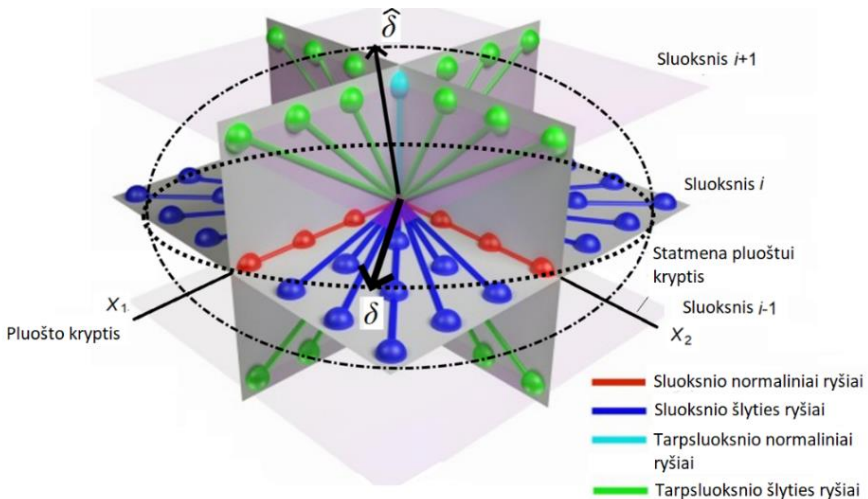
6.7 pav. Daugiasluoksnio pluoštu armuoto kompozito peridinamikos modelis

Kompozito PD parametrai a–d yra išvedami iš deformacijų energijos tankio lygybių, sulyginant PD ir CCM deformacijų energijos tankius. Kompozito modelyje yra 5 tipų ryšiai, apibrėžiami 5 skirtingais PD parametrais b: b_F – pluošto ryšiai, b_T – statmeni pluoštui ryšiai kompozito sluoksnyje, b_{FT} – šlyties ryšiai kompozito sluoksnyje, b_N – tarpsluoksnio normaliniai ryšiai, b_S – tarpsluoksnio šlyties ryšiai.

Tradicinė ryšiais grįsta PD teorija dėl medžiagos savybių apribojimų nėra tinkama modeliuoti daugelį kompozitinių konstrukcijų; gaunamos didelės paklaidos tarp modelio ir analitinių bei eksperimentinių rezultatų [120]. Būsenomis grįsta PD teorija dėl sudėtingumo negali būti realizuota daugelyje baigtinių elementų programų (išskyrus specializuotas ar atskirai rašytus PD kodus). Madenci ir kt. [146] sukūrė ryšiais grįstą PD teoriją (6.8 pav., a) su matricos ryšių pasisukimo laisvės laipsniu. Ši teorija turi tik kompozito šlyties modulio apribojimą $G_{12} = \frac{E_{22}(1-v_{12})}{2(1-v_{21}v_{12})}$ ir yra tinkama modeliuoti kompozitams bei nesunkiai realizuojama daugelyje programų.

Taikant minėtą PD teoriją, PD ryšių jėgos skaičiuojamos vertinant tiek ryšio tempimo deformaciją, tiek pasisukimo kampą:

$$\boldsymbol{f}_{xx\prime} = c_c s_{xx\prime} \boldsymbol{n}_{xx\prime} + c_d \boldsymbol{r}_{xx\prime}; \tag{6.13}$$

čia c_c ir c_d – PD ryšio tempimo ir pasisukimo standumai, $\boldsymbol{r}_{xx\prime} = \frac{(\boldsymbol{I}-\boldsymbol{n}_{xx\prime}\otimes\boldsymbol{n}_{xx\prime})}{|\xi_{xx\prime}|}\varepsilon(x)\xi_{xx\prime}$ – PD ryšio pasisukimo vektorius. Matricos ryšio pasisukimo kampas $\gamma_{xx\prime} = \frac{(\boldsymbol{u}\prime - \boldsymbol{u})\cdot\boldsymbol{n}_f}{\xi_{xx\prime}\boldsymbol{n}_t}$ skaičiuojamas kaip parodyta 6.8 pav., b.

a   b
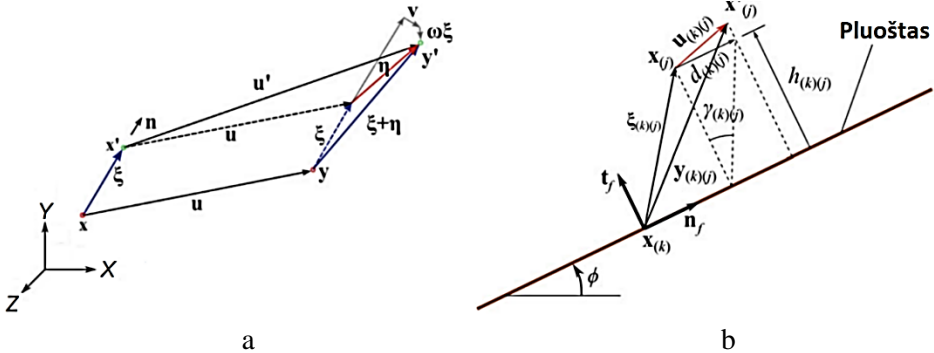
6.8 pav. Ryšiais grįsta PD su ryšių pasisukimu [120]: a – PD ryšio deformacijų principai, b – matricos ryšių pasisukimo kampo γ apibrėžimas

Kompozito atžvilgiu matricos ryšių tempimo c_{cM}, sukimo c_{dM} standumai bei pluošto ryšių tempimo standumas c_{cF} skaičiuojami taikant (14) priklausomybę:

$$c_{cM} = \frac{6}{\pi h \delta^3}(Q_{22} + Q_{12}), c_{dM} = \frac{6}{\pi h \delta^3}(Q_{22} - 3Q_{12}), c_{cF}$$
$$= \frac{2N}{\pi h \delta^3(m+1)}(Q_{11} - Q_{22}); \tag{6.14}$$

čia $Q_{11} = \frac{E_{11}}{1-v_{12}v_{21}}$; $Q_{12} = \frac{v_{12}E_{22}}{1-v_{12}v_{21}}$; $Q_{22} = \frac{E_{22}}{1-v_{12}v_{21}}$; $Q_{66} = Q_{12}$. Tarpsluoksnio ryšių standumai b_N ir b_S nustatomi pagal [105] pateiktas priklausomybes:

$$b_N = \frac{E_m}{\hat{\delta}[(h_{n+1} + h_n)V_x^{n+1} + (h_{n-1} + h_n)V_x^{n-1}]};$$ (6.15)

$$b_S = \frac{G_m}{8\pi\tilde{\delta}H_S};$$ (6.16)

kai H_S skaičiuojamas:

$$H_S = \left(\frac{h_{n+1} + h_n}{2}\right)^3 \left(\frac{\delta^2 + 2\left(\frac{h_{n+1} + h_n}{2}\right)^2}{\sqrt{\delta^2 + \left(\frac{h_{n+1} + h_n}{2}\right)^2}} - (h_{n+1} + h_n)\right)$$

$$+ \left(\frac{h_{n-1} + h_n}{2}\right)^3 \left(\frac{\delta^2 + 2\left(\frac{h_{n-1} + h_n}{2}\right)^2}{\sqrt{\delta^2 + \left(\frac{h_{n-1} + h_n}{2}\right)^2}} - (h_{n-1} + h_n)\right),$$ (6.17)

Medžiagos irimas šiuo atveju nagrinėjamas pagal du kriterijus: kritinę PD ryšio deformaciją s_c ir kritinį PD ryšio pasisukimo kampą γ_c (išskyrus pluošto ryšius, kurie negali pasisukti). Kompozito PD modelio irimo parametrų s_c ir γ_c vertes teisingiausia nustatyti iš eksperimentų.

6.2.5. Skaitmeninių vaizdų atpažinimo sistema

Skaitmeninių vaizdų atpažinimo sistema (angl. DIC) pagrįsta tiriamo objekto paviršiaus taškų sekimu su optinėmis kameromis. Naudojamos 3D DIC sistemos vaizdas parodytas 6.9 pav., o 6.10 pav., a ir b, detalizuoti pagrindiniai sistemos veikimo principai. DIC matavimai susideda iš bandinių ir sistemos paruošimo, tiriamo objekto paviršiaus nuotraukų ir rezultatų apdorojimo kompiuterine programine įranga.
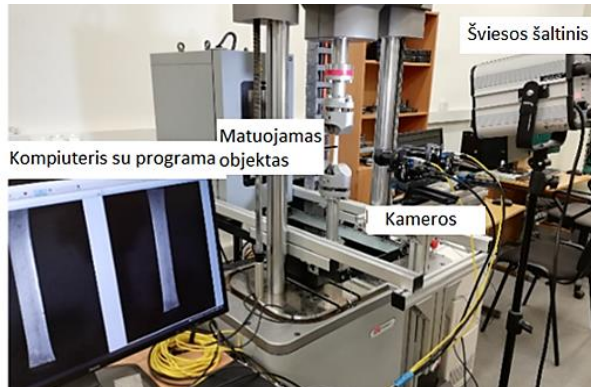
6.9 pav. Naudojamos 3D DIC sistemos bendras vaizdas
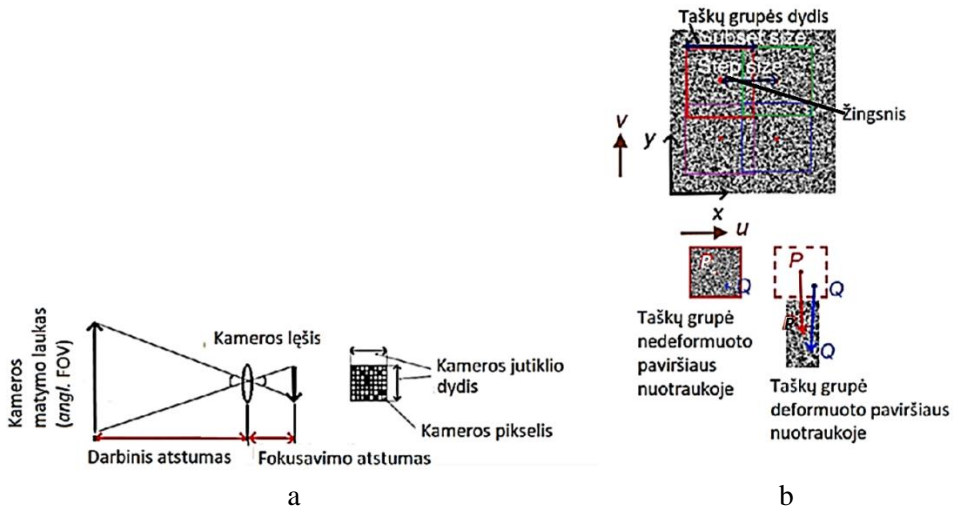
6.10 pav. Naudojama 3D DIC: a – kameros ir kiti optiniai parametrai, b – DIC taško sekimo principai [147]

Norint kameromis sekti išmatuotus objekto paviršiaus taškus, paviršiuje turi būti tam tikras raštas. Retais atvejais raštui suformuoti pakanka natūralios medžiagos paviršiaus struktūros, tačiau daugeliu atvejų būtinas dirbtinis taškinis raštas. Raštui sukurti gali būti taikomi įvairūs metodai, pavyzdžiui, dažymas, purškimas, štampai, graviravimas lazeriu ir kt. [148]. Dažytas taškinis raštas yra gana populiarus dėl metodo paprastumo, aukštos kokybės, šiame tyrime taip pat naudotas dažytas raštas, sukurtas su specialiu voleliu arba purkštuvu. Aukštos kokybės raštas pasižymi dideliu kontrastu, taškų padėtis yra atsitiktinė, o dydis vienodas. Rašto dydis parenkamas pagal matymo lauką (angl. FOV) ir turi atitikti 3×3÷7×7 kameros pikselių dydžio sąlygą. Optimalus rašto tankis yra 50 %. Taip pat svarbus geras rašto sukibimas su objekto paviršiumi.

Objekto paviršiaus taškų poslinkiams ir deformacijoms apskaičiuoti naudojama nedeformuoto taškinio rašto (objekto paviršiaus) nuotrauka ir deformuoto rašto (objekto paviršiaus) nuotraukų serija. Kameros pasirinkimas susijęs su objekto dydžiu. Svarbi ir kameros skiriamoji geba. Norint užfiksuoti lokalius kvazistatinio proceso poveikius, reikalinga didelės skiriamosios gebos kamera, kurios pikselio dydis yra mažas. Dinaminėms problemoms, pavyzdžiui, didelio dažnio cikliniam apkrovimui, reikalinga kamera su dideliu kadrų dažniu. Kadangi kameros pikseliai turi būti susiję su faktiniais objekto matmenimis, prieš darant nuotraukas reikia atlikti DIC sistemos kalibravimą. 2D DIC sistemos kalibravimui pakanka tik vieno objekto matmens, o 3D DIC reikia apie 20÷30 kalibravimo nuotraukų, padarytų skirtingais orientacijos kampais. Sistemai kalibruoti naudojamos specialios kalibravimo plokštelės su žinomu atstumo tarp taškų dydžiu. Norint atlikti patikimus DIC matavimus, labai svarbu užtikrinti tinkamą kamerų fokusavimą ir objekto apšvietimą. Šviesos šaltinis ir kameros turi būti sureguliuoti taip, kad užtikrintų pakankamą apšvietimą, tačiau ne per didelį, kad kamerų pikseliuose nebūtų pasiekta didžiausia apšvietimo vertė.

Paskutinis DIC etapas – vaizdų tolesnis apdorojimas. Vietoj atskirų modelio taškų (6.8 pav., c) stebima rašto taškų dalis, vadinama taškų grupe ar poaibiu, siekiant apskaičiuoti kiekvieno poaibio centrinio taško P poslinkius ir deformacijas. Atstumas tarp kiekvieno poaibio centro vadinamas žingsnio dydžiu (6.8 pav., c), poaibiai gali persidengti tarpusavyje. Pirmoji nuotrauka (nedeformuoto objekto paviršiaus nuotrauka) naudojama kaip atskaitos nuotrauka, kurios atžvilgiu galima apskaičiuoti poaibių centro taškų P poslinkius kitose deformuoto objekto paviršiaus nuotraukose. Poaibio forma priklauso nuo DIC programinės įrangos, pavyzdžiui, turimoje DIC sistemos programinėje įrangoje VIC-3D naudojami kvadratiniai poaibiai [150]. Poaibio ir žingsnio dydžiai yra vartotojo nustatyti parametrai VIC-3D programinėje įrangoje, tačiau DIC programinė įranga VIC-3D leidžia automatiškai parinkti poaibio dydį pagal raštą ir įvertina galimas matavimo paklaidas, susijusias su pasirinktu poaibio dydžiu. Poaibio dydžiui yra taikomas reikalavimas, kad jį turėtų sudaryti bent trys rašto taškai [148], nes per mažų poaibių negalima išskirti vienas iš kito ir beveik neįmanoma sekti rašto taškų. Tačiau per dideli poaibiai gali sudėtingai deformuotis, todėl sumažėja matavimo tikslumas. Be to, didelis poaibis padidina skaičiavimo laiką. Optimali žingsnio dydžio vertė yra maždaug 1/4 poaibio dydžio.

Deformavus matuojamo objekto paviršių, deformuoto vaizdo poaibis lyginamas su nedeformuoto vaizdo poaibiu siekiant rasti kiekvieno poaibio centro tašką P (6.9 pav., c). Formos funkcijos naudojamos nustatant kitų poaibio taškų Q poslinkius, kai žinomi centrinio taško P poslinkiai.

Kaip minima VIC-3D vadove [153], deformacijos VIC-3D skaičiuojamos ne diferencijuojant DIC poslinkio formos funkcijas, o sudarant dirbtinius trikampius baigtinius elementus. Kiekvieno trikampio viršūnės yra poaibių centriniai taškai P su anksčiau apskaičiuotais poslinkiais. Taikant kiekvieno trikampio elemento srityje apibrėžtas deformacijų formos funkcijas, galima apskaičiuoti deformacijas bet kuriame trikampio vidiniame taške. Kadangi šie trikampiai elementai yra kelių pikselių dydžio, apskaičiuotos deformacijos yra labai triukšmingos, todėl naudojamas deformacijų filtravimas jas vidurkinant pasirinkto dydžio apskritime. Deformacijų filtro dydis programoje VIC-3D apibrėžiamas kaip apskritimo, kuriame vidurkinamos deformacijos, skersmuo, išreikštas DIC žingsnio dydžiais, pavyzdžiui, filtras 5 – 5 žingsniai, filtras 35 – 35 žingsniai. Problema, su kuria susiduriama taikant tokį deformacijų skaičiavimo algoritmą, yra dideli triukšmai deformacijose dėl DIC poslinkių diferencijavimo arba sumažėjęs deformacijų tikslumas dėl deformacijų vidurkinimo siekiant sumažinti triukšmus.

6.3. EKSPERIMENTINIAI TYRIMAI

6.3.1. Naujas metodas, pagrįstas PDDO, siekiant padidinti DIC deformacijų tikslumą

Šiame tyrime analizuojami keli PPDO taikymo DIC poslinkių laukui pavyzdžiai. Pirma, DIC deformacijoms analizuoti naudojamas tempimo bandinys su skyle. Bandinio matmenys 180 mm × 35 mm ir 10 mm, skylės skersmuo pasirinkti laisvai ir nėra nurodyti jokiame bandymų standarte. Bandinio medžiaga yra DIBOND kompozitas – daugiasluoksnė medžiaga, kurios bendras storis 3 mm, sudaryta iš trijų sluoksnių: 2,4 mm storio polietileno šerdies ir 0,3 mm storio išorinių sluoksnių iš

aliuminio EN AW 5005. Eksperimento schema pateikta 6.11 pav. Tempimo bandymui mašinoje INSTRON E10000 (6.11 pav.) parinktas tempimo greitis 3 mm/min. DIC-PDDO metodo privalumas, palyginti su DIC deformacijų skaičiavimo algoritmu, matomas 6.12 pav.
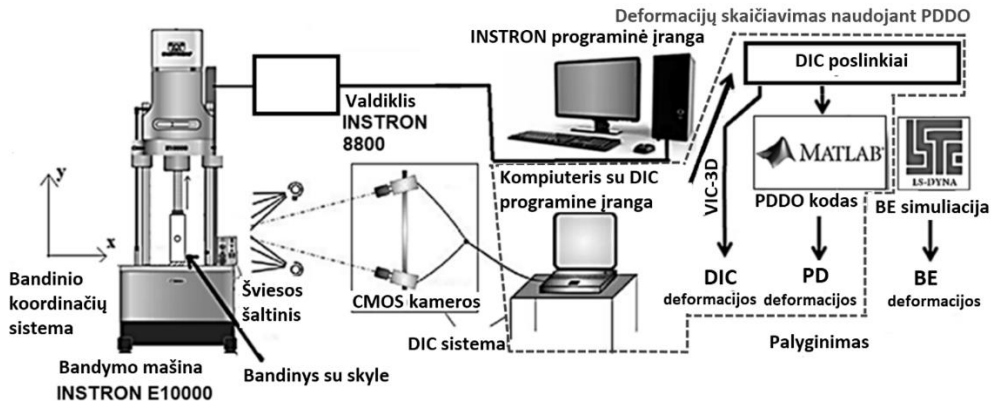
6.11 pav. Deformacijų matavimo schema taikant DIC, DIC-PDDO ir palyginimui baigtinių element (BE) simuliaciją
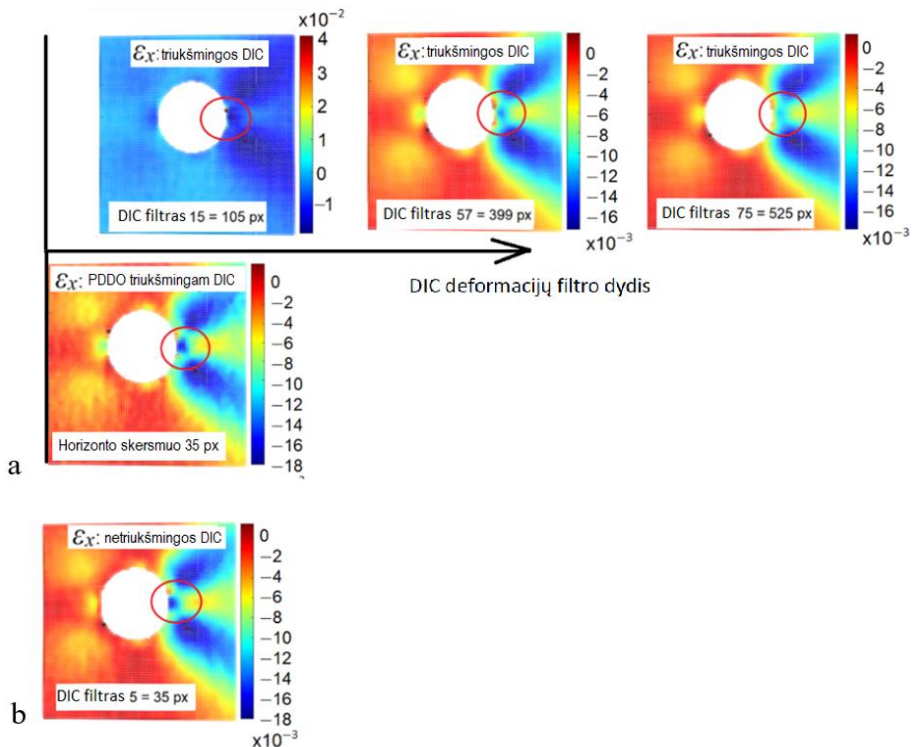
6.12 pav. Deformacijų filtravimas naudojant DIC deformacijų filtrus ir PD horizontus esant triukšmingiems DIC duomenims: a – deformacijų laukų palyginimas, b – „teisingas" deformacijų laukas

Iš 6.12 pav., a, matyti, kad mažiausias DIC deformacijų filtro dydis, reikalingas deformacijų triukšmui pašalinti ir „teisingoms" deformacijų vertėms gauti (toks pat kaip 6.12 pav.,b, „netriukšmingos DIC" deformacijos), yra 525 px. Kita vertus, tokios vertės deformacijų filtras suvidurkina deformacijų lauką taip, kad deformacijų pikai išfiltruojami (palyginti 6.12 pav., a, raudoname apskritime esančias deformacijas (filtruotas) ir 6.12 pav., b ,deformacijas („teisingas" deformacijų laukas)). PDDO atveju, taikant PDDO triukšmingam DIC poslinkiui, triukšmui sumažinti pakanka tik 35 px PD horizonto skersmens ir gaunamas beveik „teisingas" deformacijų laukas, panašus į „triukšmingo DIC" su 399 px filtru lauką, tačiau be prarastų deformacijų ekstremumų. Taigi DIC-PDDO metodas yra daugiau nei 11 kartų efektyvesnis (399 px DIC filtras ir 35 px PD H_x) deformacijų filtravimo, triukšmų pašalinimo neišfiltruojant deformacijų pikų atžvilgiu nei esamas VIC-3D deformacijų skaičiavimo algoritmas.

Siekiant išbandyti PDDO pagrįstą DIC deformacijų skaičiavimo algoritmą remiantis ne tik šiuo bandinio su skyle pavyzdžiu, naudojamas neseniai sukurtas DIC metrologinio efektyvumo rodiklis (MEI). MEI [159,160] jungia DIC erdvinę ir matavimų skiriamąsias gebas. MEI apskaičiuojamas pagal specialias DIC iššūkio 2.0 [175] „Star 6" dirbtinai sugeneruotas bandinio paviršiaus rašto nuotraukas. „Star 6" dirbtinių nuotraukų rinkinį sudaro nedeformuoto objekto etaloninis vaizdas, deformuotas „žvaigždės spindulių" formos sinusine vertikalios 5 % deformacijos amplitude vaizdas ir vaizdas su dirbtiniu triukšmu. DIC ir DIC-PDDO deformacijų skaičiavimo algoritmų palyginimas pagal MEI nustačius tokias pat erdvines skiriamąsias gebas ir pasirinkus keletą matavimo taškų pavaizduotas 6.13 pav.
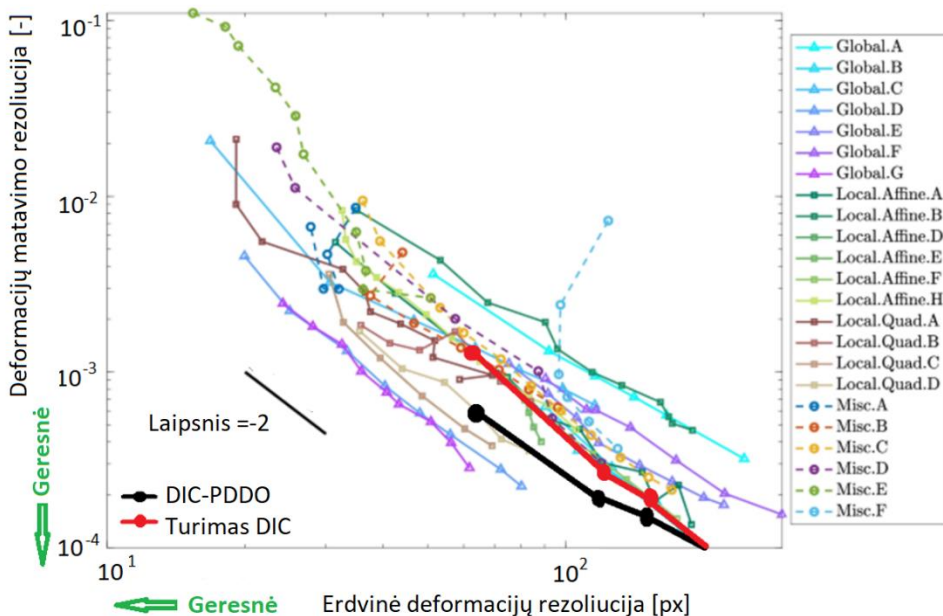
6.13 pav. DIC deformacijų skaičiavimo algoritmų palyginimas pagal erdvinę ir matavimo skiriamąsias gebas. Duomenys iš [159], papildyti išbandytais esamu DIC ir DIC-PDDO algoritmais

Esant tai pačiai $l_{10\%}$ = 207 px erdvinei skiriamajai gebai, triukšmo standartinis nuokrypis DIC atveju yra 1,13 · 10⁻⁴, o DIC-PDDO atveju 0,957·10⁻⁴. Dėl šių verčių MEI_{DIC} = 2,65 µε²·px ir $MEI_{DIC-PDDO}$ = 1,98 µε² rodo, kad DIC-PDDO metodas yra 1,34 karto efektyvesnis nei dabartinis DIC programinės įrangos algoritmas. Siūlomo DIC-PDDO metodo matavimo skiriamoji geba, palyginti su turimu DIC algoritmu, yra geresnė kiekviename bandymo taške (6.13 pav.), kai DIC ir DIC-PDDO erdvinė skiriamoji geba yra vienoda. Tai lemia DIC-PDDO geresnį efektyvumą, matomą per mažesnes MEI vertes. Be to, DIC-PDDO efektyvumas didėja esant mažesnėms erdvinės skiriamosios gebos vertėms (skirtumai tarp „DIC-PDDO" ir „Turimo DIC" kreivių 6.13 pav.), todėl DIC-PDDO metodas geriau pritaikomas lokalizuotoms deformacijoms, pavyzdžiui, nuovargio plyšio atsiradimui aptikti, defektams, pažeidimams medžiagoje nustatyti. DIC-PDDO algoritmo naudojimas vietoj įprastinio DIC atliekant nuovargio analizę yra ypač aktualus šiame tyrime.

6.3.2. Nerūdijančio plieno 316L cikliniai eksperimentai

Kaip pateikta tyrių metodikoje, nuovargio bandymams pasirinktas nerūdijantis plienas 316L Atlikti 3 eksperimentai: 1) simetrinės (R = -1) pagal deformacijas kontroliuojamos ciklinės apkrovos eksperimentas, kurio deformacijos amplitudė ε_a = 0,0018; 2) asimetrinės kintamos amplitudės ciklinės apkrovos eksperimentas, sudarytas iš 1 simetrinio ε_a = 0,006 ciklo ir 200 asimetrinių ε_a = 0.0018 ciklų blokų, kai vidutinė deformacija $\bar{\varepsilon}$ = -0,0042 (POL apkrova); 3) asimetrinės kintamos amplitudės ciklinės apkrovos eksperimentas, sudarytas iš 1 simetrinio ε_a = 0,006 ciklo ir 200 asimetrinių ε_a = 0,0018 ciklų blokų, kai vidutinė deformacija $\bar{\varepsilon}$ = 0,0042 (PUL apkrova). Iš viso atlikti 3 ciklinio apkrovimo eksperimentai (rezultatai pateikti 6.14 pav.): 1 simetrinis, 1 POL apkrovos ir 1 PUL apkrovos eksperimentas.
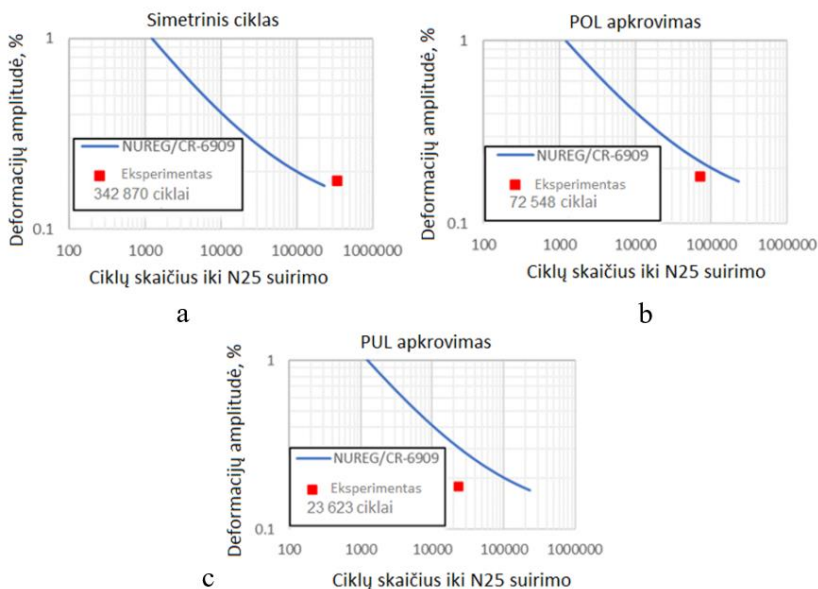
6.14 pav. Eksperimentų rezultatų (ciklų skaičius iki N25 suirimo) ir medžiagos S-N kreivės [166] palyginimas: a – simetrinė ±0,18 % deformacijos apkrova, b – POL apkrova, c – PUL apkrova

Bandinio suirimo kriterijumi, rodančiu eksperimento pabaigą, laikomas ciklo didžiausių įtempių sumažėjimas bandinyje 25 % (N25 kriterijus). Bandiniai suiro po 342870, 72548 ir 23623 N25 ciklų atitinkamai simetrinės, POL ir PUL apkrovos atvejais. Pastebėtas kelis kartus didesnis skirtumas, palyginti su medžiagos S-N kreive PUL apkrovos atveju, tačiau gautas rezultatas patenka į tokios apkrovos eksperimentų rezultatų [166] ribas. Eksperimentų metu gautos procesų histerezės kilpos pavaizduotos 6.15–6.17 pav.
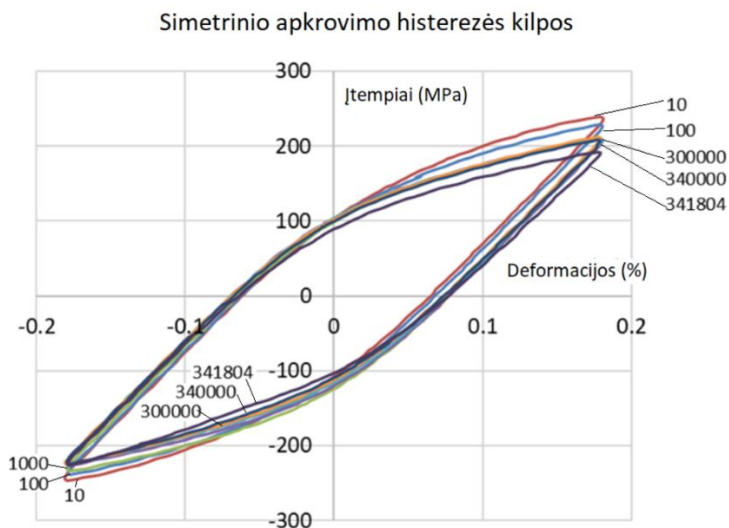
6.15 pav. Eksperimento metu gautos histerezės kilpos esant simetriniam ±0,18 % deformacijos cikliniam apkrovimui
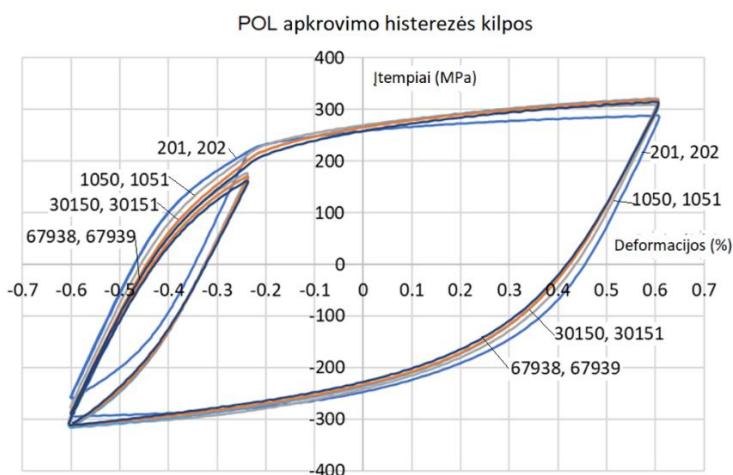
6.16 pav. Eksperimento metu gautos histerezės kilpos esant POL apkrovimui

148
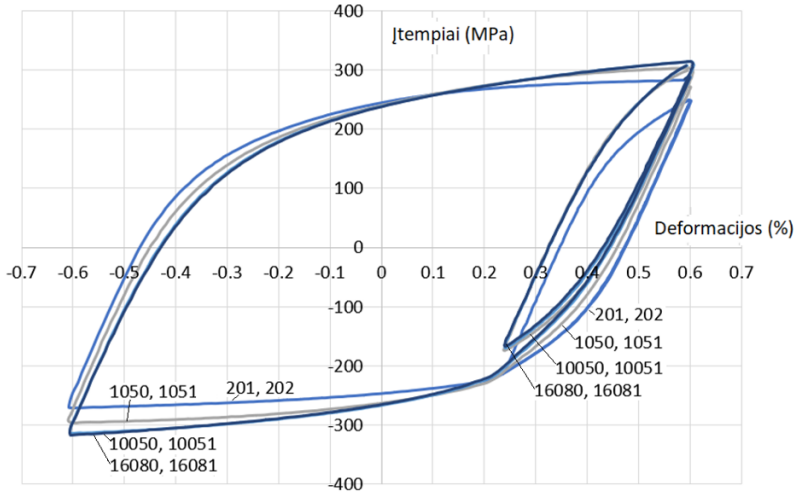
6.17 pav. Eksperimento metu gautos histerezės kilpos esant PUL apkrovimui

6.3.3. Kompozito eksperimentai

Pradžioje atlikti iš CFRP plokštės (sluoksnių išsidėstymas [(0′90)º/90 º/0º]s.) standartinių ASTM D3039 [104] kompozito bandinių tempimo eksperimentai. 0º kampu iš CFRP plokštės išpjauto bandinio suirimas įvyksta esant deformacijai, kuri apytiksliai lygi 0,0102. Bandinio stiprumo riba yra 800 MPa. Bandinys pasižymi idealiai tiesine tampriąja elgsena, kai efektinis tamprumo modulis E_{0ef} = 78 GPa, ir trapiu suirimu. Kai bandinio pjūvio kampas 45º, bandinio standumas yra maždaug 5 kartus mažesnis, palyginti su 0º kampu išpjautu bandinio standumu, o efektinis tamprumo modulis E_{45ef} = 15,2 GPa, apskaičiuotas deformacijų intervale 0,0005 ÷ 0,005. Šio bandinio suirimas įvyksta dėl šlyties, o lūžis matomas 45º kampu.

Remiantis prielaidomis, kad vidiniai kompozitinių konstrukcijų defektai turi didelę įtaką kompozito tarnavimo laikui [28] ir nė viena kompozitinė struktūra negali būti visiškai tobula, analizuojant kompozito nuovargį daugiausia dėmesio skiriama kompozitui su defektais. Tyrime iš pradžių nagrinėjami du dažniausiai pasitaikantys defektų tipai: delaminacija ir pluošto trūkimas, taip pat analizuojamas jų nustatymas naudojant DIC paviršiaus deformacijų matavimus.

Tiriant CFRP kompozito 500 mm×500 mm plokštę su 4 delaminacijomis, DIC paviršiaus deformacijų matavimų nepakako nustatyti esančioms delaminacijoms, net ir delaminacija, esanti atstumu 0,8 mm nuo tiriamo paviršiaus, nebuvo aptikta. Vis dėlto dinaminės charakteristikos, pavyzdžiui, savojo dažnio pokyčiai, leido numatyti delaminacijas. Kadangi šiame tyrime daugiausia dėmesio skiriama DIC ir nenorint išsiplėsti į dinaminių charakteristikų skaičiavimą, delaminacijų analizė CFRP kompozite plokštėje toliau nepateikiama.

Nagrinėjant pluošto trūkimus, buvo pagaminti bandiniai su imituojamais šio tipo defektais. Bandinyje išfrezuoti 1 ir 1,5 mm gylio, 10 mm ilgio, 1 mm pločio grioveliai, sudarantys 45º kampą bandinio tempimo krypčiai. CFRP bandinių su imituotais pluošto trūkimo defektais brėžinys pateiktas 6.18 pav.
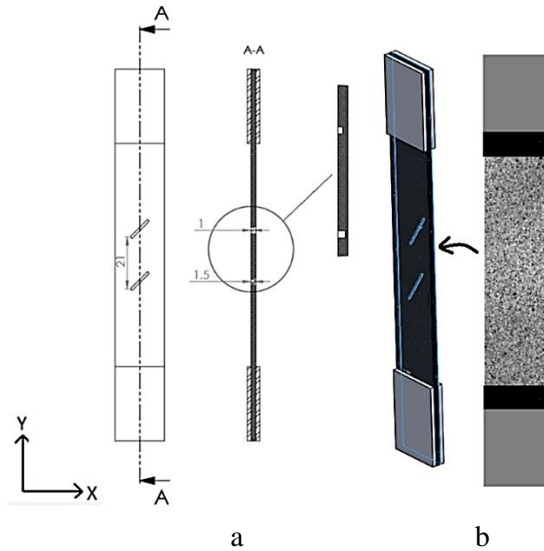
6.18 pav. CFRP bandinio su 2 įtrūkimais (išfrezuoti grioveliai) schema: a – brėžinys, b – DIC matavimams naudojamas raštas

Deformacijų laukai tempimo kryptimi *Y*, kai statinė tempimo apkrova sukurta 3000 N jėga, apskaičiuoti naudojant įprastinį DIC ir DIC-PDDO ir parodyti 6.19 pav. „Defektas 1" 6.19 pav., reiškia 1 mm gylio griovelį bandinio galinėje pusėje (jo gylis iki paviršiaus, kuriame matuojamos deformacijos, taip pat yra 1 mm); „Defektas 2" reiškia panašų griovelį, kurio gylis yra 1,5 mm (gylis iki paviršiaus, kuriame matuojamos deformacijos, yra 0,5 mm).
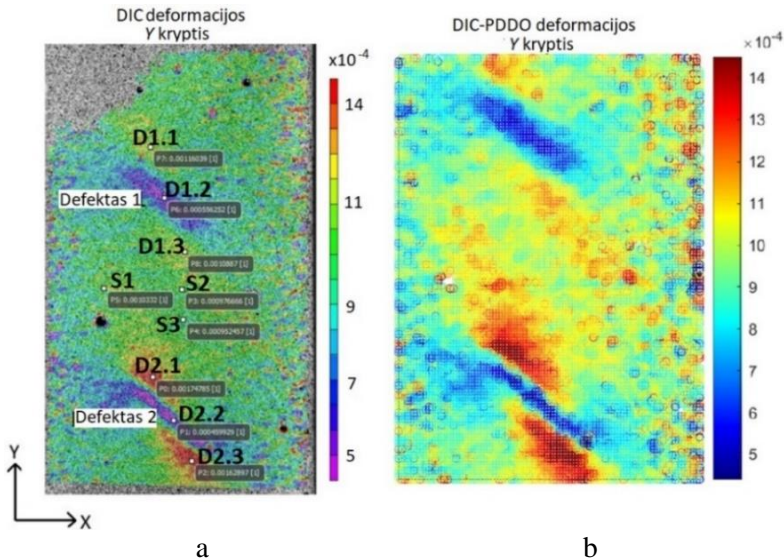
6.19 pav. Išilginių (tempimo kryptimi) deformacijų laukai CFRP bandinio su 2 pluošto įtrūkimais (išfrezuotais grioveliais) paviršiuje: a – įprastinis DIC, b – DIC-PDDO

Dirbtiniai defektai bandinyje (1 ir 2 defektai) matomi tiek DIC, tiek DIC-PDDO apskaičiuotuose bandinio paviršiaus deformacijų laukuose. Be to, pagal tokius deformacijų matavimus galima įvertinti defekto vietą ir dalinai formą (ypač „Defekto 2"). DIC-PDDO metodu apskaičiuotas deformacijų laukas yra praktiškai identiškas DIC deformacijų laukui, todėl net ir įprastinio DIC pakanka, kad būtų galima aptikti pluošto įtrūkimus kompozitinėje medžiagoje, šiuo atveju CFRP kompozite.

6.4. SKAITINIS MODELIAVIMAS

6.4.1. Izotropinės medžiagos peridinamikos modelio kalibravimas

Literatūroje [164,165] pateikiamos tokios CH83-2 epoksidinės dervos medžiagos savybės: tamprumo modulis E = 2,9÷3,4 GPa, Puasono koeficientas v = 0,3÷0,4, stiprumo riba σ_u = 5÷97 MPa ir atplėšimo energija G_c = 1,0÷1,6 kJ/m². Atlikus pagal standartą ASTM D638 - 10 [101] pagamintų 50 mm bazės ilgio, 13 mm pločio, 6,5 mm storio dervos CR83-2 bandinių tempimo eksperimentus su DIC matavimais (6.20 pav.), sukurti bandinio PD modeliai.

PD modeliai realizuoti MATLAB programoje naudojant 2D plokščių įtempių būvio formuluotę ir BBPD bei SBPD teorijas. Pasirinktas PD tinklelio dydis Δx = 1,08 mm, kai PD horizonto dydis δ =3,1Δx. PD modelio medžiagos tamprumo (tamprumo modulio E ir Puasono koeficiento v) bei irimo parametrų (kritinė PD ryšio deformacija s_c) kalibravimo procedūros schema pateikta 6.20 pav.
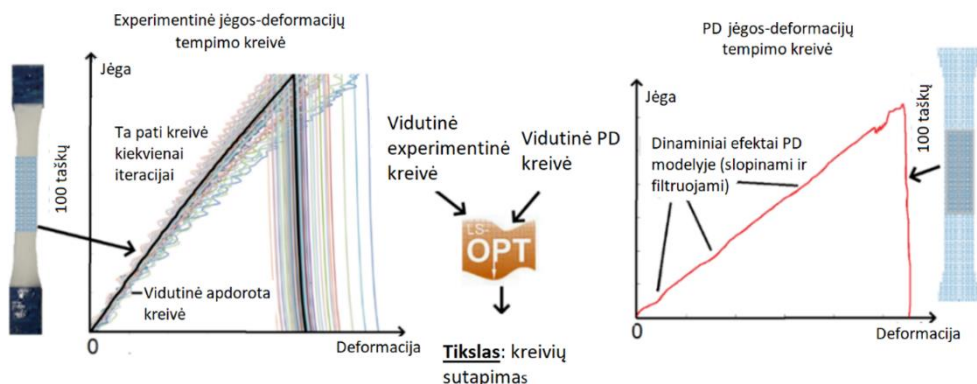
6.20 pav. PD modelio kalibravimo procedūros schema [169]

Kalibravimo procedūros metu naudoti eksperimentiniai DIC deformacijų matavimai ir sudarytos 100 bandinio paviršiaus taškų jėgos ir deformacijų kreivės. Naudojant optimizavimo programą LS-Opt, PD modelio parametrai E, v, s_c parinkti taip, kad užtikrintų mažiausius skirtumus tarp vidutinės eksperimentinės (6.20 pav.) ir PD modelio (6.20 pav.) jėgos ir deformacijų kreivių.

Po 10 iteracijų programoje LS-Opt santykiniai eksperimentinės ir modelio kreivių plotų skirtumai siekia $3\cdot10^{-4}$ BBPD modelio atžvilgiu ir 0,05 – SBPD modelio atžvilgiu. Po kalibracijos PD sumodeliuoti ir eksperimentiniai poslinkių ir deformacijų laukai, taip pat bandinio suirimo pobūdžiai pateikti 6.21 pav. Kalibruoti PD parametrai ir kita procedūros informacija pateikta 6.4 lentelėje.
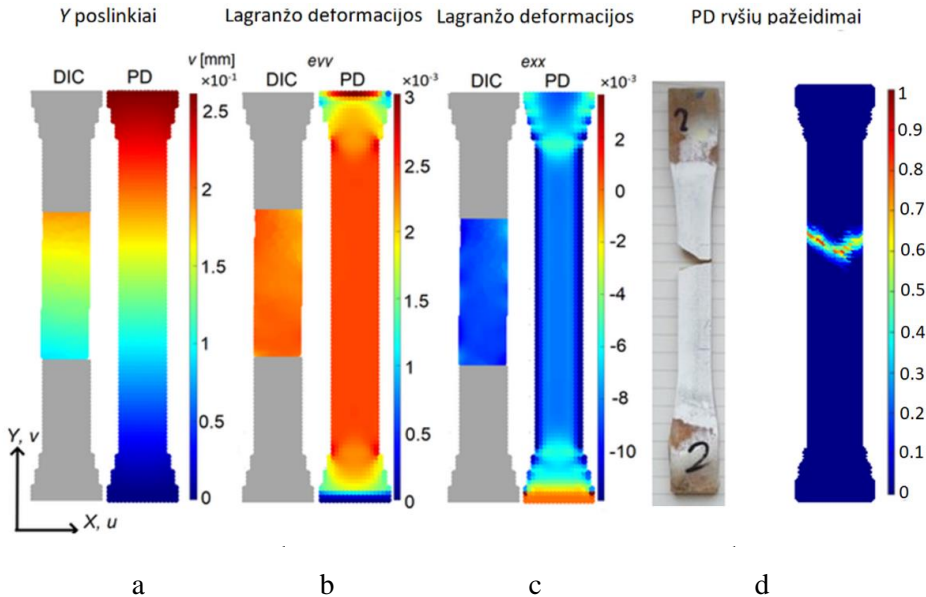
6.21 pav. Eksperimento (DIC) ir DIC kalibruoto PD modelio palyginimas [169]: a – Y poslinkio laukai, b – išilginės deformacijos ε_y, c – skersinės deformacijos ε_x, d – suirimo pobūdis

6.4 lentelė. PD modelio kalibravimo rezultatai

	BBPD	SBPD
Kalibruoti parametrai		
E [GPa]	3,13	3,26
v	0,33 (fiksuotas)	0,384
s_c	0,0173	0,0177
Trukmė [s]	1343	4379
PD modelio skaičiavimo trukmė [s]	4,2	61,8

6.21 pav. matomas kokybinis (spalvų pasiskirstymas) ir kiekybinis (reikšmės) kalibruoto PD modelio rezultatų ir DIC eksperimentinių matavimų atitikimas. Tačiau vis dar yra tam tikrų nesutapimų dėl medžiagos struktūros nehomogeniškumo, kuris akivaizdus DIC eksperimentiniuose deformacijų laukų matavimuose (6.21 pav., b ir c), ir dėl paviršiaus efektų, kurie PD sumodeliuotuose laukuose nėra visiškai eliminuoti (ypač deformacijose ε_x (6.21 pav., c) dėl pasirinktos PD modelio diskretizacijos $\varDelta x$).

PD kritinei ryšio deformacijai apskaičiuoti reikia žinoti medžiagos kritinę atplėšimo energiją G_c, o tam reikia atlikti sudėtingesnius eksperimentinius bandymus. Siūlomą kalibravimo procedūrą galima laikyti paprastesniu, veiksmingesniu ir tikslesniu metodu PD kritinei ryšio deformacijai nustatyti. Taip pat siūloma procedūra yra efektyvi esant sudėtingos medžiagos PD modelio parametrų parinkimui, pavyzdžiui, tampriai plastinė medžiaga ar kompozitas.

6.4.2. Plieno 316L ciklinio apkrovimo modeliai naudojant KTF-PD teorijas

3D BBPD teorija taikoma standartinio bandinio, pagaminto iš 316L nerūdijančio plieno, PD nuovargio modeliui (6.22 pav.). PD modelis sudarytas iš 726 medžiagos taškų (17 taškų bandinio skersmeniui), PD horizonto dydis nustatytas $\delta = 3{,}1\Delta x$ (6.22 pav.). Siekiant taupyti skaičiavimo laiką, modeliuojama tik bandinio matuojama sritis. PD ryšio suirimas aktyvus tik modelio viduryje (6.22 pav., a) siekiant išvengti klaidingo suirimo ties pridėta jėga ar įtvirtinta modelio dalimi. Bandymų sąlygose [166] nurodyta didžiausia simetrinės ciklinės apkrovos deformacijos vertė 1,8–10^{-3} pasiekiama apkraunant modelį nustatytu poslinkiu viršuje ir fiksuojant jį apačioje δ storio taškų sluoksniu (6.22 pav., b).
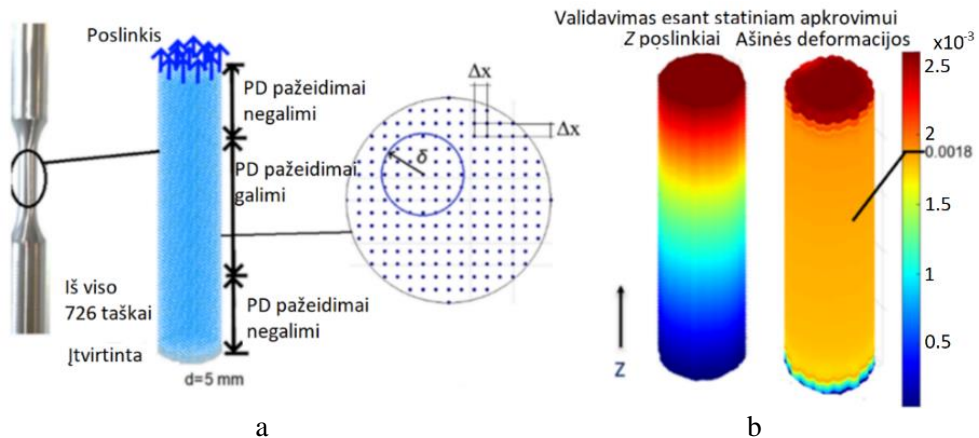
6.22 pav. Standartinio 316L nerūdijančio plieno bandinio PD modelis: a – geometrija, b – validavimas veikiant statinei apkrovai [176]

PD modelis cikliškai kalibruotas remiantis simetrinio ciklinio apkrovimo NUREG/CR-6909 S-N kreive. Taikytos dvi KTF teorijos: originali, pagal (6.11) lygtį ir modifikuota, kai įvertinami proceso energijos nuostoliai. Šiuo atveju priimama, kad energijos nuostoliai proporcingi ciklo histerezės kilpos plotui, išmatuotam iš eksperimentinių histerezės kilpų (6.15–6.17 pav.). KTF-PD sumodeliuotų, eksperimentinių ir kitose laboratorijose [166] atliktų tų pačių eksperimentų rezultatų palyginimas pateikiamas 6.23 pav.

Sumodeliuoti N25 ciklų skaičiai 183410 (įprastinė KTF) ir 190170 (modifikuota KTF) simetrinės ±0,18 % deformacijos ciklinės apkrovos atveju (6.23 pav.) atitinka teorinę 171517 ciklų prognozę pagal NUREG/CR-6909 kreivę ir eksperimentinius bandymus JNES laboratorijoje [166] (205500 ciklų). Tiek pagal įprastinę, tiek pagal modifikuotą KTF teorijas (modelis kalibruotas pagal simetrinio ciklo NUREG/CR-6909 kreivę) gaunamas panašus N25 ciklų skaičius, palyginti su prognozuojamu pagal asimetrinę NUREG/CR-6909 kreivę POL apkrovai ir VTT laboratorijos eksperimentą [166] (6.23 pav.). Nepaisant to, geresnį atitikimą su prognozuojamu POL apkrovos S-N kreivės rezultatu galima pasiekti naudojant įprastinę KTF (147060 ciklų pagal įprastinę KTF, 185280 ciklų pagal modifikuotą KTF ir 158719 ciklų pagal NUREG kreivę). Priešingai, tik modifikuotas KTF

metodas yra teisingas PUL apkrovai (6.23 pav.). Įprastinis KTF prognozuoja tik 3185 ciklus, o modifikuotas KTF – 74675 ciklus. Galima priimti, kad sumodeliuotas 74675 ciklų rezultatas yra tikslus, atsižvelgiant į NUREG kreivę PUL apkrovai, pagal kurią apskaičiuota 70029 N25 ciklų, o PUL apkrovos eksperimentiniai rezultatai (6.23 pav.) svyruoja nuo 24000 iki 70000 N25 ciklų.
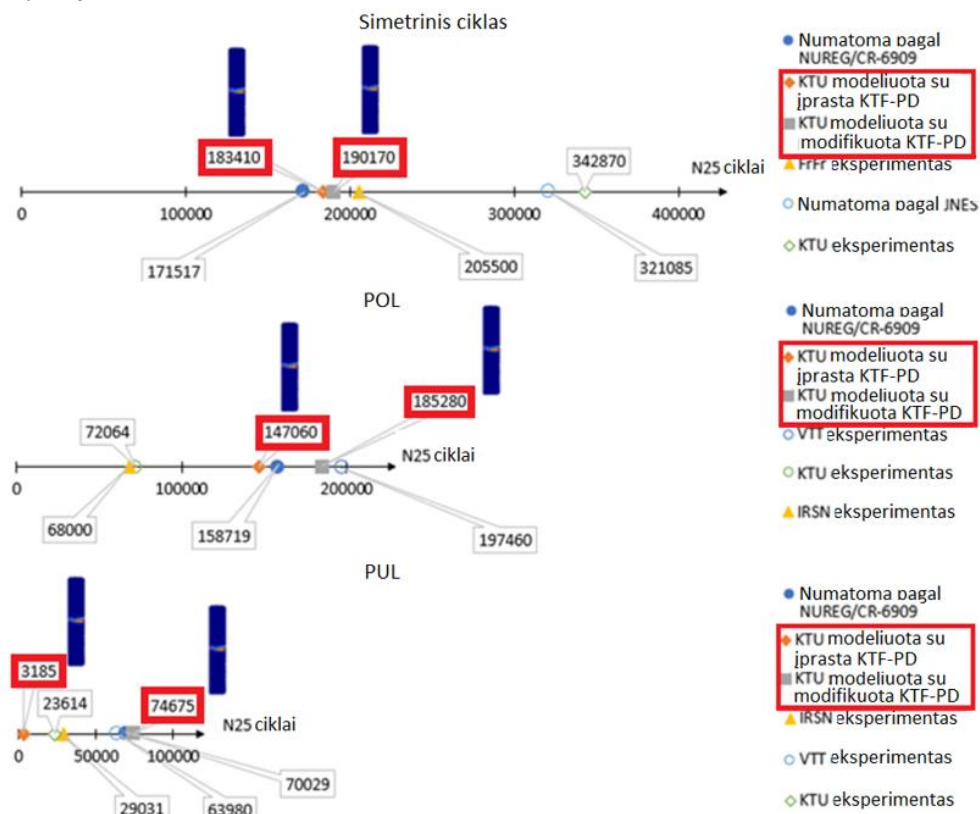
6.23 pav. Eksperimentinių (kitų laboratorijų bandymų rezultatai iš [166]) ir KTF-PD modeliavimo rezultatų palyginimas simetrinei ±0,18 % deformacijai ir asimetrinėms POL ir PUL apkrovoms kambario temperatūroje [176]

Apžvelgus eksperimentinius ir modeliavimo rezultatus (6.23 pav.) matyti, kad modifikuota KTF, kalibruota tik pagal simetrinės apkrovos S-N kreivę, prognozuoja ciklinį patvarumą esant visiems ciklinės apkrovos tipams su nuovargio analizei priimtinu atitikimu eksperimentiniams rezultatams ir NUREG CR/6909 kreivėms. Vidutinė visų apkrovimo tipų paklaida tarp modifikuoto KTF-PD modelio numatytų N25 ciklų ir eksperimentų rezultatų bei S-N kreivių siekia 15 %.

6.4.3. Kompozito defektų nustatymas naudojant DIC

Remiantis 6.19 pav. pateiktu DIC deformacijų lauku, išmatuotu ant CFRP bandinio su grioveliu kitoje pusėje, buvo sukurtas šio bandinio baigtinių elementų modelis programoje ANSYS. Medžiagos savybės modelyje parinktos taip, kad užtikrintų efektyvų modelio standumą tokį, koks buvo nustatytas eksperimentiškai

154

tiriant iš CFRP plokštės 0º ir 45º laipsnių kampais išpjautų ASTM D3039 [104] bandinių savybes. 6.24 pav., a, matoma, kad ANSYS sumodeliuotos deformacijos esant 1,.5 mm gylio defektui atitinka DIC išmatuotas. 6.24 pav., b, pateikta DIC ir ANSYS deformacijų priklausomybė nuo defekto atstumo nuo matuojamo paviršiaus. Deformacijos matuotos taške D2.1 (6.24 pav., taip pat 6.19 pav.).
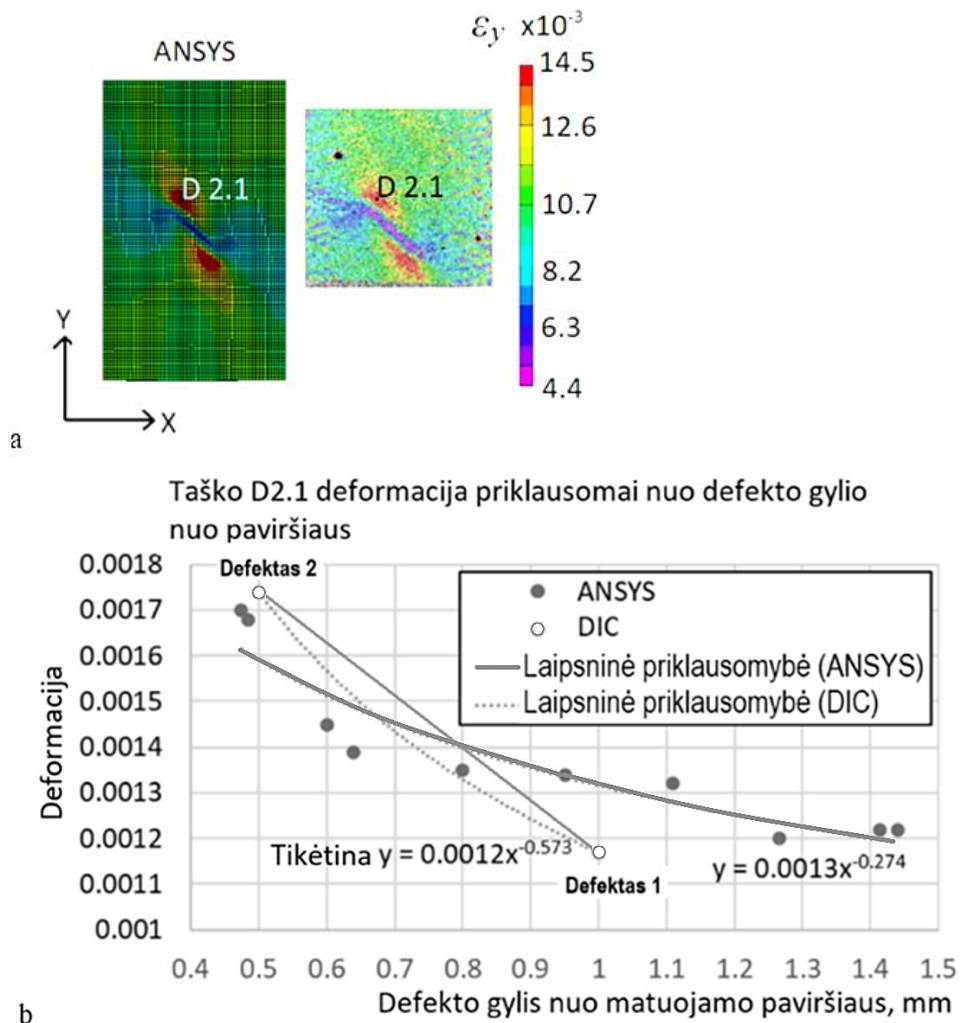
6.24 pav. CFRP defekto nustatymas naudojant DIC: a – ANSYS ir DIC deformacijų laukai, b – ANSYS ir DIC deformacijų priklausomybė nuo defekto atstumo nuo matuojamo paviršiaus

Iš rezultatų 6.24 pav. matyti, kad taško D.2.1 *Y* krypties deformacija ANSYS modelyje yra 4 laipsnio atvirkščiai proporcinga defekto gyliui nuo bandinio paviršiaus. Spėjama, kad bandinio defekto 1 ir defekto 2 eksperimentiniai DIC deformacijų matavimai (6.24 pav., b) sudaro beveik atvirkštinį kvadratinį proporcingumą, nors tokiam ryšiui patvirtinti reikia daugiau duomenų taškų. 6.24

155

pav., b, deformacijų skirtumai tarp ANSYS ir DIC didėja didėjant defekto gyliui nuo bandinio paviršiaus (gyliui 0,5 mm – deformacijų skirtumas 2,2 %, gyliui 1 mm – skirtumas iki 14 %). Iš dabartinių 6.24 pav., b, pateiktų duomenų galima daryti išvadą, kad siūlomas defektų nustatymo metodas naudojant DIC deformacijų laukus ir baigtinių elementų modeliavimą, atkartojant DIC deformacijų laukus ir siekiant nustatyti defekto formą, yra tikslus iki 0,8 mm atstumu nuo paviršiaus, ant kurio matuojamos deformacijos, esantiems defektams. Ši išvada teisinga atliktus analizę su defektu, kurio plotis yra 30 % bandinio pločio. Be to, verta atkreipti dėmesį į tai, kad medžiagų savybių ir geometrijos skirtumai, apkrovos sąlygos (šiuo atveju galimas bandinio necentriškumas bandymo mašinoje), DIC matavimo paklaidos lemia šio defektų nustatymo metodo tikslumą.

6.4.4. Kompozito PD modelis

Toks pat, kaip ir programoje ANSYS sukurtame modelyje (6.24 pav., a), CFRP kompozitinis bandinys su defektu modeliuojamas naudojant BBPD formuluotę su ryšių pasisukimu kiekvienam kompozito sluoksniui. Sujungimas tarp kompozito sluoksnių atliekamas tarpsluoksnio PD ryšiais be sukimosi galimybės. Tokio modelio tikslas yra galutinis jo pritaikymas KTF-PD pagrįstai nuovargio analizei, tačiau pirmiausia modelis turėtų būti sukalibruotas statinės apkrovos atveju. Modeliuojamas tik 45 mm ilgio bandinio fragmentas su defektu. PD modelis susideda iš 75 taškų bandinio pločiui (6. 24 pav.). Tuomet PD tinklelio atstumas Δx = 0,33 mm, o PD horizonto dydis δ = 3,1 Δx. Smulkus PD tinklelis parenkamas siekiant kuo tiksliau apibūdinti defekto geometriją. Virtualaus bandinio defektas sukuriamas kaip trūkstami PD taškai bandinio defekto zonoje. PD ryšių pažeidimai modelyje neaktyvūs, kaip parodyta 6.25 pav., taip išvengiama klaidingo statinio ir ciklinio suirimo PD modelyje.
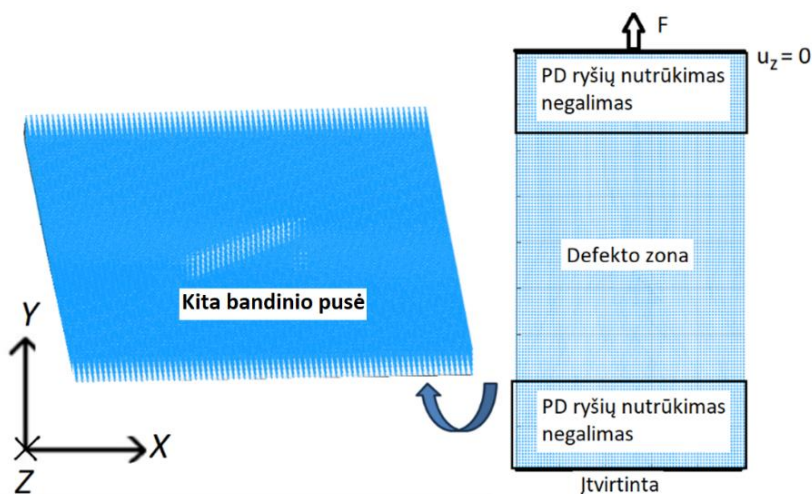
6.25 pav. CFRP bandinio su defektu PD modelis

PD modelio kraštinės sąlygos taip pat pavaizduotos 6.25 pav. Bandinio apačia yra
156

visiškai įtvirtinta, o bandinio viršaus poslinkiai suvaržyti Z kryptimi ir modelis apkraunamas F išorine jėga Y kryptimi (6.25 pav.).

Kompozitiniam BBPD su PD ryšių pasisukimu modeliui turi būti apibrėžti keturi skirtingi PD ryšiai: pluošto, matricos, tarpsluoksnio normaliniai ir tarpsluoksnio šlyties ryšiai. Kadangi PD ryšio apibrėžimas priklauso nuo PD ryšio krypties, vektoriaus $\boldsymbol{\xi}_{xx'} = [X_{x'} - X_x; Y_{x'} - Y_x; Z_{x'} - Z_x]$ komponentai naudojami nustatyti PD ryšio kryptį ir tuomet tipą. Šios procedūros MATLAB programos kodo fragmentas pateiktas 1 priede. PD modelio kalibravimas siekiant nustatyti PD ryšių standumus taip pat atliktas programoje LS-Opt lyginant 0° ir 45° laipsnių kampais iš CFRP plokštės OKE išpjautų bandinių efektinius standumus PD modelyje ir nustatytus eksperimentiškai. PD modelio irimo parametrai: kritinė PD ryšio deformacija $s_c = 0{,}0085$ ir kritinis ryšio pasisukimo kampas $\gamma_c = 0{,}0012$ nustatyti priartėjimo būdu lyginant sumodeliuotą ir eksperimento metu nustatytą bandinio suirimo pobūdį bei sumodeliuotas ir eksperimentines tempimo diagramas. Kalibruoti PD ryšių standumai pateikti 6.5 lentelėje, eksperimentinė ir sumodeliuota bandinių elgsena esant tam pačiam apkrovimui matoma 6.26–6.28 pav.

6.5 lentelė. Kalibruoti kompozito PD ryšių standumai

Parametras	Vertė
Pluošto ryšio standumas C_MAT1, GPa/m^4	$1{,}91 \cdot 10^{23}$
Matricos ryšio standumas C_MAT2, GPa/m^4	$8{,}25 \cdot 10^{22}$
Tarpsluoksnio normalinio ryšio standumas, C_MAT3, GPa/m^4	$3{,}93 \cdot 10^{24}$
Tarpsluoksnio šlyties ryšio standumas, C_MAT4, GPa/m^4	$4{,}89 \cdot 10^{16}$
Matricos ryšio pasisukimo standumas D_MAT2, GPa/m^4	$2{,}39 \cdot 10^{22}$
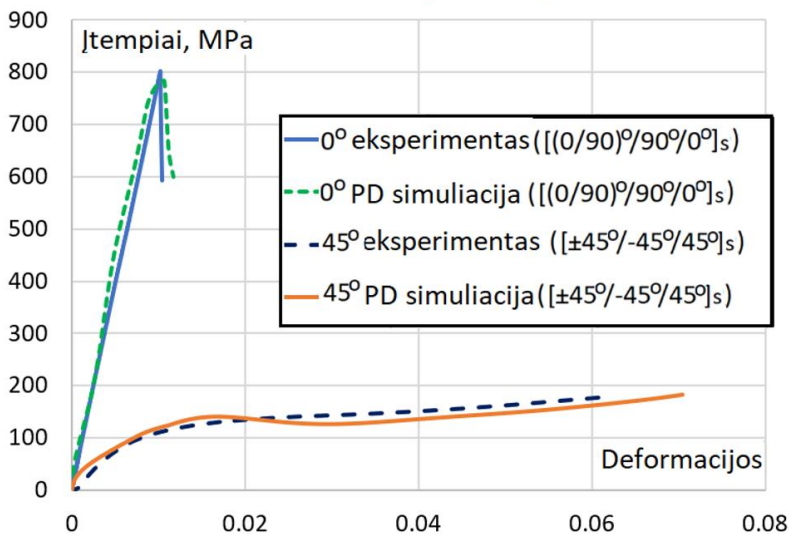
6.26 pav. BBPD su PD ryšių pasisukimu sumodeliuotų ir eksperimentinių tempimo kreivių palyginimas
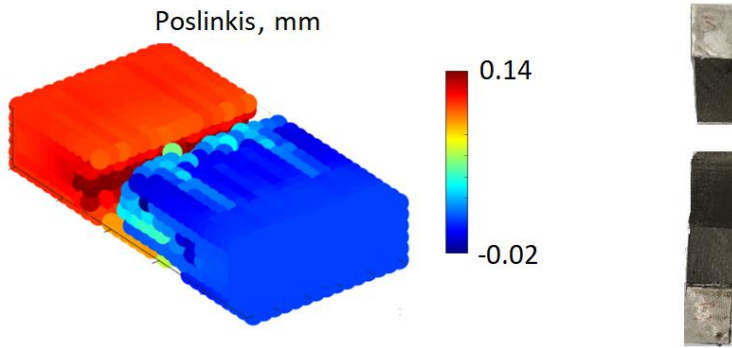
6.27 pav. BBPD su PD ryšių pasisukimu sumodeliuoto ir eksperimentinio suirimo pobūdžių palyginimas, kai bandinys išpjautas 0º kampu
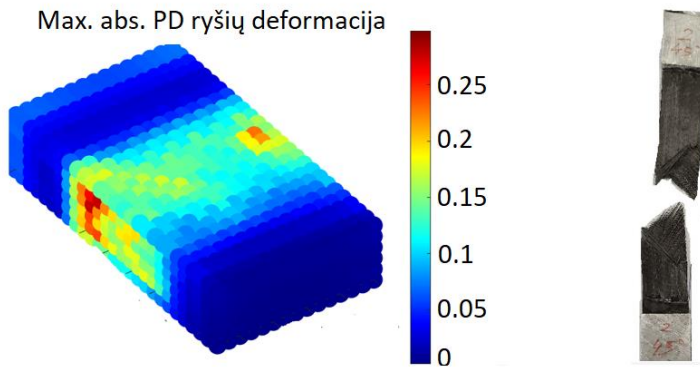
6.28 pav. BBPD su PD ryšių pasisukimu sumodeliuoto ir eksperimentinio suirimo pobūdžių palyginimas, kai bandinys išpjautas 45º kampu

Remiantis 6.26–6.28 pav. pateiktais rezultatais, matomas PD modelio atitikimas eksperimentų rezultatams esant tiek 0º, tiek 45º kampu išpjautiems bandiniams. Vis dėlto dinaminiai efektai, kuriuos sunku nuslopinti sudėtingame kompozito PD modelyje, yra matomi PD sumodeliuotose tempimo diagramose ir lemia skirtumus tarp eksperimentinių tempimo diagramų. Virtualus bandinys PD modelyje yra mažiau standus nei 0º kampu išpjautas bandinys (6.26 pav.) ir standesnis, palyginti su 45º kampu išpjautu bandiniu (6.26 pav.). Taip pat fiksuota modelio šlyties modulio vertė G_{12} lemia skirtumus iki 13 % tarp eksperimentinių ir sumodeliuotų tempimo kreivių.

6.4.5. Kompozito PD modelis esant cikliniam apkrovimui

Sukūrus PD kompozitinio bandinio modelį ir sukalibravus jo tamprumo ir irimo parametrus, galutinis PD modeliavimo etapas yra kompozito ciklinis modelis, pagrįstas KTF. CFRP bandinio su defektu nuovargio analizei naudojamas 6.25 pav. pavaizduotas PD modelis su 1 mm pločio ir 1,5 mm gylio defektu. Kadangi speciali ciklinio bandymo programa netaikoma, nuovargio modeliavimui pasirinkta simetrinė ciklinė 6000 N jėgos apkrova. Gautas efektinių įtempių $\sigma_{ef} = \sqrt{\sigma_{22}{}^2 + \tau_{12}{}^2}$ laukas

158

esant maksimaliai 6000 N tempimo apkrovai parodytas 6.29 pav., a. Sumodeliuota defekto augimo evoliucija matoma 6.29 pav., b–f.
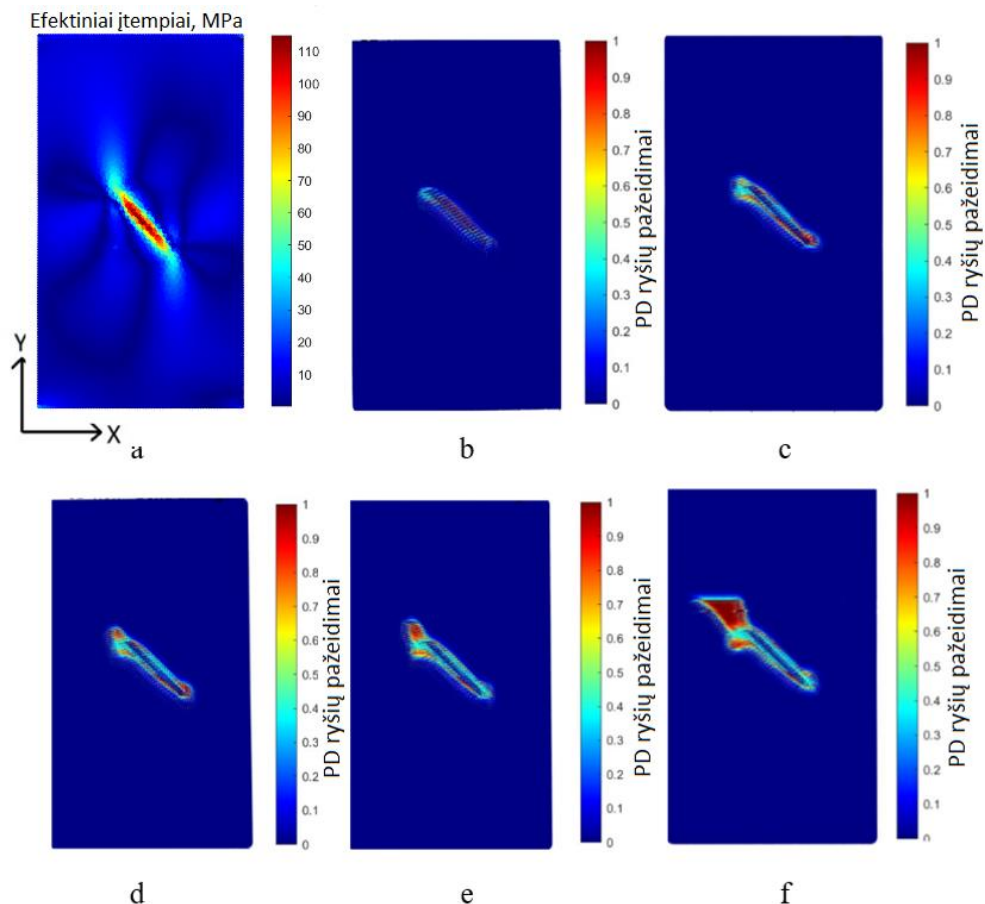
6.29 pav. CFRP kompozito ciklinis modeliavimas taikant KTF-PD teorijas: a – efektiniai įtempiai, b-f – defekto augimas, matomas PD pažeidimų laukuose

PD pažeidimų grafikai parodyti 6.29 pav., b–f. 6. 29 pav., f, grafikas buvo gautas po savaitę trukusios simuliacijos. Matoma, kad medžiagos defektas didėja didėjant ciklų skaičiui, dėl kurio bandinys vėliau suyra. Sukalibravus KTF-PD modelį pagal kompozito S-N kreives, šis gali būti naudojamas tos medžiagos kompozito konstrukcijų patvarumo prognozei.

6.5. IŠVADOS

1. Pakeitus DIC deformacijų skaičiavimo algoritmą PDDO, sumažėja deformacijų triukšmai. Demonstruojamas triukšmo filtravimo poveikis tempimo bandiniui su apskrita skyle, kurio deformacijų laukas gautas taikant PDDO triukšmingam DIC poslinkio laukui. DIC-PDDO metodu galima gauti netriukšmingą su išlikusiomis deformacijų pikų vertėmis lauką, kurio neįmanoma gauti taikant įprastinį DIC deformacijų skaičiavimo algoritmą. Be to, DIC-PDDO metodas padidina matavimo ir erdvinę deformacijų skiriamąsias gebas, kaip rodo 1,34 karto mažesnė metrologinio efektyvumo rodiklio vertė, palyginta su įprastiniu DIC. DIC-PDDO metodas yra veiksmingas lokalizuotoms deformacijoms, pavyzdžiui, medžiagos defektams, įtrūkimams, aptikti.

2. PD ryšio kritinės deformacijos kalibravimas atliekamas remiantis DIC paviršiaus deformacijų matavimais ir optimizavimo programine įranga LS-Opt pasiekiant vidutinę 0,025 optimizavimo tikslo vertę. Tokia procedūra padeda išvengti sudėtingų eksperimentinių medžiagos atplėšimo energijos bandymų ir padidinti PD modelio tikslumą tinkamai parinkus ryšio kritinės deformacijos vertę. Be to, siūloma kalibravimo procedūra supaprastina sudėtingų PD medžiagų modelių parametrų parinkimą, pavyzdžiui, kompozito, SBPD, netiesinės medžiagos ir kt.

3. Įvedus proceso energijos pataisos koeficientus, pagrįstus ciklo histerezės kilpos plotu (plotai buvo išmatuoti atliekant eksperimentinius bandymus), KTF modelis, kalibruotas pagal S-N kreivę tik simetrinei cikliniei apkrovai, teisingai prognozuoja nuovargio trukmę ciklais tiek simetrinei, tiek asimetrinei cikliniei apkrovai. Lyginant simetrinių, asimetrinių $R = -1,5$ ir $R = -0,67$ kintamos amplitudės plieno 316L ciklinio apkrovimo eksperimentų rezultatus, gautos vidutinės 15 % paklaidos tarp eksperimento ir modeliavimo. Be to, PD teorija leidžia simuliuoti nuovargio plyšio iniciacijos ir augimo fazes be jokių iš anksto nustatytų plyšio trajektorijų.

4. Defektus kompozitinėse konstrukcijose galima nustatyti iš paviršiaus deformacijų lauko, išmatuoto DIC metodu veikiant statinei apkrovai, kaip buvo pademonstruota CFRP kompozito ASTM D3039 tempimo bandinių su 1 mm pločio išfrezuotais plyšiais atveju. Defekto gylis konstrukcijoje buvo nustatytas taikant FEMU algoritmą ANSYS programinėje įrangoje su 1,8 % santykine paklaida. 30 % konstrukcijos pločio plyšius, esančius iki 0,8 mm gylyje nuo konstrukcijos paviršiaus, galima aptikti net taikant įprastinį DIC deformacijų skaičiavimo algoritmą. Delaminacijų atveju reikėtų naudoti nepažeistos ir pažeistos konstrukcijos dinaminių charakteristikų palyginimą.

5. Polimeriniai kompozitai su priimtinu tikslumu gali būti modeliuojami net ir taikant BBPD kompozito formuluotę ir įtraukus matricos PD ryšių pasisukimo galimybę. PD ryšio standumai nustatyti taikant optimizavimo metodą, užtikrinantį PD ir eksperimento tampriosios ir suirimo elgsenų atitikimą (didžiausias skirtumas iki 13 %) [(0/90)º/90º/0º]s ir [(±45)º/-45º/45º]s CFRP bandiniuose. KTF, įdiegta į sukurtą BBPD su ryšio pasisukimo kompozito modelį, leidžia modeliuoti ciklinį defekto augimą CFRP bandinyje.

REFERENCES

[1]   Stewart, R. Thermoplastic Composites — Recyclable and Fast to Process. *Reinforced Plastics*, **2011**, *55*, 22–28.

[2]   Datta, D. Introduction to EXtended Finite Element (XFEM) Method. **2013**.

[3]   Bellali, M.A.; Serier, B.; Mokhtari, M.; Campilho, R.D.S.G.; Lebon, F.; Fekirini, H. XFEM and CZM Modeling to Predict the Repair Damage by Composite Patch of Aircraft Structures: Debonding Parameters. *Compos Struct*, **2021**, *266*, 0–13.

[4]   Krueger, R. Virtual Crack Closure Technique: History, Approach, and Applications. *Appl Mech Rev*, **2004**, *57*, 109–143.

[5]   Hu, Z.-C.; Liu, B.; Wang, L.; Cui, Y.-H.; Wang, Y.-W.; Ma, Y.-D.; Sun, W.-W.; Yang, Y. Research Progress of Failure Mechanism of Thermal Barrier Coatings at High Temperature via Finite Element Method. *Coatings*, **2020**, *10*, 732.

[6]   Silling, S. Reformulation of Elasticity Theory for Discontinuities and Long-Range Forces. *J Mech Phys Solids*, **2000**, *48*, 175–209.

[7]   Diehl, P.; Prudhomme, S.; Lévesque, M. A Review of Benchmark Experiments for the Validation of Peridynamics Models. *Journal of Peridynamics and Nonlocal Modeling*, **2019**, *1*, 14–35.

[8]   Silling, S.A.; Askari, A. Peridynamic Model for Fatigue Cracking. **2014**.

[9]   Freimanis, A.; Kaewunruen, S. Peridynamic Analysis of Rail Squats. *Applied Sciences (Switzerland)*, **2018**, *8*.

[10]   Hu, Y.L.; Madenci, E. Peridynamics for Fatigue Life and Residual Strength Prediction of Composite Laminates. *Compos Struct*, **2017**, *160*, 169–184.

[11]   FERTIG, III, R.S. Relating Paris Law Fatigue Crack Growth in Composites with a Physics-Based Fatigue Model. In *American Society for Composites 2017*; DEStech Publications, Inc.: Lancaster, PA, **2017**.

[12]   DIC system https://www.correlatedsolutions.com/digital-image-correlation/ (accessed Jan 15, 2022).

[13]   McCormick, N.J.; Lord, J.D. Practical In Situ Applications of DIC for Large Structures. *Applied Mechanics and Materials*, **2010**, *24–25*, 161–166.

[14]   Sun, Y.; Pang, J.; Wei, F.; Shi, X. Micro- and Nano-DIC Deformation Analysis for Electronic Packaging Applications. In *2006 8th Electronics Packaging Technology Conference*; IEEE, **2006**; pp. 290–296.

[15]   Guo, R.; Li, C.; Niu, Y.; Xian, G. The Fatigue Performances of Carbon Fiber Reinforced Polymer Composites – A Review. *Journal of Materials Research and Technology*, **2022**, *21*, 4773–4789.

[16]   Pervaiz, S.; Kannan, S.; Huo, D.; Mamidala, R. Ecofriendly Inclined Drilling of Carbon Fiber-Reinforced Polymers (CFRP). *The International Journal of Advanced Manufacturing Technology*, **2020**, *111*, 2127–2153.

[17]   Jones, C.J.; Dickson, R.F.; Adam, T.; Reiter, H.; Harris, B. The Environmental Fatigue Behaviour of Reinforced Plastics. In *Proceedings of the Royal Society of London. A. Mathematical and Physical Sciences*; **1984**; Vol. 396, pp. 315–338.

[18]   Sisodia, S.; Gamstedt, E.K.; Edgren, F.; Varna, J. Effects of Voids on Quasi-Static and Tension Fatigue Behaviour of Carbon-Fibre Composite Laminates. *J Compos Mater*, **2015**, *49*, 2137–2148.

[19]   Naik, P.S.; Orangalu, S.A.; Londhe, N. V. Effect of Fiber Weight Fraction on Mechanical Properties of Carbon–Carbon Composites. *Polym Compos*, **2012**, *33*, 1329–1334.

[20]   Brunbauer, J.; Stadler, H.; Pinter, G. Mechanical Properties, Fatigue Damage and

Microstructure of Carbon/Epoxy Laminates Depending on Fibre Volume Content. *Int J Fatigue*, **2015**, *70*, 85–92.

[21] Behera, A.; Dupare, P.; Thawre, M.M.; Ballal, A. Effects of Hygrothermal Aging and Fiber Orientations on Constant Amplitude Fatigue Properties of CFRP Multidirectional Composite Laminates. *Int J Fatigue*, **2020**, *136*, 105590.

[22] Masaki, H.; Shojiro, O.; Gustafson, C.-G.; Keisuke, T. Effect of Matrix Resin on Delamination Fatigue Crack Growth in CFRP Laminates. *Eng Fract Mech*, **1994**, *49*, 35–47.

[23] Tian, J.; Li, C.; Xian, G. Reciprocating Friction and Wear Performances of Nanometer <scp> Sized-TiO $_2$ </Scp> Filled Epoxy Composites. *Polym Compos*, **2021**, *42*, 2061–2072.

[24] Bhowmik, S.; Kumar, S.; Mahakur, V.K. Various Factors Affecting the Fatigue Performance of Natural Fiber-Reinforced Polymer Composites: A Systematic Review. *Iranian Polymer Journal*, **2023**.

[25] Jordan, J.L.; Foley, J.R.; Siviour, C.R. Mechanical Properties of Epon 826/DEA Epoxy. *Mech Time Depend Mater*, **2008**, *12*, 249–272.

[26] Mivehchi, H.; Varvani-Farahani, A. The Effect of Temperature on Fatigue Strength and Cumulative Fatigue Damage of FRP Composites. *Procedia Eng*, **2010**, *2*, 2011–2020.

[27] Li, C.; Xian, G.; Li, H. Tension-Tension Fatigue Performance of a Large-Diameter Pultruded Carbon/Glass Hybrid Rod. *Int J Fatigue*, **2019**, *120*, 141–149.

[28] E. K, G.; R, T. Fatigue Damage Mechanisms in Unidirectional Carbon-Fibre-Reinforced Plastics. *J Mater Sci*, **1999**, *34*, 2535–2546.

[29] Hliva, V.; Szebényi, G. Non-Destructive Evaluation and Damage Determination of Fiber-Reinforced Composites by Digital Image Correlation. *J Nondestr Eval*, **2023**, *42*, 43.

[30] Bowkett, M.; Thanapalan, K. Comparative Analysis of Failure Detection Methods of Composites Materials' Systems. *Systems Science & Control Engineering*, **2017**, *5*, 168–177.

[31] Chen, J.; Yu, Z.; Jin, H. Nondestructive Testing and Evaluation Techniques of Defects in Fiber-Reinforced Polymer Composites: A Review. *Front Mater*, **2022**, *9*.

[32] Park, S.J.; Seo, M.K. *Interface Science and Composites*; **2011**; Vol. 18.

[33] Altmann, A.; Gesell, P.; Drechsler, K. Strength Prediction of Ply Waviness in Composite Materials Considering Matrix Dominated Effects. *Compos Struct*, **2015**, *127*, 51–59.

[34] Fu, Y.; Yao, X. A Review on Manufacturing Defects and Their Detection of Fiber Reinforced Resin Matrix Composites. *Composites Part C: Open Access*, **2022**, *8*, 100276.

[35] Olsson, R. *Factors Influencing the Interlaminar Fracture Toughness and Its Evaluation in Composites*; **1922**.

[36] Drake, D.A.; Sullivan, R.W. Prediction of Delamination Propagation in Polymer Composites. *Compos Part A Appl Sci Manuf*, **2019**, *124*, 105467.

[37] Mekonnen, A.A.; Woo, K.; Kang, M.; Kim, I.-G. Post-Buckling and Delamination Propagation Behavior of Composite Laminates with Embedded Delamination. *Journal of Mechanical Science and Technology*, **2020**, *34*, 1099–1110.

[38] Feng, D.; Aymerich, F. Finite Element Modelling of Damage Induced by Low-Velocity Impact on Composite Laminates. *Compos Struct*, **2014**, *108*, 161–171.

[39] Davidson, B.D.; Krafchak, T.M. Analysis of Instability-Related Delamination Growth Using a Crack Tip Element. *AIAA Journal*, **1993**, *31*, 2130–2136.

[40] Tabiei, A.; Zhang, W. Composite Laminate Delamination Simulation and

Experiment: A Review of Recent Development. *Appl Mech Rev*, **2018**, *70*.

[41]   Fu, Y.; Wang, S.; Yao, X. Compressive Damage and Heat Release of Composite Laminate with Circular Prefabricated Defect, Part I-Experimental Method. *Compos Struct*, **2022**, *279*, 114860.

[42]   Dong, Y.; Ansari, F. Non-Destructive Testing and Evaluation (NDT/NDE) of Civil Structures Rehabilitated Using Fiber Reinforced Polymer (FRP) Composites. In *Service Life Estimation and Extension of Civil Engineering Structures*; Elsevier, **2011**; pp. 193–222.

[43]   Integrity Diagnostics. Integrity Diagnostics Diagnostic Acoustic Emission Solutions for Safety and Performance http://www.idinspections.com/acoustic-emission-phenomenon/ (accessed Nov 15, 2023).

[44]   Aerospeace Engineering. Defects and Non-Destructive Testing in Composites https://aerospaceengineeringblog.com/defects-and-non-destructive-testing-in-composites/ (accessed Nov 16, 2023).

[45]   Li, H.; Zhou, Z. Detection and Characterization of Debonding Defects in Aeronautical Honeycomb Sandwich Composites Using Noncontact Air-Coupled Ultrasonic Testing Technique. *Applied Sciences*, **2019**, *9*, 283.

[46]   Vasudevan, A.; Senthil Kumaran, S.; Naresh, K.; Velmurugan, R.; Shankar, K. Advanced 3D and 2D Damage Assessment of Low Velocity Impact Response of Glass and Kevlar Fiber Reinforced Epoxy Hybrid Composites. *Advances in Materials and Processing Technologies*, **2018**, *4*, 493–510.

[47]   Vaziri Sereshk, M.; Bidhendi, H.M. Evaluation of Revealing and Quantifying Techniques Available for Drilling Delamination in Woven Carbon Fiber-Reinforced Composite Laminates. *J Compos Mater*, **2016**, *50*, 1377–1385.

[48]   Toscano, C.; Riccio, A.; Camerlingo, F.; Meola, C. On the Use of Lock-in Thermography to Monitor Delamination Growth in Composite Panels under Compression. *Science and Engineering of Composite Materials*, **2014**, *21*, 485–492.

[49]   Montanini, R.; Freni, F. Non-Destructive Evaluation of Thick Glass Fiber-Reinforced Composites by Means of Optically Excited Lock-in Thermography. *Compos Part A Appl Sci Manuf*, **2012**, *43*, 2075–2082.

[50]   Kroeger, T. Thermographic Inspection of Composites. *Reinforced Plastics*, **2014**, *58*, 42–43.

[51]   Sun, Y.; Pang, J.; Wei, F.; Shi, X. Micro- and Nano-DIC Deformation Analysis for Electronic Packaging Applications. In *2006 8th Electronics Packaging Technology Conference*; IEEE, **2006**; pp. 290–296.

[52]   Ambu, R.; Aymerich, F.; Bertolino, F. Investigation of the Effect of Damage on the Strength of Notched Composite Laminates by Digital Image Correlation. *J Strain Anal Eng Des*, **2005**, *40*, 451–461.

[53]   Crupi, V.; Guglielmino, E. Application of Digital Image Correlation for the Effect of Glass Fibres on the Strength and Strain to Failure of Polyamide Plastics. *Convegno Igf Xxii …*, **2013**, 1–3.

[54]   Laurin, F.; Charrier, J.-S.; Lévêque, D.; Maire, J.-F.; Mavel, A.; Nuñez, P. Determination of the Properties of Composite Materials Thanks to Digital Image Correlation Measurements. *Procedia IUTAM*, **2012**, *4*, 106–115.

[55]   Jones, E.; Iadicola, M.; Bigger, R.; Blaysat, B.; Boo, C.; Grewer, M.; Hu, J.; Jones, A.; Klein, M.; Raghavan, K.; Reu, P.; Schmidt, T.; Siebert, T.; Simenson, M.; Turner, D.; Vieira, A.; Weikert, T. A Good Practices Guide for Digital Image Correlation http://idics.org/guide/ (accessed Feb 18, 2022).

[56]   Pan, B. Full-Field Strain Measurement Using a Two-Dimensional Savitzky-Golay Digital Differentiator in Digital Image Correlation. *Optical Engineering*, **2007**, *46*,

033601.

[57] Swain, D.; Selvan, S.K.; Thomas, B.P.; Philip, J. Real-Time Detection of Defects on a Honeycomb Composite Sandwich Structure Using Digital Image Correlation (DIC). *Lecture Notes in Mechanical Engineering*, **2022**, 51–61.

[58] Paper, C.; Hyderabad, T. Material Characterization of Carbon Fiber Reinforced Polymer Laminate Using Virtual Fields Method Material Characterization of Carbon Fiber Reinforced Polymer Laminate Using Virtual Fields Method. **2015**, 1–10.

[59] Szebényi, G.; Hliva, V. Detection of Delamination in Polymer Composites by Digital Image Correlation-Experimental Test. *Polymers (Basel)*, **2019**, *11*.

[60] Bataxi; Chen, X.; Yu, Z.; Wang, H.; Bil, C. Strain Monitoring on Damaged Composite Laminates Using Digital Image Correlation. *Procedia Eng*, **2015**, *99*, 353–360.

[61] Devivier, C.; Thompson, D.; Pierron, F.; Wisnom, M.R. Correlation between Full-Field Measurements and Numerical Simulation Results for Multiple Delamination Composite Specimens in Bending. *Applied Mechanics and Materials*, **2010**, *24–25*, 109–114.

[62] Segers, J.; Kersemans, M.; Hedayatrasa, S.; Calderon, J.; Van Paepegem, W. Towards In-Plane Local Defect Resonance for Non-Destructive Testing of Polymers and Composites. *NDT and E International*, **2018**, *98*, 130–133.

[63] Segers, J.; Hedayatrasa, S.; Poelman, G.; Van Paepegem, W.; Kersemans, M. Backside Delamination Detection in Composites through Local Defect Resonance Induced Nonlinear Source Behavior. *J Sound Vib*, **2020**, *479*.

[64] Segers, J.; Hedayatrasa, S.; Poelman, G.; Van Paepegem, W.; Kersemans, M. Probing the Limits of Full-Field Linear Local Defect Resonance Identification for Deep Defect Detection. *Ultrasonics*, **2020**, *105*, 106130.

[65] Ilg, C.; Haufe, A.; Koch, D.; Stander, N.; Witowski, K.; Svedin, Å.; Liewald, M. Application of a Full-Field Calibration Concept for Parameter Identification of HS-Steel with LS-OPT ®. In; **2018**; pp. 1–12.

[66] Martulli, L.M.; Bernasconi, A. An Efficient and Versatile Use of the VCCT for Composites Delamination Growth under Fatigue Loadings in 3D Numerical Analysis: The Sequential Static Fatigue Algorithm. *Int J Fatigue*, **2023**, *170*, 107493.

[67] Barenblatt, G.I. The Mathematical Theory of Equilibrium Cracks in Brittle Fracture. In; **1962**; pp. 55–129.

[68] Sun, C.T.; Jin, Z.-H. Cohesive Zone Model. In *Fracture Mechanics*; Elsevier, **2012**; pp. 227–246.

[69] Nojavan, S.; Schesser, D.; Yang, Q.D. An in Situ Fatigue-CZM for Unified Crack Initiation and Propagation in Composites under Cyclic Loading. *Compos Struct*, **2016**, *146*, 34–49.

[70] Tao, C.; Mukhopadhyay, S.; Zhang, B.; Kawashita, L.F.; Qiu, J.; Hallett, S.R. An Improved Delamination Fatigue Cohesive Interface Model for Complex Three-Dimensional Multi-Interface Cases. *Compos Part A Appl Sci Manuf*, **2018**, *107*, 633–646.

[71] De Cicco, D.; Taheri, F. Delamination Buckling and Crack Propagation Simulations in Fiber-Metal Laminates Using XFEM and Cohesive Elements. *Applied Sciences*, **2018**, *8*, 2440.

[72] Serna Moreno, M.C.; Curiel-Sosa, J.L.; Navarro-Zafra, J.; Martínez Vicente, J.L.; López Cela, J.J. Crack Propagation in a Chopped Glass-Reinforced Composite under Biaxial Testing by Means of XFEM. *Compos Struct*, **2015**, *119*, 264–271.

[73] Wang, Y.; Waisman, H. Progressive Delamination Analysis of Composite Materials Using XFEM and a Discrete Damage Zone Model. *Comput Mech*, **2015**, *55*, 1–26.

[74]   Mollenhauer, D.; Zhou, E.; Hoos, K.; Iarve, E.; Braginsky, M.; Breitzman, T.; R. Multi-Scale Simulation of Delamination Migration. In; n Proceedings of the American Society for Composites: Thirty-First Technical Conference, Williamsburg, VA, USA, 19–22 September 2016; DEStech Publications, Inc.: Williamsburg, VA, USA, **2016**; p. 10.

[75]   Zhang, Y.; Deng, J.; Deng, H.; Ke, B. Peridynamics Simulation of Rock Fracturing under Liquid Carbon Dioxide Blasting. *International Journal of Damage Mechanics*, **2019**, *28*, 1038–1052.

[76]   Nishikawa, M.; Matsuda, N.; Hojo, M. Fiber-Reinforced Composites Modeling Using Peridynamics. In *Peridynamic Modeling, Numerical Techniques, and Applications*; Elsevier, **2021**; pp. 309–326.

[77]   Cao, X.; Qin, X.; Li, H.; Shang, S.; Li, S.; Liu, H. Non-Ordinary State-Based Peridynamic Fatigue Modelling of Composite Laminates with Arbitrary Fibre Orientation. *Theoretical and Applied Fracture Mechanics*, **2022**, *120*, 103393.

[78]   Ha, Y.D.; Bobaru, F. Studies of Dynamic Crack Propagation and Crack Branching with Peridynamics. *Int J Fract*, **2010**, *162*, 229–244.

[79]   Butt, S.N.; Meschke, G. Peridynamic Analysis of Dynamic Fracture: Influence of Peridynamic Horizon, Dimensionality and Specimen Size. *Comput Mech*, **2021**, *67*, 1719–1745.

[80]   Liu, B.; Wang, K.; Bao, R.; Sui, F. The Effects of α/β Phase Interfaces on Fatigue Crack Deflections in Additively Manufactured Titanium Alloy: A Peridynamic Study. *Int J Fatigue*, **2020**, *137*, 105622.

[81]   Bang, D.J.; Ince, A.; Oterkus, E.; Oterkus, S. Crack Growth Modeling and Simulation of a Peridynamic Fatigue Model Based on Numerical and Analytical Solution Approaches. *Theoretical and Applied Fracture Mechanics*, **2021**, *114*, 103026.

[82]   Jung, J.; Seok, J. Fatigue Crack Growth Analysis in Layered Heterogeneous Material Systems Using Peridynamic Approach. *Compos Struct*, **2016**, *152*, 403–407.

[83]   Hu, Y.L.; Madenci, E. Peridynamics for Fatigue Life and Residual Strength Prediction of Composite Laminates. *Compos Struct*, **2017**, *160*, 169–184.

[84]   Bazazzadeh, S.; Zaccariotto, M.; Galvanetto, U. Fatigue Degradation Strategies to Simulate Crack Propagation Using Peridynamic Based Computational Methods. *Latin American Journal of Solids and Structures*, **2019**, *16*.

[85]   Nguyen, C.T.; Oterkus, S.; Oterkus, E. An Energy-Based Peridynamic Model for Fatigue Cracking. *Eng Fract Mech*, **2021**, *241*, 107373.

[86]   Madenci, E.; Barut, A.; Yaghoobi, A.; Phan, N.; Fertig, R.S. Combined Peridynamics and Kinetic Theory of Fracture for Fatigue Failure of Composites under Constant and Variable Amplitude Loading. *Theoretical and Applied Fracture Mechanics*, **2021**, *112*, 102824.

[87]   Liu, R.; Xue, Y.; Lu, X. Coupling of Finite Element Method and Peridynamics to Simulate Ship-Ice Interaction. *J Mar Sci Eng*, **2023**, *11*.

[88]   Madenci, E.; Yaghoobi, A.; Barut, A.; Phan, N. Peridynamics / Digital Imaging Correlation for Tracking Crack Propagation Paths. **2018**.

[89]   Turner, D. Peridynamics-Based Digital Image Correlation Algorithm Suitable for Cracks and Other Discontinuities. *J Eng Mech*, **2015**, *141*, 04014115.

[90]   Li, T.; Gu, X.; Zhang, Q.; Lei, D. Coupled Digital Image Correlation and Peridynamics for Full-Field Deformation Measurement and Local Damage Prediction. *Computer Modeling in Engineering & Sciences*, **2019**, *121*, 425–444.

[91]   Madenci, E.; Yaghoobi, A.; Barut, A.; Phan, N.; Iliopoulos, A.; Michopoulos, J.G.

Peridynamics Enabled Digital Image Correlation for Tracking Crack Paths. *Eng Comput*, **2022**.

[92]   Paris, P.; Erdogan, F. A Critical Analysis of Crack Propagation Laws. *Journal of Basic Engineering*, **1963**, *85*, 528–533.

[93]   Dávila, C.G. From S-N to the Paris Law with a New Mixed-Mode Cohesive Fatigue Model for Delamination in Composites. *Theoretical and Applied Fracture Mechanics*, **2020**, *106*, 102499.

[94]   Zhurkov, S.N. Kinetic Concept of the Strength of Solids. *International journal of fracture mechanics*, **1965**, *1*, 311–323.

[95]   Coleman, B.D. Time Dependence of Mechanical Breakdown Phenomena. *J Appl Phys*, **1956**, *27*, 862–866.

[96]   Zhang, Y.; Madenci, E. A Coupled Peridynamic and Finite Element Approach in ANSYS Framework for Fatigue Life Prediction Based on the Kinetic Theory of Fracture. *Journal of Peridynamics and Nonlocal Modeling*, **2022**, *4*, 51–87.

[97]   Madenci, E.; Diyaroglu, C.; Zhang, Y.; Baber, F.; Guven, I. Combined Peridynamic Theory and Kinetic Theory of Fracture for Solder Joint Fatigue Life Prediction. *Proceedings - Electronic Components and Technology Conference*, **2020**, *2020-June*, 236–248.

[98]   Madenci, E.; Barut, A.; Yaghoobi, A.; Phan, N.; Fertig, R.S. Combined Peridynamics and Kinetic Theory of Fracture for Fatigue Failure of Composites under Constant and Variable Amplitude Loading. *Theoretical and Applied Fracture Mechanics*, **2021**, *112*, 102824.

[99]   George Genevro. Stainless Steel: A metal for all seasons https://www.aviationpros.com/home/article/10387223/stainless-steel-a-metal-for-all-seasons (accessed Feb 25, 2024).

[100]   Ansari, A.H.; Jayakumar, V.; Madhu, S. Wear and Friction Behaviours of Stainless Steel (SS 316) Wire Mesh and Carbon Fibre Reinforced Polymer Composite. In; **2021**; pp. 361–369.

[101]   ASTM International. ASTM D638-10 Standard Test Method For Tensile Properties of Plastics, **2010**.

[102]   ASTM International. *ASTM E1012 Standard Practice for Verification of Testing Frame and Specimen Alignment Under Tensile and Compressive Axial Force Application*; **2019**.

[103]   ASTM International. *ASTM E606/E606M-21 Standard Test Method for Strain-Controlled Fatigue Testing*; **2021**.

[104]   ASTM International. *ASTM D3039 Standard Test Method for Tensile Properties of Polymer Matrix Composite Materials*; **2017**; Vol. 03.

[105]   Madenci, E.; Oterkus, E. *Peridynamic Theory and Its Applications*; Springer New York: New York, NY, **2014**; Vol. 91.

[106]   Trageser, J.; Seleson, P. Bond-Based Peridynamics: A Tale of Two Poisson's Ratios. *Journal of Peridynamics and Nonlocal Modeling*, **2020**, *2*, 278–288.

[107]   Silling, S.; Epton, M.; Weckner, O.; Xu, J.; Askari, E. Peridynamic States and Constitutive Modeling. *J Elast*, **2007**, *88*, 151–184.

[108]   Javili, A.; Morasata, R.; Oterkus, E.; Oterkus, S. Peridynamics Review. *Mathematics and Mechanics of Solids*, **2019**, *24*, 3714–3739.

[109]   Warren, T.L.; Silling, S.A.; Askari, A.; Weckner, O.; Epton, M.A.; Xu, J. A Non-Ordinary State-Based Peridynamic Method to Model Solid Material Deformation and Fracture. *Int J Solids Struct*, **2009**, *46*, 1186–1195.

[110]   Wang, B.; Oterkus, S.; Oterkus, E. Determination of Horizon Size in State-Based Peridynamics. *Continuum Mechanics and Thermodynamics*, **2020**.

[111]   Freimanis, A.; Paeglitis, A. Mesh Sensitivity in Peridynamic Quasi-Static Simulations. *Procedia Eng*, **2017**, *172*, 284–291.

[112]   Ha, Y.D.; Bobaru, F. Characteristics of Dynamic Brittle Fracture Captured with Peridynamics. *Eng Fract Mech*, **2011**, *78*, 1156–1168.

[113]   Bobaru, F.; Hu, W. The Meaning, Selection, and Use of the Peridynamic Horizon and Its Relation to Crack Branching in Brittle Materials. *Int J Fract*, **2012**, *176*, 215–222.

[114]   Hu, W.; Ha, Y.D.; Bobaru, F. Peridynamic Model for Dynamic Fracture in Unidirectional Fiber-Reinforced Composites. *Comput Methods Appl Mech Eng*, **2012**, *217–220*, 247–261.

[115]   Chowdhury, S.R.; Roy, P.; Roy, D.; Reddy, J.N. A Peridynamic Theory for Linear Elastic Shells. *Int J Solids Struct*, **2016**, *84*, 110–132.

[116]   Ahadi, A.; Melin, S. Capturing Nanoscale Effects by Peridynamics. *Mechanics of Advanced Materials and Structures*, **2018**, *25*, 1115–1120.

[117]   Silling, S.A.; Askari, E. A Meshfree Method Based on the Peridynamic Model of Solid Mechanics. *Comput Struct*, **2005**, *83*, 1526–1535.

[118]   Silling, S.A.; Bobaru, F. Peridynamic Modeling of Membranes and Fibers. *Int J Non Linear Mech*, **2005**, *40*, 395–409.

[119]   Wang, F.; Liu, L.; Liu, Q.; Zhang, Z.; Su, L.; Xue, D. Studies of Bimaterial Interface Fracture with Peridynamics. **2015**.

[120]   Madenci, E.; Roy, P.; Behera, D. *Advances in Peridynamics*; Springer International Publishing: Cham, **2022**.

[121]   Karpenko, O.; Oterkus, S.; Oterkus, E. An In-Depth Investigation of Critical Stretch Based Failure Criterion in Ordinary State-Based Peridynamics. *Int J Fract*, **2020**, *226*, 97–119.

[122]   Dipasquale, D.; Sarego, G.; Zaccariotto, M.; Galvanetto, U. A Discussion on Failure Criteria for Ordinary State-Based Peridynamics. *Eng Fract Mech*, **2017**, *186*, 378–398.

[123]   Willberg, C.; Rädel, M. An Energy Based Peridynamic State-based Failure Criterion. *Pamm*, **2018**, *18*, 3–4.

[124]   Foster, J.; Silling, S.A.; Chen, W. AN ENERGY BASED FAILURE CRITERION FOR USE WITH PERIDYNAMIC STATES. *Int J Multiscale Comput Eng*, **2011**, *9*, 675–688.

[125]   Madenci, E.; Barut, A.; Dorduncu, M. *Peridynamic Differential Operator for Numerical Analysis*; Springer International Publishing: Cham, **2019**.

[126]   Li, P.; Hao, Z.M.; Zhen, W.Q. A Stabilized Non-Ordinary State-Based Peridynamic Model. *Comput Methods Appl Mech Eng*, **2018**, *339*, 262–280.

[127]   Seleson, P.; Littlewood, D.J. Convergence Studies in Meshfree Peridynamic Simulations. *Computers & Mathematics with Applications*, **2016**, *71*, 2432–2448.

[128]   Le, Q. V.; Bobaru, F. Surface Corrections for Peridynamic Models in Elasticity and Fracture. *Comput Mech*, **2018**, *61*, 499–518.

[129]   Macek, R.W.; Silling, S.A. Peridynamics via Finite Element Analysis. *Finite Elements in Analysis and Design*, **2007**, *43*, 1169–1178.

[130]   Sarego, G.; Le, Q. V.; Bobaru, F.; Zaccariotto, M.; Galvanetto, U. Linearized State-based Peridynamics for 2-D Problems. *Int J Numer Methods Eng*, **2016**, *108*, 1174–1197.

[131]   Speronello, M. Study of Computational Peridynamics, Explicit and Implicit Time Integration, Viscoelastic Material, University of Padua: Padua, **2015**.

[132]   Kilic, B.; Madenci, E. An Adaptive Dynamic Relaxation Method for Quasi-Static Simulations Using the Peridynamic Theory. *Theoretical and Applied Fracture*

Mechanics, **2010**, *53*, 194–204.

[133] Underwood, P. Dynamic Relaxation. *Computational Methods for Transient Analysis*, **1983**, *1*, 245–265.

[134] Group, C. and M.M. Methodology - Meshfree Method https://www.lstc-cmmg.org/peri-dynamics (accessed Nov 20, 2023).

[135] Kahraman, T.; Yolum, U.; Guler, M.A. Implementation of Peridynamic Theory to LS-DYNA for Prediction of Crack Propagation in a Composite Lamina. *10th European LS-DYNA Conference 2015*, **2015**, 3–12.

[136] Parks, M.L.; Littlewood, D.J.; Mitchell, J.A.; Silling, S.A. Peridigm Users' Guide v1.0.0 (SAND 2012-7800). *Sandia National Laboratories*, **2012**, *7800*.

[137] Parks, M.L.; Lehoucq, R.B.; Plimpton, S.J.; Silling, S.A. Implementing Peridynamics within a Molecular Dynamics Code. *Comput Phys Commun*, **2008**, *179*, 777–783.

[138] MATLAB peridynamics open source code https://github.com/chtld/BB_PD (accessed Jan 4, 2022).

[139] Huang, D.; Lu, G.; Qiao, P. An Improved Peridynamic Approach for Quasi-Static Elastic Deformation and Brittle Fracture Analysis. *Int J Mech Sci*, **2015**, *94–95*, 111–122.

[140] Hansen, A.C.; Baker-Jarvis, J. A Rate Dependent Kinetic Theory of Fracture for Polymers. *Int J Fract*, **1990**, *44*, 221–231.

[141] Bhuiyan, F.H.; Fertig, R.S. A PFA Methodology to Investigate UD Composites in Fatigue Comprising a KTF-Based Model for Matrix Damage and Stochastic Fiber Failure Prediction. *Compos Struct*, **2022**, *279*, 114724.

[142] Kawai, M.; Suda, H. Effects of Non-Negative Mean Stress on the Off-Axis Fatigue Behavior of Unidirectional Carbon/Epoxy Composites at Room Temperature. *J Compos Mater*, **2004**, *38*, 833–854.

[143] Fertig, R.S.; Kenik, D.J. Predicting Composite Fatigue Life Using Constituent-Level Physics. *Collection of Technical Papers - AIAA/ASME/ASCE/AHS/ASC Structures, Structural Dynamics and Materials Conference*, **2011**, 1–11.

[144] Fertig III, R.S.; Kenik, D.J. Physics-Based Fatigue Life Prediction of Composite Structures. *Nafems 2011*, **2011**, 1–12.

[145] Bhuiyan, F.H.; Fertig, R.S. A Combined Creep and Fatigue Prediction Methodology for Fiber-Reinforced Polymer Composites Based on the Kinetic Theory of Fracture. In *Creep and Fatigue in Polymer Matrix Composites*; Elsevier, **2019**; pp. 349–402.

[146] Madenci, E.; Barut, A.; Phan, N. Bond-Based Peridynamics with Stretch and Rotation Kinematics for Opening and Shearing Modes of Fracture. *Journal of Peridynamics and Nonlocal Modeling*, **2021**, *3*, 211–254.

[147] Vaitkunas, T.; Griskevicius, P.; Adumitroaie, A. Peridynamic Approach to Digital Image Correlation Strain Calculation Algorithm. *Applied Sciences*, **2022**, *12*, 6550.

[148] digitalimagecorrelation.org. A practical guide to DIC https://digitalimagecorrelation.org/#patterning (accessed Feb 5, 2022).

[149] Correlated Solutions. Minimizing noise and bias in 3D DIC http://www.correlatedsolutions.com/supportcontent/dic-noise-bias.pdf (accessed Feb 28, 2022).

[150] Correlated Solutions. VIC-3D Reference Manual http://www.correlatedsolutions.com/supportcontent/VIC-3D-8-Manual.pdf (accessed Feb 23, 2022).

[151] Correlated Solutions. Subset, Step Size and Strain Filter Selection https://correlated.kayako.com/article/44-subset-step-size-and-strain-filter-selection (accessed Feb 19, 2022).

[152] Schreier, H.; Orteu, J.-J.; Sutton, M.A. *Image Correlation for Shape, Motion and Deformation Measurements*; Springer US: Boston, MA, **2009**.

[153] Correlated Solutions. *Application Note AN -1703 Strain Filter Selection*; **2017**; Vol. 49.

[154] Jones, E.; Iadicola, M.; Bigger, R.; Blaysat, B.; Boo, C.; Grewer, M.; Hu, J.; Jones, A.; Klein, M.; Raghavan, K.; Reu, P.; Schmidt, T.; Siebert, T.; Simenson, M.; Turner, D.; Vieira, A.; Weikert, T. A Good Practices Guide for Digital Image Correlation http://idics.org/guide/ (accessed Feb 18, 2022).

[155] DIC Challenge. Test images https://idics.org/challenge/ (accessed Jun 20, 2022).

[156] Turner, D.; Lehoucq, R.; Reu, P. A Nonlocal Strain Measure for DIC. *Conference Proceedings of the Society for Experimental Mechanics Series*, **2016**, *3*, 79–83.

[157] Turner, D. *Towards DIC Methods Robust Enough to Characterize Degradation of Materials*; **2015**.

[158] Turner, D. How Nonlocal Formulations Are Changing the Modeling and Simulalation Landscape at Sandia. **2017**.

[159] Reu, P.L.; Blaysat, B.; Andó, E.; Bhattacharya, K.; Couture, C.; Couty, V.; Deb, D.; Fayad, S.S.; Iadicola, M.A.; Jaminion, S.; Klein, M.; Landauer, A.K.; Lava, P.; Liu, M.; Luan, L.K.; Olufsen, S.N.; Réthoré, J.; Roubin, E.; Seidl, D.T.; Siebert, T.; Stamati, O.; Toussaint, E.; Turner, D.; Vemulapati, C.S.R.; Weikert, T.; Witz, J.F.; Witzel, O.; Yang, J. DIC Challenge 2.0: Developing Images and Guidelines for Evaluating Accuracy and Resolution of 2D Analyses. *Exp Mech*, **2022**, *62*, 639–654.

[160] Blaysat, B.; Neggers, J.; Grédiac, M.; Sur, F. Towards Criteria Characterizing the Metrological Performance of Full-Field Measurement Techniques: Application to the Comparison Between Local and Global Versions of DIC. *Exp Mech*, **2020**, *60*, 393–407.

[161] Stander, N.; Witowski, K.; Ilg, C.; Basudhar, A.; Svedin, A.; Gandikota, I.; Haufe, A.; Du Bois, S.; Kirpicev, D. DIC-Based Full-Field Calibration Using LS-OPT: An Update. *15th International LS-DYNA® Users Conference*, **2018**, *2*, 1–18.

[162] DYNAmore GmbH. Full Field Calibration using LS-OPT 6 https://www.youtube.com/watch?v=hQJ9rM3blXU (accessed Jan 15, 2022).

[163] Stander, N.; Basudhar, A.; et. al. *LS-OPT User ' s Manual: A Design Optimization and Probabilistic Analysis Tool for the Engineering Analyst*; **2019**.

[164] Product Data Sheet. Biresin CH83 Composite resin system (Version 04/2021) https://industry.sika.com/content/dam/dms/global-industry/o/Biresin-CR83-New.pdf (accessed Jan 26, 2022).

[165] Bajpai, A.; Alapati, A.K.; Klingler, A.; Wetzel, B. Tensile Properties, Fracture Mechanics Properties and Toughening Mechanisms of Epoxy Systems Modified with Soft Block Copolymers, Rigid Tio2 Nanoparticles and Their Hybrids. *Journal of Composites Science*, **2018**, *2*, 1–17.

[166] Beswick, J.; Roux, J.C. Le; Martin, L.; Doremus, O. INCEFA-SCALE Project – Phases 1 and 2 of Testing Programme. In *ASME Pressure Vessels and Piping Conference PVP2023*; Atlanta, USA, **2022**.

[167] Mahato, S.; Špakauskas, K.; Vaitkūnas, T.; Griškevičius, P. Embedded Defect Identification of a Multi-Layered Carbon Fibre Composite by Combining Different Numerical Model and DIC Technique. In *Proceedings of 27th International Scientific Conference MECHANIKA 2023*; Kaunas, **2023**; pp. 1–6.

[168] Andresen, H.W.; Echtermeyer, A.T. Critical Energy Release Rate for a CSM Reinforced Carbon Fibre Composite/Steel Bonding. *Compos Part A Appl Sci Manuf*, **2006**, *37*, 742–751.

[169] Vaitkunas, T.; Griskevicius, P.; Adumitroaie, A. Peridynamic Material Model

Calibration Based on Digital Image Correlation Experimental Measurements. *Mechanics of Advanced Materials and Structures*, **2022**, 1–14.

[170]   Madenci, E. *Peridynamics Theory and Applications for Computational Mechanics Basics of Peridynamics*; **2021**.

[171]   Karpenko, O.; Oterkus, S.; Oterkus, E. Peridynamic Investigation of the Effect of Porosity on Fatigue Nucleation for Additively Manufactured Titanium Alloy Ti6Al4V. *Theoretical and Applied Fracture Mechanics*, **2021**, *112*, 102925.

[172]   Shin, D.S.; Kim, Y.S.; Jeon, E.S. Approximation of Non-Linear Stress-Strain Curve for GFRP Tensile Specimens by Inverse Method. *Applied Sciences (Switzerland)*, **2019**, *9*.

[173]   Chopra, O.; Stevens, G.L. *Effect of LWR Water Environments on the Fatigue Life of Reactor Materials Final Report*; **2018**.

[174]   Faserverbundwerkstoffe Composite Technlogy. Carbon fibre plates OKE https://www.r-g.de/en/art/616F (accessed Dec 11, 2023).

[175]   Pan, B.; Qian, K.; Xie, H.; Asundi, A. Two-Dimensional Digital Image Correlation for in-Plane Displacement and Strain Measurement: A Review. *Meas Sci Technol*, **2009**, *20*, 062001.

[176]   Vaitkunas, T.; Griskevicius, P.; Dundulis, G.; Courtin, S. Numerical Investigation of Asymmetric Strain Controlled Fatigue Behaviour Using Kinetic Theory of Fracture and Peridynamics. **2023**.

CURRICULUM VITAE
Tomas Vaitkūnas
tomas.vaitkunas@ktu.lt

Education:
2014-2018 Bachelor's degree in Mechanical Engineering, Kaunas University of Technology (KTU), Kaunas, Lithuania
2018-2020 Master's degree in Mechanical Engineering, Kaunas University of Technology (KTU), Kaunas, Lithuania
2020-2024 PhD studies in Mechanical Engineering, Kaunas University of Technology (KTU), Kaunas, Lithuania

Professional experience:
Since Apr 01, 2023: Project *SITPComp* Junior Researcher at the Department of Mechanical Engineering, Kaunas University of Technology
Since Feb 01, 2023: Project *INCEFA* scale 2020–2025 Junior Researcher at the Department of Mechanical Engineering, Kaunas University of Technology
Apr 01, 2021 04 01 – Jun 30, 2022: *CompExSHM* Project Junior Researcher at the Department of Mechanical Engineering, Kaunas University of Technology
2020: Junior Researcher at Department of Mechanical Engineering at Kaunas University of Technology
2020: Mechanical engineer at enterprise *Vaizduotė*

Research interests:
Digital Image Correlation, Peridynamics, Fracture mechanics, Fatigue, Composite materials

LIST OF PUBLICATIONS ON THE SUBJECT OF THE DOCTORAL THESIS

ARTICLES IN PEER-REVIEWED SCIENTIFIC PUBLICATIONS
Indexed in the Web of Science with Impact Factor
International (foreign) publishers

1. [S1; US] Vaitkunas, Tomas; Griskevicius, Paulius; Adumitroaie, Adi. Peridynamic material model calibration based on digital image correlation experimental measurements // *Mechanics of Advanced Materials and Structures*. Philadelphia, PA: Taylor & Francis. ISSN 1537-6494. eISSN 1537-6532. 2023, Vol. 30, iss. 20, p. 4132–4145. DOI: 10.1080/15376494.2022.2089934. [Science Citation Index Expanded (Web of Science); Scopus] [IF: 2.800; AIF: 5.100; IF/AIF: 0.549; Q2 (2022, InCites JCR SCIE)] [CiteScore: 5.10; SNIP: 1.351; SJR: 0.669; Q1 (2022, Scopus Sources)] [FoR: T 009] [Input: 0.334]
2. [S1; CH; OA] Vaitkunas, Tomas; Griskevicius, Paulius; Adumitroaie, Adi. Peridynamic approach to digital image correlation strain calculation algorithm // *Applied Sciences*. Basel: MDPI. ISSN 2076-3417. 2022, Vol. 12, iss. 13, art. No. 6550, p. 1–20. DOI: 10.3390/app12136550. [Science Citation Index Expanded (Web of Science); Scopus; Dimensions] [IF: 2.700; AIF: 5.550; IF/AIF: 0.486; Q2 (2022, InCites JCR SCIE)] [CiteScore: 4.50; SNIP: 0.974; SJR: 0.492; Q1 (2022, Scopus Sources)] [FoR: T 009] [Input: 0.334]

National (Lithuanian) publishers

1. [S1; LT; OA] Vaitkūnas, Tomas; Griškevičius, Paulius; Špakauskas, Kęstutis. Interlaminar strength analysis of bonded carbon fiber rods // *Mechanika*. Kaunas: KTU. ISSN 1392-1207. eISSN 2029-6983. 2021, Vol. 27, No. 2, p. 101–106. DOI: 10.5755/j02.mech.25872. [Science Citation Index Expanded (Web of Science); Scopus; Academic Search Complete] [IF: 0.579; AIF: 4.412; IF/AIF: 0.131; Q4 (2021, InCites JCR SCIE)] [CiteScore: 1.00; SNIP: 0.331; SJR: 0.169; Q4 (2021, Scopus Sources)] [FoR: T 009] [Input: 0.334]

Indexed in other Web of Science or Scopus publications International (foreign) publishers

1. [P1a; GB; OA] Eidukynas, D.; Adumitroaie, A.; Griškevičius, P.; Grigaliūnas, V.; Vaitkūnas, T. Finite element model updating approach for structural health monitoring of lightweight structures using response surface optimization // IOP conference series: Materials science and engineering: 16th international conference: *Mechatronic Systems and Materials* (MSM 2021), 30.06 – 02.07.2021, Vilnius, Lithuania. Bristol: IOP Publishing. ISSN 1757-8981. eISSN 1757-899X. 2022, Vol. 1239, art. No. 012002, p. 1–7. DOI: 10.1088/1757899X/1239/1/012002. [Conference Proceedings Citation Index – Science (Web of Science)] [SNIP: 0.517; SJR: 0.000 (2022, Scopus Sources)] [FoR: T 009] [Input: 0.200]

National (Lithuanian) publishers

1. [P1b; LT; OA] Khan, Mehran; Mahato, Swarup; Eidukynas, Darius; Vaitkunas, Tomas. Influence determination of damage to mechanical structure based on modal analysis and modal assurance criterion // *Vibroengineering Procedia*: 56th international conference on vibroengineering, Zittau, Germany, May 16, 2022. Kaunas: JVE international. ISSN 2345-0533. eISSN 2538-8479. 2022, Vol. 42, p. 27–32. DOI: 10.21595/vp.2022.22554. [Scopus; Dimensions; Scilit] [CiteScore: 1.00; SNIP: 0.308; SJR: 0.165; Q3 (2022, Scopus Sources)] [FoR: T 009] [Input: 0.250]

In peer-reviewed conference proceedings (not indexed in the Web of Science or Scopus) National (Lithuanian) publishers

1. [P1d; LT] Mahato, Swarup; Špakauskas, Kęstutis; Vaitkūnas, Tomas; Gunasekaran, Kishorekanna; Griškevičius, Paulius. Embedded defect identification of a multi-layered carbon fibre composite by combining different numerical model and DIC technique // *Mechanika 2023*: proceedings of the 27th international scientific conference, 26 May 2023, Kaunas University of Technology, Lithuania: proceedings. Kaunas: Kaunas University of Technology. ISSN 2783-5677. 2023, p. 70–75. [FoR: T 009] [Input: 0.200]

Scientific Conferences:

1. T. Vaitkūnas, P. Griškevičius, A. Adumitoraie, V. Grigaliūnas, *Peridynamic approach improving strain calculation accuracy in Digital Image Correlation system*, *Mechanika 2021*, May 21, 2021, Kaunas, Lithuania
2. T. Vaitkūnas, P. Griškevičius, A. Admitroaie, V. Grigaliūnas, D. Eidukynas, *Combining Peridynamics and Digital Image Correlation algorithms for challenging strain calculations*, *16th U.S. National Congress on Computational Mechanics*, July 25–29, 2021.
3. T. Vaitkūnas, P. Griškevičius, A. Adumitoraie, *Peridynamics for fatigue crack evaluation in cylindrical test specimens*, *2nd International Conference on Computations for Science and Engineering*, August 30 – September 2, 2022, Rimini Riviera, Italy
4. Mahato, Swarup & Špakauskas, Kęstutis & Vaitkūnas, Tomas & Griškevičius, Paulius. (2023). *Embedded defect identification of a multi-layered carbon fibre composite by combining different numerical model and DIC technique*, *Mechanika 2023*, May 26, 2023, Kaunas, Lithuania
5. T. Vaitkūnas, P. Griškevičius, E. Jasiunienė, K. Špakauskas, *Composite Structural Integrity Evaluation Based on Digital Image Correlation together with Peridynamics and Finite Element Updating*, *3rd International Conference on Computations for Science and Engineering*, *20–23 September 2023*, Naples, Italy

Appendix A. Matlab code for PD bond definition according to the PD bond direction

```matlab
% Build bond data - determine the bond type and
stiffness connecting node
% [(0/90)/90/0]s layup

Layer=nNODES/6;
for kBond=1:nBONDS

    nodei=BONDLIST(kBond,1);
    nodej=BONDLIST(kBond,2);
    dzeta=COORDINATES(nodej,:)-COORDINATES(nodei,:);
    bondStiffnessTemp_C=C_MAT2;
    bondStiffnessTemp_D=D_MAT2;
    BONDTYPE(kBond)=1;

  if  dzeta(3)==0

     if nodei<=Layer & nodej<=Layer
         if dzeta(1)==0 | dzeta(2)==0
    bondStiffnessTemp_C=C_MAT1;
    bondStiffnessTemp_D=D_MAT1;
    BONDTYPE(kBond)=0;
         end
     end

     if nodei>5*Layer & nodej>5*Layer
         if dzeta(1)==0 | dzeta(2)==0
    bondStiffnessTemp_C=C_MAT1;
    bondStiffnessTemp_D=D_MAT1;
    BONDTYPE(kBond)=0;
         end
     end

     if (nodei>Layer & nodei<=2*Layer) & (nodej>Layer &
nodej<=2*Layer)
         if  dzeta(1)==0
    bondStiffnessTemp_C=C_MAT1;
    bondStiffnessTemp_D=D_MAT1;
    BONDTYPE(kBond)=0;
         end
     end
```

```matlab
    if (nodei>4*Layer & nodei<=5*Layer) &
(nodej>4*Layer & nodej<=5*Layer)
        if  dzeta(1)==0
    bondStiffnessTemp_C=C_MAT1;
    bondStiffnessTemp_D=D_MAT1;
    BONDTYPE(kBond)=0;
        end
     end

    if (nodei>2*Layer & nodei<=4*Layer) & (nodej>2*Layer
& nodej<=4*Layer)
        if  dzeta(2)==0
    bondStiffnessTemp_C=C_MAT1;
    bondStiffnessTemp_D=D_MAT1;
    BONDTYPE(kBond)=0;
        end
     end

    if dzeta(3)~=0
        if dzeta(1)==0 & dzeta(2)==0
    bondStiffnessTemp_C=C_MAT3;
    bondStiffnessTemp_D=D_MAT3;
    BONDTYPE(kBond)=2;
        end
        if dzeta(3)*dzeta(2)*dzeta(1)~=0
    bondStiffnessTemp_C=C_MAT4;
    bondStiffnessTemp_D=D_MAT4;
    BONDTYPE(kBond)=2;
        end
    end
 end
```

```matlab
% Build bond data - determine the bond type and
stiffness connecting node
% [(+-45)/-45/45]s layup

Layer=nNODES/6;
for kBond=1:nBONDS
    nodei=BONDLIST(kBond,1);
    nodej=BONDLIST(kBond,2);
    dzeta=COORDINATES(nodej,:)-COORDINATES(nodei,:);
    bondStiffnessTemp_C=C_MAT2;
    bondStiffnessTemp_D=D_MAT2;
    BONDTYPE(kBond)=1;

 if  dzeta(3)==0

     if nodei<=Layer & nodej<=Layer
         if abs(dzeta(1)-dzeta(2))<1e-12 |
abs(dzeta(1)+dzeta(2))<1e-12
    bondStiffnessTemp_C=C_MAT1;
    bondStiffnessTemp_D=D_MAT1;
    BONDTYPE(kBond)=0;
         end
     end

     if nodei>5*Layer & nodej>5*Layer
         if abs(dzeta(1)-dzeta(2))<1e-12 |
abs(dzeta(1)+dzeta(2))<1e-12
    bondStiffnessTemp_C=C_MAT1;
    bondStiffnessTemp_D=D_MAT1;
    BONDTYPE(kBond)=0;
         end
     end

     if (nodei>Layer & nodei<=2*Layer) & (nodej>Layer &
nodej<=2*Layer)
         if    abs(dzeta(1)+dzeta(2))<1e-12
    bondStiffnessTemp_C=C_MAT1;
    bondStiffnessTemp_D=D_MAT1;
    BONDTYPE(kBond)=0;
         end
     end

     if (nodei>4*Layer & nodei<=5*Layer) &
(nodej>4*Layer & nodej<=5*Layer)
         if    abs(dzeta(1)+dzeta(2))<1e-12
    bondStiffnessTemp_C=C_MAT1;
```

```matlab
    bondStiffnessTemp_D=D_MAT1;
    BONDTYPE(kBond)=0;
        end
     end

    if (nodei>2*Layer & nodei<=4*Layer) & (nodej>2*Layer
& nodej<=4*Layer)
        if  abs(dzeta(1)-dzeta(2))<1e-12
    bondStiffnessTemp_C=C_MAT1;
    bondStiffnessTemp_D=D_MAT1;
    BONDTYPE(kBond)=0;
        end
     end
 end
    if dzeta(3)~=0
        if dzeta(1)==0 & dzeta(2)==0
    bondStiffnessTemp_C=C_MAT3;
    bondStiffnessTemp_D=D_MAT3;
    BONDTYPE(kBond)=2;
        end
        if dzeta(3)*dzeta(2)*dzeta(1)~=0
    bondStiffnessTemp_C=C_MAT4;
    bondStiffnessTemp_D=D_MAT4;
    BONDTYPE(kBond)=2;
        end
    end

if  MATERIALFLAG(nodej)==0
BONDTYPE1(kBond)=1;
end
```

ACKNOWLEDGEMENTS